

# ORIENT

## Directional Data Analysis Software

Frederick W. Vollmer

Version 3.24  
July 1, 2024



This page intentionally left blank

Cover: Crenulation cleavage ( $S_2$ ) in Mount Merino Formation argillite, Dutchess County, New York, formed during the Middle Ordovician emplacement of the Taconic Allochthon. Bedding ( $S_0$ ) is subparallel to an early slaty cleavage ( $S_1$ ). The cleavages are axial planar to two generations of superimposed folds. Width of view 6 mm CPL. Photograph by F.W. Vollmer, from Vollmer and Walker (2009).

---

## Preface

### License

Orient software and accompanying documentation are Copyright ©1986-2024 Frederick W. Vollmer. They come with no warranties or guarantees of any kind. The software is free and may be downloaded and used without cost, however the author retains all rights to the source, binary code and accompanying files. It may not be redistributed or posted online. Citation must be given for any usage that leads to publication.

This software and any related documentation are provided as is without warranty of any kind, either express or implied, including, without limitation, the implied warranties or merchantability, fitness for a particular purpose, or non-infringement. The entire risk arising out of use or performance of the software remains with you.

### Citation

Orient is the result of countless hours of work over more than three decades. Algorithms used in the program come from numerous sources, however many have been developed by the author. Some of these have not yet been published and are the subject of papers in preparation. The program is released freely with the hope that the scientific community will find it useful, and will respect priority of unpublished algorithms. In return for free use, any significant use of the software for analyzing data or preparing diagrams should be cited in publications, presentations, reports, or other works. Please cite

- [Vollmer, F. W., 1995](#). C program for automatic contouring of spherical orientation data using a modified Kamb method. *Computers & Geosciences*, v. 21, p. 31-49.  
[https://doi.org/10.1016/0098-3004\(94\)00058-3](https://doi.org/10.1016/0098-3004(94)00058-3)
- [Vollmer, F. W., 2015](#). Orient 3: a new integrated software program for orientation data analysis, kinematic analysis, spherical projections, and Schmidt plots. *Geological Society of America Abstracts with Programs*, v. 47, n. 7, p. 49.

and any of the following as appropriate

- [Vollmer, F. W., 1990](#). An application of eigenvalue methods to structural domain analysis. *Geological Society of America Bulletin*, v. 102, p. 786-791.  
[https://doi.org/10.1130/0016-7606\(1990\)102<0786:AAOEMT>2.3.CO;2](https://doi.org/10.1130/0016-7606(1990)102<0786:AAOEMT>2.3.CO;2)
- [Vollmer, F. W., 2020](#). Representing progressive fabric paths on a triangular plot using a fabric density index and crystal axes eigenvector barycenters. *Geological Society of America Abstracts with Programs*, v. 52, n. 6,  
doi: 10.1130/abs/2020AM-358862
- [Vollmer, F. W., 2022](#). An eigenvalue based k-means approach to geologic cluster analysis. *Geological Society of America Abstracts with Programs*. v. 54, n. 5.  
doi: 10.1130/abs/2022AM-383667
- [Vollmer, F. W., 2024](#). Orient: Directional data analysis software.  
<https://vollmerf.github.io/orient/>

Registration of the software is free and only requires an email. This helps determine usage, and justify the time spent in its upkeep. To register, send an email to [vollmerf@gmail.com](mailto:vollmerf@gmail.com) with your user name, affiliation, and usage. You will not be placed on a mailing list or contacted again, other than my response with a thank you. For example, send me an email with something like

User: Dr. Frederick Vollmer

Affiliation: SUNY New Paltz, Geology Department

---

Usage: Research on joint orientation analysis, Catskill Mountains, NY; fault kinematics in the Hudson Valley fold and thrust belt. Teaching an undergraduate structural geology course with approximately 35 students per year.

If you are specific about the type of project, this can help me in developing future releases. If you are using it in a teaching environment, I am interested to know the course and approximate number of students. I am happy to take questions, bug reports, and feature requests, although given this is done in my spare time, I apologize in advance if an email does not get answered in a timely fashion. Also please take the time to read the fine manual before asking a question, I have put a lot of time into it, and your question may be answered herein.

## Installation

Orient runs on the majority of modern laptop and desktop computers. It is compiled for 64 bit macOS (Intel and ARM), Windows (Intel/AMD64), and Linux (Intel/AMD64) operating systems. There are two versions for macOS, Intel and ARM, the ARM version is substantially faster on the newer M1+ (Apple silicon) Macs. The Linux version is only tested on Ubuntu, but should work on related distributions.

On Windows, unzip the zip file (zip) using the *Extract All* option, and drag the Orient application (Orient.exe) to any desired location. Do not try to run the Orient application from inside the zip file, this is a common installation problem. The Example Data folder should also be copied for use in the tutorials.

On Linux unpack the gzip file (tar.gz), and copy the Orient application (Orient) to any desired location. The Example Data folder should also be copied for use in the tutorials. The graphical toolkit GTK2 is required, but is most likely preinstalled.

On Macintosh macOS, double click the disk image file (dmg), and drag the Orient application to your *Applications* folder, or other desired location. Do not try to run the software from the disk image installation window, it must be moved to another location on your computer. The Example Data folder can also be copied to the same location.

Gatekeeper in macOS must be set to allow applications other than from the *App Store* to be opened. To do so, open the macOS *System Preferences* and the *Security & Privacy* option. Under *General* select *Allow apps downloaded from: Anywhere*. If that is not available, try *App Store and identified developers*. The first time you run Orient *Control-Click* on the icon, and select *Open*. In recent versions of macOS, Apple has become increasingly strict about requiring developers to register. This requires a \$99 annual fee, which I am reluctant to pay as a free software developer.

The User Manual is a separate download, or can be accessed from the *Help - Orient User Manual* command. To deinstall simply delete the Orient application, and optionally delete the preference folder, which is stored in your computer's application preferences folder. No other files are installed on your computer.

## Troubleshooting

First, see if your question is answered in this user manual. Second, check to make sure you are using the latest version. Third, on Windows, double check to make sure that the Orient folder was completely extracted from the zip file. This option appears when right, or Control, clicking on the zip file. Fourth, try quitting Orient and restarting it while holding down the Shift key. This allows deletion of the preferences file (Orient.json) and will restore the default settings.

If all else fails, you may have found a bug. I am happy to get bug reports, as it helps me improve the program. To report a bug please email me with full information about your operating system, such as Windows 7 Professional, Macintosh macOS 10.10.5, or Ubuntu 16.04.1, and which version of Orient you are using (check the About dialog). If an error message occurs, take a screen shot or copy down the exact wording. Include any additional details, for example the data file that causes the

---

error, and the exact sequence of commands that cause the error. A screenshot may also help. If it is one of the provided example data files, include the name and extension (e.g., csv or xls). I normally respond quickly, but programming is done in my spare time, so don't be offended if I am not on top of it. If confirmed, your help will be acknowledged in my list of bug hunters.

# Contents

## Preface

<b>1</b>	<b>Introduction</b>	<b>1</b>
1.1	Overview . . . . .	1
1.2	Tutorial: Quick Start . . . . .	3
1.3	List of Symbols . . . . .	6
1.4	Graphics Export . . . . .	6
1.5	Gradients and Colormaps . . . . .	7
<b>2</b>	<b>Data Entry and Import</b>	<b>11</b>
2.1	Data Entry . . . . .	12
2.2	Interactive Data Entry . . . . .	13
2.3	Hidden Data Display . . . . .	13
2.4	Linking and Line-Plane Pairs . . . . .	14
2.5	Spreadsheet Integration . . . . .	16
2.6	Tutorial: Spreadsheet Data . . . . .	18
2.7	Data File Import . . . . .	19
2.7.1	StraboSpot . . . . .	19
2.7.2	Moment Tensor (CMT) . . . . .	21
2.7.3	Kinematic Data Import . . . . .	23
2.8	Data File Templates . . . . .	24
2.9	Project Files . . . . .	24
2.10	Digitizing Data . . . . .	25
2.11	Simulating Data . . . . .	26
2.12	Data Weighting and Sampling Correction . . . . .	28
2.13	Weight and Characteristic Classification . . . . .	31
<b>3</b>	<b>Circular Plots</b>	<b>33</b>
3.1	Scatter Plots . . . . .	33
3.2	Circular Histograms . . . . .	33
3.3	Kernel Density Estimate . . . . .	37
3.4	Circular Mean . . . . .	38
3.5	Circular Median . . . . .	39
3.6	Rayleigh Uniformity Test . . . . .	39
3.7	Vertical Component and Rake Plots . . . . .	40
<b>4</b>	<b>Spherical Projections</b>	<b>43</b>
4.1	Geometry of Spherical Projections . . . . .	43
4.2	Orthographic Projection . . . . .	44
4.3	Stereographic Projection . . . . .	44
4.4	Equal-Area Projection . . . . .	45
4.5	Equidistant Projection . . . . .	46
4.6	Density Distortion . . . . .	46
4.7	History and Terminology . . . . .	47
4.8	Maxima and Eigenvectors . . . . .	49
4.9	Tutorial: Scatter Plots . . . . .	51
4.10	Contouring . . . . .	51
4.11	Tutorial: Contour Plots . . . . .	53
4.12	Transparency, Animation, and Lighting . . . . .	54

<b>5</b>	<b>Coordinates and Rotations</b>	<b>57</b>
5.1	Geographic Coordinates . . . . .	57
5.2	Tutorial: Geographic Coordinates . . . . .	61
5.3	Tutorial: Rotation to Maxima . . . . .	61
5.4	Net Rotation . . . . .	62
5.5	Data Rotation . . . . .	62
<b>6</b>	<b>Confidence and Uniformity</b>	<b>64</b>
6.1	Spherical Distributions . . . . .	64
6.2	Parameter Estimation . . . . .	65
6.3	Bootstrapping . . . . .	68
6.4	Bingham Uniformity and Intensity . . . . .	69
6.5	Fabric Density Index . . . . .	70
6.6	Uniformity Tests . . . . .	70
<b>7</b>	<b>Eigenvalue Fabric Plots</b>	<b>73</b>
7.1	Triangular Fabric Plot . . . . .	73
7.2	Fabric Domain Plot . . . . .	74
7.3	Fabric Barycenter Plot . . . . .	75
<b>8</b>	<b>Conical Data, Small Circles, and Ellipses</b>	<b>78</b>
8.1	Conical Data . . . . .	78
8.2	Small Circles . . . . .	79
8.3	Small Circle Confidence . . . . .	80
8.4	Spherical Ellipses . . . . .	80
<b>9</b>	<b>Kinematic and Dynamic Analysis</b>	<b>83</b>
9.1	Entering Line-Plane Pairs . . . . .	83
9.2	Orthonormalization and Line Calculation . . . . .	84
9.3	M Planes and Tangent Lines . . . . .	84
9.4	Moment Tensors . . . . .	87
9.5	Coulomb Stress Inversion . . . . .	88
9.6	Stress Tensor Inversion . . . . .	90
9.7	Moment Triangle Plot . . . . .	91
<b>10</b>	<b>Frames</b>	<b>95</b>
10.1	Rotation Matrices . . . . .	95
10.2	Rotation Plots . . . . .	96
10.3	LS Tectonites . . . . .	97
10.4	Kinematics . . . . .	101
<b>11</b>	<b>Cluster Analysis</b>	<b>106</b>
11.1	Axis Partitioning . . . . .	106
11.2	Vector Partitioning . . . . .	108
11.3	Girdle Partitioning . . . . .	111
11.4	Slip Partitioning . . . . .	111
11.5	Distance Minimization . . . . .	113
11.6	Evaluation of Partitioning . . . . .	114
11.7	Fuzzy Partitioning . . . . .	115
11.8	Density Partitioning . . . . .	116



<b>12 Slope Stability</b>	<b>117</b>
12.1 Plane Failure . . . . .	117
12.2 Wedge Failure . . . . .	118
12.3 Toppling Failure . . . . .	119
<b>13 Multiple Point Calculations</b>	<b>122</b>
13.1 Maxima Calculations . . . . .	122
13.2 Trend Surface Analysis . . . . .	123
<b>14 Ternary Plots</b>	<b>125</b>
14.1 Geometry of Ternary Plots . . . . .	125
14.2 Tutorial: QFL Plot . . . . .	125
14.3 Contouring Ternary Plots . . . . .	126
<b>15 UTM, Web Maps, and Google Earth</b>	<b>128</b>
15.1 UTM, Latitude, Longitude, Conversion . . . . .	128
15.2 Google and Web Maps . . . . .	128
15.3 Google Earth . . . . .	128
15.4 Tutorial: UTM Conversion and Web Maps . . . . .	130
15.5 Tutorial: Web Maps and Google Earth . . . . .	130
<b>16 Orientation Fields and Domains</b>	<b>132</b>
16.1 Orientation Fields . . . . .	132
16.2 Structural Domain Analysis . . . . .	133
16.3 Tutorial: Domain Analysis . . . . .	135
<b>Acknowledgements</b>	<b>139</b>
<b>Disclaimer</b>	<b>139</b>
<b>References</b>	<b>140</b>
<b>FAQ</b>	<b>145</b>
<b>Appendix I</b>	<b>146</b>

# 1 Introduction

Orient is a fast, professional, easy to use spherical projection and directional data analysis program. In 1986 the first release of Orient implemented modified Kamb contouring (Figure 1.1a), triangular fabric plots (Figure 1.4b), orientation fields (Figure 1.4a), and automated structural domain analysis (Vollmer, 1988, 1989, 1990, 1993, 1995). Continued development over decades has increased speed, added implementations on multiple operating systems, numerous new tools, including interactive data analysis, UTM coordinate conversions, cluster analysis, bootstrap statistics, data digitizing, kernel density estimation, ternary plots, kinematic and fault stress analysis, and file integration with applications such as Microsoft Excel, LibreOffice, Adobe Illustrator, InkScape, CorelDRAW, StraboSpot, Google Maps, and Google Earth.

## 1.1 Overview

Orient is for plotting and analyzing directional data, data that can be described by the orientation of an axis or vector in space or, equivalently, by a position on a sphere or circle. Examples of data that are represented by unit vectors (directed) or axes (undirected) include geologic bedding planes, fault planes, fault slip directions, fold axes, paleomagnetic vectors, glacial striations, current flow directions, crystallographic axes, earthquake epicenters, cosmic ray arrival directions, comet orbital planes, positions of galaxies, and the locations of objects on the Earth. Orient can be used to analyze a wide variety of data types, although many examples come from structural geology, which requires extensive manipulation and analysis of directional data.

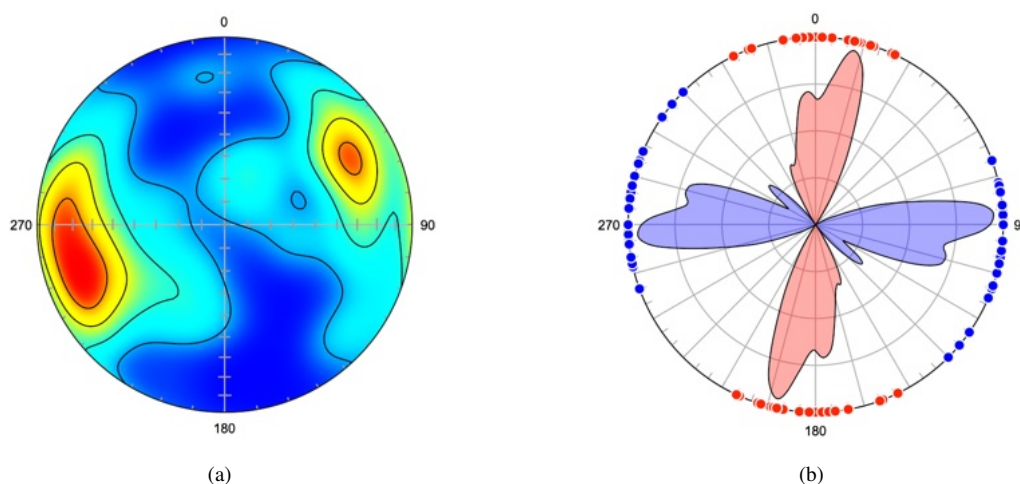


Figure 1.1: Examples of axis (undirected) data plots. (a) Lower hemisphere equal-area modified Kamb contour plot of ice crystallographic axes with contours at  $2\sigma$ , an example of undirected axis data. Data from Kamb (1959). (b) Kernel density estimates on a circular plot of the mean strikes of two joint sets in each of 24 counties in central New York. Data from Parker (1942).

Spherical projections (Figure 1.1a and 1.2) are used to display three dimensional directional data by projecting the surface of a sphere, or hemisphere, onto a plane. Lines and planes in space are considered to pass through the center of a unit sphere, so lines are represented by two diametrically opposed piercing points. Planes are represented by the great circle generated by their intersection with the sphere or, more compactly, by their normal.

Common spherical projections include *equal-area*, used for creating Schmidt nets, and *stereographic*, used for creating Wulff nets (stereonets), these can be plotted on either upper or lower hemispheres. Point distributions are analyzed by contouring and by computing eigenvectors of undirected data from orientation tensors, or vector means of directed data. Figure 1.2 is an example of directed data plotted on both upper and lower hemispheres. Data sets and projections can be rotated about any axis in space, or to principal axes. For two-dimensional data, such as wind or current directions,

circular plots and circular histograms, including equal-area and frequency polygon diagrams, can be prepared (Figure 1.1b).

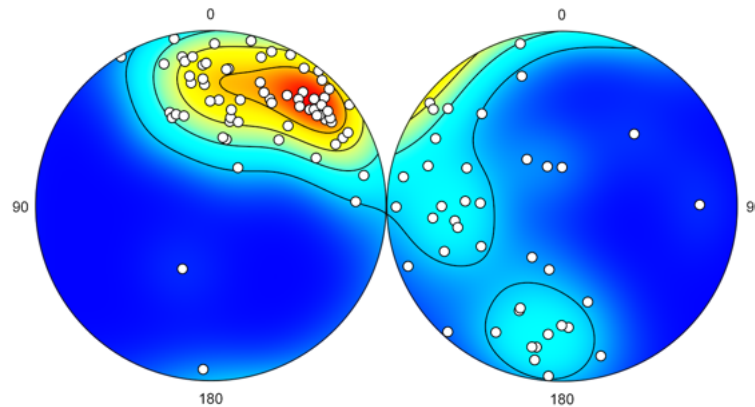


Figure 1.2: Examples of vectorial (directed) data plots. Schmidt plots of magnetic remanence directions from Precambrian volcanics, with modified Kamb contours at 20% of the maximum density. Projection on left is inverted to display upward directed data on a lower hemisphere plot. The two plots were created separately, and combined with an image editing program. Data from Schmidt and Embleton (1985) in Fisher et al. (1987, Table B6)

Data can be input as spherical coordinates, longitude and latitude, azimuth and altitude, declination and inclination, trend and plunge, strike and dip, or other measurements. Routines are available for kinematic and dynamic analysis of fault data, which are represented by a plane and the direction of slip within that plane, by generating P and T kinematic axes, tangent line diagrams (Figure 1.3a), and beachball plots (Figure 1.3b).

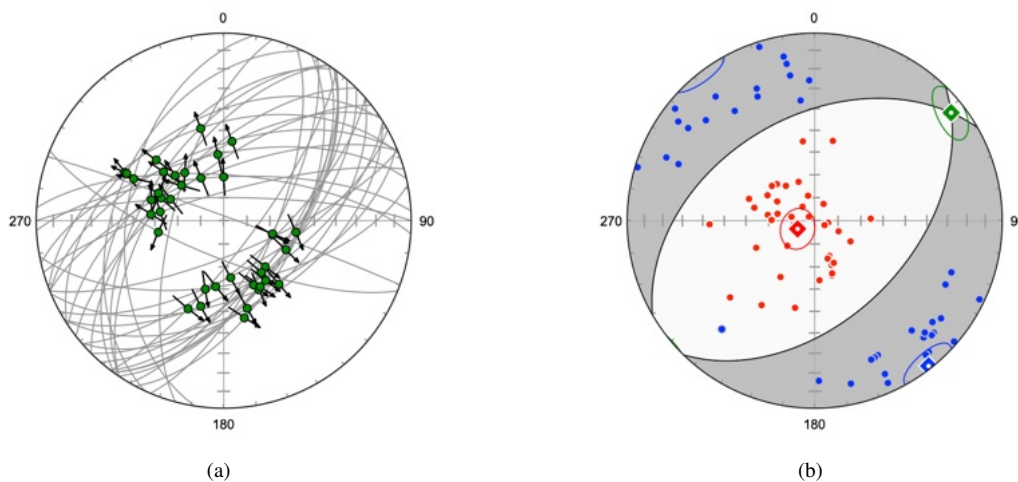


Figure 1.3: Examples of kinematic data on lower hemisphere equal-area (Schmidt) plots. (a) Slip tangent plot of 38 normal faults from Crete, Greece. Each data point is defined by both a plane and a directed line. The fault planes are plotted as gray arcs, and the slip lineations in them are plotted as green circles. The arrows are tangent lines at the lineation, and represent the instantaneous motion (vorticity vector) of the hanging wall. (b) Lower hemisphere equal-area beachball diagram of data in (a) showing quadrants of P shortening (red) and T extension (blue) kinematic axes. The plot includes 95% bootstrap confidence cones about the maximum axes. Data from Angelier (1979).

Spherical projections represent data directions, but not spacial locations. Therefore routines for orientation maps are included to analyze spacial distributions of orientation data, such as the location of domains of cylindrical folding in polydeformed regions (Figures 1.4). The distribution of data can be plotted globally (Figure 1.5a), and located on internet maps, such as Google Maps, and in Google Earth.

Additional features include statistical confidence cones, bootstrap analysis, plotting of conical

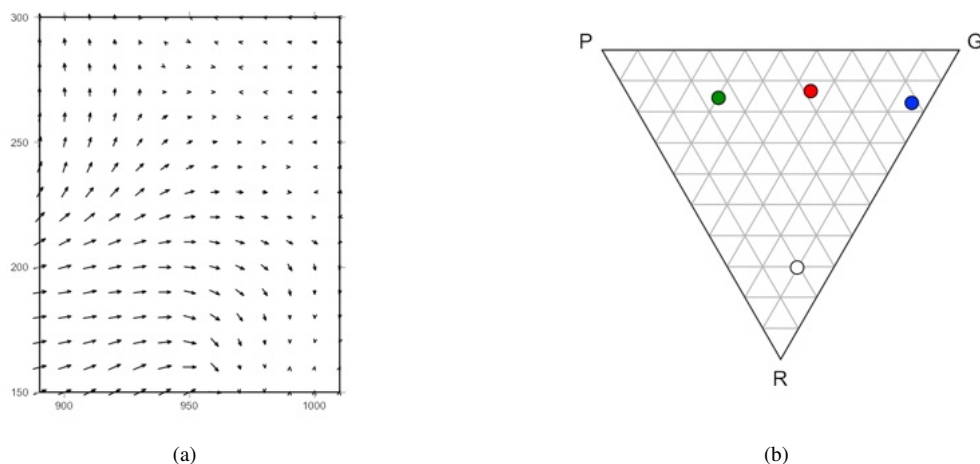


Figure 1.4: Examples of Orient map domain analysis plots. (a) An axis orientation field of eigenfoliation dip lines derived from 625 foliation planes, Dovrefjell mountains, Norway. (b) Triangular fabric diagram (PGR) diagram showing the variations in orientation data symmetry among three structural domains defined from the data. Data from Vollmer (1985).

data, small circle fitting with confidence regions, triangular plots, and projection and data rotations. Figure 1.5b, for example, is a projection of poles to bedding in graywacke rotated to display fold a cylindrical axis.

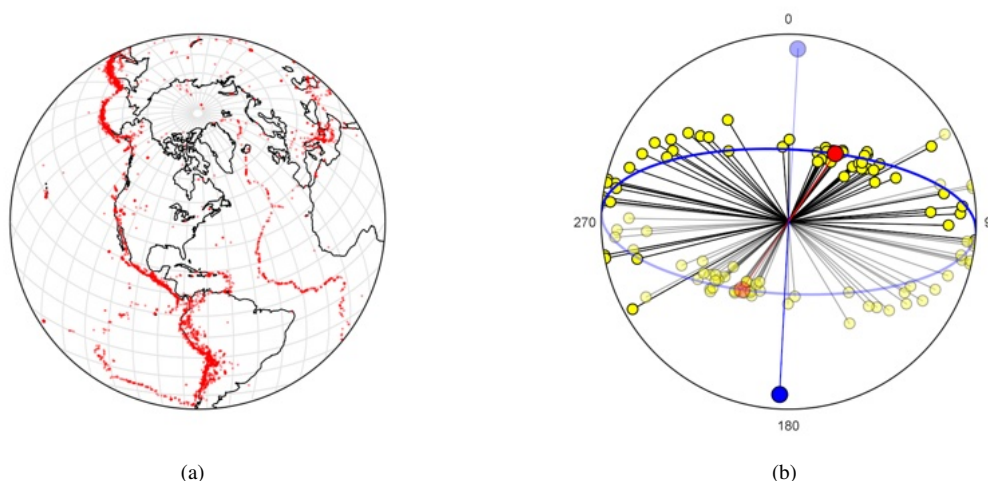


Figure 1.5: (a) Upper hemisphere equal-area projection of 14,229 earthquake epicenters (1980-1990) with continental outlines, an example of directed data plotted by latitude and longitude. Data from NOAA. (b) Lower hemisphere orthographic projection of 56 poles to bedding in graywacke, Albany County, New York rotated to visualize the relationship of bedding plane normals to the fold axis. Data from Vollmer (1981).

## 1.2 Tutorial: Quick Start

Open the Orient application to display the data entry spreadsheet, the main data display area (Figure 1.6a). By default, columns for *ID*, *Station*, *Strike*, *Dip*, *Trend*, and *Plunge* are displayed. The *ID* is an integer that should be unique for each measurement, *Station* is any alphanumeric string to identify the measurement. The command *View - Data Columns* displays all available columns. Measurements for planes should be entered in the strike and dip columns, and lines in the trend and plunge columns, these can be changed, for example, if you prefer dip direction instead of strike.

Use the mouse to examine the icons in the toolbar, from left to right these are *Open*, *Save As*, *Spherical Projection*, *Circular Histogram*, *PGR Plot*, *Orientation Map*, and *Preferences*. Most of

the controls in Orient have tooltips, or help hints displayed when the mouse is over the control. Click on the *Spherical Projection* icon to display the default Schmidt net (Figure 1.6b). The toolbar icons in the spherical projection window are *Export Image As*, *Find*, *Zoom In*, *Zoom Out*, *Zoom Fit*, and *Preferences*. *Export Image As* will save the image to a graphics file in various raster (Adobe Photoshop and GIMP compatible) and vector (Adobe Illustrator and Inkscape compatible).

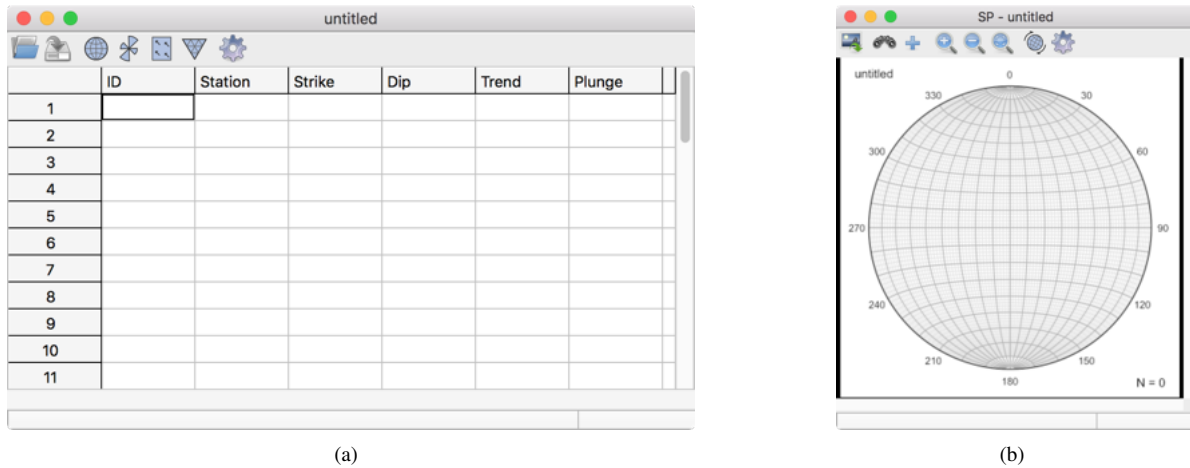


Figure 1.6: (a) The Orient data window showing the default spreadsheet. (b) Spherical projection displaying the default Schmidt net.

Begin entering numbers into the strike and dip columns, and the spherical projection will automatically update to display them. The *ID* number is automatically incremented, although a different number can be entered. To identify individual measurements, click on the *Find* icon in the spherical projection window. In this mode any selected data point will be highlighted in the other window, a colored bar in the spreadsheet, and a selection icon in the spherical projection window (Figure 1.7). Double-clicking on a plotted data point will bring up the spreadsheet with the data point selected. This is useful for check potential data point outliers.

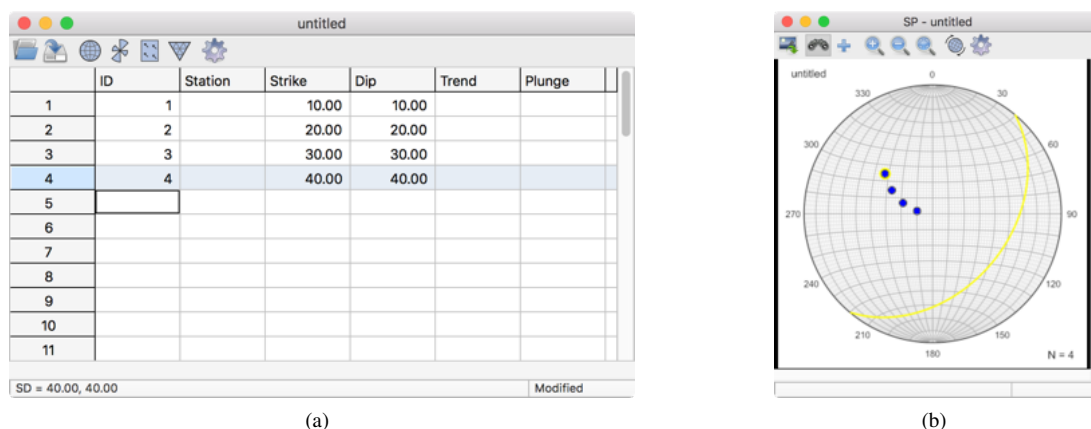


Figure 1.7: Display of entered data in spreadsheet and spherical projection plot (Schmidt plot). The data point can be selected in either window, and will be highlighted in the other window by using the *Plot - Find* command.

To only display data items selected in the spreadsheet, turn on the *Plot - Selected* option in the *Graph* menu. In this case only the selected data will be displayed on the spherical projection plot. Turn this off before continuing the tutorial.

Next, open the *Preferences* dialog by clicking its icon. Select the *Spherical Projection - Symbols* panel. Notice that the data *Type* is listed as *Default.S*. A dot namespace notation is used to identify data type subsets. In this case, no data *Type* has been specified, so it is named *Default*, and *S* indicates that it is a plane, using common geological notation (Turner and Weiss, 1963). Check the *Great circle*

checkbox (Figure 1.8a), and press *OK*. The Schmidt plot will update to show great circle arcs for each of the data points (Figure 1.8b).

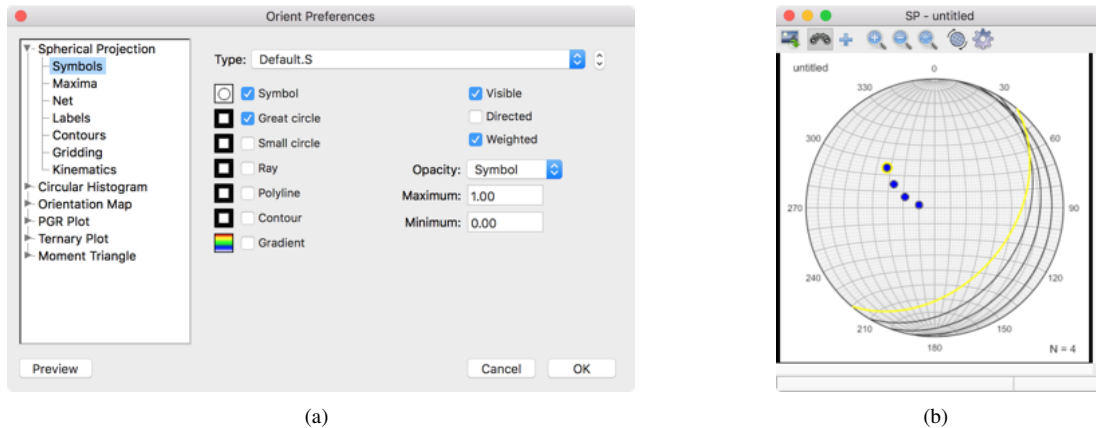


Figure 1.8: (a) The *Orient Preferences* dialog showing *Spherical Projection* data *Symbols* options with the *Great circle* option checked. (b) The spherical projection plot after checking the *Great circle* option.

A common calculation required for geologic data analysis is to determine the intersection between two planes, such as bedding and cleavage, or of multiple bedding planes to find a fold axis. To do this, select the planes, the result is displayed in the status bar, and plotted on the spherical projection. The result is displayed in the status bar as the calculated maximum (*Max*) and minimum (*Min*) eigenvectors, and also displayed on the spherical projection plot (Figure 1.9a). If two planes are selected, these correspond to the mean (*Max*) and plane intersection (*Min*). If multiple data points are selected the maximum (*Max*) is the mean, and the minimum (*Min*) is the best-fit intersection, or axis (Section 4.8).

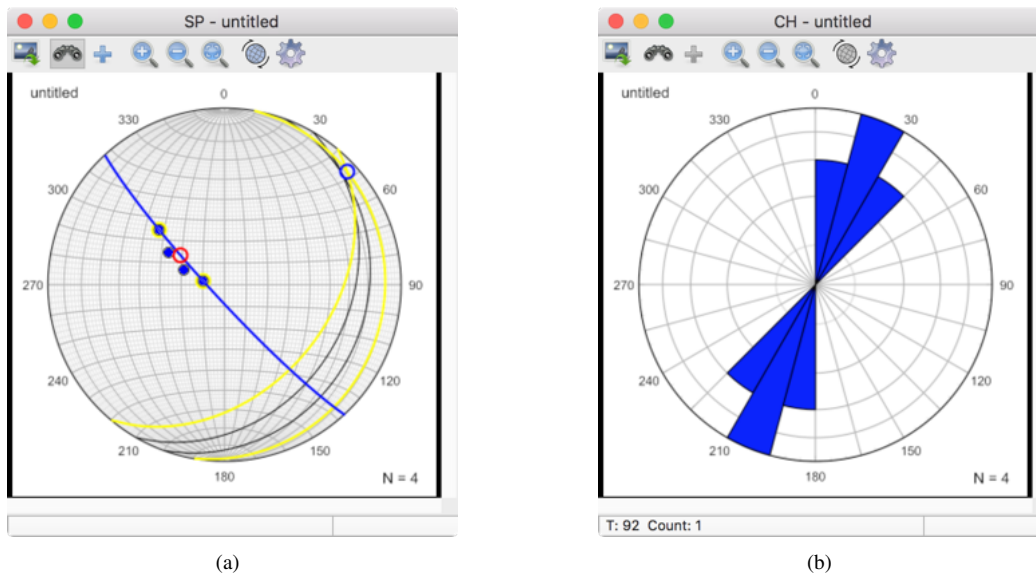


Figure 1.9: (a) The Schmidt plot after selecting two data points. The planes intersection is shown as a blue circle, and the corresponding plane passing through the data points, as a blue great circle arc. The mean of the two planes is displayed as a red circle. (b) Circular histogram of the data displayed using their undirected strikes.

Finally, click on the *Circular Histogram* icon to display a circular histogram, or rose diagram, of the data (Figure 1.9b). By default the data is displayed as undirected data, and planes are displayed by their strikes. This can be changed to directed data, or, for example, dip directions.

### 1.3 List of Symbols

Table 1.2 lists the symbols used in this document. The *Header* column is the text equivalent that is used in the spreadsheet column headers, control labels, or output in the log window.

Symbol	Header	Meaning
$A_n, G_n, F_n$		Test statistics for uniformity.
$c_n$		Concentration parameter for spherical cross-validation estimation.
$d_i$	Fit	Goodness of fit, $-1 \dots 1$ , for the $i^{\text{th}}$ fault plane, $i = 1 \dots n$ .
$d_A$		Similarity measure ("distance") between axes, $0 \dots 1$ .
$d_V$		Similarity measure ("distance") between vectors, $0 \dots 1$ .
$\bar{D}$		Normalized goodness of fit, $-1 \dots 1$ , for a sample of $n$ faults.
$f_k$		Estimated density at the $k^{\text{th}}$ grid location.
$I, I_P$		Bingham eigenvalue fabric intensity and protolith intensity indexes.
$K, H, d_K$		Kernel density function, bandwidth matrix, and their dimensions.
$L$		Line orientation defined by unit vector or axis.
$n$		Number of measurements in a sample.
$p_i$		The normal to the $i^{\text{th}}$ plane in a sample, $i = 1 \dots n$ .
$P, G, R, B, D$		Triangular fabric plot eigenvalue indexes.
$P, M, T$		Kinematic strain rate or dynamic stress axes, depending on context.
$\bar{R}$		Mean resultant vector.
$R_f$		Rotation matrix for an orthogonal frame.
$s_i$		The slip direction in the $i^{\text{th}}$ plane in a sample, $i = 1 \dots n$ .
$\bar{S}$		Plane orientation defined by unit normal vector or axis.
$S_e$	Se	Standard error in degrees.
$U$		Bingham eigenvalue uniformity statistic.
$V$		Circular variance.
$w_i$	Weight	Weight of the $i^{\text{th}}$ unit axis or vector of a sample, $i = 1 \dots n$ .
$x_i$		The $i^{\text{th}}$ axis or vector of a sample, where $i = 1 \dots n$ .
$\bar{x}$		Spherical mean vector.
$\bar{x}_0$		Normalized spherical mean vector.
$X, Y, Z$		Cartesian references axes, default is Right or East, Top or North, and Up.
$Z_\alpha$		Z statistic for a given confidence level $\alpha$ .
$\alpha_c$	AlphaC	Semi-apical angle of a cone.
$\epsilon_i$		Eigenvectors of the normalized orientation tensor, $i = 1 \dots 3$ .
$\kappa$	Kappa	von Mises distribution concentration parameter.
$\mu_F, \phi_F, C_0$	MuF, PhiF	Coefficient of friction, angle of friction, Coulomb cohesion.
$\mu_{ij}$		Cluster inclusion coefficient of data point $i$ in cluster $j$ .
$\tau_i$		The traction vector on the $i^{\text{th}}$ plane in a sample, $i = 1 \dots n$ .
$\tau_{Ni}$		The normal traction vector on the $i^{\text{th}}$ plane in a sample, $i = 1 \dots n$ .
$\tau_{Si}$		The shear traction vector on the $i^{\text{th}}$ plane in a sample, $i = 1 \dots n$ .
$\sigma$		Standard deviation.
$\bar{\sigma}$		Stress tensor.
$\sigma_1, \sigma_2, \sigma_3$		Maximum, intermediate, and minimum principal values of the stress tensor.
$\theta, \phi$	various	Horizontal and vertical direction angles (Table 2.2).
$\theta$		Circular vector mean direction.
$\psi_{ij}$		The angle between the $i^{\text{th}}$ and $j^{\text{th}}$ axis of vector of a sample.
$\phi_B$		Bishop's stress ratio.
$\Omega$		Normalized orientation tensor.

Table 1.2: List of symbols used. *Header* is text used in the column header in the data spreadsheet, for control labels, or in the output log file.

### 1.4 Graphics Export

Plots can be output to bitmap (raster) and vector graphics files (Table 1.3). Bitmap files are compatible with image editing programs such as Adobe Photoshop and GIMP, and can be imported into most word processing programs. Formats include Portable Networks Graphics (PNG), Windows Bitmap (BMP), Tagged Image File Format (TIFF) and Joint Photographic Experts Group (JPEG). The default format is a png file, a widely supported optimally compressed non-lossy format. bmp and tiff files

are also non-lossy and widely supported. The jpg file format was designed mainly for photographic images, and is less suitable for plots and illustrations.

Vector graphics files allow editing in programs such as Adobe Illustrator, CorelDRAW, Inkscape, and Computer Aided Design (CAD) programs such as AutoCAD and QCAD. Orient supports Scaled Vector Graphics (SVG), Portable Document Format (PDF), Encapsulated PostScript (EPS), and AutoCAD Drawing Exchange (DXF) formats. The SVG vector format is an open standard vector graphics format that is supported by most modern browsers and vector graphics editing software, including Adobe Illustrator, Inkscape, and CorelDRAW. Opening a svg file in Firefox, for example will display the image, or identify any errors.

The vector graphics file formats vary in their support of drawing features. SVG is the most complete, including full support for transparency. SVG graphics can easily be rescaled in a vector graphics editing program. SVG can include bitmaps with transparency, such as color gradients. These will have a width and height in pixels as set in the *Page Size* dialog. Bitmaps in svg are compressed in png format and have an alpha channel to support transparency. SVG does not support layers, but grouped elements can be moved to layers once opened in a vector graphics editing program.

The PDF graphics implementation is almost as complete as SVG, however, transparency (alpha channel) is not supported for vector objects such as polygons. Vector objects with transparency will appear as a solid color, and will obscure any underlying objects. Transparency is, however, supported for bitmap images, such as gradients.

EPS is also a good choice for vector graphics, and can include bitmaps. Transparency is not supported for vector objects or bitmaps however. Bitmaps, such as multiple gradient fills, are flattened so multiple gradient layers will appear brighter, but they will not be transparent and will obscure underlying objects.

The DXF format supports layers, but not transparency. Only simple polygon fills are supported, and line styles, text, and colors may vary from other formats.

The svg files generated by Orient conform to the World Wide Web Consortium (W3C) standard, however some, mostly older, versions of Adobe Illustrator contain bugs that prevent it from opening valid svg files. A work around is to open the svg file in another program, such as Inkscape, and save it in different format, such as pdf. Another option is to save the plot as a pdf or eps file which Illustrator should be able to open.

Format	Extension	Format	Notes
Portable Network Graphics	png	Bitmap	Best for bitmap
Tagged Image File Format	tif or tiff	Bitmap	Good for bitmap
Windows Bitmap	bmp	Bitmap	Good for bitmap
Joint Photographic Experts Group	jpg or jpeg	Bitmap	Poor for line art, good for photos
Scaled Vector Graphics	svg	Vector	Best for vector graphics, layers and transparency
Portable Document Format	pdf	Vector	Good, Adobe format, partial transparency
Encapsulated PostScript	eps	Vector	Good, Adobe format, no transparency
AutoCAD Drawing Exchange	dxf	Vector	Poor, but standard for CAD software

Table 1.3: Summary of supported graphics file output formats.

## 1.5 Gradients and Colormaps

Most plots can be colored using a gradient to emphasize gradations in data density. The default method is to interpolate a color among two to five colors. The interpolation is done using either a red-blue-green (RGB) color model, or a hue-saturation-lightness (HSL) model. A linear interpolation between two colors  $c_1$  and  $c_2$  is

$$c_t = (t - 1)c_1 + tc_2 \quad (1.1)$$

where  $t$  is the interpolation factor from 0 to 1. Narrow color bands may occur as artifacts of linear interpolation among multiple colors, which may give a false impression of sharp density transitions.



Sinusoidal interpolation can widen these bands to give a more consistent color variation

$$\begin{aligned} u &= (\sin(t180^\circ - 90^\circ) + 1)/2 \\ c_t &= (u - 1)c_1 + uc_2 \end{aligned} \quad (1.2)$$

HSL colors are expressed with hue as an angular value from  $0^\circ$  to  $360^\circ$ , so circular interpolation must be used, and colors can be rotated. The default rotation is  $60^\circ$ , which cycles through red, yellow (Y), green, cyan (C), blue, and magenta (M). A circular interpolation between two angular values  $\alpha_1$  and  $\alpha_2$  is

$$\begin{aligned} \delta &= \arctan2(\sin(\alpha_2 - \alpha_1), \cos(\alpha_2 - \alpha_1)) \\ c_t &= (\alpha_1 + t\delta + 360^\circ) \bmod 360^\circ \end{aligned} \quad (1.3)$$

Colors include an *alpha* channel, a measure of transparency (T). Preset linear gradients are provided for TR, TY, TG, TC, TB, and TM. These are particularly useful when plotting multiple data sets on the same plot (Figure 1.10).

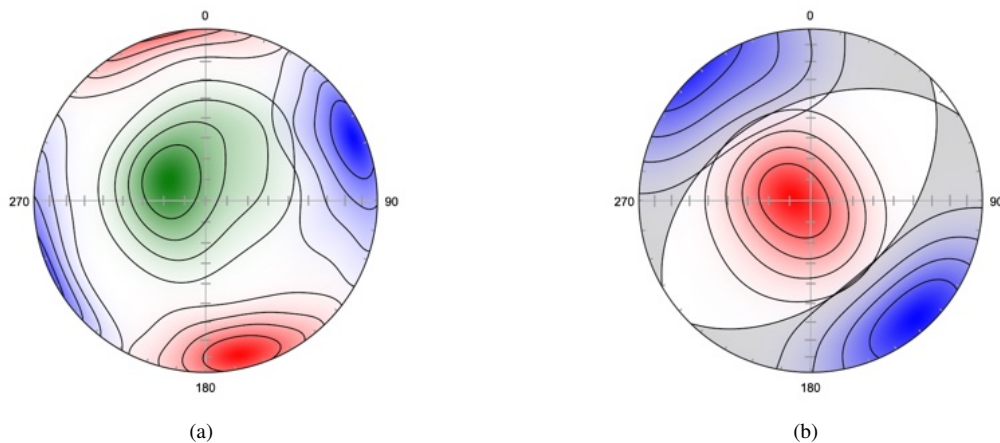


Figure 1.10: Schmidt plots illustrating the use of transparent colors to display multiple data sets on a single plot. Modified Kamb contour interval is 20% density. (a) Fracture data (Shanley and Mahtab, 1975) after cluster analysis. The data are colored with transparent-red (TR), transparent-green (TG), and transparent-blue (TB) linear gradients. (b) Contoured P (TR) and T (TB) kinematic axes of normal fault data (Angelier, 1979) superimposed on a beachball diagram.

Gradients are applied by calculating a *colormap*, using Eq 1.1, 1.2, or 1.3, and mapping the colors to estimated densities. More complex gradients can be applied using pre-calculated colormaps. Colormaps are used by data analysis software including MATLAB, Octave, Matplotlib, R, and many others. Colormaps that are widely supported include *jet* (former default for MATLAB), *rainbow*, *autumn*, *hot*, and *cool*. Additional newer colormaps include a suggested replacement for *jet*, *turbo* (Mikhailov, 2019), the diverging *coolwarm* (Figure 1.13a), and the sequential *blackbody* (Moreland, 2015). The default colormap *sinusoid* is similar to *jet*, but is lighter at the extrema and has wider color bands in the cyan and yellow range (Appendix I).

Many data samples contain large areas of low density, and it may be desirable to use a color gradient that begins at white. Figure 1.12 shows examples using the preset WBGYR and WR gradients.

*Perceptually uniform* colormaps, in which lightness, rather than hue, increases in equal steps, have been suggested to better allow the human brain to perceive changes (Moreland, 2015). Four sequential perceptually uniform color maps, *viridis*, *plasma*, *inferno*, and *magma* (Smith et al., 2015), originally implemented in Matplotlib, are provided. *Viridis* is the default colormap for Matplotlib and Octave (Figure 1.13b). Nuñez et al. (2018) developed a perceptually uniform colormap, *cividis*, based on *viridis*, optimized for those with red-green colorblindness.

Perceptually uniform colormaps are, by design, dark at low values, which may not be ideal for plots with large areas of low density. It is, therefore, possible to invert the colormaps, and to limit their bounds to decrease the darker, or lighter, color values.

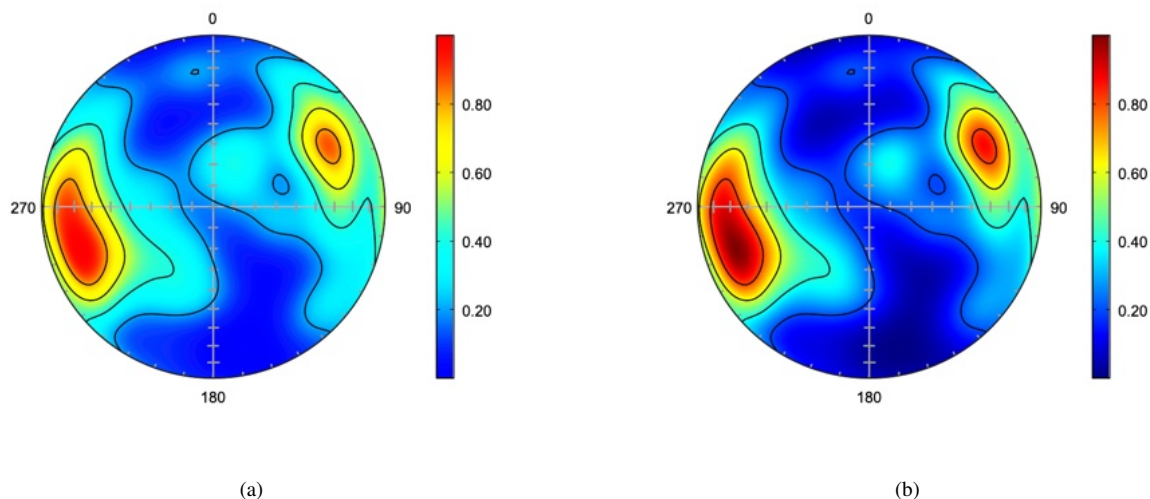


Figure 1.11: Schmidt plots of ice crystallographic axes (Kamb, 1959) with modified Kamb contours at 20%. (a) Plot using the default BCYR sinusoidal colormap *sinusoid*. See Appendix I for implementation details. (b) Plot using the *jet* colormap. Note the narrow color bands in the cyan and yellow ranges.

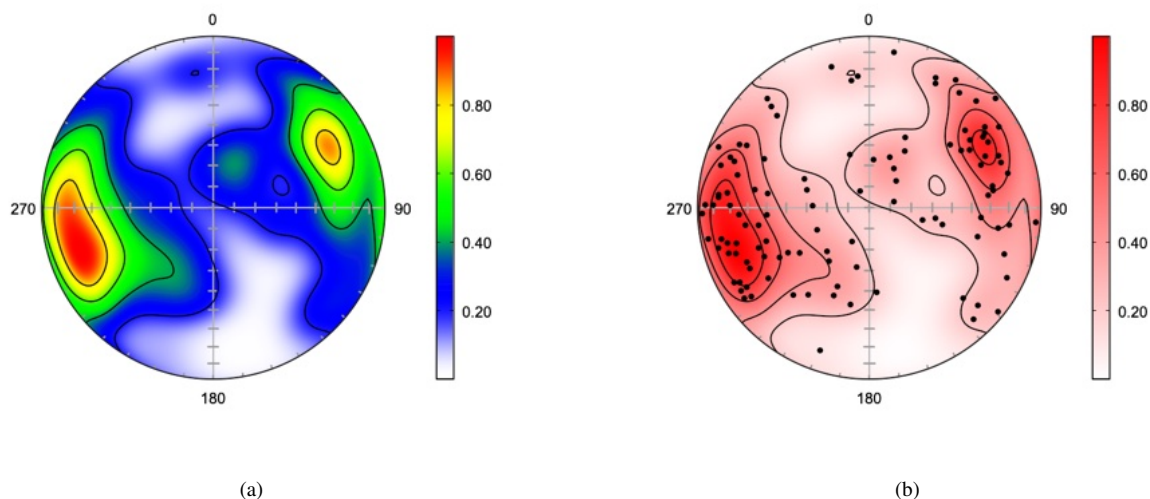


Figure 1.12: Example plots using gradients beginning with white. Schmidt plots of ice crystallographic axes (Kamb, 1959) with modified Kamb contours at 20%. (a) Plot using the preset sinusoidal WBGYR gradient. (b) Plot using the preset sequential linear WR gradient, showing the data points.

The contour, and colormap, ranges are *tight* by default, meaning that the range is set independently for each plot. When comparing multiple plots, it may be useful to explicitly set the contour range. To do so, in the *Spherical Projection - Contours* settings pane, chose *Contour interval*, uncheck *Automatic range*, and enter a *Min* (e.g., 0.0) and *Max* value to be used for all plots. The units may be either standard deviations ( $\sigma$ ), or multiples of uniform density (MUD).

Contours can also be filled in discrete solid color levels by using the *Fill contours* options on the *Spherical Projection - Contours* pane. This option is also available on several other plots, including the *Moment Triangle*, and *Ternary* plots.

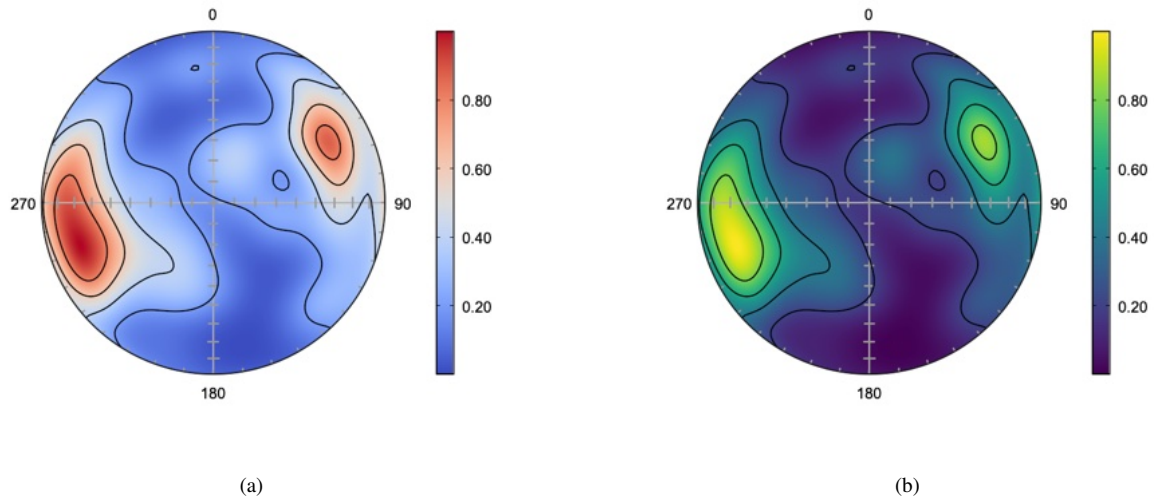


Figure 1.13: Example plots using pre-calculated colormaps. Schmidt plots of ice crystallographic axes (Kamb, 1959) with modified Kamb contours at 20%. (a) Plot using the diverging *coolwarm* colormap. (b) Plot using the sequential perceptually uniform *viridis* colormap.

## 2 Data Entry and Import

Orient is designed to be used with all types of directional measurements and coordinate systems, and converts to and from user coordinates for data entry and output. The user does not normally need to be concerned about the underlying coordinate system, except in the case of rotations or selecting different geographic coordinates (Section 5.1). A standard right-handed spherical coordinate system is used defined with default axes X, Y, Z = Right, Top, Up. In geologic usage these normally correspond to East, North, Up (ENU), which conforms to map coordinate systems using easting, northing, and elevation. Section 5.1 explains how the default coordinates can be changed to any other orientation, such as global geographic. Thirteen standard coordinate systems are supported, which can be modified by rotations about any axis.

Spherical coordinates are specified by two angles,  $\theta$  (theta) and  $\phi$  (phi). The standard mathematical definitions are that  $\theta$  is the longitude, or the counterclockwise angle from X in the XY plane, and that  $\phi$  is the colatitude, the angle from Z. However, there are numerous ways to specify the same information with two angles, typically specified by the scientific discipline, such as geology, geography, or astronomy (Fisher et al., 1987; Mardia and Jupp, 2000). Planes are represented by their normal, or pole. The user can specify  $\theta$  and  $\phi$  for lines and planes according to their data or discipline (Table 2.2).

Geographic data are generally given using longitude as the horizontal angle, the vertical angle is commonly latitude or colatitude, azimuth and altitude are used in astronomy. Geologic data are typically specified using azimuths for horizontal angles, measured clockwise from North (Y), and dips or plunges for vertical angles, measured down from horizontal (the XY plane). Geologic angles are typically strike and dip for planes, and trend and plunge for lines. All common conventions (Table 2.2) are supported, however, as well as conversion among them.

To convert between formats or to set the default format for data entry, open the *Data - Orientation Formats* dialog. This will set the data format entered in the spreadsheet, and will convert any preexisting values to the new format. For example, a common conversion is from strike and dip, to dip and dip direction. The data will be saved in the new format, and reopening the file will retain the format as saved.

Due to the standard use of geographic locations, typically from Global Positioning System (GPS) positioning, of data points in geology, a distinction is required between two usages of latitude and longitude. A geologist typically records data locations expressed as Cartesian coordinates, such as Universal Transverse Mercator (UTM), or as latitude and longitude pairs, as well as collecting directional data at that location. Therefore it is necessary to determine whether a latitude, longitude pair is meant as the *location* of a data point, or if it is *direction* of a data point. The convention adopted here is that latitude, longitude (or lat, long) refer to a data point location, and that latitude sphere, longitude sphere (or lats, longs) refer to the data point direction to be plotted on a spherical projection.

There are several conventions for strike and dip, including two contradictory ones, unfortunately both called the right-hand rule (Ragan, 2009, p. 4). A distinction must be made, so by default, the (American) convention that the dip is to the right looking along the strike (Pollard and Fletcher, 2005; Twiss and Moores, 2007; Fossen, 2016) is used. This can be remembered as when the *fingers* of the right hand, placed on the top of the plane, point down dip, the thumb points in the strike direction.

A second (British) convention, where the dip is to the left, and the *thumb* of the right hand points down the dip (Barnes, 1995), is referred to as Strike B (or strikeb). This convention can be selected using the *Data - Orientation Formats* command. A third convention, using a dip octant (N, NE, E, SE, etc.) is automatically converted to one of the above as described in Section 2.1. Finally, dip and dip direction, another common convention for giving the orientation of a plane, is also supported.

The rake, or pitch, of a line in a plane is often used instead of expressing the line's trend and plunge separately. Expressing the strike, dip, trend, and plunge of a line-plane pair is over constrained as only three angles are required, and generally results in an angular error between them. This error is reported in the Error column, and can be corrected using the *Data - Calculate Lines* command (Section 9.1). If rakes are entered as data, the trend and plunges of lines should be calculated using

Column Header	Abbreviation	Notes
<b>Plane <math>\theta</math></b>		Horizontal angle of plane.
Strike	strike or strikea	Clockwise from North (Y), dip is to right (American).
Strike B	strikeb	Clockwise from North (Y), dip is to left (British).
Dip Direction	dipdir	Azimuth of dip line.
<b>Plane <math>\phi</math></b>		Vertical angle of plane.
Dip		Angle from XY plane down toward -Z.
<b>Line <math>\theta</math></b>		Horizontal angle of line.
Azimuth	az	Clockwise angle from North (Y).
Declination	dec	Equal to azimuth.
Longitude Sphere	longs	Counterclockwise angle from X.
Theta		Equal to longitude sphere.
Trend		Equal to azimuth.
<b>Line <math>\phi</math></b>		Vertical angle of line.
Altitude	alt	Equal to latitude.
Colatitude	colat	Angle from Z down toward XY plane.
Inclination	inc	Angle from XY plane down toward -Z.
Latitude Sphere	lats	Angle from XY plane up toward Z.
Nadir		Angle from -Z up toward XY plane.
Phi		Equal to colatitude.
Plunge		Equal to inclination.
Zenith		Equal to colatitude.
<b>Line in Plane</b>		
Rake		Rake, or pitch, clockwise from strike.
Rake AR		Rake anticlockwise from strike (Aki-Richards).

Table 2.2: Column headers used to specify directional data formats. The header or its abbreviation is used in data files to identify a column of data. A plane requires two headers, such as Strike and Dip. A line also requires two headers, such as Trend and Plunge.

the *Data - Calculate Lines* command. Rakes can also be calculated from line trends using the same command. *Orthonormalizing* (Section 9.2) will calculate rakes from trends and plunges after fixing any mismatch errors.

Two conventions are available for the rake (Table 2.2), and one should be chosen before converting rakes. The default convention is that the rake angle is measured clockwise (downward) from the strike (Pollard and Fletcher, 2005; Ragan, 2009). This is a positive angle taking the strike, dip line, and *downward* normal as a reference frame. In this convention, a normal fault slip has a positive rake. For example, a fault with a  $90^\circ$  striae rake is a pure normal fault with no strike slip component. An alternative convention, often used for seismic data, uses the *upward* normal of a plane, and a positive rake is taken as the counterclockwise (upward) angle. In this convention, a normal fault slip has a negative rake, such as  $-90^\circ$ . To use this convention, use the *Data - Orientation Formats* dialog to select *Rake AR* (Aki-Richards convention) before converting rakes. When reading data from a file, use the column header *Rake AR* instead of *Rake*.

## 2.1 Data Entry

Each data point must include a pair of angles specifying its orientation in space. The first angle is measured in a horizontal plane ( $\theta$ ), and the second in a vertical plane ( $\phi$ ). For typical geologic data, these are strike and dip for planes, and trend and plunge for lines. However, all common formats are supported (Table 2.2). Two dimensional data require horizontal angles only.

Before entering data, select the desired data format using the *Data - Orientation Formats* command. You may also wish to hide or show appropriate columns using the *View - Data Columns* command. Separate columns are used for planes and lines, so make sure the required columns are visible. The Type column can contain any alphanumeric identifier, for example S0 and S1 are often used in geology to designate bedding and cleavage. This is required if multiple data types are entered in a single file. All settings, such as symbol sizes and color, are saved for each type. Additional data attributes include

station identifiers, location coordinates, domains, and notes (Table 2.9).

Several data conversions are done automatically. If data is entered as a bearing with compass quadrants it is converted to a numerical azimuth. Bearings are given as degrees east or west of north or south, for example, N30W will be converted to 330. A conversion is also done for planes in *Strike* and *Dip*, or *Strike B* and *Dip*, formats if a dip octant (N, NE, E, SE, S, SW, W, or NW) is given. The *Strike* (or *Strike B*) will be corrected if necessary. For example a strike, dip pair entered as 10, 30W will be converted to 190, 30 when using the *Strike* format.

Normally only one plane or line is entered in a row, however kinematic analysis requires the entry of plane-line pairs, which introduces additional complexity. Data entry for this type of data is covered in Section 9.1.

Each data point may be individually weighted by entering a value into the Weight column. The default weight is 1, enter 0 to discount the point, or a positive value to increase or decrease its weight. This can be used, for example, to weight joint or fault data by exposed length or surface area. See Section 2.12 for examples of weighting. Weighting applies to all calculations except bootstrap confidence cones, which require the resampling of equally weighted points.

Planes with a dip of zero plot as a full circle instead of an arc on either hemisphere. If they are obscured by the net frame, increase the stroke width, or decrease the opacity of the *Frame* (e.g., to 50%). Undirected lines with a plunge of zero on either hemisphere plot as two diametrically opposed symbols. Similarly, if represented by a ray, the ray will be plotted as a diameter instead of a radius. This option can be turned on or off using the *Mirror* checkbox in the *Preferences* dialog *Spherical Projection* pane.

## 2.2 Interactive Data Entry

Data lines and planes can be digitized interactively from a spherical projection by using the *Append Data* command. Select an open spherical projection, and the *Append Data* command. The *Append Data* dialog box allows selection of *Lines* or *Planes* for entry, the data *Type*, and whether to round the values to the nearest degree (Figure 2.1). Use the *Plot - Cursor Symbols* command to change the cursor display symbols.

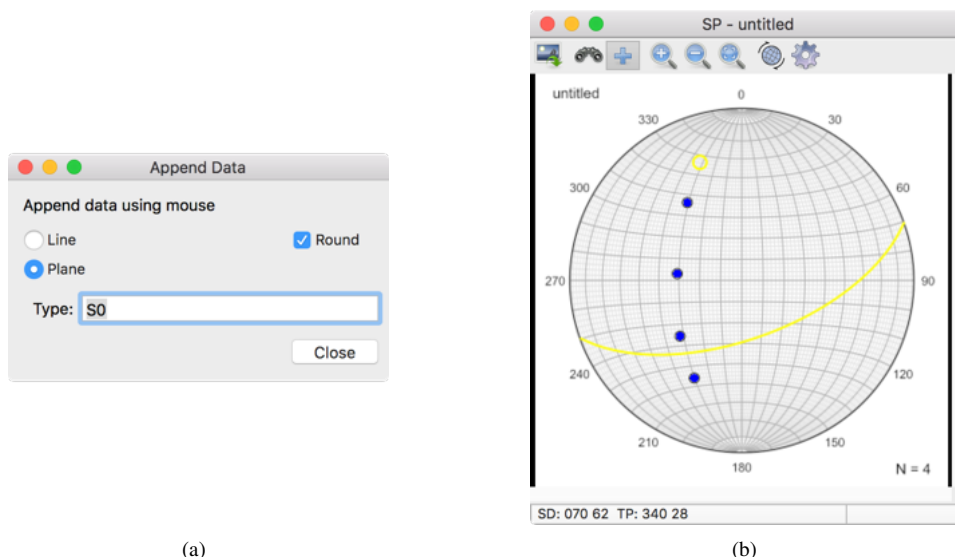


Figure 2.1: (a) The *Append Data* dialog box. (b) Schmidt plot showing the use of the *Append Data* command.

## 2.3 Hidden Data Display

Directed data (vectors) intersect the sphere at only one point, which may occur in either hemisphere. Consequently, some of the data point symbols may be hidden from view. One option is to plot both

hemispheres separately (e.g., Figure 1.2, which shows two Schmidt plots, one with a 180° rotation about Y), however it may also be useful to plot the data points on the hidden hemisphere on the same plot using transparency. In the *Preferences* dialog *Spherical Projection* pane, the *Directed* option can be selected to plot hidden contours, confidence cones, and symbols at 10% to 90% opacity, so they appear semitransparent (Figure 2.2). This data is in the example data file Paleomagnetism/Schmidt and Embleton FLE 1987 B6.

Alternatively, symbols on the hidden hemisphere may be plotted as *Unfilled*, or using the *Dot* option. With the *Dot* option a symbol on the hidden hemisphere will be displayed with a central dot, or, if it has a central dot, it will be displayed without the dot.

Undirected data (axes) intersect the sphere at two diametrically opposed points, by convention usually only one is plotted. For example, the one in the lower hemisphere is normally plotted in structural geology, and the one in the upper hemisphere in mineralogy. However, it is sometimes useful to plot both symbols on the same plot, which can be done using the *Undirected* option, which similarly allows plotting of hidden contours, confidence cones, and symbols. See Section 4.12 for additional examples.

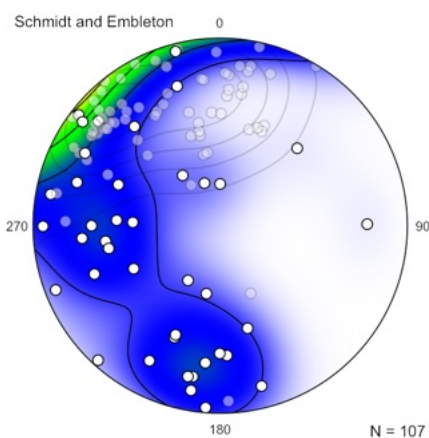


Figure 2.2: Schmidt plot showing an example of hidden data display, the upper hemisphere data is plotted as 30% opaque. Magnetic remanence data with contours at multiples of uniform density (MUD). Compare with Figure 1.2. Data from Schmidt and Embleton (1985) in Fisher et al. (1987, Table B6).

## 2.4 Linking and Line-Plane Pairs

This section discusses the construction of plane intersections using linking, entering line-plane pairs, and constructing line-plane pairs using linking. These are commonly used in constructing bedding-cleavage intersections, and for kinematic analysis (Chapter 9).

A common construction on a Schmidt, or Wulff, net is to determine the intersection of two planes, for example the intersection of bedding (S0) and cleavage (S1) planes is used as a predictor of an associated fold axis. The intersection ( $S0 \wedge S1$ ) can be determined either by using the mouse to locate the intersection on a Schmidt plot of the data, or by selecting the two rows in the spreadsheet window. In both cases the intersection (or minimum) is displayed in the window's status bar.

To plot a symbol at the intersection, and to allow the calculation of  $S0 \wedge S1$  statistics, enter the ID of S1 in the Link column as shown in Table 2.3. The resulting Schmidt plot is shown in Figure 2.3. The intersection will now show up as a data type ( $S0 \wedge S1$ ) for display and calculation of statistics.

ID	Link	Strike	Dip	Type
1	2	20.00	40.00	S0
2		40.00	80.00	S1

Table 2.3: Example data for construction and display of a bedding-cleavage intersection (Figure 2.3).

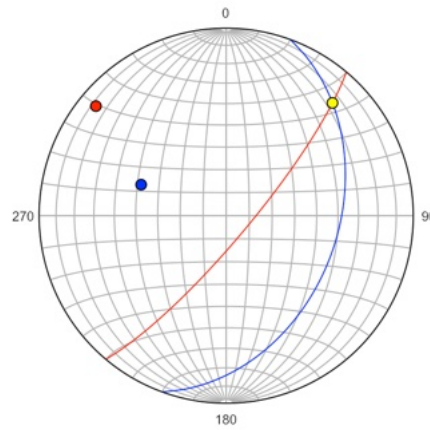


Figure 2.3: Schmidt plot of bedding (S0, blue) and cleavage (S1, red) with bedding-cleavage intersection ( $S0^S1$ , yellow) constructed by linking as shown in Table 2.3.

In some situations it is useful to measure the rake (pitch) of a lineation in a plane, instead of its trend and plunge. The *Data - Calculate Lines* command is used to determine the orientation of a line in a plane, given its trend or rake, as well as to remove errors from over-constrained line plane pairs by orthonormalizing them to an orthogonal frame. See Section 9.2 for a discussion of orthonormalizing kinematic data, and Section 9.1 for a more complete discussion of entering line-plane pairs.

Table 2.4 shows fault data entered as the strike and dip of a slickenside plane, and the rake of the slickenside lineation. After selecting the line, run the *Calculate Lines* command with the from *Rake* option, the data then appears as in Table 2.5, and plots on a Schmidt plot as in Figure 2.4a.

ID	Link	Strike	Dip	Trend	Plunge	Sense	Rake	Error	Type
1		0.00	50.00				60.00		F

Table 2.4: Fault plane (slickenside) and lineation entered as rake. Table 2.5 shows the data after running the *Calculate Lines* command with the from *Rake* option.

ID	Link	Strike	Dip	Trend	Plunge	Sense	Rake	Error	Type
1		0.00	50.00	48.07	41.56		60.00	0.00	F

Table 2.5: Fault plane (slickenside) and lineation entered as rake, after using the *Data - Calculate Line* command with the from *Rake* option. The data is plotted in Figure 2.4a.

Minor structures associated with a fault or shear zone can be used to construct a slip direction. Fault slip direction can be determined, for example, from minor veins, fractures, cleavage, or foliated gouge. Similarly, the asymmetry of SC and C' shear band fabrics can be used as shear sense indicators in mylonitic rocks. These can be subdivided into *acute* and *obtuse* angle shear sense indicators, depending on the angle subtended from the minor structure to the shear direction. SC fabrics, fault-related cleavage, and similar strain-induced structures are *acute* indicators. Fault-related veins, extension fractures, and C' shear bands are *obtuse* indicators.

As an example, Table 2.6 shows data from a fault (F) and an associated extensional vein (V). The fault data includes a link (Link = 2) to the vein data (ID = 2). Table 2.7 is the data after executing the *Calculate Lines* command with the *Obtuse shear* option. Figure 2.4b is the resulting Schmidt plot.



ID	Link	Strike	Dip	Trend	Plunge	Sense	Rake	Error	Type
1	2	0.00	50.00						F
2		10.00	80.00						V

Table 2.6: Data from fault plane and (F) associated extensional vein (V). A link from the fault to the vein data is entered in the Link. Table 2.7 shows the result after executing the *Calculate Lines* command with the *Obtuse shear* option.

ID	Link	Strike	Dip	Trend	Plunge	Sense	Rake	Error	Type
1	2	0.00	50.00	118.48	46.33		109.23	0.00	F
2		10.00	80.00						V

Table 2.7: Data from fault plane and (F) associated extension vein (V), after executing the *Calculate Lines* command with the *Obtuse shear* option. Figure 2.4b is the resulting Schmidt plot.

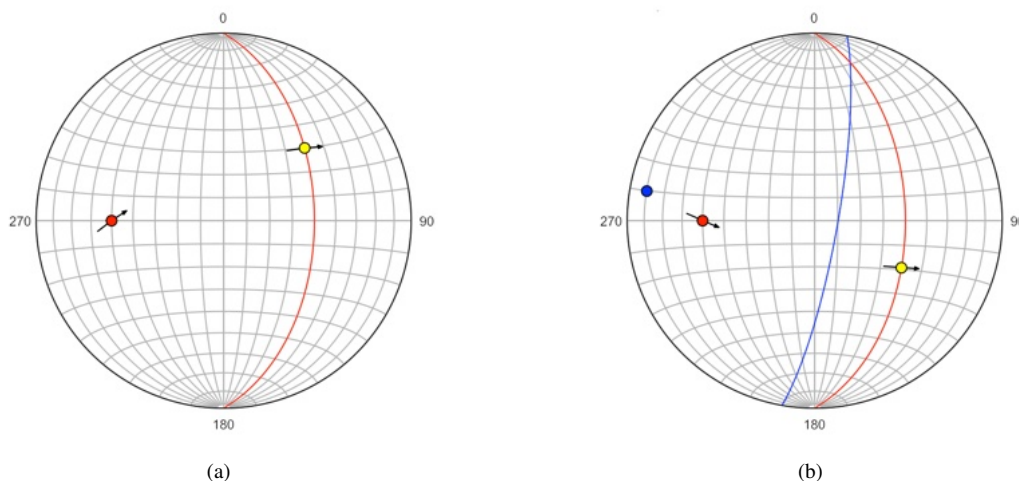


Figure 2.4: Schmidt plots of constructed fault data. Arrows are tangent lines showing hanging wall motion (Section 9.3). (a) Fault plane (red) and lineation (yellow) constructed from rake, as shown in Table 2.5. (b) Fault (F, red) and associated extension vein (V, blue) with constructed slip direction (yellow). Data is in Table 2.7.

## 2.5 Spreadsheet Integration

Data entered into the spreadsheet window can be saved in several spreadsheet formats: Tab Separated Values (tsv), Comma Separated Values (csv), OpenDocument spreadsheet (ods), Microsoft Excel (xls andxlsx). These are all compatible with most spreadsheet programs, including Microsoft Excel and LibreOffice (Table 2.8).

All of these formats can be read, allowing users to enter data files into Microsoft Excel, LibreOffice, or other spreadsheet software. The only requirements are that the data have a header row, consisting of headers listed in Tables 2.2 and 2.9 and that any initial comment lines start with two slashes (//). Table 2.10 gives a simple example, and Table 2.11 gives a more complete example. The simplest possible file would be a list of horizontal angles, such as trends or azimuths, for two dimensional analysis. Three dimensional analysis also requires vertical angles, such as dips or plunges.

Data may also be copied from a spreadsheet and pasted into Orient. The header row must be selected along with the data rows so the columns can be correctly assigned. The data is copied as tab delimited text (tsv) into the clipboard, which can be imported into Orient using the *Edit Paste* command.

Microsoft Excel has some worksheet naming conventions that must be followed. The name must be unique within a workbook, the name cannot exceed 31 characters, and the characters \ / \* ? : [ ] are not allowed. Only the first worksheet in the file is opened. Although OpenDocument files (ods) are less restrictive, these worksheet naming conventions are required for Excel compatibility. The included folder Example Data has numerous examples of compatible files. Open them in Excel or LibreOffice to examine them, they are used in subsequent examples and tutorials.

Format	Extension	Notes
Excel XML Spreadsheet	xlsx	Microsoft Excel 2007 and later
Excel Spreadsheet	xls	Microsoft Excel pre-2007
OpenDocument XML Spreadsheet	ods	LibreOffice/OpenOffice, open source software
Tab Separated Value	tsv	Text format with values separated by tabs
Comma Separated Value	csv	Text format with values separated by commas

Table 2.8: Summary of spreadsheet formats supported for opening and saving data.

Column Header	Alternative	Notes
ID	N	Integer identification number for data point.
Link		Link to another data row by ID.
Station		Alphanumeric station identifier.
Zone		Alphanumeric zone, such as UTM grid zone.
Easting	East, X	X or easting coordinate of data location.
Northing	North, Y	Y or northing coordinate of data location.
Elevation	Z	Elevation of data location.
Latitude	lat	Latitude of data location (D°, D°M', or D°M' S").
Longitude	long	Longitude of data location (D°, D°M', or D°M' S").
Strike, ... (Plane $\theta$ )	various	Horizontal angle of plane from Table 2.2.
Dip (Plane $\phi$ )		Vertical angle of plane from Table 2.2.
Trend, ... (Line $\theta$ )	various	Horizontal angle of line from Table 2.2.
Plunge, ... (Line $\phi$ )	various	Vertical angle of line from Table 2.2.
Rake		Clockwise rake of line in plane.
Rake AR		Counterclockwise rake of line in plane (Aki-Richards).
Sense		Kinematic movement sense, Normal or Reverse.
Error		Angular error of line in plane (read only).
PhiF		Angle of friction.
AlphaC		Semi-apical angle of cone.
Xa	E1	Ternary component A, or maximum eigenvalue.
Xb	E2	Ternary component B, or intermediate eigenvalue.
Xc	E3	Ternary component C, or minimum eigenvalue.
P, G, R, B, D		Eigenvector fabric indexes (read only).
Weight		Data point weight, default is 1.
Type		Alphanumeric data type, such as S0, S1, or J1.
Label		Alphanumeric label.
Domain		Integer identification number for domain.
Notes	Comment	Alphanumeric notes or comment.

Table 2.9: Column headers used to specify data attributes. The header or its abbreviation is used in data files to identify a data field. See Table 2.2 for data angles  $\theta$  and  $\phi$ .

Strike	Dip						
230	24						
018	54						
141	15						

Table 2.10: Example of a simple data file as displayed in a spreadsheet, such as Microsoft Excel or LibreOffice, with strikes and dips of planes. See Table 2.9 for other possible column headers.

// text							
Easting	Northing	Strike	Dip	Trend	Plunge	Type	Notes
8452.05	12885.05	230	24			S0	approx
8456.03	12825.03	018	54			S0	overturned
8432.12	12922.30	141	15			S1	spaced
8466.08	12865.40			138	02	L	S0/S1
8492.01	12872.00			140	09	L	mineral

Table 2.11: Example of a more complex data file as displayed in a spreadsheet, such as Microsoft Excel or LibreOffice, with an initial text comment, data locations, multiple data types, and notes. See Table 2.9 for other possible column headers.

While a number of data files formats are supported (Table 2.8), tab separated value (tsv) files are recommended for long term storage and archiving data. The format is a simple text file that can be read by virtually any text editor, word processor, or spreadsheet program. While the comma separated value (csv) format is also simple, the fact that text often contains commas requires additional processing. Note that text file formats (csv and tsv) use decimal point (“.”) format to represent floating point (real) numbers, this is also the case for scaled vector graphics (svg) files, Google Earth keyhole markup language (kml), and most latitude-longitude urls.

## 2.6 Tutorial: Spreadsheet Data

Open a spreadsheet program, such as LibreOffice or Microsoft Excel, and enter the data shown in Table 2.12. Then save the file using a standard format (Table 2.8).

// My data file				
Strike	Dip	Trend	Plunge	Type
60	65			S0
10	45			S0
40	60			S0
310	60			S0
280	70			S0
		90	40	FH
330	55			S1

Table 2.12: Example of a data file for the tutorial. Enter this into a spreadsheet such as LibreOffice or Microsoft Excel.

Open the file using the *File Open* command. Click on the *Spherical Projection* icon, to get a plot as in Figure 2.5a. If you have previously modified settings, however, they will still be in effect. The *Help - Restore Defaults* command can be used to reset all settings to default.

To prepare a plot for publication, it is good to simplify it and focus on the data, so change some of the settings as follows. From the spherical projection window, press the *Preferences* icon. In the *Spherical Projection - Net* pane, turn off the great circles and small circles options for the Y axis, select major tick marks for the X, Y, and Z axes, and set *Axes* on. In the *Labels* pane, set the *Inc* to -90. Click on *Preview* to see the result.

Next, assign different colors to the data types. Select data type S1.S (cleavage) and assign its *Fill Color* to green, and the FH.L (fold hinge) symbol *Fill Color* to yellow. Press *Preview*, and the plot should be as shown in Figure 2.5b.

Now add great circles to represent the planes. In the *Symbols* pane select data type S0 again and check the great circle checkbox. Then select data type S1.S, check the great circle checkbox, and set the stroke color to green (Figure 2.6a). A plot of planes represented by their great circles is a  $\beta$  diagram. With a lot of data this type of diagram becomes crowded, and loses statistical significance, but for a small number of points it can help with visualization. A plot with planes represented by their poles is a  $\pi$ , or S-pole diagram, and is preferred over a  $\beta$  diagram as a better statistical representation.

Finally, add the S0.S maxima. In the *Maxima* pane select the S0.S data type, and check visible. For this plot just add the minimum eigenvector, which gives a best-fit fold axis. Uncheck the symbol for both the maximum and intermediate eigenvectors. For the minimum eigenvector check the symbol and great circle checkboxes, and set their colors to red (Figure 2.6b).

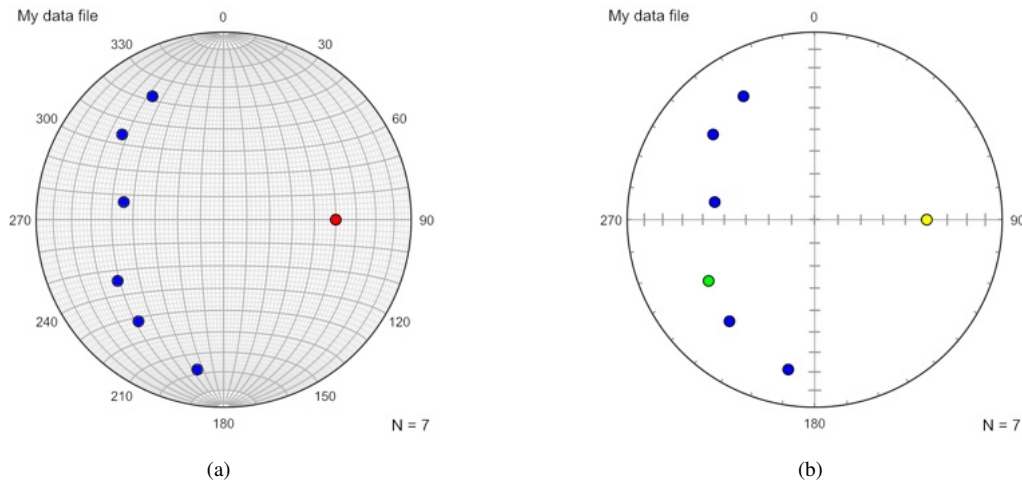


Figure 2.5: (a) Schmidt plot of data from Table 2.12. (b) Schmidt plot after removing the net, adding tick marks, and assigning colors to the data symbols.

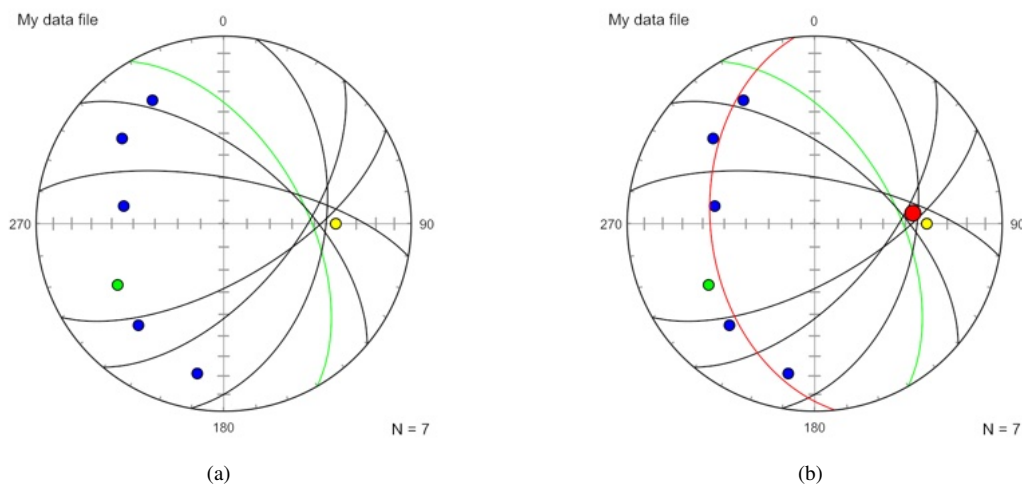


Figure 2.6: (a) Schmidt plot as in Figure 2.5b with planes represented as great circles. (b) Schmidt plot as in Figure 2.6a with best-fit great circle and pole given by the minimum eigenvector of  $S_0.S$  (bedding).

## 2.7 Data File Import

There are numerous data file formats for directional and kinematic data sets. Many of them are spreadsheet compatible, and can be converted for use in Orient. This section covers several such data file formats.

### 2.7.1 StraboSpot

StraboSpot ([www.strabospot.org](http://www.strabospot.org)) is an online database of geologic map, structural geology, and tectonics data. To open a StraboSpot dataset, download it in Microsoft Excel format, and open it in Orient. Table 2.13 lists the field equivalencies when imported into Orient.

StraboSpot has numerous Type and Notes fields (e.g., Fracture Type, Planar Feature Type, Planar Feature Notes, etc.). The usage and priority of these fields is determined by the user, therefore only the first encountered non-empty Type and Notes field is read for each line of data. The headers in the StraboSpot spreadsheet file can be edited if different fields are required to be imported (Table 2.13).

If two StraboSpot Type fields are used for a single data row, for example, *Planar Feature Type = fracture* and *Fracture Type = joint*, Orient will read *Type = fracture*. To ensure that *Type = joint* is read instead, edit the spreadsheet header by changing *Planar Feature Type* to *Planar Feature -Type*.

(note the minus sign). Orient will then not read that field.

StraboSpot Field	Orient Field
Name	Station
Latitude	Latitude
Longitude	Longitude
Strike	Strike
Dip	Dip
Trend	Trend
Plunge	Plunge
Rake	Rake
Dip Direction	Dip Direction
Label	Label
* Type	Type
* Notes	Notes

Table 2.13: StraboSpot field equivalencies when imported from an Excel spreadsheet file. StraboSpot has numerous Type and Notes fields (e.g., Fracture Type, Planar Feature Type, Planar Feature Notes, etc.), therefore only the first non-empty Type and Notes field is read for each line of data. To ignore a specific Type or Notes field, edit the spreadsheet to place a minus sign directly in front of Type or Notes (e.g., Planar Feature -Type).

The example file Diligencia Basin, Blair Schoene.xlsx, in the Example Files/StraboSpot folder, is provided to demonstrate StraboSpot import. This dataset is publicly available on the StraboSpot website, and contains structural data collected by Blair Schoene in the Orocopia Mountains, California, east of the Salton Sea. The file was downloaded from the StraboSpot website without modification. A Google Earth kml file (Section 15.3) of bedding created from this data by Orient is included in the Example Files/Google Earth folder. Open this in Google Earth to view the data (Figure 2.8).

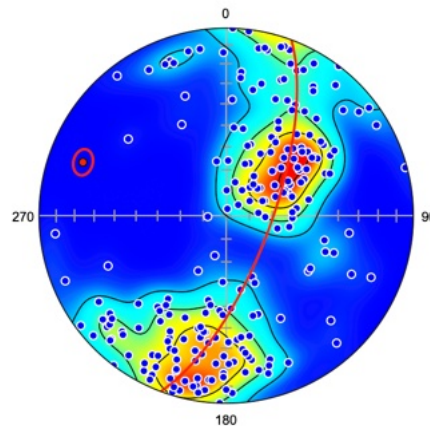


Figure 2.7: Schmidt plot of poles to bedding (blue circles) of data downloaded from the StraboSpot website (Diligencia Basin, Blair Schoene.xlsx). The best-fit girdle and fold axis are shown in red, with a 95% bootstrap confidence interval. Contour interval is multiples of uniform density.



Figure 2.8: View of the Diligencia data in Google Earth using the file Diligencia Basin, Blair Schoene.klm. The klm file was created in Orient, see Section 15.3.

### 2.7.2 Moment Tensor (CMT)

A global database of earthquake moment tensor solutions is maintained by the Global Centroid Moment Tensor (CMT) Project (Dziewonski et al., 1981; Ekström et al., 2012, [www.globalcmt.org](http://www.globalcmt.org)). These data include the locations and moment tensors of earthquakes  $M > 5$ , including nodal planes derived from first motion studies. The CMT data are available in a ndk file format. Information is extracted from these files, including latitude, longitude, depth, magnitude, and the strikes, dips, and rakes of the two nodal planes, the data fields are listed in Table 2.14.

Orient Field	CMT Data
Station	Unique CMT event identifier.
Elevation	Negative CMT depth in kilometers.
Latitude	CMT latitude.
Longitude	CMT longitude.
Strike	Strike of first or second nodal plane, depending on domain value.
Dip	Dip of first or second nodal plane, depending on domain value.
Rake	Rake in first or second nodal plane, depending on domain value.
Weight	Scalar moment recalculated as $M_w$ (see text).
Type	“CMT”
Domain	1 = first nodal plane, 2 = second nodal plane.
Notes	Geographical location as text.

Table 2.14: Data types extracted from Central Moment Tensor (CMT) ndk file.

The scalar moment extracted from the CMT ndk file is converted from  $M_0$  in dyne-cm to  $M_w$  by

$$M_w = \log_{10} M_0 / 1.5 - 10.7 \quad (2.1)$$

(Kanamori, 1978), and is reported in the *Weight* field. To display the nodal plane’s slip directions, and P and T axes, the lines need to be calculated using the *Calculate Lines* command with the *from Rake* option (Section 9.1).

The file *jan76\_dec17.ndk*, available for download from the CMT website, contains data for approximately 50,000 earthquakes from 1976 through 2017. When opened in Orient each of the two

nodes are displayed on separate lines (Domain 1 = first nodal plane, Domain 2 = second nodal plane), giving about 100,000 fault plane solutions. Rather than plotting the entire data set, a subset should be extracted by latitude and longitude, and possibly depth, to isolate a tectonic feature of interest.

An example of data from the southern Mid-Atlantic Ridge, between  $55^\circ$  S and  $16^\circ$  N, and  $55^\circ$  W and  $0^\circ$  E, is shown in Figure 2.9a. A moment tensor generates two nodal planes, either can represent the fault plane, so additional information, such as a fault surface trace, is required to determine which is related to the fault plane. Figure 2.9b shows the data after cluster analysis (Chapter 11) which highlights four clusters likely representing transform and ridge segments. In this case, the steeply dipping, east-west striking nodal planes (red) likely represent the transform segments. This data is given in the example data file `Seismology/CMT jan76_dec17 SMAR.tsv`, a subset of data from `jan76_dec17.ndk` from the CMT Project.

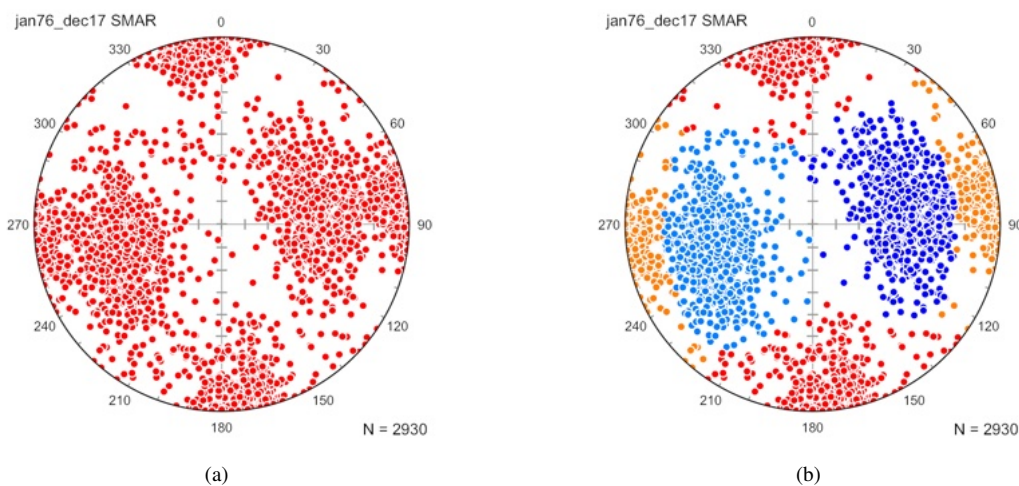


Figure 2.9: (a) Schmidt plot of poles to nodal planes of 1465 CMT mechanisms for earthquakes along the southern Mid-Atlantic Ridge between  $55^\circ$  S and  $16^\circ$  N, and  $55^\circ$  W and  $0^\circ$  E. Each moment tensor generates two nodal planes, only one of which represents the fault plane. Data from CMT Project. (b) Schmidt plot of poles to the nodal planes after cluster analysis (Chapter 11) to highlight four nodal plane clusters likely related to transform and ridge segments.

A second example is shown for intermediate depth earthquakes (100 to 300 km) from the Tonga-Kermadec region, epicenters between  $16^\circ$  S and  $28^\circ$  S, and  $175^\circ$  E and  $170^\circ$  W. A Schmidt plot of poles to nodal planes is shown in Figure 2.10a, after cluster analysis (Chapter 11) to highlight the two clusters of nodal planes. In this case, two clusters of nodal planes are apparent, the sub-horizontal planes, with steeply plunging poles, are likely the fault planes (Warren et al., 2007). Figure 2.10b shows the same data rotated to the approximate slab reference frame ( $20^\circ$  about Z, then  $35^\circ$  about Y, Section 5.5). The cluster with west plunging poles (red) represent the likely fault planes. This data is given in the example data file `Seismology/CMT jan76_dec17 TK.tsv`.

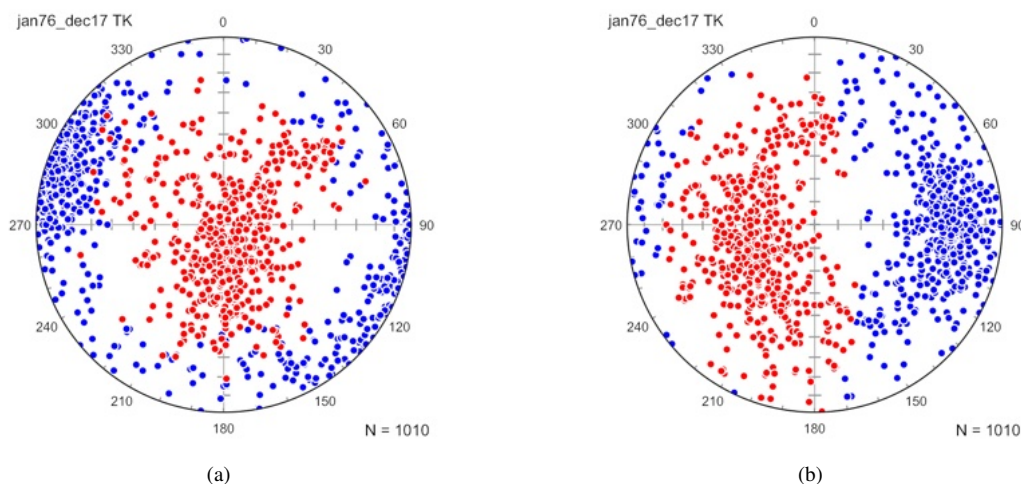


Figure 2.10: Schmidt plot of poles to CMT nodal planes for intermediate depth earthquakes (100 to 300 km) from the Tonga-Kermadec region, epicenters between  $16^{\circ}\text{S}$  and  $28^{\circ}\text{S}$ , and  $175^{\circ}\text{E}$  and  $170^{\circ}\text{W}$ , after cluster analysis (Chapter 11). (a) The sub-horizontal nodal planes are likely the fault planes (Warren et al., 2007). (b) The nodal planes rotated by  $20^{\circ}$  about Z, and  $35^{\circ}$  about Y (Section 5.5) to the approximate slab reference frame. The cluster with west plunging poles (red) likely represent fault planes related to slab extension.

### 2.7.3 Kinematic Data Import

There are multiple conventions for representing kinematic data, as discussed more fully in Section 9.1. When collecting field data it is common to measure the strike and dip of a fault surface, and the trend and plunge of the fault slip line. While the *upward* directed lineation can be recorded in the field, standard measuring techniques commonly record the orientation of the *downward* directed line. Therefore, it is necessary to use some convention to identify the sense of slip (relative motion of the hanging wall). Several conventions are recognized for data file import (Table 2.15).

The fault and kinematic analysis software *FaultKin* (Allmendinger, 2019) can export a data set as a tab-delimited txt file, which can be directly opened in Orient. In this format, slip lines are given as downward directed lines, and one of TR (thrust, or reverse, right), TL (reverse left), NR (normal right), or NL (normal left) is used to designate the sense. Fault and lineation orientations, slip sense, latitude, longitude, elevation, and station identifiers are preserved when importing this file format.

A quadrant notation used for some fault slip surveys by the United States Geological Survey (USGS) is to enter slip lines with trends and (downward) plunges. One of *REV* (reverse), *NOR* (normal), *DEX* (dextral or right), or *SIN* (sinistral or left) is then used to distinguish the sense (J.S. Caine, personal communication, see Disclaimer). These identifiers may be imported or entered into the *Sense* field. Leaving the *Sense* identifier blank assumes that the values entered may include negative striae plunges.

Faults with a dip of  $90^{\circ}$  should be correctly interpreted, a rake of 0 is sinistral, and a rake of 180 is dextral, however, since the hanging wall is undefined, it is prudent to enter a dip of  $89.9^{\circ}$  for clarity. Similarly faults with a dip of  $0^{\circ}$  can be problematic, since the strike is undefined, and it is prudent to enter a dip of  $0.1^{\circ}$  for these. See Section 9.1 for additional information.



Imported Slip Sense	Shortcut	Orient Sense
Reverse	R	Rev
Normal	N	Nor
Dextral	D	Dex
Sinistral	S	Sin
Thrust	T	Rev
Right		Dex
Left		Sin
Rev	R	Rev
Nor	N	Nor
Dex	D	Dex
Sin	S	Sin
TR		Rev
TL		Rev
NR		Nor
NL		Nor

Table 2.15: Slip sense identifiers that can be entered in the *Sense* field of an Orient data file.

## 2.8 Data File Templates

Preferences for individual data files are stored in json files in the Application Support folder for your system (e.g., on a Macintosh, it is in Users/yourname/Library Support/Orient). These are JSON (JavaScript Object Notation) Unicode UTF-8 text files that are widely supported, and can be read by text editors and internet browsers.

This works well for individual files, but when working with multiple files for similar data sets it can be tedious to set the preferences for each file separately. It is therefore possible to save the preferences for a data file as a *template* using the *Save Template* command, and to reload them for a different data file using the *Open Template* command.

For example, if you plan to create plots for 9 data files of slickensides, Data1 ... Data9. Open Data1, set all the plot preferences as desired, and save them using the *Save Template* command. For each additional file, open it and use the *Open Template* command to duplicate the preferences.

## 2.9 Project Files

Orient stores settings in an Orient.json project file that is by default stored in the Application Support folder for your system (e.g., on a Macintosh, it is in Users/yourname/Library Support/Orient). In the same directory is a folder Lists that contains settings for each data file. Note that these files are hidden from the user by default, system settings need to be changed to view them.

It is possible, however, to save the project file to another directory. The project file contains links to all the data files in the project, as well as all of the global settings. No data is stored in the project file, and remains untouched in your spreadsheet files. When reopening the project file, if the data files are moved or renamed, and Orient can not find them, simply locate and reopen them. Deleting the project file has no effect on the data.

When saving a project, you may wish to save the Orient.json project file into a separate folder, for example Orient, in the same directory as your project data files. This folder will then contain the settings for all the data files in the project. For example a directory structure for a project might be

```
MyProject
  MyDataFile1.xlsx
  MyDataFile2.xlsx
  Orient
    Lists
      MyDataFile1.json
      MyDataFile2.json
```

## Orient.json

The project file is a JSON (JavaScript Object Notation) Unicode UTF-8 text file, an open standard format widely used for data files. It consists of ordered key-value pairs stored in recursively nested dictionaries. JSON files are designed to be both human-readable and machine-readable, and can be viewed in text editors and internet browsers. They contain only formats for the plots, and can be safely deleted. If you wish to reuse the settings for one data file for a new data file, use the *Save Preferences* and *Open Preferences* commands (Section 2.8).

## 2.10 Digitizing Data

When digital data files or text listings of directional data are not available, data can be digitized from scanned images of spherical projections or maps. To digitize a spherical projection from a suitable source image, insure that the image is undistorted, that is circular, and that the north point is unrotated. An image editing program such as Adobe Photoshop or GIMP can remove distortion and rotate the image if necessary. An example spherical projection image, Kamb 1959.png, is provided in the Example Data/Crystal Fabric folder.

Open the image using the *Open Image* command, which will display the digitizing window (Figure 2.11a), and open a new spreadsheet for the data using the *File - New* command. Click on the *Digitize* icon to display the digitize dialog (Figure 2.11b). Select the correct options for the spherical projection, stereographic, equal-area, or orthographic, and upper-hemisphere or lower-hemisphere. One hopes the author specified these correctly, if it is labeled *stereonet* you will have to guess (Section 4.7). Select the data type, line or plane, and press *OK*.

When digitizing a spherical projection, a prompt will ask for three points on the perimeter of the projection, after entering these, a circle will be drawn over the projection. If the circle is a reasonable fit, proceed to digitize the points, which will appear in the spreadsheet. If not, the circle can be reinitialized, or distortion of the image may need to be removed. Spurious data points can be deleted in the spreadsheet as necessary. If digitizing needs to be interrupted, save the file and reopen the file and image later to resume. To change data type, lines or planes, reopen the digitize dialog, select the desired one, press enter, and continue digitizing.

Digitizing directional data from a map is similar. Make sure the image is undistorted, and that the X and Y directions are orthogonal with north to the top. The X and Y coordinate scales do not need to be equal, but they must each be scaled linearly within the map area. If necessary, remove any distortion using an image editor. Select *Map* as the source, line or plane, and press *OK*. There will be a prompt for two points with known coordinates to define the area and coordinates. If the result is satisfactory, begin digitizing the elements by clicking on a start point and then an end point. The coordinates entered into the spreadsheet will be the center point between the two points.

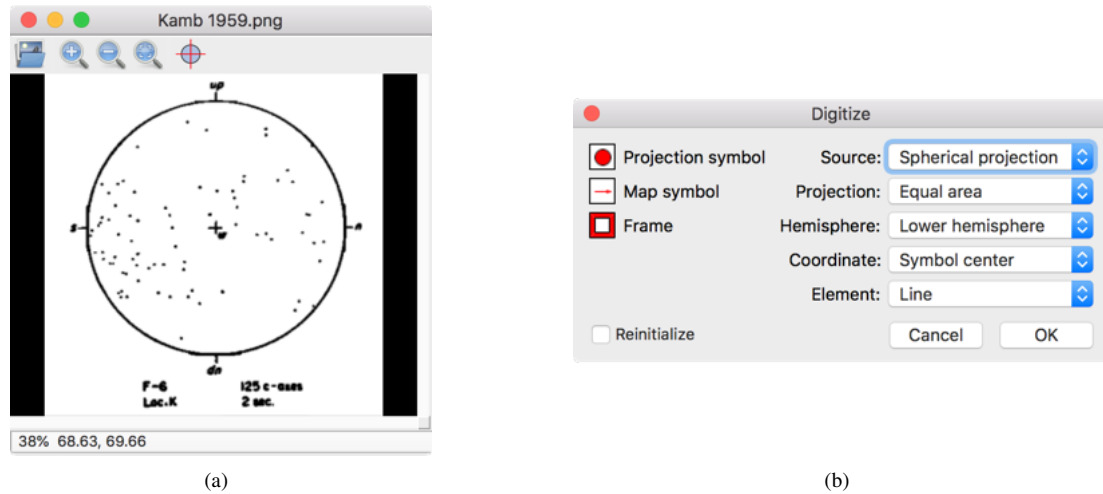


Figure 2.11: Example of digitizing data from a spherical projection. (a) An image of a spherical projection from Kamb (1959), opened with the *Open Image* command, displayed in the digitizing window. (b) The digitize dialog showing the options for digitizing orientation data from images.

## 2.11 Simulating Data

The *Simulate Data* command is used to generate simulated data distributions on the sphere. The *Fibonacci* option generates a spherical grid of points on the sphere that are virtually uniform and isotropic, with an equal area for each grid point. There are only two antipodal compact singular regions on the sphere that deviate from uniformity (Swinbank and Purser, 2006). Figure 2.12a is a Schmidt plot of 1000 vectors that define a Fibonacci grid.

The *Uniform* option is used to generate uniformly distributed data on the sphere. The data is constructed by generating random rotation matrices (Arvo, 1992) and applying them to a unit vector. Figure 2.12b is a Schmidt plot of 1000 vectors plotted as directed data, and illustrating a random sample from a uniform distribution.

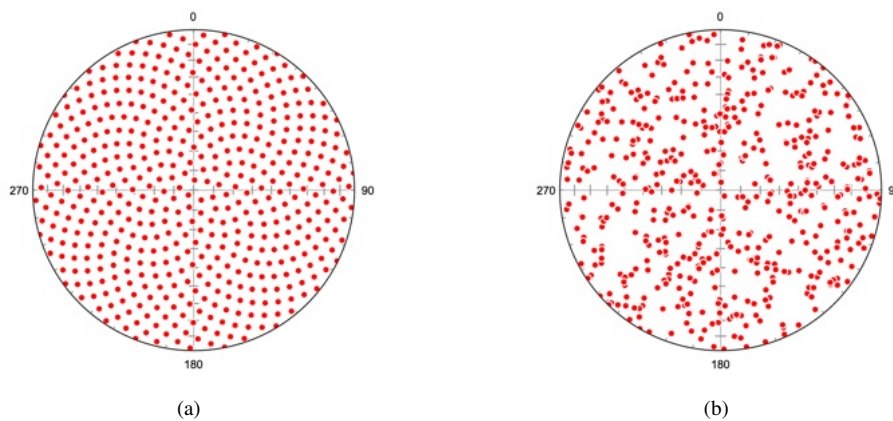


Figure 2.12: Schmidt plots of data generated using the *Simulate Data* command. Upper hemisphere data is not displayed. (a) Fibonacci grid of 1000 unit vectors which are virtually uniform and isotropic, the small area at the center of the plot deviates from uniformity. (b) 1000 unit vectors generated with the *Uniform* option plotted as directed data. This simulates a random sample from a uniform distribution.

Spherical distribution models are discussed in Sections 6.1 and 6.2. The simplest of these is the Fisher distribution, analogous to the well known Gaussian, or normal, distribution. The Fisher distribution,  $f_p(x; \mu, \kappa)$ , parameters are the vector mean,  $\mu$ , given by  $(\theta, \phi)$ , and the concentration parameter,  $\kappa$ . Given these three parameters, it is possible to select random unit vectors from the distribution to form a simulated data sample (Fisher et al., 1987, Section 3.6.2). Figure 2.13 shows

Schmidt plots of 1000 unit vectors drawn randomly from a Fisher distribution using the *Simulate Data* command *Fisher* option. The distribution means ( $\mu$ ) are centered at trend, plunge =  $315^\circ, 0^\circ$ , for  $\kappa = 2$  and  $\kappa = 8$ .  $\kappa$  must be a positive number, for  $\kappa \leq 0$  a uniform distribution is returned.

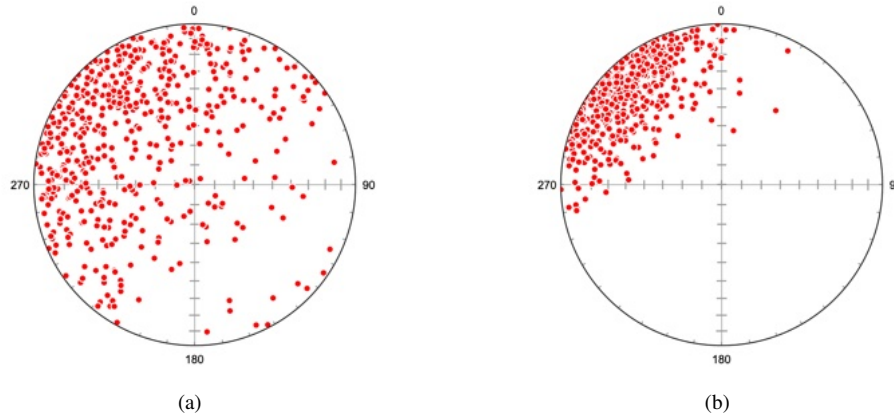


Figure 2.13: Schmidt plots of 1000 unit vectors drawn randomly from a Fisher distribution (Section 6.1) using the *Simulate Data* command *Fisher* option. The distribution means,  $\mu$ , are centered at trend, plunge =  $315^\circ, 0^\circ$ . Upper hemisphere data is not displayed. (a) Data sample for concentration parameter  $\kappa = 2$ . (b) Data sample for concentration parameter  $\kappa = 8$ .

The Watson, or Dimroth-Watson, distribution (Sections 6.1 and 6.2) is the simplest distribution for undirected axes. The parameters for the Watson distribution are the maximum eigenvector,  $\mu$ , and the concentration parameter,  $\kappa$ . For  $\kappa > 0$  the distribution is bipolar, for  $\kappa < 0$  the distribution is a girdle, for  $\kappa = 0$  the distribution is uniform.

Given these parameters, it is possible to select random unit axes from the distribution to form a simulated data sample (Best and Fisher, 1986; Li and Wong, 1993). Figure 2.14 shows Schmidt plots of 1000 unit vectors drawn randomly from a Watson distribution using the *Simulate Data* command *Watson* option. The distribution means,  $\mu$ , are centered at trend, plunge =  $315^\circ, 0^\circ$ , for  $\kappa = 2$  and  $\kappa = 8$ .

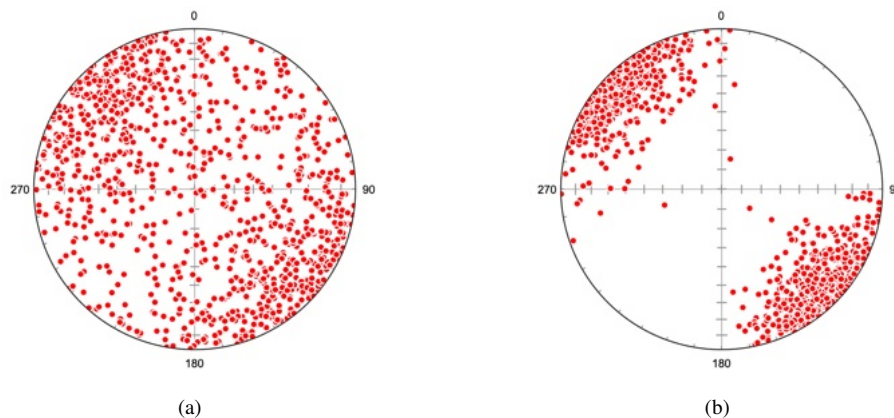


Figure 2.14: Schmidt plots of 1000 unit axes drawn randomly from a Watson bipolar distribution (Section 6.1) using the *Simulate Data* command *Watson* option. The distribution means ( $\mu$ ) are centered at trend, plunge =  $315^\circ, 0^\circ$ . (a) Data sample for concentration parameter  $\kappa = 2$ . (b) Data sample for concentration parameter  $\kappa = 8$ .

For a girdle distribution, random unit axes can also be selected from the distribution to form a simulated data sample (Li and Wong, 1993). Figure 2.15 shows Schmidt plots of 1000 unit vectors drawn randomly from a Watson distribution using the *Simulate Data* command *Watson* option. The distribution means,  $\mu$ , are centered at trend, plunge =  $315^\circ, 0^\circ$ , for  $\kappa = -2$  and  $\kappa = -8$ .

The Kent distribution (Sections 6.1 and 6.2) is a distribution for unit vectors that is not symmetrical about the mean axis,  $\mu$ . Jammalamadaka and Terdik (2022) discuss the family of generalized

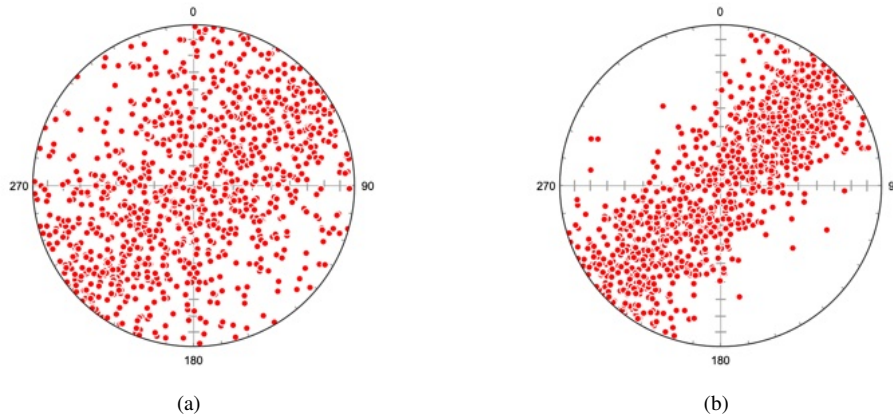


Figure 2.15: Schmidt plots of 1000 unit axes drawn randomly from a Watson girdle distribution (Section 6.1) using the *Simulate Data* command *Watson* option. The distribution means,  $\mu$ , are centered at trend, plunge =  $315^\circ, 0^\circ$ . (a) Simulated sample for concentration parameter  $\kappa = -2$ . (b) Simulated sample for concentration parameter  $\kappa = -8$ .

Fisher-Bingham (*GFB*) distributions which include all of the previously discussed models. Simplified models are derived from the general *GFB* by setting some parameters to zero. In this family, the Kent distribution is the five parameter  $GFB_{5,\kappa}$ , given as  $f_p(x; \mu, \kappa, \beta, \psi)$ . This distribution depends on the parameters  $\mu$  and  $\kappa$ , but additionally requires an ovalness parameter,  $\beta$ , and an orientation parameter,  $\psi$ , describing the rotation about the mean axis. The Kent distribution (Kent, 1982) is normally confined to  $0 \leq 2\beta \leq \kappa$  to give a unimodal distribution, however, Jammalamadaka and Terdik (2022) discuss the extension of the distribution to  $2\beta > \kappa$ , for which the distribution is bimodal. The angle between the two modes is given by  $\eta$ , where  $\cos \eta = \kappa/2\beta$ .

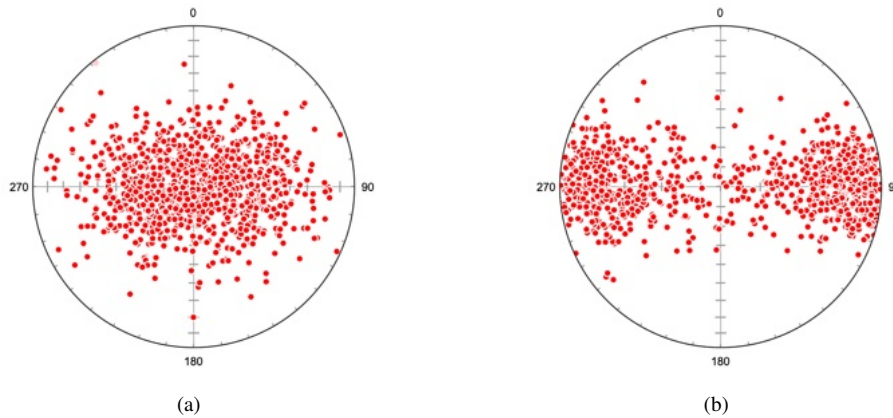


Figure 2.16: Schmidt plots of 1000 unit vectors drawn randomly from a Kent distribution (Section 6.1) using the *Simulate Data* command *Kent* option. The distribution means,  $\mu$ , are centered at trend, plunge =  $0^\circ, 90^\circ$ . Upper hemisphere data not shown. (a) Simulated sample for distribution parameters  $\kappa = 8, \beta = 2, \psi = 0^\circ$ . Since  $2\beta < \kappa$ , this gives a unimodal sample. (b) Simulated sample for concentration parameters  $\kappa = 4, \beta = 6, \psi = 0^\circ$ . Since  $2\beta > \kappa$ , this gives a bimodal sample with two modes at  $\eta = 70.5^\circ$  apart.

## 2.12 Data Weighting and Sampling Correction

In many studies it is desirable to give some data points a higher weight than other data points. For example, when analyzing fault data, exposure length or gouge thickness may serve as a proxy for (unknown) displacement. Each data point can be assigned a weight, and the weight can be taken into account in all calculations, except bootstrap statistics. Bootstrap statistics require random sampling of data points, which must be equally weighted. This section focuses on the use and calculation of weights based on sampling methodologies.

A common methodology for estimating fracture, or other planar feature, orientations and frequency is to measure the orientations and positions of fractures intersecting a *scan line*. The scan line may be a line selected along an outcrop, or parallel to a drill core. A second common method is to sample all fractures exposed within a selected area on a planar outcrop surface. Depending on the goals of the study, it may be useful to identify and focus on specific joint sets, rather than attempting to measure all fractures. Various parameters will be measured depending on the study, such as trace length, fracture filling, gouge, shear offset, and extension.

This section explains how weighting can be applied to the graphical display and statistics of fracture orientations, assuming that a suitable sampling methodology and numerical weighting has been chosen. Second, a calculation to reduce the frequency bias due to the orientations of the fractures with respect to the scan line or outcrop surface is given.

Example data file Fractures/Caine 2001.tsv (Caine, 2001) is from a scan line (SL1 285 S) of fracture data used to characterize a fracture network and fault-related hydraulic parameters in the Turkey Creek watershed, Colorado Rocky Mountain Front Range. The scan line, with a trend and plunge of  $347^\circ, 00^\circ$ , was made along an outcrop face of gneiss with a strike and dip of  $347^\circ, 36^\circ$ . Figure 2.17a is a contoured Schmidt plot of the poles to fracture orientations with no weighting applied. Figure 2.17b is a similar plot, but using the *fracture trace length* as a weight. This weighting emphasizes the three apparent modes in the distribution. The selection of trace length for weighting is only one option, and is used here to illustrate the concept.

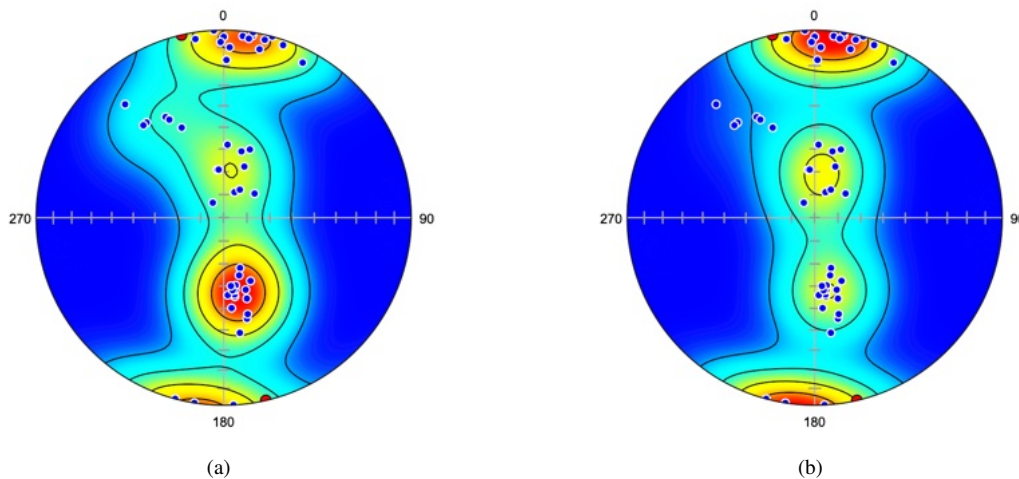


Figure 2.17: Schmidt plots of 47 poles to fracture planes measured along a horizontal scan line trending  $347^\circ$  within the Turkey Creek watershed (Caine, 2001). The scan line is the red circle. Contours are 20% density. (a) Plot with no weighting applied. Note the high density of joints nearly perpendicular to the scan line, the set and dipping steeply south. (b) Plot with the fracture trace length used for weighting. Note the increased density of joints nearly perpendicular to the scan line, the set dipping steeply south.

The scan line methodology is useful and widely used, however, it is inherently biased towards fractures whose orientations intersect the scan line at high angles. Fractures sets perpendicular to the scan line will give a true spacing and frequency, while fracture sets oblique to the scan line will have a greater apparent spacing, and lower apparent frequency (Figure 2.18).

Terzaghi (1965) gives a correction for the apparent frequency in the linear scan line case

$$\begin{aligned} w_f &= d_f/d_f' \\ &= 1/\cos \alpha_f \\ &= 1/(s_f \cdot n_f) \end{aligned} \quad (2.2)$$

Where  $w_f$  is the weighting correction, the ratio between the apparent and actual frequency. As  $\alpha_f$  approaches  $90^\circ$  the weighting goes to infinity, therefore it is necessary to define a *blind zone* angle,  $\beta_b$ , where it is recognized that it is not possible to accurately weight the frequency. The blind zone is

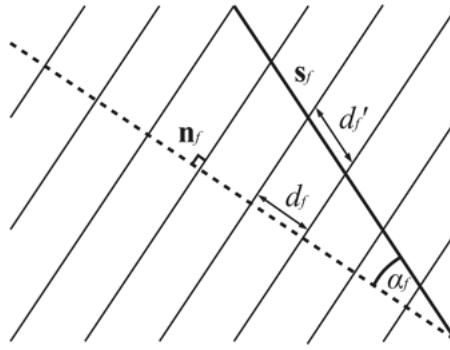


Figure 2.18: Relationship between a scan line ( $s_f$ ) and the apparent frequency of fracture planes.  $\alpha_f$  is the angle between the fracture normals ( $n_f$ ) and the scan line. Measurements along the scan line give an apparent frequency ( $1/d'_f$ ), which is less than the true frequency ( $1/d_f$ ).

the minimum angle between the fracture planes and the scan line used for weighting, commonly  $\beta_b = 5^\circ$  to  $25^\circ$ . All fractures within the blind zone are given a weight

$$w_b = 1/\cos(90^\circ - \beta_b) \quad (2.3)$$

A second common methodology is the measure *all* fractures within a selected area on a plane. In this case the frequency correction is made based on the angle  $\beta_f$  between the normal to the outcrop plane and the fracture plane,  $n_f$ . The frequency correction for the planar case is

$$w_f = 1/\sin\beta_f \quad (2.4)$$

The blind zone,  $\beta_b$ , here is the minimum angle for a calculated weight between the outcrop plane normal and the fracture normals, and weighting within the blind zone is

$$w_b = 1/\sin\beta_b \quad (2.5)$$

These corrections can be applied using the *Calculate Weights* command. Figure 2.19 shows the fracture data as in Figure 2.17 with linear frequency correction applied, and a blind zone of  $15^\circ$ . This replaces any existing weights with the calculated correction. Figure 2.19a shows the data as in Figure 2.19b with a linear frequency correction multiplied by the trace length weight, this modifies the existing weight by the correction. These examples illustrate some of the considerations to take into account during a fracture analysis study. There is an extensive literature on the characterization of fractures within a rock body, which should be consulted prior to such a study.

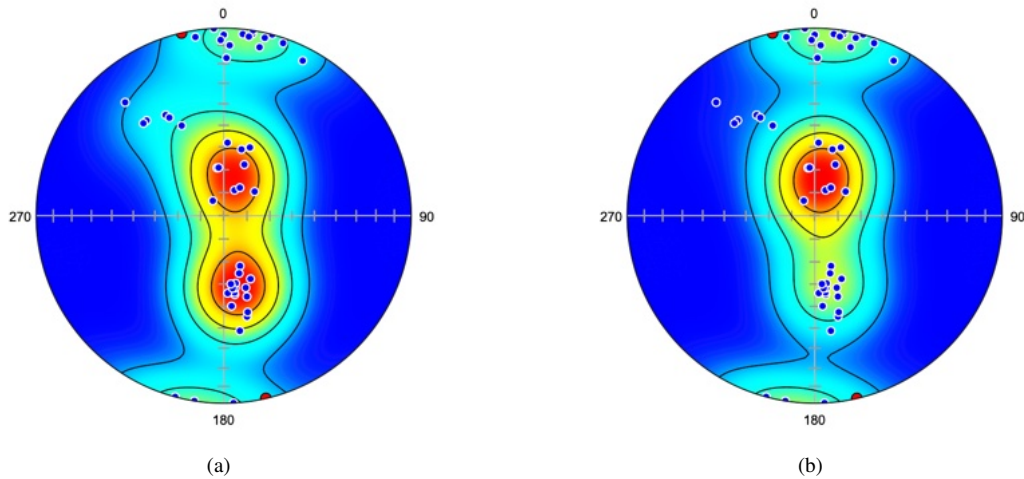


Figure 2.19: Schmidt plots of fracture data as in Figure 2.17 with corrections applied along the horizontal  $347^\circ$  scan line (red circle) using the *Calculate Weights* command, and a blind zone of  $15^\circ$ . (a) Data with a linear frequency correction (Eq 2.2, 2.3) applied along the scan line. This applies the correction without using existing weights, compare to Figure 2.17a. Note the decreased density of joints at a high angle to the scan line, the set dipping steeply south. (b) Data with the trace length weight multiplied by the linear frequency correction, using the *Multiply* option. This applies the correction to existing weights, compare to Figure 2.17b. Note the decreased density of joints at a high angle to the scan line, the set dipping steeply south.

### 2.13 Weight and Characteristic Classification

The *Weight* data attribute can be used for a variety of measurements that may better characterize the significance of certain data. These could include fracture length, gouge thickness, bedding thickness, cleavage intensity, distance from a shear zone, stream reach lengths, or other numeric parameters. In some cases it may be useful to classify these measurements into discrete intervals. The *Classify Weights* command allows the classification of weights into either a selected number of *levels* over the range of weights, or a set *interval*. The weights are classified into discrete *domains* identified as attributes in the *Domain* data column.

Weight classification can also be done manually by setting the domains to desired values (see Section 7.2 for an example). Non-numeric characteristics, such as lithology or vein fill, must be classified manually by assigning a *Domain* number, a non-zero positive integer, to each characteristic.

The example data file *Fractures/Caine 2001.tsv* (Caine, 2001) from a scan line of fracture data used to characterize a fracture network in the Turkey Creek watershed, Colorado Rocky Mountain Front Range, is used as an example. Open the data file and use the *Classify Weights* command to open the *Classify Weights* dialog. In the *Classify Weights* dialog select *Levels*, enter 5 in the *Levels* edit box, check *Zero min*, check *Decreasing*, and press *OK*. This will subdivide the data into 5 domains as given in the *Domain* data column. Selecting *Zero min* causes the intervals to start at zero, rather than the minimum weight. Selecting *Decreasing* causes the domain numbers to decrease with increasing weight.

Figure 2.20 is a cumulative equal-area circular histogram of the strikes of fractures from each of the five domains, J.S.D1 (red) to J.S.D5 (blue). Because *Decreasing* was selected, domain 1 contains the maximum weights, and domain 5 contains the minimum weights. In this case, the histogram emphasizes the greater abundance of the shorter segments in domain 5, J.S.D5 (blue).



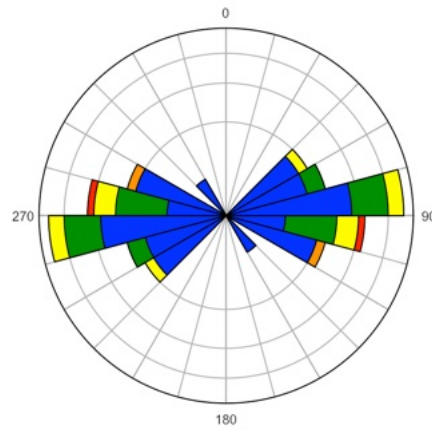


Figure 2.20: Equal-area circular histogram of the strikes of fractures along a scan line (Caine, 2001). The data has been classified into five levels using the *Classify Weights* command. The histogram is *cumulative* with different colors selected for each domain, J.S.D1 (red) to J.S.D5 (blue). Because *Decreasing* is selected, domain 1 has the maximum weights, and domain 5 the minimum weights. The histogram emphasizes the greater abundance of the shorter fracture segments in domain 5, J.S.D.5 (blue).

### 3 Circular Plots

Circular plots for two dimensional directional data include scatter plots, circular histograms, and circular frequency polygons (Davis, 1986, 2002; Fisher et al., 1987; Cheeney, 1983; Howarth, 1999; Mardia and Jupp, 2000). Circular plots can also be used to display the horizontal angles of lines and planes, such as the trends of lineations, or the strikes of plane. For planes it is possible to plot the strike direction, dip direction, or the azimuth of the plane normal. The data may be directed or undirected. Undirected data plots two points at  $180^\circ$ , or can be plotted on a double angle, modulo  $180^\circ$ , plot. The settings for these plots are in the *Preferences* dialog in the *Circular Histogram* pane. In fault kinematic studies, it may be useful to plot histograms of line plunges or pitches.

#### 3.1 Scatter Plots

A simple circular scatter plot shows the data distribution on a circular plot, normally the perimeter of a unit circle (Davis, 1986, 2002; Cheeney, 1983; Mardia and Jupp, 2000). Symbols are plotted on the perimeter, and rays may be drawn from the circle center. The vector mean, for directed or undirected data (Section 3.4), can also be displayed. There are many variations on scatter plots, Orient implements ray plots with lines drawn from the center, and with symbols on the perimeter (Figure 3.1).

Figure 3.1a is a circular scatter plot of the travel directions of 76 turtles after laying eggs, data from Gould (Mardia and Jupp, 2000, Table 1.5), an example of directed circular directional data. In order to better visualize overlapping data points, the opacity of the data point symbols is set to 50%. Figure 3.1b is a plot of the mean strikes of two joint sets from each of 24 counties in central New York, data from Parker (1942). This data is plotted as strike azimuths, an example of undirected data. Although joints are planar features, these are all near vertical, and their dips were not reported.

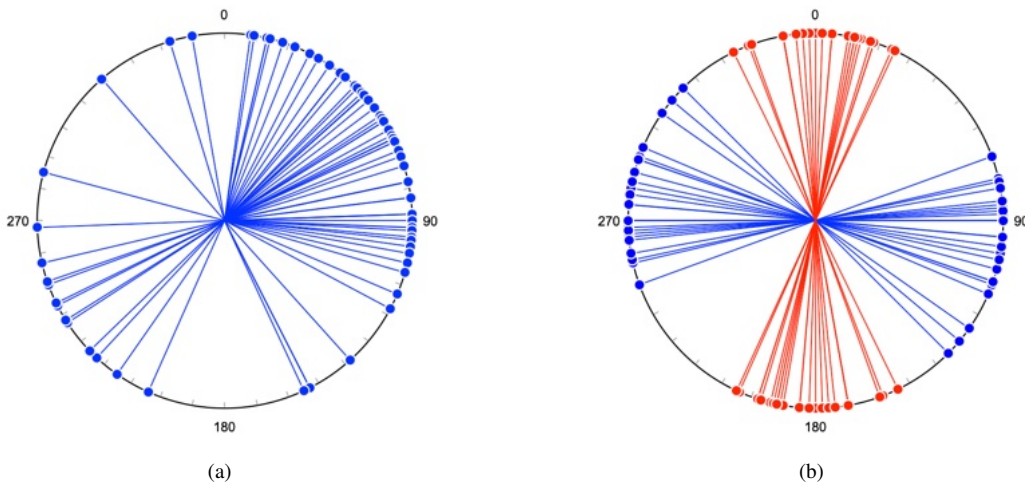


Figure 3.1: Examples of circular scatter plots. (a) Circular scatter plot of the orientations of 76 turtles after laying eggs. Data from Gould (Mardia and Jupp, 2000, Table 1.5). (b) Circular scatter plot of the mean strikes of two joint sets from each of 24 counties in central New York. Data from Parker (1942).

#### 3.2 Circular Histograms

Two dimensional directional data is commonly displayed as a circular frequency histogram, where the data count is tallied for bins or sectors of a set angular width. A commonly used histogram is constructed with sector *radii* proportional to class frequency, an *equidistant* rose diagram. Unfortunately, such a diagram is biased, and not a true histogram, because the area displayed for a single count increases with the radius. An unbiased plot is an *equal-area* circular histogram, or polar area

diagram, where each count has an equal area, and the sector area is proportional to class frequency (Nightingale, 1858; Cheeney, 1983; Nemeč, 1988; Mardia and Jupp, 2000).

Both equal-area rose and *kite* plots appear in reports from 1858 by Florence Nightingale on mortality statistics for epidemic disease in the Crimean War. These reports, with their effective graphical plots, eventually lead to much needed sanitary reforms. The earliest of these reports contained kite diagrams (Nightingale, 1858, Diagrams I, K), Figure 3.2a. Nightingale used the term *bat's wing* ("the great black bat's wing on the right-hand of the diagram") to describe the plot on the righthand side of Figure 3.2a (Nightingale, 1858, p. 5), but probably did not intend it as a general name for such plots. In the later reports these were replaced by equal-area rose diagrams, Figure 3.2b, to better represent the data in an unbiased way (Andrews, 2022). Nightingale apparently did not give a name to the new plot, although *wedge* and *coxcomb* have been suggested, however *rose* is commonly used. To clarify, and distinguish it from the biased *rose*, it is referred to as an *equal-area rose* here. As recognized by Nightingale, it is the preferred plot for an unbiased representation of the data.

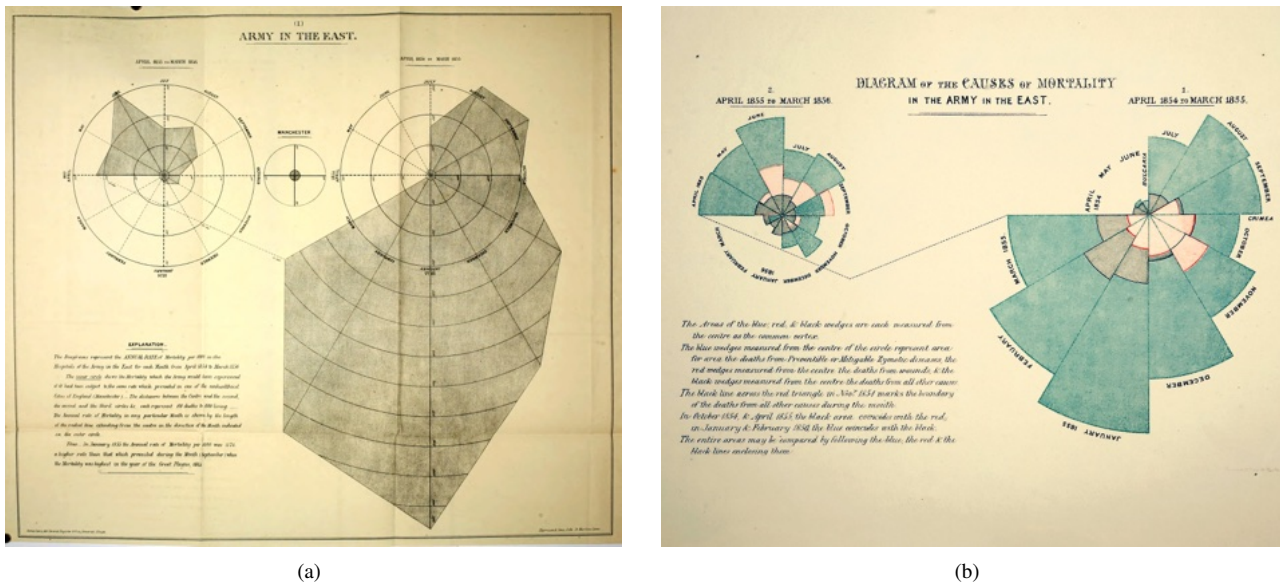


Figure 3.2: Circular histograms illustrating mortality rates associated with epidemic disease responsible for British deaths in the Crimean War. (a) Kite plots from the early report of Nightingale (1858) (Diagram I). Nightingale used the term *bat's wing* to describe the plot on the righthand side, but probably did not intend it as a general name for such plots. (b) In subsequent reports Nightingale replaced the kite plots with equal-area rose plots to better represent the data in an unbiased way (Andrews, 2022). Figure from the National Library of Medicine.

Figure 3.3 shows examples of both equidistant and equal-area rose diagrams for turtle directions, and Figure 3.4 shows examples of equidistant and equal-area rose diagrams for undirected joint strike data. Each of these plots is drawn with 24 bins, or  $15^\circ$  sectors, the selection of bin size can significantly change the appearance of the diagram.

A circular frequency polygon (Howarth, 1999, citing Haughton 1864), or *kite* plot (Davis, 1986, 2002; Swan and Sandilands, 1995), is an alternative plot for displaying circular directional data. In a circular frequency polygon plot the bin sector centers are connected by straight lines to form a polygon. Figure 3.5a is a circular frequency polygon plot of the turtle direction data, shown in Figure 3.3, using the same size bin sectors. Figure 3.5b is a similar plot of the undirected joint data shown in 3.4. Kite plots were initially used by Nightingale (1858) in an early report on epidemic disease, however Nightingale replaced them with the less biased equal-area rose diagrams in subsequent reports. To summarize, it has been understood since 1858 that, of the three plots presented in this section, the equal-area rose gives the least biased representation of the data.

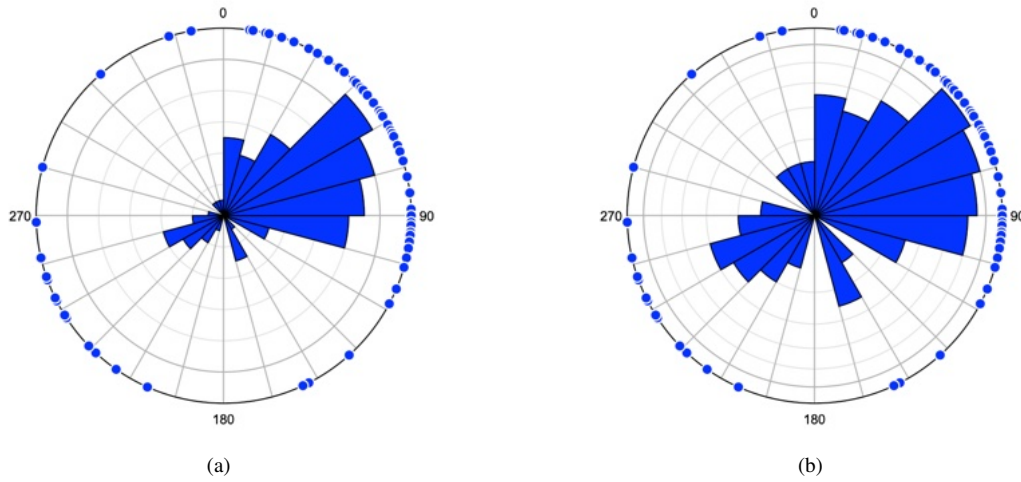


Figure 3.3: Examples of equidistant and equal-area circular histograms for turtle directions (Mardia and Jupp, 2000, Table 1.5, from Gould). (a) Equidistant rose diagram. The increasing area for larger bin counts results in an area bias, so this is not a true histogram. (b) Equal-area rose diagram. Each count has an equal area, removing area bias.

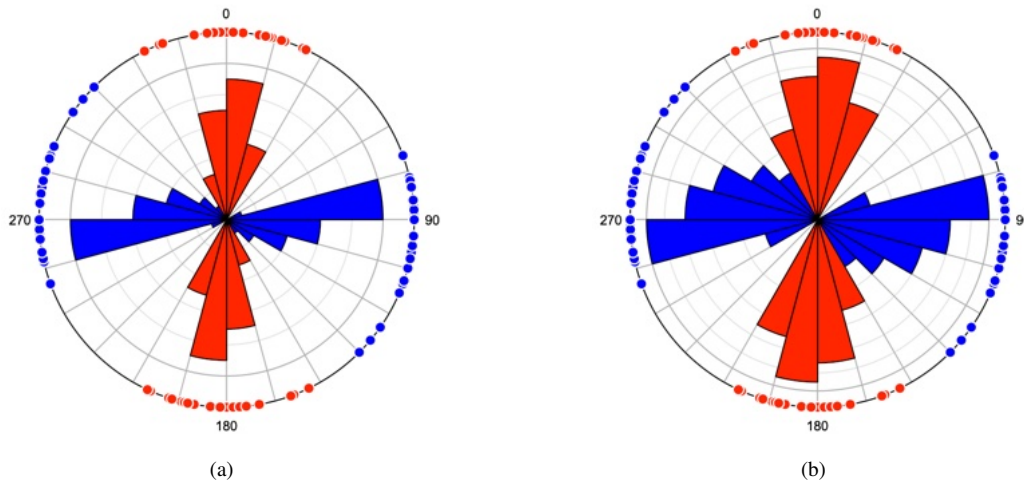


Figure 3.4: Examples of equidistant and equal-area circular histograms of undirected joint strikes from Parker (1942). (a) Equidistant circular histogram of the data. The increasing area for larger bin counts results in an area bias, so this is not a true histogram. (b) Equal-area circular histogram of the data. Each count has an equal area, removing area bias.

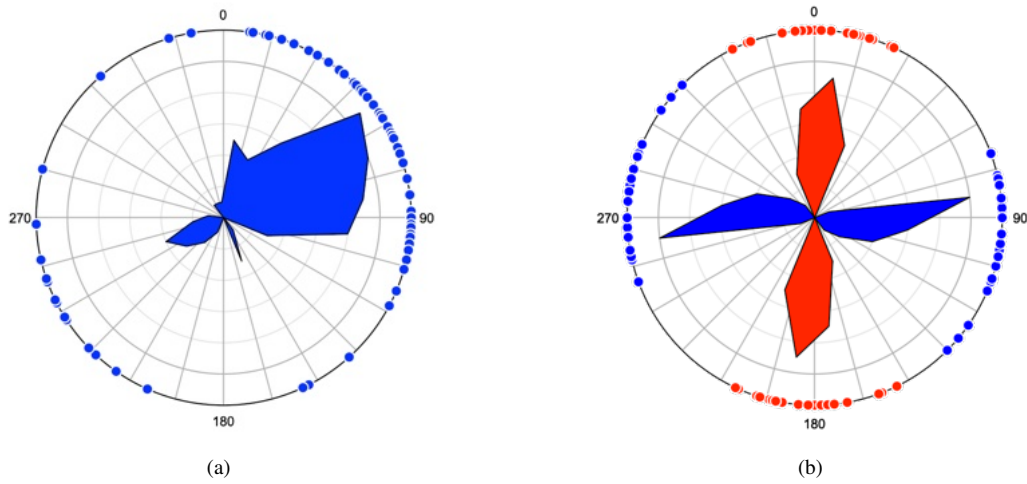


Figure 3.5: Circular frequency polygon plots, or kite diagrams. As noted by Nightingale (1858), equal-area rose diagrams (Figures 3.3b and 3.4b) give less biased representations of the data. (a) Plot of the turtle direction data shown in Figure 3.3. (b) Plot of the undirected joint strike data shown in Figure 3.4.

### 3.3 Kernel Density Estimate

Circular histograms, or rose diagrams, are constructed by specifying a grouping interval, or bin width, such as  $10^\circ$  or  $15^\circ$ . The sectors should be constructed with radii proportional to the square root of the bin count, to form an equal-area rose diagram. The bin width controls the smoothing of the data, and is a key parameter in defining the histogram's shape. Unfortunately, the need to specify a bin width is an undesirable property of all histograms, and can have a considerable effect on their shape.

The construction of a histogram is an attempt to characterize a density estimate of the data. Kernel density estimation (KDE) is an alternative approach that produces a continuous, rather than discrete, estimate (Silverman, 1986). A kernel density function is effectively slid along the data sample to produce a moving average. KDE has been applied to von Mises distributions (Fisher, 1989; Jammalamadaka and Sengupta, 2001; Taylor, 2008; García-Portugués, 2013), a suitable kernel function for a von Mises distribution is

$$\hat{f}(\theta; h) = \frac{1}{n2\pi I_0(1/h)} \sum_{i=1}^n \exp(\cos(\theta - \theta_i)/h) \quad (3.1)$$

where  $h$  is the bandwidth,  $\theta$  is the location on the histogram, and  $I_0$  is a modified Bessel function of the first kind of order 0. The density function defines a continuous density estimate for all  $\theta$ ,  $0^\circ$  to  $360^\circ$ , based on the sample  $\theta_i$ . The selection of  $h$ , which controls smoothing, is not straightforward, especially for multimodal samples that deviate significantly from a von Mises distribution.

Two options are given for the estimation of  $h$ , one uses the method of Taylor (2008), the second uses the rule of thumb (*ROT*) given by García-Portugués (2013), which has been shown to be an improvement. The estimate, which is based on a unimodal Von Mises distribution, can be refined by setting the *Smooth* parameter. If an alternative method is available for choosing  $h$ , select *None*, and enter it as the *Smooth* parameter.

Refining the estimated  $h$  can be done by varying the *Smooth* factor, which  $h$  is multiplied by. A small smooth factor will emphasize individual data points, while a large value loses details of the distribution, a smooth factor of 1.0 gives the unmodified estimate. Although complex in detail (García-Portugués, 2013), estimates of  $h$  from multimodal samples will likely be over-smoothed. It is recommended that a smooth value be selected that reveals details of the sample variations, without being overly effected by individual data points. The kernel density estimates are scaled so the maximum value plots at a radius equal to the plot radius, and may be scaled by specifying the *Scale* factor.

Examples of rule of thumb kernel density estimates for directed and undirected data samples are given in Figure 3.6. Figure 3.6a is a sample of 76 directed azimuths of turtle paths (Mardia and Jupp, 2000, Table 1.5, from Gould). The smooth factor is 1.0, and the scale factor is 0.95. Figure 3.6b is a sample of 48 means of undirected joint strikes subdivided into two groups, from Parker (1942). The smooth factor is 1.0, and the scale factor is 0.95. Plots with lower smooth parameters are shown in Figure 3.7.

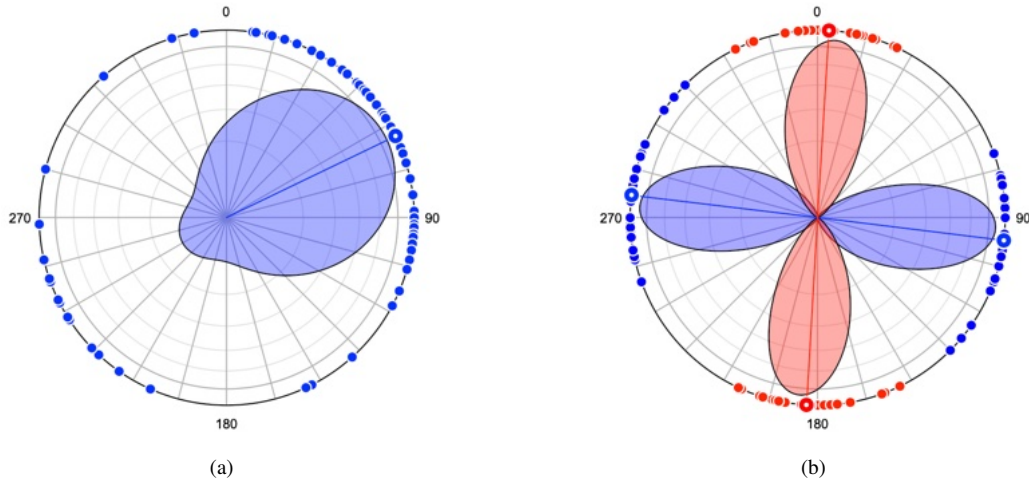


Figure 3.6: Examples of rule of thumb kernel density estimates for directed and undirected data samples. (a) 76 directed azimuths of turtle orientations (Mardia and Jupp, 2000, Table 1.5, from Gould). The smooth factor is 1.0, and the scale factor is 0.95. The vector mean, Section 3.4 is displayed as a large circle. (b) Sample of 48 undirected joint strikes subdivided into two groups, from Parker (1942). The smooth factor is 1.0, and the scaling factor is 0.95. The axial means, Section 3.4 are displayed as large circles.

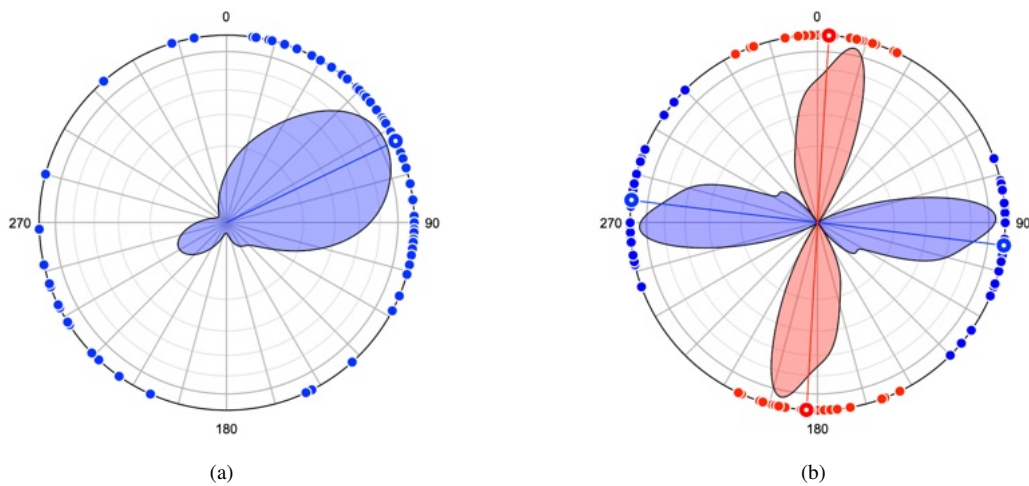


Figure 3.7: Examples of rule of thumb kernel density estimates for directed and undirected data samples with modified smooth factors. (a) 76 directed azimuths of turtle orientations (Mardia and Jupp, 2000, Table 1.5, from Gould). The smooth factor is 0.2, and the scaling factor is 0.95. The vector mean, Section 3.4 is displayed as a large circle. (b) Sample of 48 undirected joint strikes subdivided into two groups, from Parker (1942). The smooth factor is 0.2, and the scale factor is 0.95. The axial means, Section 3.4 are displayed as large circles.

### 3.4 Circular Mean

A simple measure of location, or best-fit, to circular directional data is the *mean direction*, which is calculated as a vector sum. For directed data the two sums are calculated

$$\begin{aligned}\bar{C} &= \frac{1}{n} \sum_{i=1}^n \cos \theta_i \\ \bar{S} &= \frac{1}{n} \sum_{i=1}^n \sin \theta_i\end{aligned}\tag{3.2}$$

Then the *mean resultant length*,  $\bar{R}$ , and direction,  $\bar{\theta}$ , or center of mass of the coordinates, is calculated as

$$\begin{aligned}\bar{R} &= \sqrt{\bar{C}^2 + \bar{S}^2} \\ \bar{\theta} &= \arctan(\bar{S}/\bar{C})\end{aligned}\tag{3.3}$$

Since the mean resultant length approaches 1 as directions converge, it is common to cite the sample *circular variance*

$$s_0^2 = 1 - \bar{R}\tag{3.4}$$

which is 0 when all the directions are identical. The approximate standard error is

$$s_e = 1 - \sqrt{(n\bar{R}\kappa)}\tag{3.5}$$

where  $\kappa$  is the concentration parameter (Davis, 1986). An approximate confidence interval is given by

$$ci_\alpha = \bar{\theta} \pm Z_\alpha s_e\tag{3.6}$$

See Section 6.2 for details on the estimation of  $\kappa$ .

For undirected, axial, data the same calculation is done, however  $\theta$  is doubled prior to the summation, and the result is halved. For details of statistical measures and tests for circular directional data see Mardia (1972), Cheeney (1983), Davis (1986), Fisher et al. (1987), and Mardia and Jupp (2000). Figure 3.6a shows an example vector mean, and Figure 3.6 shows example axial means.

### 3.5 Circular Median

The circular mean is the most common measure of the central tendency of a sample of circular directions, however the mean can be strongly effected by outliers, especially for small samples. In such cases it may be appropriate to calculate the circular median. The median subdivides the data into two parts, selecting the median as the value with equal numbers on each side of a value.

A diameter passing through the median should divide the circle into two semi-circles, each with an equal number of data points, and the majority of the data should lie closer to the median than the anti-median (median + 180°). For an odd number of data points, the median will be one of the data points, for an even number of points, the median will lie half way between two adjacent data points. Such a value may be found by minimizing the *circular mean deviation* (Mardia and Jupp, 2000, eq 2.3.14)

$$d(\hat{\theta}) = \pi - \frac{1}{n} \sum_{i=1}^n |\pi - |\theta - \hat{\theta}||\tag{3.7}$$

where  $\hat{\theta}$  is the estimate of the median. Minimization is done by testing each data value for an odd number of data points, or the mid-points between adjacent data points for an even number.

This calculation can lead to non-unique estimates of the circular median, since there may be two or more diameters that divide the data equally and have the same circular mean deviation. In this case all such directions are reported with their mean, which gives a unique estimate of the median (Sango Otieno and Anderson-Cook, 2003).

### 3.6 Rayleigh Uniformity Test

The values for  $\bar{R}$  and  $\kappa$  give a measure of the spread of the data around the mean that can be used to test a sample for uniformity assuming the observations came from a von Mises distribution. In particular a null hypothesis,  $H_0$ , and an alternative hypothesis,  $H_1$  can be posed

$$\begin{aligned}H_0 &: \kappa = 0 \\ H_1 &: \kappa > 0\end{aligned}\tag{3.8}$$



The test rejects the null hypothesis of uniformity depending on the magnitude of the test statistic,  $\bar{R}$  and the size of the sample,  $n$ . Tables of critical values for  $\bar{R}$  are tabulated (Mardia, 1972; Davis, 1986; Swan and Sandilands, 1995), and the reported critical values are based on these tables either directly or interpolated. The null hypothesis can be rejected if  $\bar{R}$  is greater than the critical value.

A common alternative is to use an estimated p-score (probability score). The p-score is calculated from  $\bar{R}$  and  $n$  using an empirical formula based on calculated values, and the null hypothesis can be rejected for low p-scores (Jammalamadaka and Sengupta, 2001; Berens, 2009).

### 3.7 Vertical Component and Rake Plots

A circular histogram is commonly used to display two-dimensional azimuthal data, however in some cases it may be desirable to display other angles or vector components, such as the dips of planes, the inclinations of lines, or the rakes of lines in planes. The data file of fault slickenside data, Faults/Angelier 1979, is used to illustrate examples of such plots. The data is given a *Type* SL, so fault planes are designated SL.S, and fault slip lineations SL.L.

The data is first orthonormalized using the *Data - Calculate Lines* command, which removes misfit errors and calculates rakes (Section 9.2). Figure 3.8 shows the *Preferences* dialog settings to display a histogram of the fault plane (SL.S) strikes. The *Components* drop-down menu allows the selection of *Horizontal* (default), *Vertical*, and *Rake* components. The *Quadrants* drop-down menu allows the selection of all, two adjacent, or a single quadrant. This is useful, for example, to display data such as the dips of planes, which vary from  $0^\circ$  to  $90^\circ$ . Note that the numerical labels *Start* position, in the *Circular Histogram - Labels* pane, need to be modified from 90 to 0 for vertical component and rake plots.

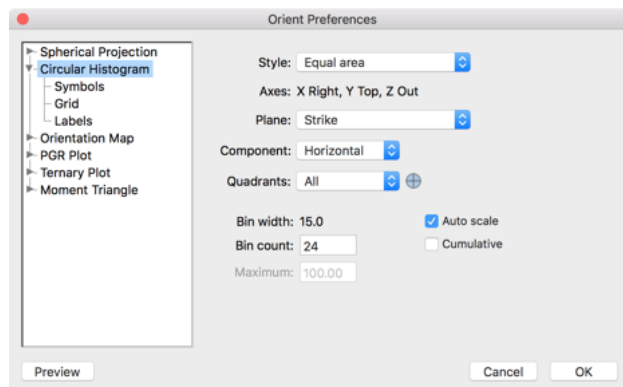


Figure 3.8: The *Preferences* dialog showing options for a *Circular Histogram*. Note that the *Plane* style is set to *Strike*, the selected *Component* is *Horizontal*, and *Quadrants* are set to *All*.

Figure 3.9a is a circular frequency polygon of the strikes of the 38 fault planes (SL.S) displayed as non-directed data, using the settings shown in Figure 3.8. Figure 3.9b shows the same data plotted as directed dip directions, illustrating the asymmetry of the fault plane dip directions. For this plot, the *Plane* selection in the drop-down menu is set to *Dip* direction.

A fault dip frequency polygon plot of the SL.S data, Figure 3.10a, is created by setting *Component* to *Vertical*, and *Quadrants* to 4 (the fourth quadrant). The *Start* position (for  $X = \text{Right}$ ) of the numerical labels has been modified from 90 to 0, in the *Circular Histogram - Labels* pane, as the  $X$  axis is now horizontal instead of East. A plunge frequency polygon of the SL.L data is shown in Figure 3.10b, the settings are the same, except the SL.L data is plotted instead of the SL.S data.

A rake plot of the fault data is shown in Figure 3.11a using the default Rake convention that uses the reference frame of the footwall to show the direction of the hanging wall motion, in this case hanging wall down, or a normal sense. Figure 3.11b is a similar plot, but with the Rake AR convention (Section 9.1) that uses a hanging wall reference frame to show the displacement sense of the footwall, in this case footwall up, or a normal sense. Rake angles are computed using composite line in plane data, and do not have their own data type in the drop-down data Type selection menus,

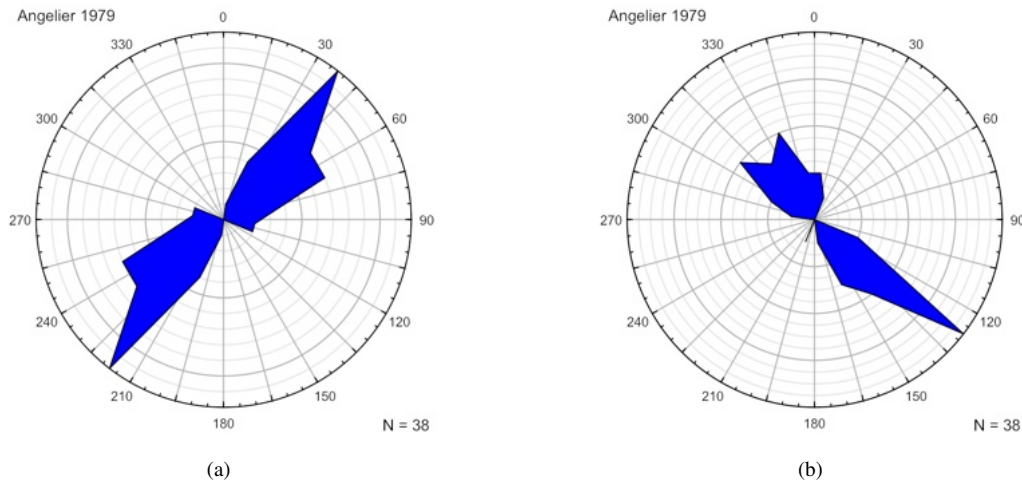


Figure 3.9: Circular frequency polygon plots of 38 fault planes (SL.S), corrected by orthonormalizing the data (Section 9.2). Data from Angelier (1979). (a) Plot of fault plane strikes displayed as undirected lines, giving a symmetrical plot. Maximum bin count = 12. (b) Circular frequency polygon plot of the fault dip directions displayed as directed data, illustrating the asymmetry of the dip directions. Maximum bin count = 19.

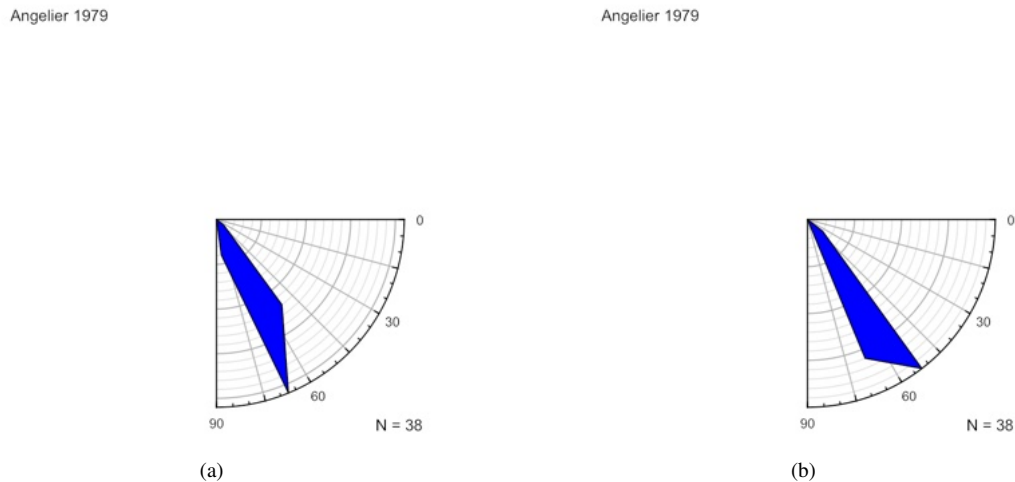


Figure 3.10: Vertical component frequency polygon plots of the fault plane and lineation data. In each plot *Component* is set to *Vertical*, *Quadrants* is set to 4 (the fourth quadrant), and the *Start* position of the numerical labels is set to 0. (a) Fault plane (SL.S) dip component plot. Maximum bin count = 21. (b) Fault lineation (SL.L) plunge component plot. Maximum bin count = 20.

use the line data type (SL.L) to set plot symbols. The plots have numerical labels starting at 0 (strike), the *Rake* convention has an increment of  $-30$ , and the *Rake AK* has an increment of  $30$ .

The slight discrepancy between the two rake plots is due to one fault ( $ID = 20$ ) that has a rake of exactly  $90^\circ$  (or  $-90^\circ$ ). As this sits on a histogram bin boundary, the sign change between the two conventions shifts the bin into which it is counted (an angle  $\alpha$  falls into a bin if it is  $\leq \beta_j$ , the bin start, and  $< \beta_j + 1$ , the bin end:  $90^\circ$  is a bin start,  $-90^\circ$  is a bin end).

A second example, of 2930 nodal planes from the southern Mid-Atlantic Ridge between  $55^\circ S$  and  $16^\circ N$ , and  $55^\circ W$  and  $0^\circ E$ , is shown in Figure 3.12. A moment tensor generates two nodal planes, either can represent the fault plane. Both frequency polygon plots display maxima which represent transform and ridge segments. This data is given in the example data file *Seismology/CMT/jan76\_dec17 SMAR.tsv*, a subset of data from *jan76\_dec17.ndk* (Section 2.7.2) from the CMT Project.

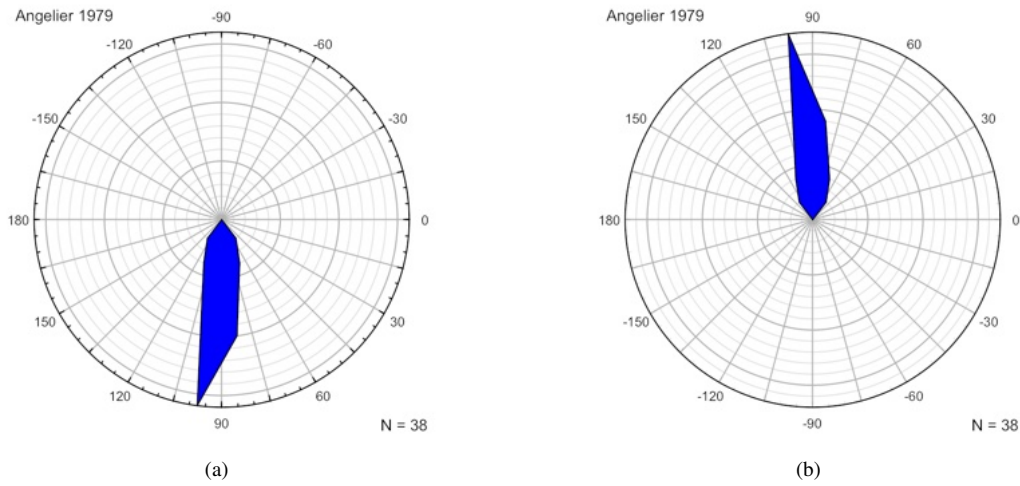


Figure 3.11: Rake plots of the fault data showing the rake of slickenlines on the fault surface. (a) Plot using the default *Rake* convention, where a positive rake angle indicates the motion of the hanging wall, in this case hanging wall down, or normal sense. Maximum bin count = 16. (b) Rake plot using the *Rake AR* convention, where the rake indicates the motion of the footwall, in this case footwall up, or normal sense. Maximum bin count = 17.

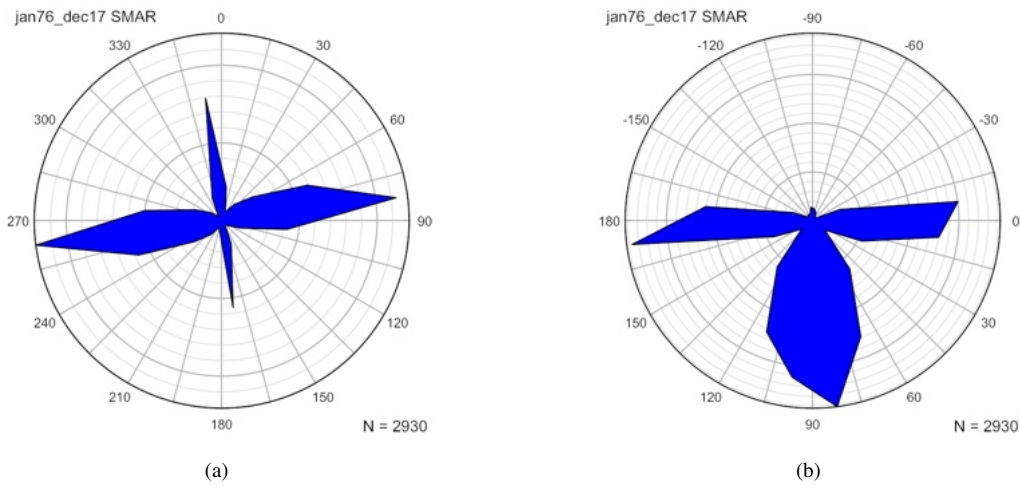


Figure 3.12: Frequency polygon plots of 2930 nodal planes from the southern Mid-Atlantic Ridge between  $55^{\circ}S$  and  $16^{\circ}N$ , and  $55^{\circ}W$  and  $0^{\circ}E$ . The major grid interval is 1000. Data from CMT Project. (a) Dip direction plot. (b) Rake plot.

## 4 Spherical Projections

Spherical projections of directional data, in particular azimuthal spherical projections that project the surface of a sphere onto a plane, are widely used in the earth sciences and other disciplines. This chapter discusses mathematical concepts related to spherical projections, in particular the geometry of several common projections, and the spherical nets which are commonly used to display and work with these projections. For those desiring additional details, Snyder (1987) provides a comprehensive summary of azimuthal spherical and related projections. A final section on nomenclature discusses terminology and common errors that appear in the literature.

### 4.1 Geometry of Spherical Projections

A spherical projection is a mathematical transformation that maps points on the surface of a sphere to points on another surface, most commonly a plane. Astronomers, cartographers, geologists, and others have devised numerous such projections over thousands of years, however two, the *stereographic* and *equal-area* projections, are particularly useful for displaying the angular relationships among lines and planes in three-dimensional space. A third projection, the orthographic projection, is less commonly used, but is important for some applications, and gives a natural visualization of a sphere. These are all azimuthal spherical projections, projections of a sphere onto a plane that preserve the directions (azimuths) of lines passing through the center of the projection. This is an important characteristic, as azimuths, or horizontal angles from north (strike, trend, etc.), are standard measurements in structural geology, geophysics, and other scientific disciplines.

The directions of lines and planes in space are fundamental measurements in structural geology. Since planes can be uniquely defined by the orientation of the plane's pole, or normal, it is sufficient to describe the direction of a line. If only the direction of a line, and not its position, is being considered, it can be described in reference to a unit sphere, of radius  $R = 1$ . A right-handed Cartesian coordinate system is defined with zero at the center of the sphere. A standard convention, used here, is to select  $X, Y, Z = \text{East, North, Up}$  (see Section 5.1 for alternative conventions). A line,  $L$ , passing through the center of the sphere, the origin, will pierce the sphere at two diametrically opposed points (Figure 4.1).

If the line represents undirected axis data, such as a fold axis or the pole to a joint plane, it is allowable to choose either point. In structural geology the convention is to choose the point on the lower hemisphere,  $P$ , the opposite convention is used in mineralogy. The three coordinates of point  $P$  are known as *direction cosines*, and uniquely define the direction of the line. More commonly, the trend (azimuth or declination) and plunge (inclination) of the line are given. In Figure 4.1, the trend of the line is  $090^\circ$ , and its plunge is  $\delta$ . It is a helpful reminder in field notes to designate horizontal angles using three digits, where  $000^\circ = \text{North}$ ,  $090^\circ = \text{East}$ ,  $180^\circ = \text{South}$ , etc., and to specify vertical angles using two digits, from horizontal,  $00^\circ$ , to vertical,  $90^\circ$ . Note that directed data, such as fault slip directions, may have negative, upward directed, inclinations.

An important tool for plotting line and plane data by hand, and for geometric problem solving, is a *spherical net*. A spherical net is a grid formed by the projection of great and small circles, equivalent to lines of longitude and latitude. Nets are commonly either Meridianal or polar, that is, projected onto a meridian (often the equator) or a pole. The terms equator and pole (or axis) will be used to refer to the equivalent geometric features on the net, it is essential to remember that they do not have an absolute reference frame, that is, the net axis is not equivalent to geographic North. When used to plot data by hand, an overlay with an absolute geographic reference frame (North, East, South, etc.) is used (Ragan, 2009).

The projections described here are spherical projections, so equal-area projection is assumed to mean equal-area spherical projection. Other projections are possible, such as hyperboloidal projections, which include equal-area and stereographic hyperboloidal projections (Yamaji, 2008; Vollmer, 2011, 2018). In these projections the surface of a hyperboloid is projected onto a plane. These are used in the context of strain analysis, and are unlikely to be confused with the more common spherical projections.

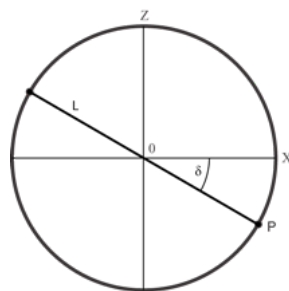


Figure 4.1: Definition of the point,  $P$ , on the unit sphere that defines the orientation of the undirected line  $L$ . The line is trending toward  $X$  (East) and its plunge is  $\delta$ . The  $Y$  coordinate axis (North) is into the page.

## 4.2 Orthographic Projection

The orthographic projection is an important projection in which points are projected along parallel rays, as if illuminated by an infinitely distant light source. Figure 4.2a gives the geometric definition of the orthographic spherical projection. A corresponding orthographic polar net is shown in Figure 4.2b, and an orthographic Meridional net in Figure 4.2c. The projection of point  $P$  in the sphere to point  $P'$  on the plane is parallel to the Cartesian axis  $Z$ , effectively giving a projection following a ray from  $Z$  equals positive infinity. This type of projection gives a realistic view of a distant sphere, such as the moon viewed from Earth. It is azimuthal, but angles and area are not generally preserved. When plotting geologic data it is important that area, and therefore data densities, are preserved, so the orthographic projection unsuitable for such purposes. The net does, however, have other uses, such as the construction of block diagrams (Ragan, 2009, p. 539-540).

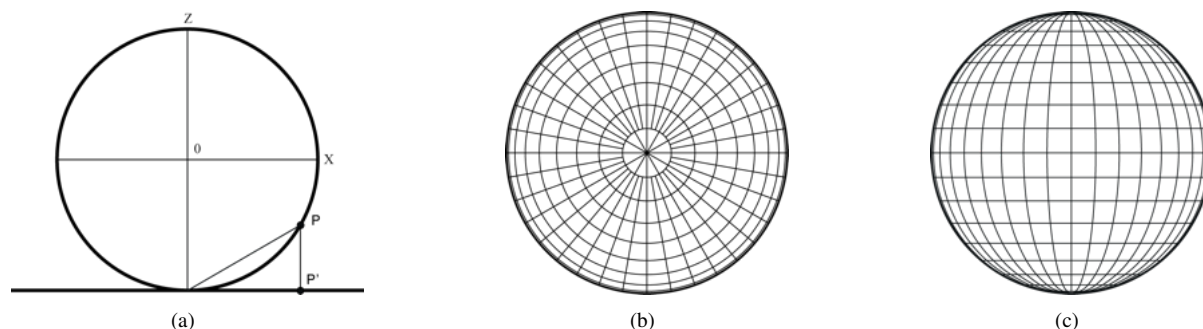


Figure 4.2: (a) Geometric definition of the orthographic spherical projection. Point  $P$  on the sphere is projected to point  $P'$  on the plane. (b) Polar orthographic net. (c) Meridional orthographic net.

## 4.3 Stereographic Projection

The stereographic or equal-angle spherical projection is widely used in mineralogy and structural geology. It was known to the Greeks Hipparchus and Ptolemy, and given its present name by François d'Aguilón in 1613 (Aguilón, 1613; Snyder, 1987). It is defined geometrically by a ray passing from a point on the sphere (here  $Z = 1$ ) through a point  $P$  on the sphere to the projected point  $P'$  on the plane (Figure 4.3a).

The corresponding stereographic nets are shown in Figures 4.3b and 4.3c. Both hemispheres can be represented, however the convention in structural geology is to use the lower hemisphere. Walter H. Bucher (Bucher, 1944) coined the term *stereonet* as shorthand for a meridional *stereographic net* (Figure 4.3c) and the term *stereogram* for a plot made using such a net (Bucher, 1944; Billings, 1954; Donn and Shimer, 1958; Badgley, 1959). An earlier term for a stereographic net is *Wulff net*, named after the crystallographer G.V. Wulff who published a stereographic net in 1902 (Whitten, 1966), although a much older example was published by François d'Aguilón in 1613 (Aguilón, 1613, Section 4.7). Wulff nets are commonly used in mineralogy, however, the convention is to use the

upper hemisphere. It is therefore good practice to clearly label all projections, for example lower-hemisphere stereographic projection.

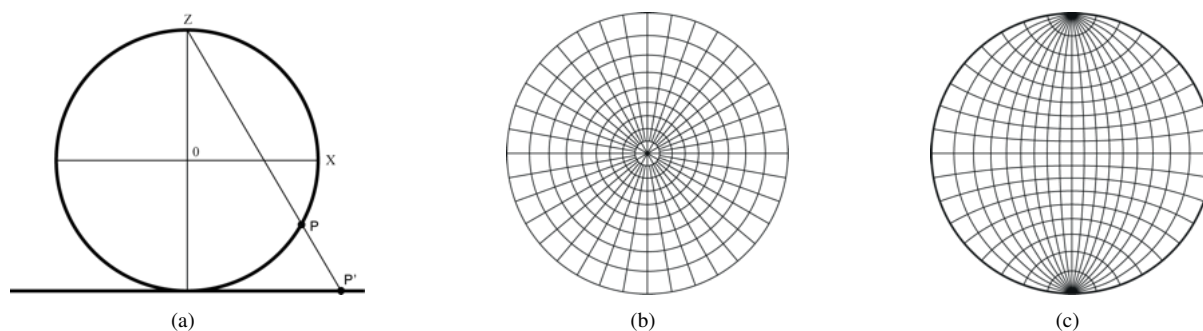


Figure 4.3: (a) Geometric definition of the stereographic spherical projection. Point  $P$  on the sphere is projected to point  $P'$  on the plane. (b) Polar stereographic net. (c) Meridional stereographic net, also known as a Wulff net (Whitten, 1966) or stereonet (Bucher, 1944).

The projection is azimuthal, so lines passing through the center of the projection have true direction, these represent great circles. Note that area in Figures 4.3b and 4.3c is distorted, the projection preserves angles (is conformal), but it does not preserve area. An important consequence is that great circles (such as meridians) and small circles project as circular arcs. These properties make it useful for numerous geometric constructions in structural geology (Bucher, 1944; Phillips, 1954; Donn and Shimer, 1958; Badgley, 1959; Lisle and Leyshorn, 2004; Ragan, 2009).

#### 4.4 Equal-Area Projection

The *Lambert azimuthal equal-area spherical projection* was presented by Johann Heinrich Lambert in 1772 as a map projection that preserved area (Lambert, 1772; Snyder, 1987, Section 4.7). It is not conformal, however it preserves area, so densities are not distorted. This equal-area projection is used widely in the geologic literature for the presentation of directional data, and is the most likely spherical projection to be encountered in literature related to structural geology. Figures 4.3a, 4.3b, and 4.3c illustrate the geometric definition, polar net, and meridional net respectively.

In 1925 Walter Schmidt (Schmidt, 1925, Section 4.7) recognized that the equal-area projection should be used for plotting samples of rock fabric, such as crystallographic axes, to avoid the area distortion of the stereographic projection. This was later extended to fabric studies of rock foliations, joints, and other directional data (Schmidt, 1925; Sander, 1970; Phillips, 1954; Badgley, 1959; Turner and Weiss, 1963; Whitten, 1966; Ramsay, 1967; Hobbs et al., 1976; Fisher et al., 1987; Mardia and Jupp, 2000; Van der Pluijm and Marshak, 2004; Pollard and Fletcher, 2005; Twiss and Moores, 2007; Ragan, 2009; Fossen, 2016).

The term *azimuthal* indicates that, like stereographic and orthographic projections, lines passing through the center have true direction, and that it is projected onto a plane. This distinguishes it from other equal-area projections, which include the projection of a sphere onto conical and other surfaces, however, in structural geology, it can usually be referred to simply as an equal-area projection without ambiguity. The projection is also known as the *Schmidt projection*, after Walter Schmidt who first used it in structural geology (Schmidt, 1925; Turner and Weiss, 1963), and the meridional equal-area net (Figure 4.10), is known as a *Schmidt net* (Knopf and Ingerson, 1938; Billings, 1942; Sander, 1970; Mardia and Jupp, 2000). The polar equal-area net, or *Billings net* (Figure 4.3b), is useful for rapidly plotting measurements by hand.

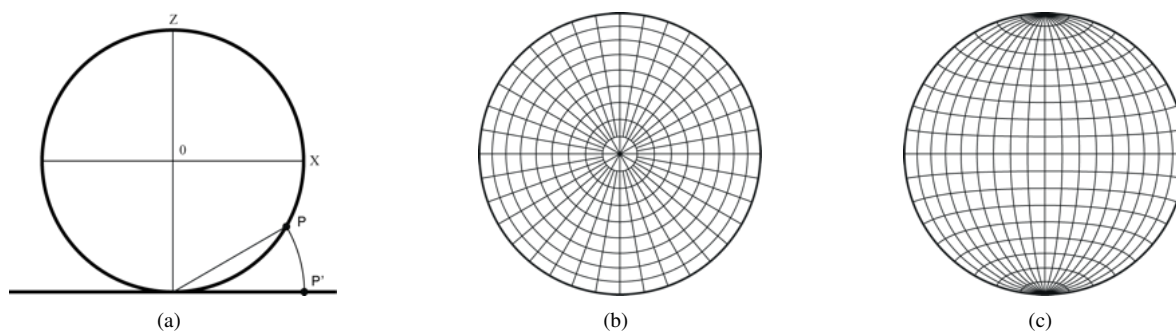


Figure 4.4: (a) Geometric definition of the equal-area spherical projection. Point  $P$  on the sphere is projected to point  $P'$  on the plane. (b) Polar equal-area net, also known as a *Billings net*. (c) Meridional equal-area net, also known as a *Schmidt net* (Knopf and Ingerson, 1938).

## 4.5 Equidistant Projection

The azimuthal equidistant spherical projection preserves distances from the center of the projection, but is not equal-area or conformal. In its polar form parallels (small circles) are equally spaced circles. Like the orthographic and stereographic projections, it was used in ancient times, probably by the Egyptians for star charts (Snyder, 1987). The equidistant property makes it useful for showing distances from the center point of projection, such as airline flight distances, radio transmission paths, and seismic rays.

## 4.6 Density Distortion

It is commonly required to plot a sample of directional data to evaluate their density distribution, a descriptive statistical procedure intended to identify significant clusters, girdles, or other patterns. In 1925 Walter Schmidt (Schmidt, 1925) recognized that the distortion of area makes the stereographic projection unsuitable for studying fabric data, and proposed the use of the Lambert equal-area projection (Lambert, 1772) for such directional data (Section 4.4, Figure 4.4).

To illustrate the effect of density distortion, 2048 directed data points were calculated on a spherical Fibonacci grid (Section 2.11) and plotted using orthographic (Figure 4.5a), stereographic (Figure 4.5b), Lambert equal-area (Figure 4.6a), and equidistant (Figure 4.6b) projections. The points have equal densities on the sphere (with an exception at the very center), but the densities are highly distorted by the orthographic and stereographic projections.

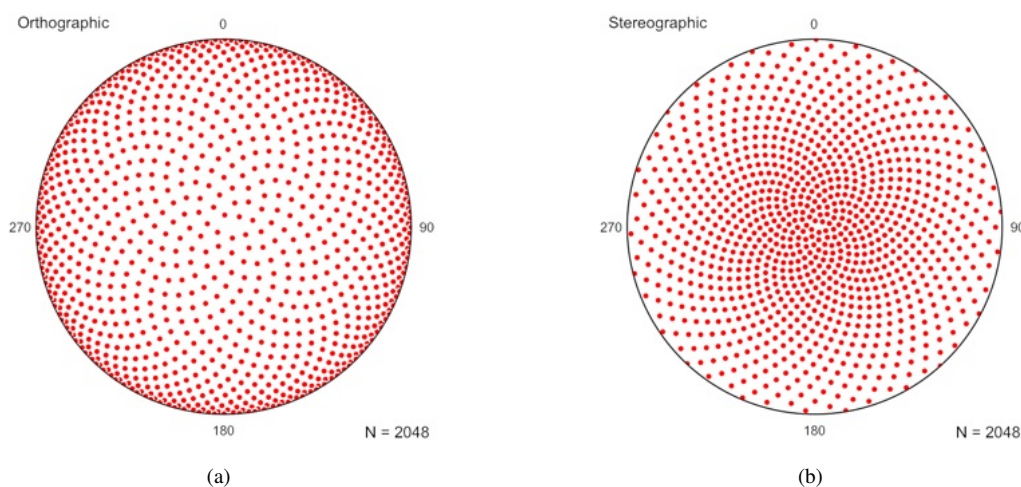


Figure 4.5: Lower-hemisphere projections of 2048 directed data points on a spherical Fibonacci grid to illustrate density distortion. The *Simulate Data* command will generate this distribution. (a) Orthographic projection of the data. (b) Stereographic projection of the data, also known as a *stereogram* (Bucher, 1944).

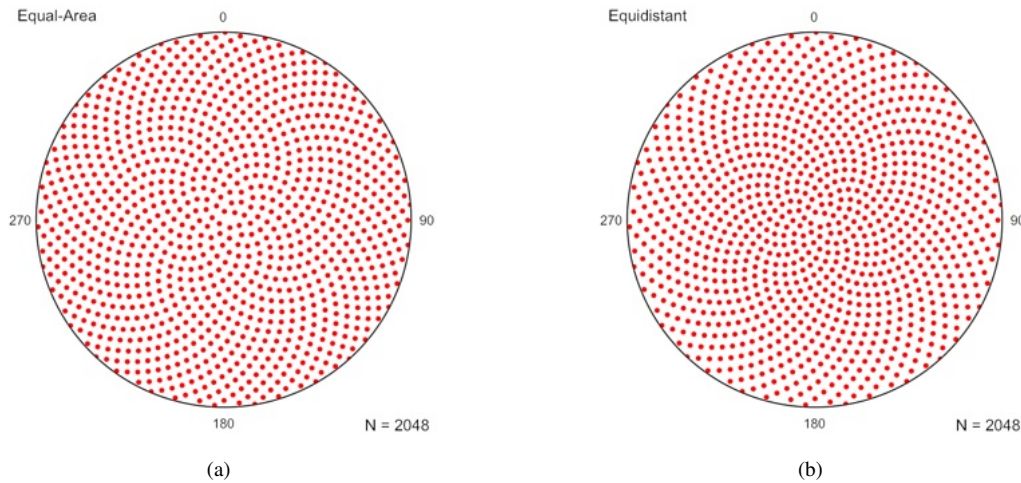


Figure 4.6: Lower-hemisphere projections of 2048 directed data points on a spherical Fibonacci grid to illustrate density distortion. The *Simulate Data* command will generate this distribution. (a) Equal-area projection. (b) Equidistant projection.

The lack of density distortion in Figure 4.6a illustrates the advantage of the Lambert equal-area projection for plotting fabric data (Schmidt, 1925; Sander, 1970; Phillips, 1954; Badgley, 1959; Turner and Weiss, 1963; Whitten, 1966; Ramsay, 1967; Hobbs et al., 1976; Fisher et al., 1987; Mardia and Jupp, 2000; Van der Pluijm and Marshak, 2004; Pollard and Fletcher, 2005; Twiss and Moores, 2007; Ragan, 2009; Fossen, 2016). The term *Schmidt plot* has been proposed for such a plot (Vollmer, 2015, Section 4.7), and is used in subsequent sections.

## 4.7 History and Terminology

Spherical projections have long been used for mapping the terrestrial and celestial spheres. The stereographic projection was known to the Greeks Hipparchus and Ptolemy, and was given its present name by François d'Aguilón in 1613 (Aguilón, 1613; Snyder, 1987, Figures 4.7 and 4.8). The more recent Lambert azimuthal equal-area projection was derived by Johann Heinrich Lambert in 1772 (Lambert, 1772; Snyder, 1987, Figure 4.9). Mathematically, on a unit radius net, a line with a plunge  $p = 0^\circ \dots 90^\circ$  will plot at a distance  $d_S$  (stereographic) or  $d_E$  (equal-area) from the center of the net (Hobbs et al., 1976)

$$d_S = \tan(45^\circ - p/2) \quad (4.1)$$

$$d_E = \sqrt{2} \sin(45^\circ - p/2) \quad (4.2)$$

which are equal only at  $p = 0^\circ$  and  $p = 90^\circ$ .

In 1925 Walter Schmidt recognized that the stereographic projection was unsuitable for directional data analysis due to its distortion of area (Section 4.6, Figure 4.5b), and introduced the use of the Lambert equal-area projection for fabric analysis. Rejecting the stereographic, or Wulff, net used by mineralogists, Schmidt introduced the equal-area net, or Schmidt net, as well as data contouring (Figures 4.10a and 4.10b) for geologic fabric analysis.

In 1944 Walter H. Bucher introduced the stereographic net for use in structural geology in North America (Bucher, 1944; Billings, 1954; Donn and Shimer, 1958; Badgley, 1959). Bucher coined the term *stereonet* as shorthand for stereographic net (Bucher, 1944, p. 193), and *stereogram* as a plot produced using the stereographic net (Bucher, 1944, p. 194). As stereonets and stereograms are created using the stereographic projection, they are, by definition, not equal-area.

The equal-area projection is correctly referred to as the Lambert azimuthal equal-area projection (Snyder, 1987), although in the context of directional data analysis, it is usually referred to simply it as the equal-area projection. The projected hemisphere should be given, as lower hemisphere equal-area projection. Note that other spherical equal-area projections exist, such as the cylindrical equal-





Figure 4.7: Illustration by Peter Paul Rubens showing a globe held by Atlas illuminated by winged putti to illuminate the construction of a stereographic net (Aguilón, 1613).

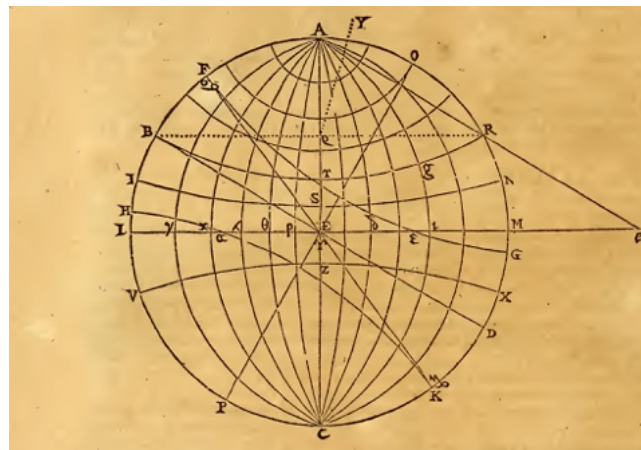


Figure 4.8: Geometric construction for a stereographic net, published by François d'Aguilón in 1613. In geology it is commonly referred to as a Wulff net, after the Russian mineralogist George Yuri Viktorovich Wulff, who proposed its use in crystallography in 1902. A shorthand term for stereographic net, stereonet, was introduced by Walter Hermann Bucher of Columbia University in 1944.

area projection (Snyder, 1987). Additionally, hyperboloidal equal-area and stereographic projections exist, and are used for some geologic data (Yamaji, 2008; Vollmer, 2011, 2018). The term *Schmidt projection* is also used for the equal-area projection (Mardia and Jupp, 2000), and the term *Schmidt plot* for plots produced using the projection (Vollmer, 2015).

Early references (Schmidt, 1925; Billings, 1942, 1954; Bucher, 1944; Sander, 1970; Phillips, 1954; De Sitter, 1956; Donn and Shimer, 1958; Badgley, 1959; Turner and Weiss, 1963; Hills, 1963; Whitten, 1966; Ramsay, 1967; Hobbs et al., 1976) are careful to distinguish between stereographic and equal-area projections, as are most current structural geology texts (Marshak and Mitra, 1988; Van der Pluijm and Marshak, 2004; Pollard and Fletcher, 2005; Twiss and Moores, 2007; Ragan, 2009; Fossen, 2016). Note that

- *Equal-area* and *stereographic* are different mathematical projections (Lambert, 1772)
- A *stereonet* is a stereographic net (Bucher, 1944)

Fig. 19.

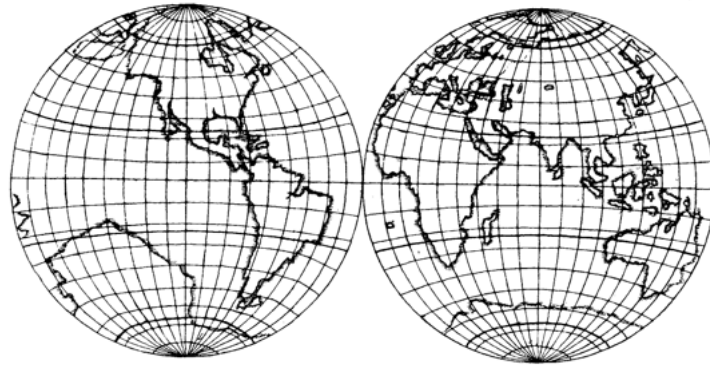


Figure 4.9: Illustration of the Lambert azimuthal equal-area projection by Johann Heinrich Lambert (Lambert, 1772).

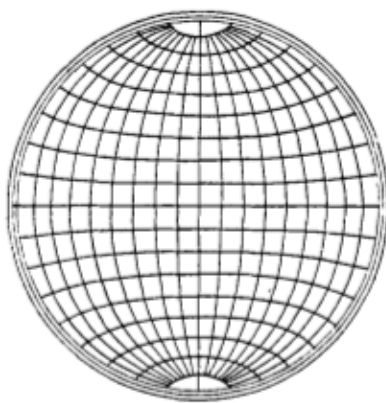


Fig. 1.

(a)

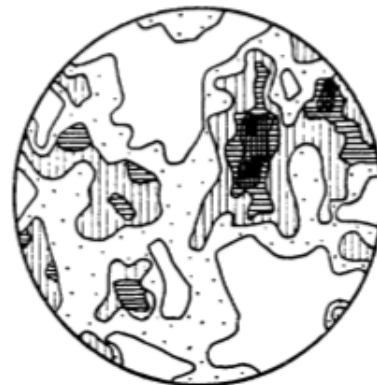


Fig. 2. Granit, Uhligstal.

(b)

Figure 4.10: (a) Lambert equal-area net, or Schmidt net, as published by Walter Schmidt in 1925. (b) Contoured lower hemisphere equal-area projection, or Schmidt plot, of crystallographic fabric (Schmidt, 1925).

- A *stereogram* is a stereographic projection of lines or planes (Bucher, 1944)
- Stereonets and stereograms are not equal-area
- Schmidt nets and Schmidt plots are not stereonets (Schmidt, 1925)

Some may question the need for precise terminology, however it has become common for *any* circular plot of directional data to be referred to as a “stereonet” requiring the reader to guess what projection was used to create it. This is akin to calling all feldspar-bearing rocks “granite”. To quote Streckeisen (1976), “If the concepts of our knowledge are not clear and unambiguous, scientific communication will hardly be successful”.

Diagrams produced using Schmidt’s equal-area method (Schmidt, 1925) are ubiquitous in structural geology, geophysics, and tectonics. While the phrase *lower hemisphere equal-area projection* is clear, it is not succinct. The phrase *Schmidt plot*, is a clear and concise alternative (Vollmer, 2015). These plots, which are often contoured, have been in common use in structural geology, tectonics, and related disciplines, since their introduction by Walter Schmidt in 1925 (Figure 4.10b).

## 4.8 Maxima and Eigenvectors

Spherical directional data is characterized by either directed unit vectors or undirected axes in space. The concept of a mean value is familiar when dealing with scalar values like temperature. Determining such a value for directional data is more complex, averaging trends and plunges separately is not

valid. As with circular data, a useful measure is the *vector mean*, the center of mass for directed data. The procedure for finding the mean is similar to that for directed circular data. A data point on a unit sphere can be represented by three coordinates, which are its direction cosines. If we designate this point as the column vector  $x_i = [x_1, x_2, x_3]^T$ , then the mean vector is the normalized sum

$$\begin{aligned}\bar{x} &= \frac{1}{n} \sum_{i=1}^n x_i \\ &= \frac{1}{n} \sum_{i=1}^n \begin{bmatrix} x_1 \\ x_2 \\ x_3 \end{bmatrix}_i\end{aligned}\quad (4.3)$$

with mean resultant length

$$\bar{R} = \|\bar{x}\| \quad (4.4)$$

and a mean direction given by the normalized mean vector

$$x_0 = \bar{x} \bar{R}^{-1} \quad (4.5)$$

Axial data requires the computation of *eigenvectors*, or principal values, an important concept that gives best-fit values, or moments of inertia, for tensors, such as the principal stresses of a stress tensor. In the context of directional data, imagine that each line (axis) passing through the center of the unit sphere is represented by a small mass at each of the two points where it pierces the sphere. The eigenvectors are then the moments of inertia of this weighted sphere. The maximum eigenvector is the axis aligned with the greatest concentration of axes, the minimum corresponds to the axis aligned with the smallest concentration, and the intermediate is  $90^\circ$  from the other two. As an example, Figure 4.11a is a Schmidt plot of bedding plane normals, represented by points on the lower hemisphere.

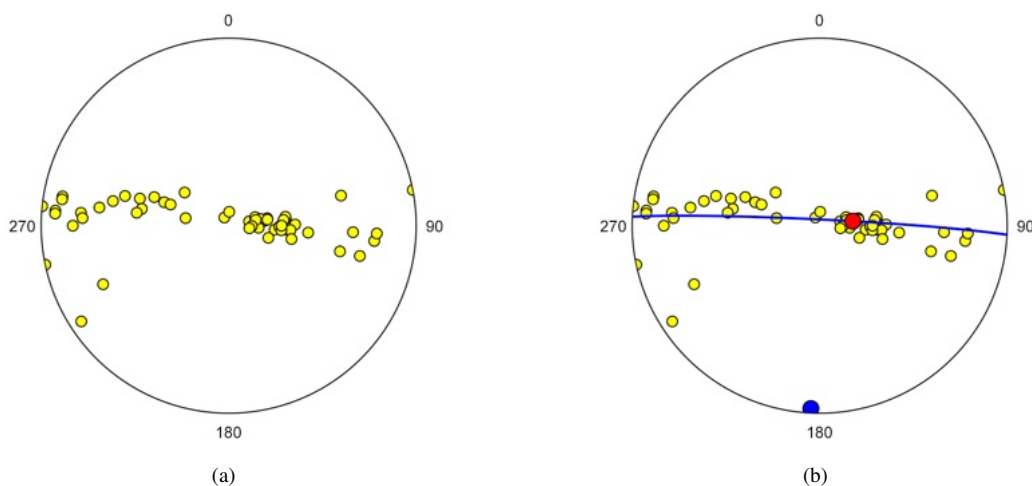


Figure 4.11: Schmidt scatter plots of 56 poles to folded bedding in graywacke, Albany County, New York. Data from Vollmer (1981). (a) Scatter plot of the data. (b) Scatter plot with maximum (red), minimum (blue) eigenvectors, and the great circle normal to the minimum eigenvector. The minimum eigenvector is an estimate of the fold axis.

The orientation tensor, or scatter matrix (Scheidegger, 1965; Watson, 1966; Fisher et al., 1987; Mardia and Jupp, 2000), is given by the normalized sum of the outer products of the direction cosines

and their transpose

$$\begin{aligned}
 \Omega &= \frac{1}{n} \sum_{i=1}^n x_i x_i^T \\
 &= \frac{1}{n} \sum_{i=1}^n \begin{bmatrix} x_1 \\ x_2 \\ x_3 \end{bmatrix}_i \begin{bmatrix} x_1 & x_2 & x_3 \end{bmatrix}_i \\
 &= \frac{1}{n} \sum_{i=1}^n \begin{bmatrix} x_1 x_1 & x_1 x_2 & x_1 x_3 \\ x_2 x_1 & x_2 x_2 & x_2 x_3 \\ x_3 x_1 & x_3 x_2 & x_3 x_3 \end{bmatrix}_i
 \end{aligned} \tag{4.6}$$

The eigenvectors of this matrix are determined can be plotted. In Figure 4.11b the maximum eigenvector is plotted as a red circle, and the minimum a blue circle. In cylindrical folds the minimum eigenvector of poles to bedding gives an estimate of the fold axis, and a great circle normal to the minimum eigenvector gives the best-fit plane through the plane poles (Figure 4.11b).

See Figure 1.5b and Section ?? for a visualization of this data. For details of statistical measures and tests for spherical directional data see Mardia (1972); Cheeney (1983); Davis (1986, 2002); Fisher et al. (1987); Mardia and Jupp (2000).

The *Calculate Best-Fit* command uses these methods to allow the rapid calculation of best-fit means and other planes and lines from a selection of two or more data items. This includes common calculations such as bedding-cleavage intersections, minor fold axes, and determining a plane's orientation from two or more apparent dips.

## 4.9 Tutorial: Scatter Plots

Open the file Vollmer 1981a from the Example Data/Folds folder, in any of the file formats, and click on the *Spherical Projection* icon. If not already done, remove the Schmidt net from the background. Click on the *Preferences* icon, and the *Spherical Projection - Net* pane. Uncheck *Great circles* and *Small circles* for the Y axis, check *Axes*, and *Tick marks Major* for each of the X, Y, and Z axes. Next, in the *Labels* pane, change *Inc* to -90.

In the *Symbols* pane, *Data type S0.S* should be selected, and the *Symbol* checkbox checked. Set the symbol *Fill Color* to yellow. At this point the plot should look as in Figure 4.11a. To add eigenvector maxima, select the *Maxima* pane, and check *Visible*. Under *Maximum eigenvector* check *Symbol*, and under *Minimum eigenvector* check *Symbol* and *Great gircle*. Set the great circle stroke width to 2. The plot should now look as in Figure 4.11b. This type of scatter plot gives a simple summary of the data distribution. Section 4.10 shows how to add contouring, and Section 6.1 discusses how to add confidence cones about the maxima.

## 4.10 Contouring

A simple Schmidt scatter plot of data using an equal-area projection (Figure 4.11a), or with maxima displayed (Figure 4.11b) may suffice for some data sets. However, since the first use of lower hemisphere equal-area (Schmidt) plots for displaying geologic directional data (Schmidt, 1925), they have been contoured to bring out underlying patterns such as girdles or point clusters (Figure 4.12).

Schmidt (1925) devised a method to hand-contour directional data using counting circles of 1% area of the unit circle. This, however, does not take into account the sample size, the size of the counting circle should be a function of the sample size,  $n$ . Kamb (1959) therefore introduced a method based on binomial statistics, giving a greater statistical validity to the contours (Kamb, 1959; Vollmer, 1995). The function used to estimate density at a location is referred to as a *kernel*, and the area considered the *bandwidth* (Silverman, 1986). In these two methods, the number of points falling within a counting circle is the kernel, and the circle size is the bandwidth. These hand-contouring methods, or variants of them, are still used, although they have been generally superseded by computerized methods (Vollmer, 1995; Ragan, 2009).

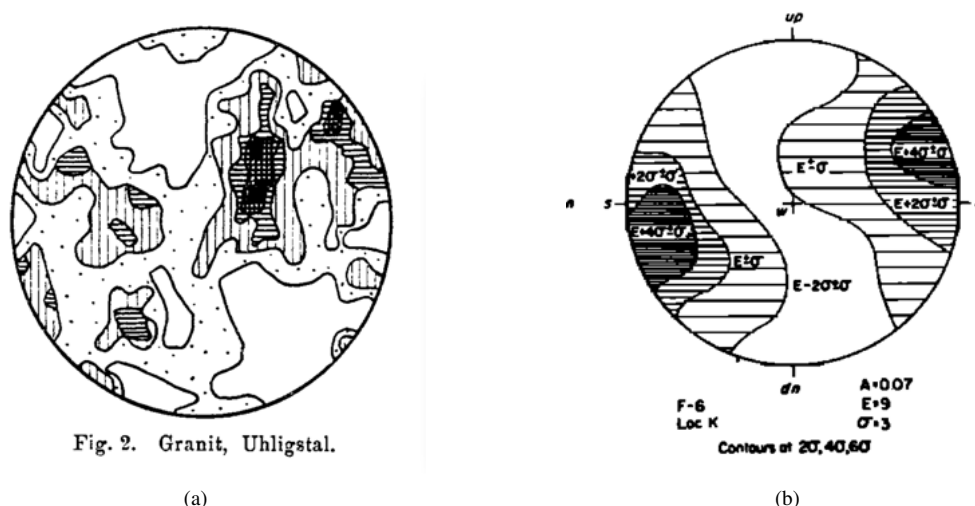


Fig. 2. Granit, Uhligstal.

(a)

(b)

Figure 4.12: Early examples of contoured lower hemisphere equal-area (Schmidt) plots. (a) Crystallographic fabric in a sample of granite (Schmidt, 1925). (b) Crystallographic axes in a sample of ice (Kamb, 1959).

A problem with both the Schmidt and Kamb methods, in addition to being hand-contouring methods, is that the density estimations are done on the projection plane after projecting the data points from the sphere. Therefore a modified Kamb method, which estimates density directly on the sphere, was introduced in Orient in 1986 (Vollmer, 1988, 1990, 1993, 1995). An alternative method using kernel estimation and cross-validation, is given by (Diggle and Fisher, 1985). The modified Schmidt, modified Kamb, and Diggle-Fisher methods are all implemented, although the modified Schmidt method is not recommended.

The settings related to contouring are in the *Preferences* dialog on the *Spherical Projection - Contours* panel. Gridding is the first step in contouring, in which density estimates,  $f_k$ , are calculated at the nodes of a regular grid. Select either the *Modified Kamb* (default) or *Diggle-Fisher* methods. Normally *Exponential* (spherical Gaussian) weighting should be selected, with *Sigma* at the default 3, and *Calculate c* checked. Details for these settings can be found in Vollmer (1995) and Diggle and Fisher (1985). The *Nodes* option sets the number of calculated grid nodes, the default of 100 gives 10,000 calculated nodes, and generally gives very good resolution.

Once the gridding method is selected, set the number and type of contour lines. Figure 4.13a is a Schmidt scatter plot of crystallographic axes of ice, data from Kamb (1959), in the example data file *Crystal Fabric/Kamb 1959*. Figure 4.13b is a Schmidt plot of the data contoured using modified Kamb density estimation with a contour interval of  $2\sigma$ . This is the same data and contour levels that Kamb used to hand-contour Figure 4.12b. For this plot, the *Contour interval* option is selected, and an *Interval* of 2 entered, giving a contour interval of  $2\sigma$ . The *Uniform* option must be deselected. A scale bar can also be optionally displayed for the color gradient scale, as shown in Figure 4.14a.

Instead of contour intervals of  $\sigma$  (standard deviation), it is possible to scale the intervals to multiples of uniform density (MUD), by selecting the *Uniform* option. This option rescales the grid  $f_k$  values so the contour interval is in multiples of the expected uniform density, that is, the expected density for a perfectly uniform distribution (Figure 2.12b) with the same number of data points. Figure 4.14b is a Schmidt plot with modified Kamb contour intervals as multiples of uniform density.

An alternative to using a set contour interval ( $\sigma$  or uniform density), is to contour the full range ( $f_{min}$  to  $f_{max}$ ) of estimated density  $f_k$  values at equal density levels. Figure 4.14a is a modified Kamb contour plot of this data contoured at 5 equally spaced levels over the range of estimated densities, or 20% of the density range. To do this, select *Contour levels* in the *Contours* panel, and enter the number of contour levels, in this case 5. Note that the contour intervals will be identical whether  $f_k$  are in units of  $\sigma$  or uniform density.

An additional option for selecting contours is to use equally spaced levels over the estimated *probability* (Fisher et al., 1987, Section 3.3.3), using the *Probability* option. In this case the  $f_k$  values

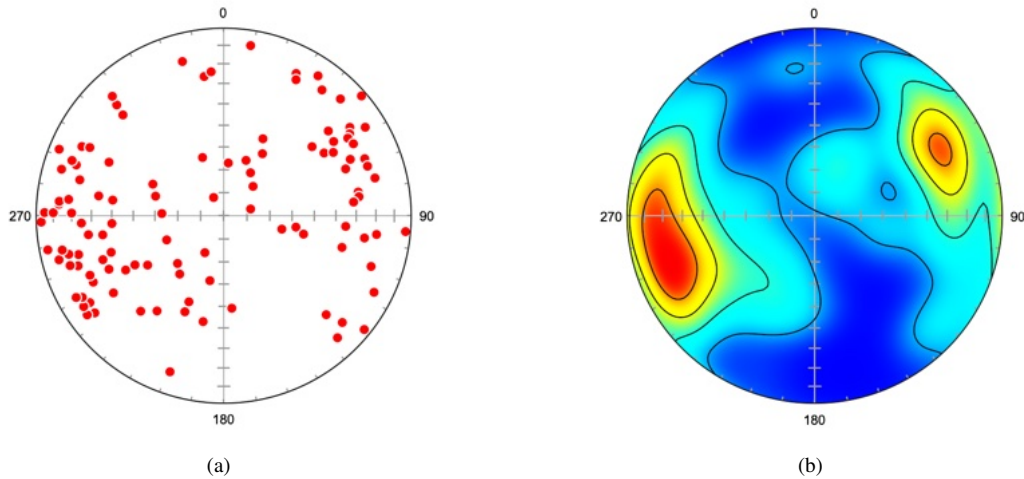


Figure 4.13: Schmidt plots of crystallographic axes of ice. Data digitized from Kamb (1959). (a) Simple scatter plot. (b) Schmidt plot with modified Kamb contours using a contour interval of  $2\sigma$ . Compare with Figure 4.12b, which is hand-contoured using the same options.

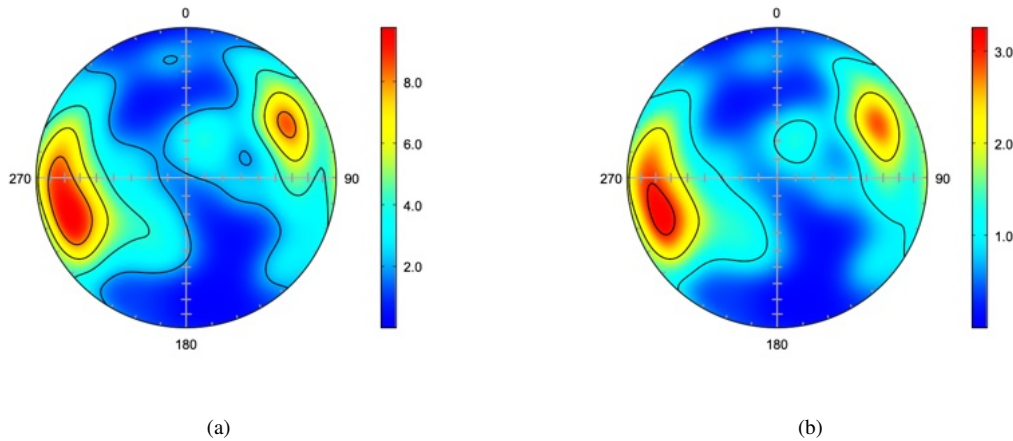


Figure 4.14: Schmidt plot of ice crystallographic data with modified Kamb contours. (a) Contour interval of  $2\sigma$ , as in Figure 4.13b, with a scale bar. (b) Contour interval of 1 multiple of uniform density (MUD). The *Uniform* option must be selected.

are subdivided into approximately equal probability levels.

The original Kamb hand-contouring method uses a counting circle of variable size, the density is estimated by counting points within the circle when centered at nodes across a planar projection. In this case the kernel is a step function, used to evaluate the density at grid locations,  $f_k$ , on the projection. A critical parameter is the size of the counting circle, or bandwidth, which controls the smoothing. The preceding examples use modified Kamb density estimation which uses an exponential kernel function calculated on the sphere (spherical Gaussian) that uses all data points (Vollmer, 1995).

An alternative method proposed by Diggle and Fisher (1985), uses a kernel based on unimodal Fisher (vector) and Watson (axis) density models, with a smoothing parameter estimated by cross-validation. The estimate is made at grid nodes, giving  $f_k$  density values. The critical smoothing (bandwidth) parameter is  $c_n$ , where

$$c_n \propto n^{1/3} \quad (4.7)$$

The value of  $c_n$  is estimated by cross-validation. Cross-validation, however, may not give a good estimate for distributions that depart significantly from unimodal Fisher or Watson density models, such as distributions with girdles or multiple modes, where it may be necessary to subjectively modify

$c_n$ . To use this method, select the *Diggle-Fisher* method, and *Calculate c*. The calculated value of  $c_n$  will be displayed in the edit box after plotting, and may then be modified subjectively, decreasing  $c_n$  increases smoothing. An example plot is shown in Figure 4.15b for equal density levels over  $f_{min}$  to  $f_{max}$ .

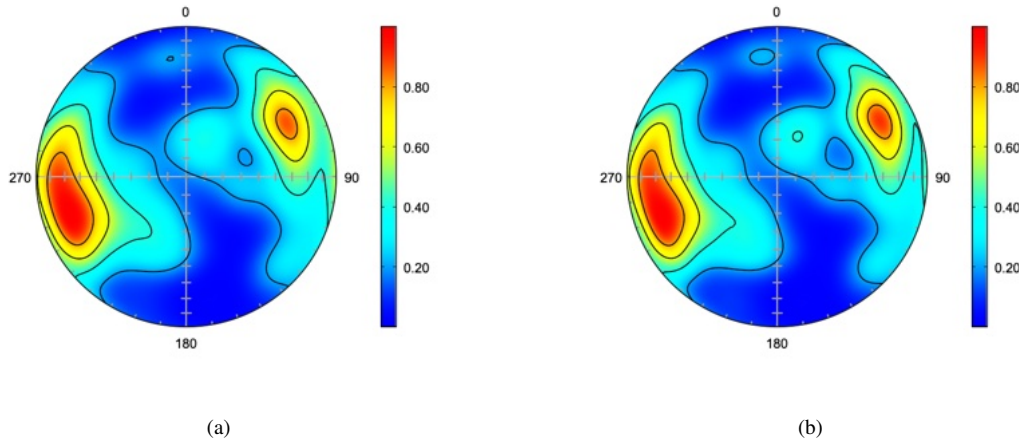


Figure 4.15: Schmidt plot of ice crystallographic data with contours at 5 equal spaced density levels, or 20% density, over the estimated  $f_k$  density values  $f_{min}$  to  $f_{max}$ . (a) Plot using modified Kamb method contours. (b) Plot using cross-validated kernel estimation (Diggle-Fisher) method contours. The estimated value  $c_n = 16.419$  was automatically calculated.

#### 4.11 Tutorial: Contour Plots

Open the file Vollmer 1981a from the Example Data/Folds folder, any of the file versions, and click on the *Spherical Projection* icon, or select the command *Plot - Spherical Projection*. The plot should appear as in Figure 4.16a, if the default options have not been modified. The *Restore Defaults* command can be used to reset the preferences if desired. In the *Settings (Preferences on macOS)* dialog, select the *Spherical Projection - Symbols* pane, set the *Symbol* fill color to red, the stroke color to white, select the *Contour* and *Gradient* options, and press *Preview*. The default contours are modified Kamb 20% density levels. Note that the spherical net is no longer visible, as the gradient image is above it.

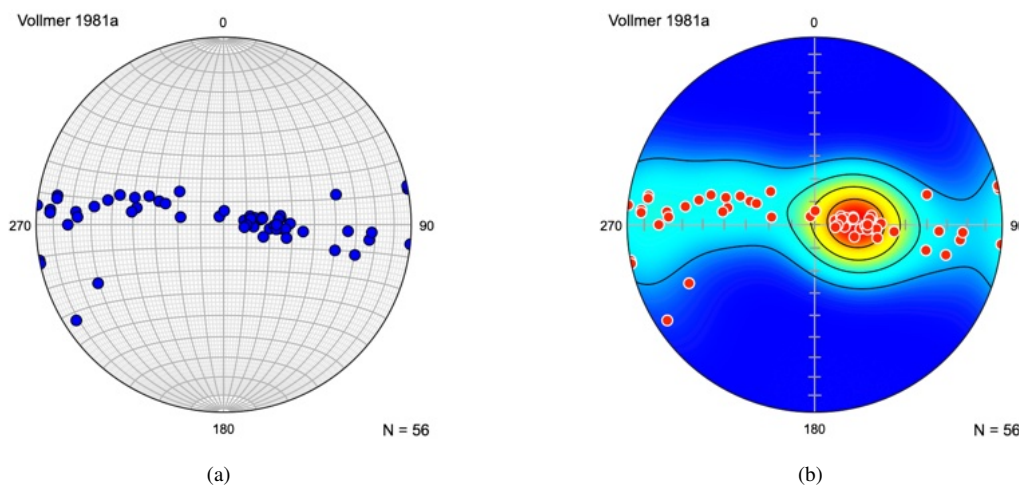


Figure 4.16: Schmidt plots of 56 poles to folded Ordovician graywacke beds from Vollmer (1981). (a) Plot with default options. (b) Plot after changing symbol colors and turning on the *Contour* and *Gradient* options in the *Spherical Projection - Symbols* pane. The default contours are modified Kamb 20% density levels.

To modify the appearance of the net, select the *Net* pane under the *Spherical Projection* settings. Select the *Above* option, and uncheck the *Great circles* and *Small circles Major* and *Minor* options. For each of the X, Y, and Z axes (right, top, and up), check the *Tick marks Major* option, and press OK. The plot should now appear as in Figure 4.16b.

## 4.12 Transparency, Animation, and Lighting

Spherical projections can be difficult to visualize, especially if the data being displayed is abstract, such as poles to bedding planes on a lower hemisphere projection. One option is to display the hidden hemisphere as semi-transparent. Figure 4.17a is a Schmidt plot of 129 poles to folded bedding from Bear Valley Strip Mine, near the town of Shamokin, Pennsylvania. The data (Example Data/Folds/Bear Valley 2016) is displayed to show rays connecting the projection center with the data points, and upper hemisphere data is shown with 30% opacity (*Spherical Projection - Undirected - 30%*). The minimum eigenvector and its normal plane are shown in blue. Figure 4.17b shows the same plot after a rotation of  $30^\circ$  about the *Y* axis using the *Plot - Rotate Projection* command. See Chapter 5 for more information on projection rotation.

Display of the hidden hemisphere may help in visualizing the data, especially for persons unaccustomed to working with spherical projections. The projections can be rotated using the mouse or keyboard (*X*, *Y*, *Z*, *Shift* for negative rotations), allowing interactive visualization. Another option is to create an animation using the *Plot - Animate Rotation* command. This command creates an animated rotation, and saves it to either an animated GIF file, or a series of PNG files as animation frames. The animation frames can be opened in GIMP using its *File - Open as Layers* command, and then saved as an animated GIF or WebP. This allows greater flexibility, can give higher quality results, and smaller files using the WebP format.

An example output file is given as Example Data/Folds/Bear Valley 2016 200.gif, this file has been resized to 200 pixels, as the animation files are quite large. The animation was created using  $5^\circ$  increments of rotation about the *Y* axis, and a delay of 200 milliseconds.

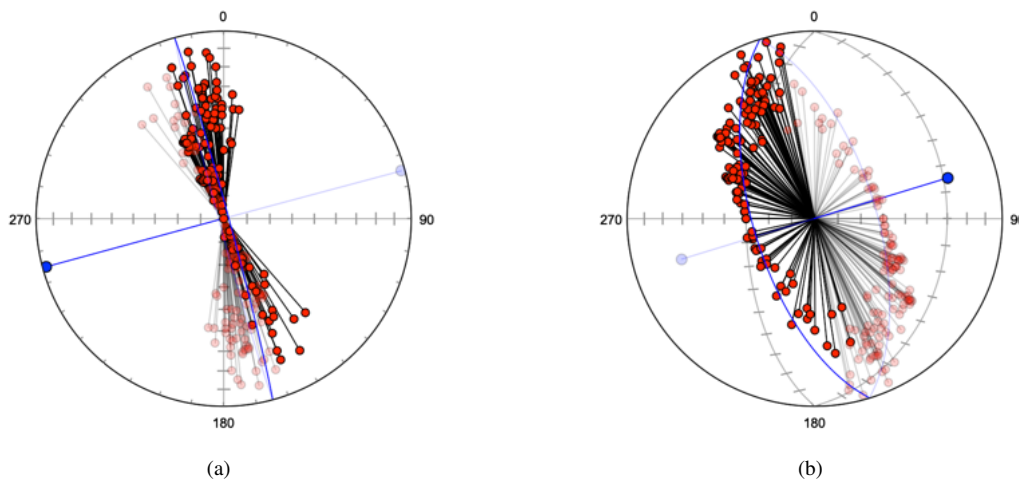


Figure 4.17: Schmidt plots of 129 poles to bedding measured in the Bear Valley Strip Mine, Northumberland County Pennsylvania, near the town of Shamokin, Pennsylvania. The data is displayed to show rays connecting the projection center with the data points, and upper hemisphere data is shown with 30% opacity. (a) Unrotated plot. (b) Plot after a rotation of  $30^\circ$  about the *Y* axis. A small animated version is given as Example Data/Folds/Bear Valley 2016 200.gif.

Transparency can also be used to display directed data on the hidden hemisphere. Schmidt plots of magnetic data from Schmidt and Embleton (1985) in Fisher et al. (1987, Table B6) are shown in Figure 4.18, rotated to different views, with directed data on the upper hemisphere displayed at 30% transparency. A small animated version is given in the file Example Data/Paleomagnetism/Schmidt and Embleton FLE 1987 B6 200.gif. This animation was also created using  $5^\circ$  increments of rotation



about the  $Y$  axis, and a delay of 200 milliseconds, and was resized to 200 pixels due to the large file size.

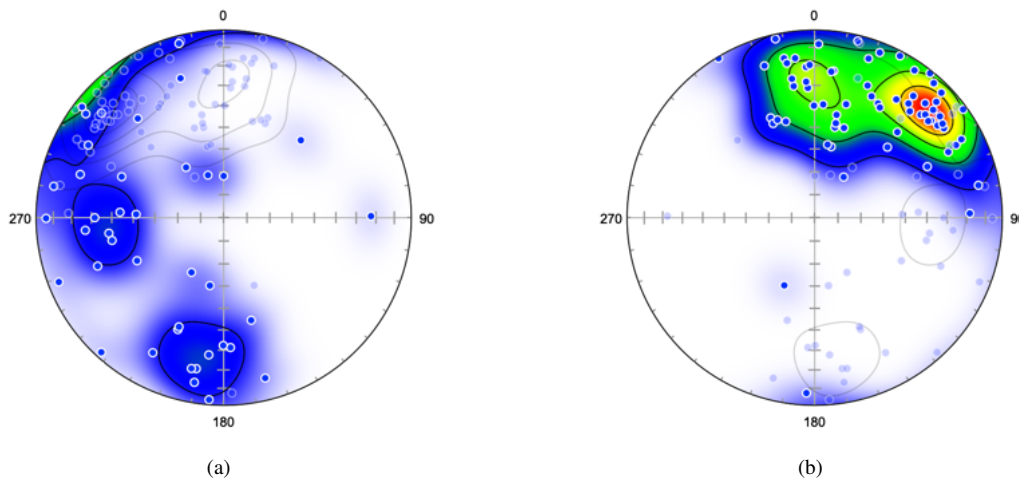


Figure 4.18: Example plots displaying directed data on the hidden hemisphere. Two Schmidt plots of magnetic data from Schmidt and Embleton (1985) in Fisher et al. (1987, Table B6) rotated to different views, with directed data on the upper hemisphere displayed at 30% transparency. (a) Default lower hemisphere plot. (b) Plot after a rotation of  $180^\circ$  about  $Y$ , equivalent to an upper hemisphere plot. A small animated version is given in the file `Example Data/Paleomagnetism/Schmidt and Embleton FLE 1987 B6 200.gif`.

Finally, it may be easier to visualize a spherical projection as an upper hemisphere (globe) or lower hemisphere (bowl) if directed lighting is applied. The *Preferences - Spherical Projection* pane has a *Shade* checkbox, if checked the longitude (counterclockwise angle from  $X$ ), and colatitude (angle from  $Z$ ) can be set to define the direction of lighting. Additionally, maximum (black = 0) and minimum (white = 100) levels can be adjusted. The lighting is done using Lambertian reflectance, a diffuse reflection model published by Johann Heinrich Lambert in 1760.

Figure 4.19 shows examples of equal-area upper hemisphere plots using the data in the file `Example Data/Seismology/Earthquakes with Continents`, displayed with shading. A small example animation is given in the file `Example Data/Seismology/Earthquakes with Continents 200.gif`. Fittingly, these are Lambertian shaded Lambert equal-area projections. See Section 5.1 for additional examples of plots using this data.

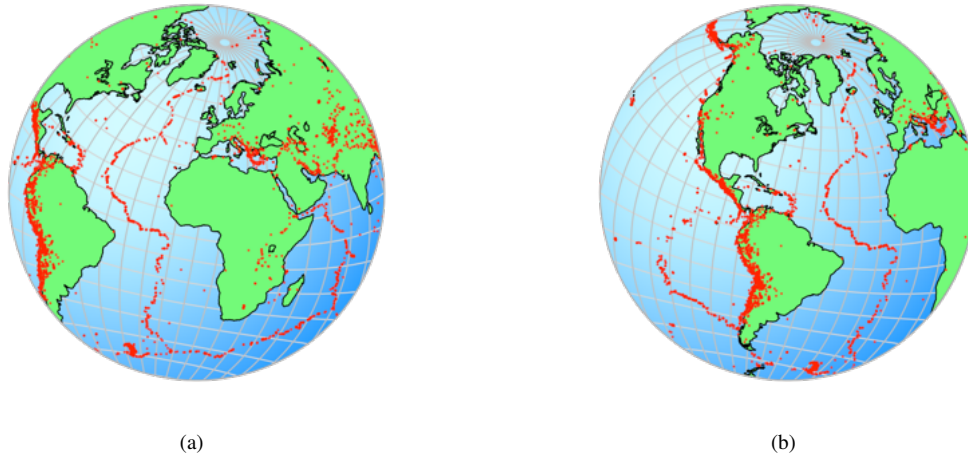


Figure 4.19: Examples of upper hemisphere Lambert equal-area plots using the data in the file `Example Data/Seismology/Earthquakes with Continents`, using the *Shade* option to create a Lambertian refraction model. (a) Plot after a rotation of  $-20^\circ$  about  $Y$  from the *Equatorial 0* view, followed by a rotation of  $-10^\circ$  about  $X$ . (b) Plot after an additional rotation of  $60^\circ$  about  $Z$ . A small animated version is given as `Example Data/Seismology/Earthquakes with Continents 200.gif`. See Section 5.1 for additional examples of plots using this data.

## 5 Coordinates and Rotations

Rotations used for projection and data display are normally transparent to the user, and the default settings are sufficient in most cases. The default coordinates are local coordinates commonly used in geology (North at the top, and East at the right), however, Orient is easily configured for other common geographic or spherical coordinate systems, this is the first topic covered in in this section.

The second topic is coordinate system rotation, or projection rotation. In some cases it is useful or necessary to view data in a more specialized coordinate system, for example centered over a specific location, or chosen parallel to one of the data maxima. The third topic is data rotation, which may be required for a number of reasons, such as paleomagnetic fold tests, or rotation of paleocurrent measurements back to horizontal.

For directed data, symbols for data not on the current hemisphere will not appear. Rotations involving directed data will therefore often hide those data points. The *Directed* and *Undirected* drop-down menus contain options to display hidden directed data, as well as the hidden duals of undirected data. See Section 2.3 for a discussion of these options.

The *Spherical Projection* and *Rotation Plot* can be rotated interactively using the mouse, or the arrow keys. Simply click and drag on a location on the projection and drag it to another location, and the projection will automatically update. The arrow keys rotate the projection about the *X* and *Y* axes by the angle specified in the *Rotate Projection* dialog. Additionally, the *X*, *Y*, and *Z* keys may be used, holding down *Shift* gives a negative rotation. *Premultiply* effects the order of the applied rotation, a premultiplied rotation occurs about the current (unrotated) axes, while a post-multiplied rotation occurs about the initial (rotated) axes. The *Rotation Plot* has a setting in the *Preference Dialog* to set the amount of rotation, and is always post-multiplied.

### 5.1 Geographic Coordinates

The primary coordinate system is selected in the *Preferences* dialog in the *Spherical Projection* settings panel (Figure 5.1). In addition to the *Projection* and *Hemisphere* drop-down menus, there is an *Orientation* drop-down menu from which six geographic coordinate systems (*Polar*, *Antipolar*, *Equatorial 0*, *Equatorial 90*, *Equatorial 180*, and *Equatorial 270*) and six spherical systems (*XY*, *ZX*, *YZ*, *YX*, *XZ*, and *ZY* planes) can be selected. These options allow views along any of the three axes in either direction. Additionally, there are checkboxes for inverting the projection about the *Y* and *X* axes. These are used, for example, to produce plots like Figure 1.2, a plot of directed magnetic data displayed on both hemispheres, as they essentially flip the hemisphere over. The Axes display changes when any of these are modified, so the current coordinate system is clear, for example *X Right*, *Y Top*, *Z Out* is displayed for local coordinates.

Figures 5.2 to 5.4 are upper hemisphere Lambert equal-area projections of 14,229 earthquake epicenters with magnitudes greater than 4.5 from 1980 to 1990 (data from NOAA) plotted on the six standard geographic coordinate systems.

The standard coordinate systems provide views of data along all coordinate axes, however it is possible to select a view along an arbitrary axis using the *Rotate Projection* command. The *Rotate Projection* dialog is shown in Figure 5.5. For example, to produce a projection centered at latitude, longitude  $41.764^\circ$ ,  $-74.156^\circ$ , first set the coordinate system to *Equatorial 0*. The projection, as in Figure 5.2a, is now centered at  $0^\circ, 0^\circ$ , with *X Out*, *Y Right*, *Z Top*. Set *Z* as the Axis, enter 74.156 into the Angle edit box, and press *Apply*. The projection is now centered at  $0^\circ, -74.156^\circ$ . Then set *Y* as the Axis, enter 41.764 into the Angle edit box, and press *Apply*. The projection is now centered at  $41.764^\circ, -74.156^\circ$  (Figure 5.6).

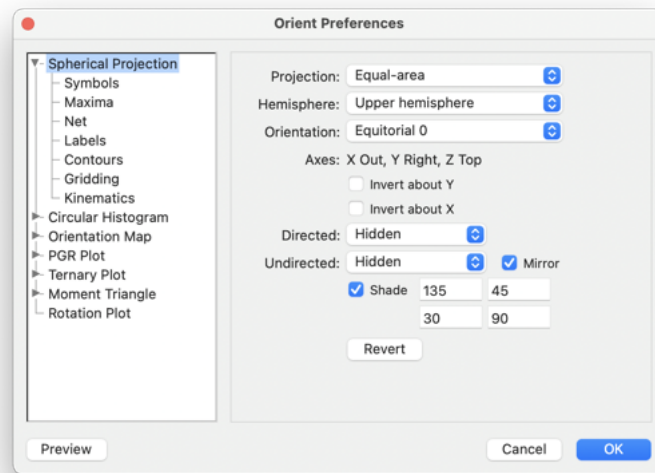


Figure 5.1: The *Preferences* dialog *Spherical Projection* settings pane displaying options for projections. The Axes display, here *X Right, Y Top, Z Out*, gives the current positions of the coordinate axes.

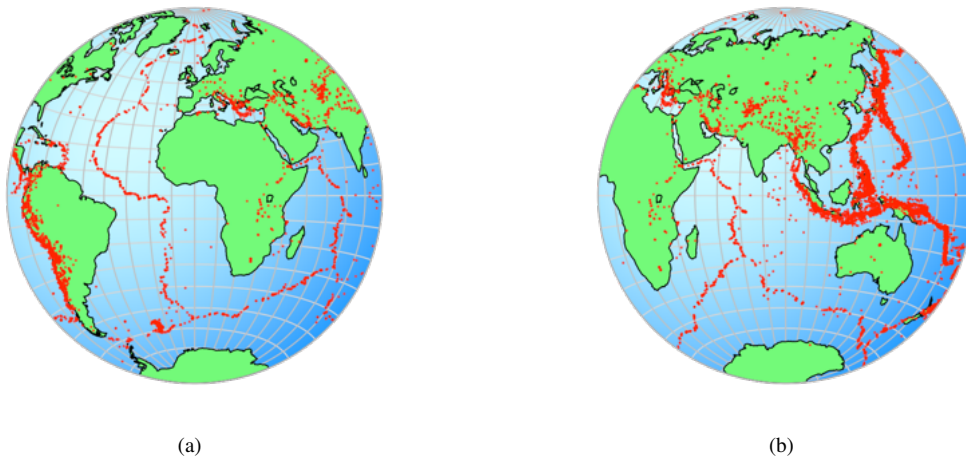


Figure 5.2: Upper hemisphere equal-area projections of 14,229 earthquake epicenters with magnitudes greater than 4.5 from 1980 to 1990. Data from NOAA. (a) Centered at latitude, longitude  $0^\circ, 0^\circ$ , the Equatorial 0 coordinate system. (b) Centered at  $0^\circ, 90^\circ$ , the Equatorial 90 coordinate system. Compare with Figure 4.9 from Lambert (1772).

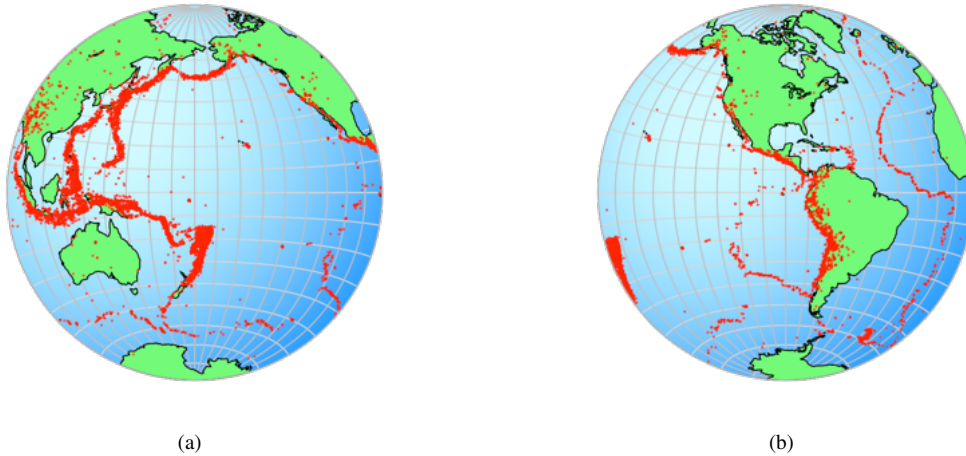


Figure 5.3: Upper hemisphere equal-area projections of 14,229 earthquake epicenters with magnitudes greater than 4.5 from 1980 to 1990. Data from NOAA. (a) Centered at latitude, longitude  $0^\circ, 180^\circ$ , the Equatorial 180 coordinate system. (b) Centered at  $0^\circ, -90^\circ$ , the Equatorial 270 coordinate system. Compare with Figure 4.9 from Lambert (1772).

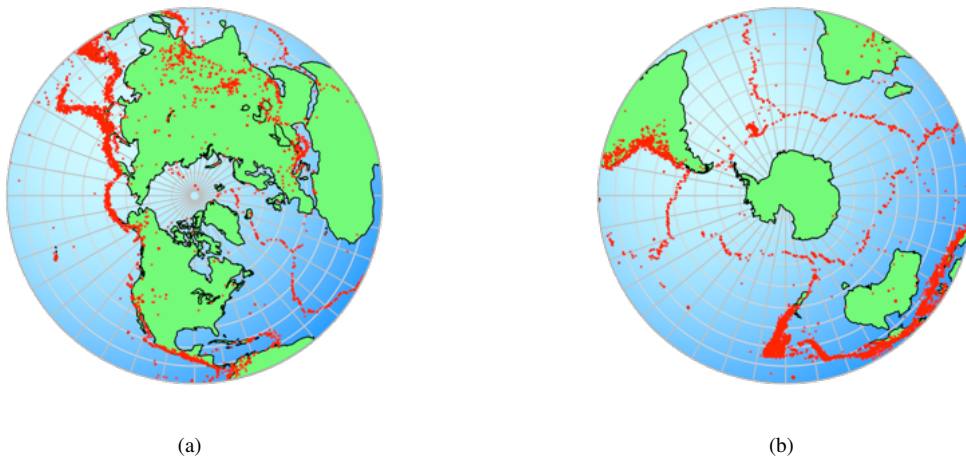


Figure 5.4: Upper hemisphere equal-area projections of 14,229 earthquake epicenters with magnitudes greater than 4.5 from 1980 to 1990. Data from NOAA. (a) Centered at latitude, longitude  $90^\circ, 0^\circ$ , the Polar coordinate system. (b) Centered at  $-90^\circ, 0^\circ$ , the Antipolar coordinate system. Compare with Figure 4.9 from Lambert (1772).

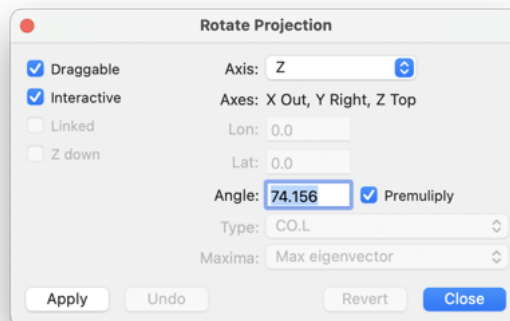


Figure 5.5: The *Rotate Projection* dialog showing the settings for a rotation of  $74.156^\circ$  about the Z axis, which is currently at the top of the projection.



Figure 5.6: Upper hemisphere equal-area projections of 14,229 earthquake epicenters with magnitudes greater than 4.5 from 1980 to 1990 centered at latitude, longitude  $41.764^\circ, -74.156^\circ$  by rotating the projection  $74.156^\circ$  about the  $Z = \text{Top}$  axis, and then  $41.764^\circ$  about the  $Y = \text{Right}$  axis. Data from NOAA.

## 5.2 Tutorial: Geographic Coordinates

Open the file Example Data/Seismology/Earthquakes With Continents, and click on the *Spherical Projection* icon. The projection will appear extremely cluttered. To remedy this, first open the *Preferences* dialog and elect the *Spherical Projection* panel. Set the *Hemisphere* to *Upper hemisphere*, and *Orientation* to *Equatorial 0*. The projection is now centered at latitude, longitude  $0^\circ, 0^\circ$ , X is out, Y is right, Z is at the top. Check the *Shade* checkbox.

Next select the *Symbols* pane. For the data type CO, uncheck *Symbol*, check *Polygon*, and check *Directed*. Set the polygon fill color to light green. For the data type EQ, set the symbol size to 1, the stroke color and fill color to red, and the stroke and fill opacities to 50%. Check *Directed*.

Then select the *Net* pane, uncheck *Axes*, and check *Net*. For the Y axis, uncheck both major and minor great circles and small circles. For the Z axis, check major great circles and major small circles, and set both stroke colors to a very light gray. In the *Labels* pane uncheck *Title*, *N Label*, and *Numbers*. Set the *Frame* fill color to light blue. The plot should now appear as in Figure 5.2a.

To center the projection at latitude, longitude  $41.764^\circ, -74.156^\circ$ , open the *Rotate Projection* dialog (Figure 5.5). Set Z as the *Axis*, enter 74.157 into the *Angle* edit box, and press *Apply*. The projection is now centered at  $0^\circ, -74.157^\circ$ . Then set Y as the *Axis*, enter 41.764 into the *Angle* edit box, and press *Apply*, and *Close*. The projection is now centered at  $41.764^\circ, -74.156^\circ$  (Figure 5.6).

## 5.3 Tutorial: Rotation to Maxima

Open the file Example Data/Folds/Vollmer 1981a (any of the formats), and click on the *Spherical Projection* icon. Restore the projection to lower hemisphere and local coordinates if necessary. If not already done, remove the Schmidt net from the background. Click on the *Preferences* icon, and the *Net* pane under the *Spherical Projection* settings. Uncheck great circles, small circles, and minor tick marks. Set the major tick marks on for the X, Y, and Z axes. Check *Axes*, and *Above*. Next, uncheck *Numbers*, *N Label*, and *Title* in the *Labels* pane.

In the *Symbols* pane, uncheck *Symbol* for the S0.S data type, and check both *Contour* and *Gradient*. Finally, in the *Contours* pane check *Contour interval* and set *Interval* to 1. This gives modified Kamb contours at multiples of expected density (MUD), and the plot should appear as in Figure 5.7a.

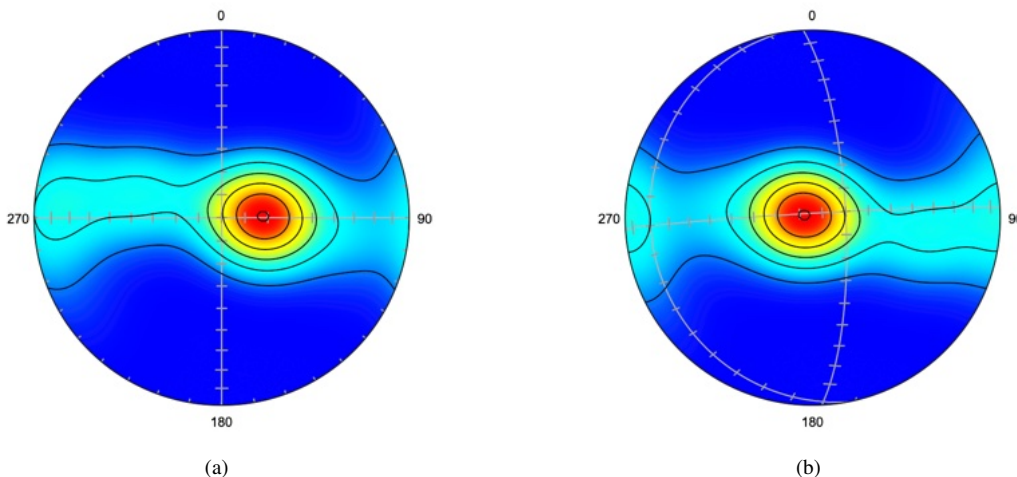


Figure 5.7: Schmidt plot with modified Kamb contours of poles to graywacke bedding data (Vollmer, 1981). The contours interval is multiples of expected density (MUD). (a) Unrotated projection. (b) Plot with projection rotated to the maximum eigenvector of the data.

Use the *Rotate Projection* command to open the *Rotate Projection* dialog (Figure 5.5). Set *Axis* to *Maxima*, *Data Type* to S0.S, and *Eigenvector* to maximum to produce Figure 5.7b, intermediate for Figure 5.8a, and minimum for Figure 5.7b.

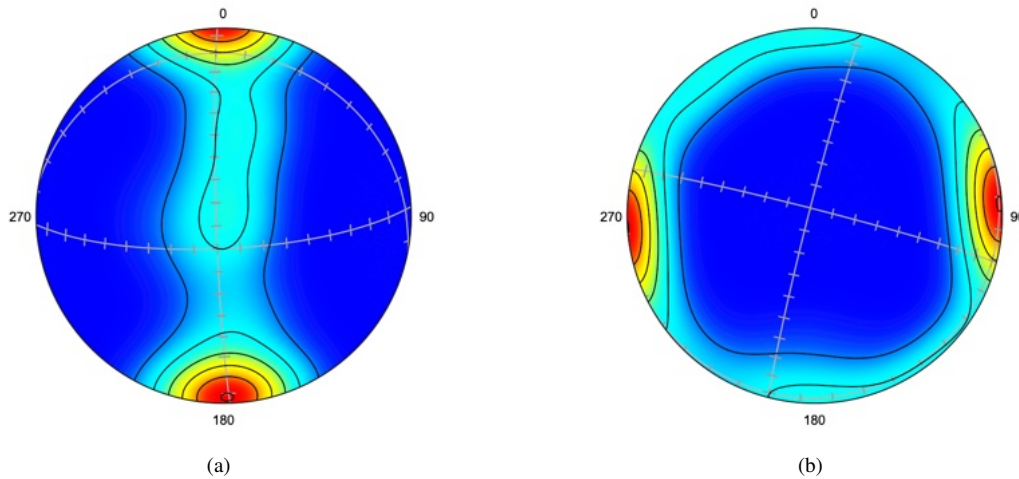


Figure 5.8: Schmidt plot with modified Kamb contours of poles to graywacke bedding data (Vollmer, 1981). The contours are multiples of expected density (MUD). (a) Plot with projection rotated to the intermediate eigenvector of the data. (b) Plot rotated to the minimum eigenvector of the data.

## 5.4 Net Rotation

In some cases it is useful to plot data on a net whose axes are not parallel to the standard axes. The *Net Rotation* command allows a spherical net to be constructed in any orientation. Note that, unlike the *Projection Rotation* command, the view of the plotted data is unchanged. Only the orientation of the net itself is changed. One application, for example, would be to quickly enter data points along a great circle arc of some desired orientation using the *Append Data* command (Section 2.2).

There are several ways to define rotations of coordinate systems, one of the most common is to use Euler angles, as is used here. The *Projection Rotation* allows up to three rotations about any of the three X, Y, Z coordinate axes allowing twelve possible sequences. The rotation convention is extrinsic, meaning that the rotations are each about the fixed X, Y, Z coordinate axes.

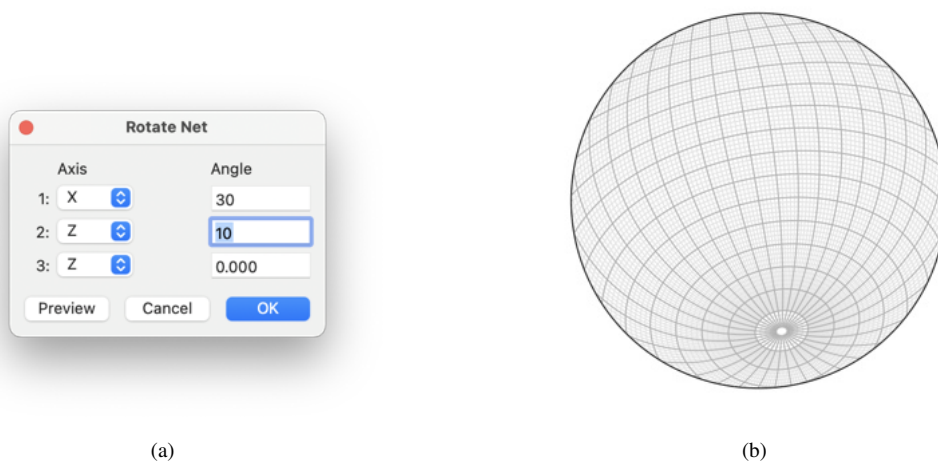


Figure 5.9: Rotation of a Schmidt (lower hemisphere equal-area) net using the *Rotate Net* command. (a) The *Rotate Net* command dialog box, with settings for a rotation of  $30^\circ$  about the X axis (right), followed by a  $10^\circ$  rotation about the Z axis (out of page). (b) Net produced using these settings.

## 5.5 Data Rotation

The principal of data rotation is the same as projection rotation however the rotations are applied to the data, not the projection. The data can be sequentially rotated about any of the coordinate axes



(Figure 5.10), or about an arbitrary axis. The individual extrinsic rotations are about the fixed X, Y, Z coordinate axes, as given in the *Rotate Data* dialog. Before using this command be sure you have a backup file of your data, as this will change the values in the data window spreadsheet. If *Directed* is checked the data will remain confined to one hemisphere.

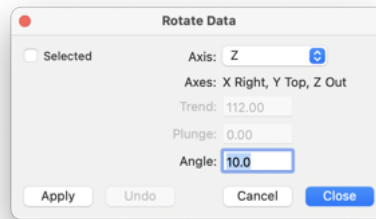


Figure 5.10: The *Rotate Data* dialog allows rotation of the data about any of the coordinate axes, or about an arbitrary axis of any orientation.

Rotating line-plane or kinematic data (Section 9.1) requires extra care. Data rotation will rotate lines and planes, however rakes and slip senses use strike lines for a reference, and rotation of the planes will likely change the strike line. If the data contains rakes, but not lines, lines must be calculated from the rakes using the *Data - Calculate Lines* command (Section 9.2). After the rotation, rakes and slip sense can be recalculated from the rotated lines and planes using the same command. See Section 9.7 for an example of kinematic data rotation.

## 6 Confidence and Uniformity

Section 4.8 introduced the concept of calculating maxima for samples of directional data. In particular, the maximum, intermediate, and minimum eigenvectors for undirected, or axis, data, and the vector mean for directed, or vector data. The maximum eigenvector and vector mean are measures of the mean value, or direction about which the samples cluster. The minimum eigenvector is used to locate the center of a great circle girdle, such as a cylindrical fold axis. The relative magnitudes of the eigenvectors give additional information about the type of distribution, this is discussed further in Section 7.1. The best fit small circle is discussed in Section 8.2.

The estimate of a mean value is essential in data analysis, but it does not say anything about the certainty of the estimate. In general, any estimate of a mean value should also include an estimate of its certainty. This chapter discusses ways to provide uncertainty estimates, in particular deriving confidence cones about the mean, using several spherical distributions and bootstrapping. Second, several tests and indexes for measures of deviation from uniformity are discussed. Only a basic overview is provided here, the statistical analysis of directional data is discussed in detail by Fisher et al. (1987), and Mardia and Jupp (2000). These texts should be consulted for additional details and statistical tests.

### 6.1 Spherical Distributions

There are a number of models for distributions of spherical directional data (Mardia, 1972; Fisher et al., 1987; Mardia and Jupp, 2000; Jammalamadaka and Terdik, 2022). By analogy, the Gaussian, or normal, distribution is a familiar model for scalar data. Four important distributions on the sphere are the Fisher, Kent, Watson, and Bingham distributions. An important distinction is whether the data is to be treated as undirected axes, or as directed vectors. For vectorial data, the vector mean is calculated, and the Fisher and Kent distributions are applicable. For axis data, the eigenvectors are calculated, and the Watson and Bingham distributions are applicable. The numerical values for these are given in a log file using the *Data Statistics* command. Data point weighting is implemented for Fisher, Kent, Watson, and Bingham confidence cones.

The Fisher (or von Mises-Fisher) distribution is the basic model for unimodal rotationally symmetric directed data, so, for example, is applicable to paleomagnetic vectors. This is a general and useful statistic for directed data. A confidence region is calculated for a symmetrical unimodal distribution, which gives a circular confidence cone.

The Kent distribution (Kent, 1982) is also a model for unimodal directed data, but does not assume the distribution is rotationally symmetric, so the confidence cone is elliptical, rather than circular. The Kent statistic is calculated using moment estimation, similar to the Watson and Bingham statistics, but is centered on the vector mean (Mardia and Jupp, 2000, p. 205-206).

The Watson (or Dimroth-Watson) distribution serves as the basic model for rotationally symmetric undirected lines, or axes. The distribution has rotational symmetry as a bipolar or girdle distribution. The confidence region is bipolar, giving two confidence cones centered  $180^\circ$  apart in opposing hemispheres. Confidence cones can be calculated for the three axes of asymmetrical polar, girdle, or multimodal distributions, giving elliptical confidence cones (Fisher et al., 1987, p. 162-163, 180-181, 192). This distribution can be used for features such as normals to joint planes, or quartz c-axes. It is common to determine the axes of folded bedding surfaces using the pole to a girdle, although assigning a younging direction to bedding allows it to be treated as vectorial data.

The Bingham distribution is also for undirected lines, but does not assume rotational symmetry. It can be regarded as an extension of the Watson distribution, which is the Bingham distribution with rotational symmetry (Mardia and Jupp, 2000, p. 181-182). Confidence cones are similarly bipolar. Fisher et al. (1987, p. 155) recommend the simpler Watson model in most cases. Confidence cones can be calculated for each of the three axes, giving elliptic cones.

Using these models, confidence cones can be drawn around either the mean direction (Fisher or Kent), or the eigenvectors (Watson or Bingham), at confidence levels of 90%, 95%, or 99%. Note that

a minimum sample size of 25 is required for these, bootstrapping (Section 6.3) must be applied for sample sizes less than 25.

Figure 6.1a shows directed paleomagnetic data from Schmidt and Embleton (1985) in Fisher et al. (1987, Table B6) with a 95% confidence cone based on the Fisher distribution. Figure 6.1b shows the same data with a 95% confidence cone based on the Kent distribution. Although the confidence cone for the Kent distribution cone is elliptical, the two models give identical cone axes.

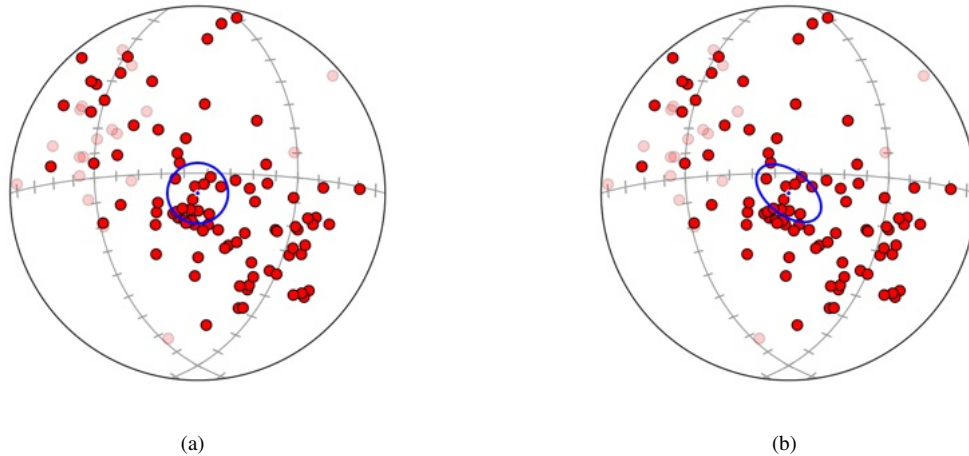


Figure 6.1: Schmidt plots of paleomagnetic data from Schmidt and Embleton (1985) in Fisher et al. (1987, Table B6) rotated to the maximum vector mean with 95% confidence cones. Upper hemisphere data shown as 30% opaque. (a) 95% confidence cone based on a Fisher distribution. (b) 95% confidence cone based on a Kent distribution.

Figure 6.2a shows 95% confidence cones about the three distribution eigenvectors using the Watson distribution for ice crystallographic axes. Figure 6.2b shows confidence cones based on the Bingham distribution for the same data. Although there are small differences in the confidence cones between the two models, their axes are identical.

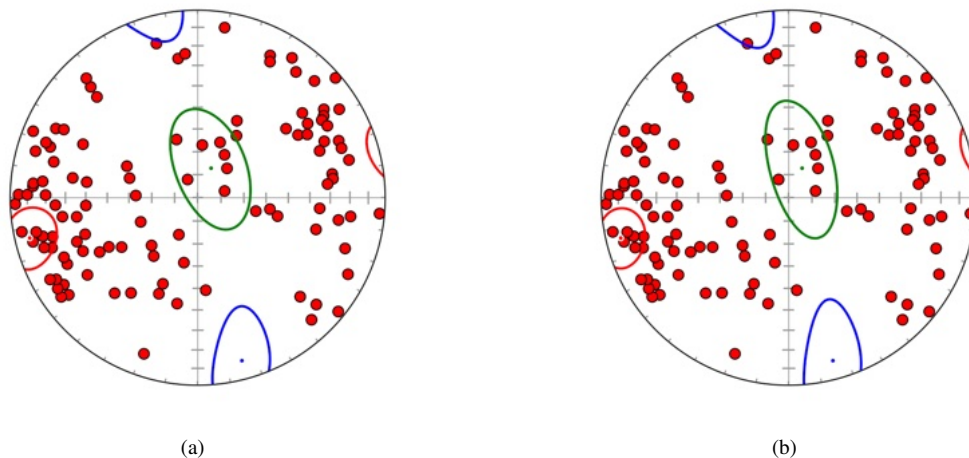


Figure 6.2: Schmidt plots of ice crystallographic axes with 95% confidence cones about the three eigenvectors, colored: maximum = red, intermediate = green, minimum = blue. Data digitized from Kamb (1959). (a) Plot with 95% confidence cones based on the Watson distribution. (b) Plot with 95% confidence cones based on the Bingham distribution.

## 6.2 Parameter Estimation

The parametric models discussed in Section 6.1 are analogous to the well known Gaussian or normal distribution, which is characterized by two parameters, its mean and standard deviation. It is similarly

desirable to estimate directional model parameters, from which confidence intervals and statistical tests can be derived. This section gives a brief discussion on how model parameters are determined. In particular, the von Mises and Fisher distributions concentration parameter  $\kappa$  is often estimated using simple approximations only valid for certain ranges, or tabulated values requiring interpolation (Davis, 1986, 2002; Fisher et al., 1987; Mardia and Jupp, 2000), a more accurate implementation is used here.

The von Mises-Fisher distribution applies to directed unit vectors on circles, spheres, and higher dimension hyperspheres. The circular case is commonly referred to as the von Mises distribution, while the spherical case is often referred to as the Fisher distribution. These are probability density functions with parameters,  $f_p(x; \mu, \kappa)$ , where  $x$  is the data,  $\mu$  is the vector mean, defined on the sphere by  $\theta, \phi$ , and  $\kappa$  is the concentration parameter. The goal is to find the best estimates of the parameters,  $\hat{\mu}$  and  $\hat{\kappa}$ , given a sample of data,  $x$

$$\hat{\mu} = \frac{\sum_{i=1}^n x_i}{\left\| \sum_{i=1}^n x_i \right\|} \quad (6.1)$$

$$\hat{\kappa} = A_p^{-1}(\bar{R}) \quad (6.2)$$

Values of  $A_p^{-1}$  are tabulated in statistics texts (Davis, 1986; Fisher et al., 1987; Mardia and Jupp, 2000), although errors in the sources for the tables are noted by Hill (1981). In any case, it is desirable to have a robust numerical solution. Such a solution can be found by determining the inverse of the function

$$A_p(\kappa) = \frac{I_{p/2}(\kappa)}{I_{p/2-1}(\kappa)} \quad (6.3)$$

where  $I_s(\kappa)$  denotes the modified Bessel function of the first kind. A simple approximation such as

$$\hat{\kappa}_0 = \frac{\bar{R}(p - \bar{R}^2)}{1 - \bar{R}^2} \quad (6.4)$$

can be improved by iterating one or two times with Newton-Raphson steps, minimizing the computationally expensive Bessel function calls. With the proper selection of parameters, the method can converge to a desired numerical precision (Hill, 1981; Sra, 2012). The values here are reported to 4 decimal places in the log, but are calculated to an accuracy of at least 5 decimal places.

The Kent model has five parameters,  $f_p(x; \mu, \kappa, \beta, \psi)$ , where  $\beta$  is the *ovalness*, and  $\psi$  is a rotation about  $\mu$ . Similar to the Fisher model, it is for directed unit vectors, but it does not assume symmetry about the axis,  $\mu$ . Parameter estimation for large  $\kappa$  follows Kent (1982); Fisher et al. (1987); Tauxe (2003). Paleomagnetic measurements from the Great Whin Sill (example data file Creer et al 1959 FLE 1987 B9), are used as a test of the parameter estimation. Fisher et al. (1987) (Section 5.3.3, p. 138) report  $\hat{\kappa} = 41.8, \hat{\beta} = 8.37$ . The values calculated in Orient are  $\hat{\kappa} = 41.7617, \hat{\beta} = 8.3735$  (Figure 6.3a).

The Watson model,  $f_p(x; \mu, \kappa)$ , applies to undirected unit axes, and  $\kappa$  may apply to either bipolar or girdle distributions. Estimation is done using a lookup table with values from Mardia and Jupp (2000), Appendix 3.4 and 3.5. The eigenvectors,  $\omega_1, \omega_2, \omega_3$  and corresponding eigenvalues  $\varepsilon_1, \varepsilon_2, \varepsilon_3$  of the normalized orientation matrix,  $\Omega$ , are calculated. These form three orthogonal axes corresponding to the maximum, intermediate, and minimum moments of the distribution respectively. If  $(\varepsilon_1 - \varepsilon_2) \geq (\varepsilon_2 - \varepsilon_3)$  then a bipolar model is indicated, if not, a girdle distribution is indicated. Measurements of cleavage and bedding plane intersections of folds in Ordovician turbidites (example data file Powell et al 1985 FLE B18 subset), are used as a test of the parameter estimation. Fisher et al. (1987) (Section 6.3.2, p. 176) report  $\hat{\kappa} = 20.5$ . The value calculated in Orient is  $\hat{\kappa} = 20.4862$  (Figure 6.3b). The data before removing two outliers is in file Powell et al 1985 FLE B18. For this sample Fisher et al. (1987) report  $\hat{\kappa} = 15.8$ , the value calculated in Orient is  $\hat{\kappa} = 15.8574$ ).

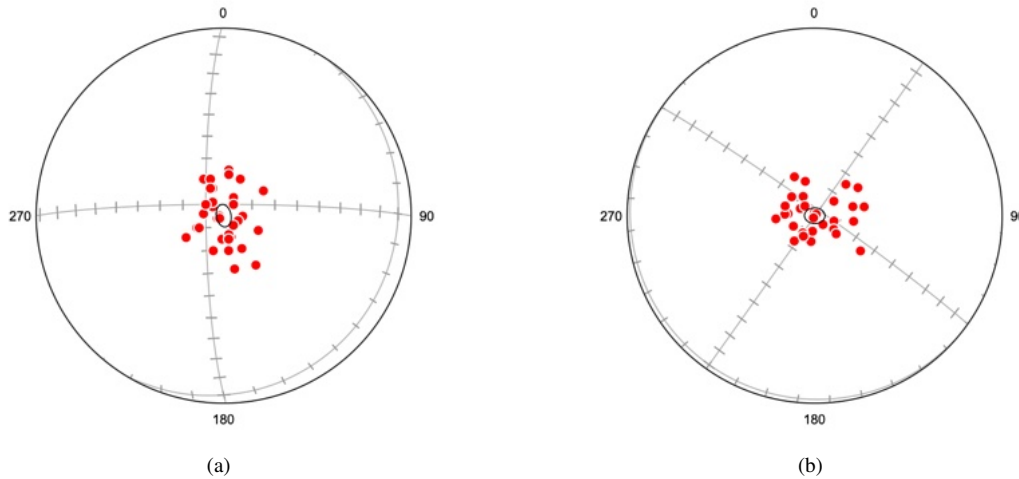


Figure 6.3: Schmidt plots of example data sets rotated to the maximum vector or axis with 95% confidence cones. (a) Paleomagnetic measurements from the Great Whin Sill (Creer et al 1959 FLE 1987 B9), with confidence cone based on the Kent distribution.  $\hat{\kappa} = 41.7617$ ,  $\hat{\beta} = 8.3735$ . (b) Measurements of cleavage and bedding plane intersections of folds in Ordovician turbidites (Powell et al 1985 FLE B18 subset), with confidence cone based on the Watson distribution.  $\hat{\kappa} = 20.4862$ .

The Bingham model, a generalization of the Watson model, is the most complex. The parameters are the three orthogonal axes,  $\varepsilon_1, \varepsilon_2, \varepsilon_3$ , identical to the axes of the Watson model, and the parameters,  $\kappa_1, \kappa_2, \kappa_3$ . Fisher et al. (1987) (Section 6.1, p. 155-156) note that when using the Bingham model it is difficult to check for the goodness-of-fit, and that adequate results can be found using simpler methods. In particular, the axes are identical to those given by the Watson distribution, and the confidence regions are often similar. Orient calculates confidence cones for the Bingham model following Fisher et al. (1987), and gives maximum likelihood estimates  $\hat{\kappa}_1, \hat{\kappa}_2, \hat{\kappa}_3$  using a lookup table with values from Mardia and Zemroch (1977).

Interpretation of the relative magnitudes of  $\kappa_1, \kappa_2, \kappa_3$  is not intuitive, however it may be useful to consider some limiting cases. When  $\kappa_1 = \kappa_2 = \kappa_3 = 0$ , the distribution is isotropic. When  $\kappa_1 = \kappa_2 > \kappa_3$  the distribution is equivalent to the Watson girdle distribution. When  $\kappa_1 > \kappa_2 = \kappa_3$  the distribution is equivalent to the Watson bipolar distribution.

For an example calculation, the data file Bingham 1964 T30-1 (Hansen 1963) contains 150 c-axis orientations of calcite grains from limestone from the Taconic Mountains of New York (data from Hansen, 1963), as tabulated in Table 30.1 of Bingham (1964). Table 6.1 compares the results. The values of  $\varepsilon$  deviate a small amount, suggesting small differences between the tabulated data and those used in Bingham's calculations. The Schmidt plot shown in Figure 30.1 of Bingham (1964), also in Figure 1 of Bingham (1974), shows 3 points that clearly differ from the tabulated data by  $10^\circ$  in plunge, noted in the data file, suggesting the possibility of typographical errors. Figure 6.4a shows 95% confidence cones on the axes, and, for comparison, Figure 6.4b shows 95% confidence cones on the axes calculated using the Watson model.

	$\varepsilon_1$	$\varepsilon_2$	$\varepsilon_3$	$\hat{\kappa}_1$	$\hat{\kappa}_2$	$\hat{\kappa}_3$
Bingham 1974	0.5891	0.2546	0.1562	0.0	-1.956	-3.518
Orient	0.5883	0.2546	0.1570	0.0	-1.9505	-3.4822

Table 6.1: Comparison of calculated values for the eigenvalues,  $\varepsilon$ , and Bingham parameters,  $\kappa$ , for a sample of 150 c-axis orientations of 150 calcite grains from limestone from the Taconic Mountains of New York (data from Hansen, 1963), (Bingham, 1964, Table 30.1). Discrepancies in the  $\varepsilon$  values suggest there are small differences between the tabulated values and those used in Bingham's calculation.

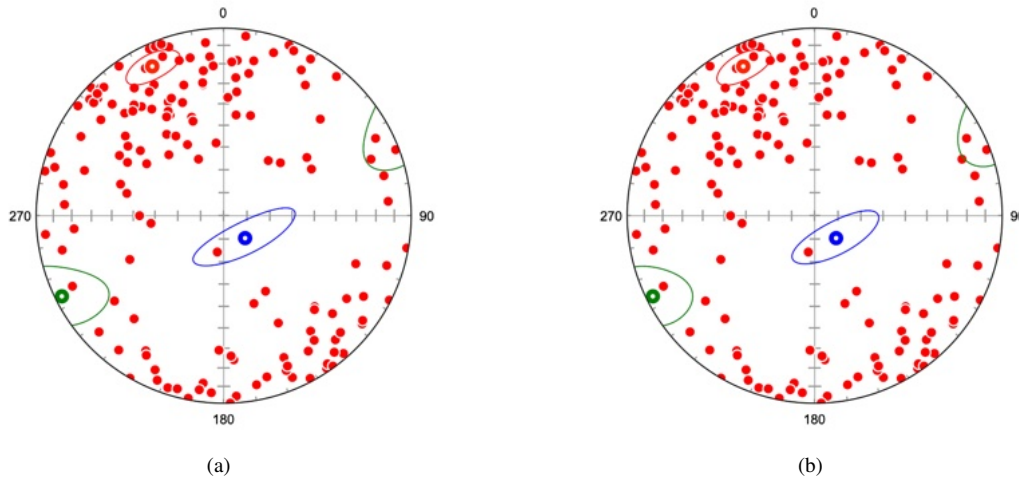


Figure 6.4: Schmidt plots of the orientations of the c-axis of 150 calcite grains from limestone from the Taconic Mountains of New York. Data from Hansen, 1963 (Bingham, 1964, Table 30.1). (a) Plot with 95% Bingham confidence cones,  $\hat{\kappa}_1 = 0.0$ ,  $\hat{\kappa}_2 = -1.9607$ ,  $\hat{\kappa}_3 = -3.4117$ . (b) Plot with 95% Watson confidence cones, bipolar  $\hat{\kappa} = 2.5635$ . The axes, which are identical in both plots, are colored: maximum - red, intermediate - green, minimum - blue.

### 6.3 Bootstrapping

The models discussed in Section 6.1 assume an underlying distribution model and require a minimum sample size of 25. An alternative is to use bootstrapping to infer confidence regions about the mean. The data set is resampled with replacement numerous times and the mean calculated each time to give a large number of replicate means, which can be used to determine elliptical confidence regions (Fisher et al., 1987; Mardia and Jupp, 2000). This approach is particularly useful for small samples, and is required for sample sizes less than 25, or where the underlying distribution model can not be assumed.

Figure 6.5a shows bootstrap confidence cones for the ice crystallographic data of Kamb (1959), with an example of the replicates shown in Figure 6.5b. While no underlying model is assumed, the confidence cones generated are nearly identical to those generated using the Watson distribution, as shown in Figure 6.2a.

A bootstrap confidence cone about the vector mean can similarly be calculated for vectorial data. Figure 6.6a shows bootstrap confidence cones for the magnetic data, with an example of the replicates shown in Figure 6.6b. Again, no underlying model is assumed, however for this data the confidence cones generated are nearly identical to those generated using the Kent distribution, as shown in Figure 6.1b.

Note that, while data point weighting is implemented for Fisher, Kent, Watson, and Bingham confidence cones (Section 6.1), it is not implemented for bootstrap confidence cones because bootstrapping creates replicates by random selection, and assumes each data point is equally weighted.

Bootstrapping requires creating a large number of replicates, the default is 1000, with an allowed range from 100 to 100,000. The means of the resamples can be displayed if desired (Figures 6.5b and 6.6b). The process involves pseudorandom Mersenne twister number generation, and the resulting confidence regions will vary slightly each time. Confidence results are presented in the *Log* window using the *Data - Statistics* command, this displays the axis of the elliptic cone (mean of the resample means), which may differ slightly from the mean, and the semi-apical angles and directions of the major and minor semi-axes of the elliptic cone.

The *Log* file generates a large number of results, however in most cases it is probably sufficient to report one or two mean values, either the vector mean for directed data, the maximum eigenvector for undirected data, or the minimum eigenvector for a girdle pole, along with a measure of uncertainty, such as the confidence cone's semi-apical angles.

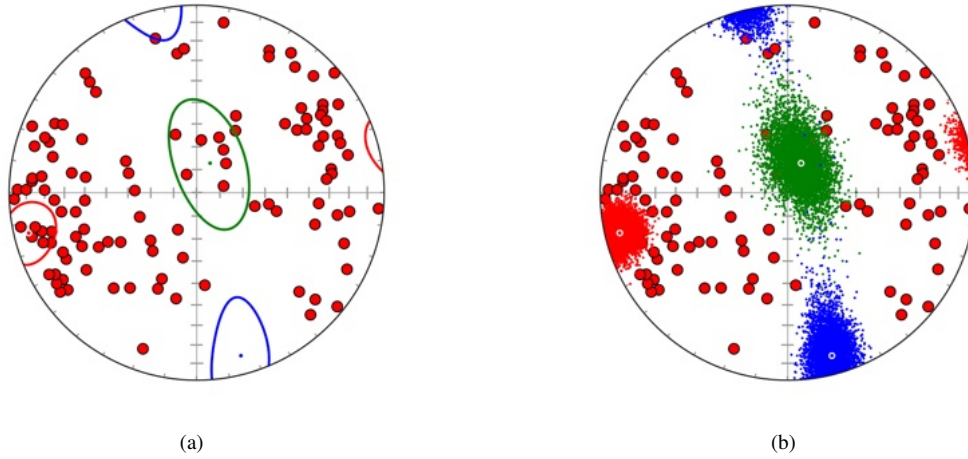


Figure 6.5: Schmidt plot of ice c-axis data, from Kamb (1959). (a) Plot with 95% bootstrap confidence regions. Although no underlying model is assumed, for this data the confidence cones are nearly identical to the cones calculated using the Watson model (Figure 6.2a). (b) Plot showing example means of 5000 bootstrap replicants on each of the eigenvectors, used to calculate the cones.

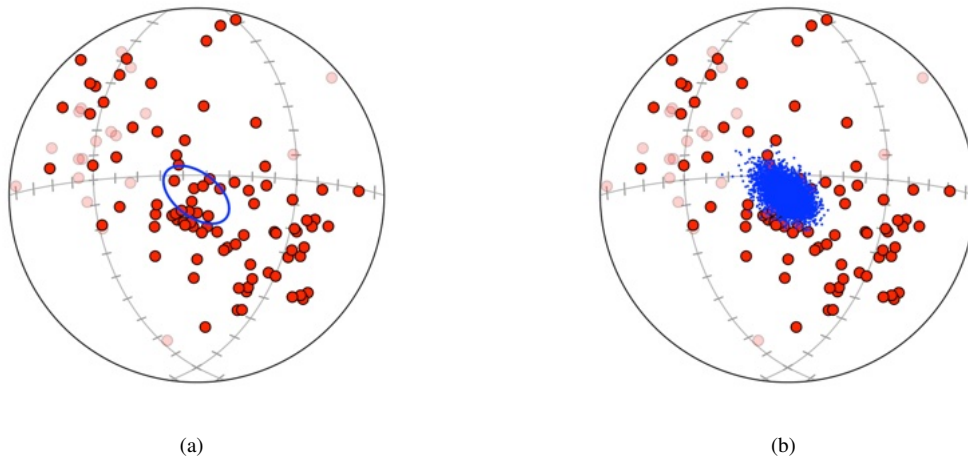


Figure 6.6: Schmidt plots of paleomagnetic data from Schmidt and Embleton (1985) in Fisher et al. (1987, Table B6) rotated to the maximum vector mean. Upper hemisphere data shown as 30% opaque. (a) Plot with 95% bootstrap confidence cone. For this data, the confidence cone generated using the Kent distribution is nearly identical (Figure 6.1b). (b) Plot showing example means of 5000 bootstrap replicants of the vector mean, used to calculate the cone.

## 6.4 Bingham Uniformity and Intensity

Given the normalized eigenvectors,  $\varepsilon_i$ , of the orientation tensor,  $\Omega$  (4.6), the Bingham test statistic for uniformity of axis data on the sphere is (Mardia and Jupp, 2000, eq. 10.7.1)

$$U = n \frac{15}{2} \left( \varepsilon_1^2 + \varepsilon_2^2 + \varepsilon_3^2 - \frac{1}{3} \right) \quad (6.5)$$

or equivalently (Lisle, 1985; Vollmer, 1990)

$$U = n \frac{15}{2} \sum_{i=1}^3 \left( \varepsilon_i - \frac{1}{3} \right)^2 \quad (6.6)$$

Written in this form it illustrates that the statistic is a measure of the “squared distance“ (Mardia and Jupp, 2000, p. 233) of the orientation tensor from the expected value,  $\varepsilon_E$ , which, for a uniform distribution, is  $\varepsilon_E = [1/3, 1/3, 1/3]$ . The critical value for rejecting the null hypothesis of a uniform distribution at the 95% level is  $U = 11.07$ , and  $U = 15.09$  at the 99% level.

A sample-size independent index based on the Bingham test statistic is the intensity (Lisle, 1985; Vollmer, 1990)

$$I = \frac{U}{n} \quad (6.7)$$

This can be useful when comparing multiple samples with varying sample sizes. The intensity varies from 0 to 5,  $I = 0.0$  for a perfectly uniform distribution,  $I = 1.25$  for perfect girdle pattern, and  $I = 5.0$  for a perfect point distribution. Note the misprints in Lisle (1985) and Mainprice et al. (2015).

A potential issue with the Bingham statistic is that natural samples will never be completely isotropic. In a study of quartz CPO fabrics associated with the Main Central Thrust, Himalaya, Hunter et al. (2018) suggest modifying the intensity index by using the fabric of an undeformed quartzite, the presumed protolith, as the expected value, compared to the values obtained from deformed samples

$$I_P = \frac{15}{2} \sum_{i=1}^3 (\varepsilon_i - \varepsilon_{Ei})^2 \quad (6.8)$$

where  $\varepsilon$  are the orientation tensor eigenvalues for a deformed sample, and  $\varepsilon_E$  are the expected orientation tensor eigenvalues derived from an undeformed protolith. These indexes are further discussed with examples in Section 7.1.

## 6.5 Fabric Density Index

A drawback of the intensity index is that it is non-linear. It is based on the “squared distance“ (Mardia and Jupp, 2000, p. 233) from R, so has a gradient that increases at higher values. This results in a small range of values near  $\varepsilon = [1/3, 1/3, 1/3]$ , and a high gradient near  $\varepsilon = [1, 0, 0]$ . This is reflected in the values of  $I = 5.0$  for a perfect point distribution, versus  $I = 1.25$  for perfect girdle pattern. An alternative to the fabric intensity index, is the fabric density index, D, defined as (Vollmer, 2020)

$$D = \left[ \frac{3}{2} \sum_{i=1}^3 \left( \varepsilon_i - \frac{1}{3} \right)^2 \right]^{1/2} \quad (6.9)$$

and  $D_E$  for non-uniform expected fabrics

$$D_E = \left[ \frac{3}{2} \sum_{i=1}^3 (\varepsilon_i - \varepsilon_{Ei})^2 \right]^{1/2} \quad (6.10)$$

D has the values 0.0 for a perfect uniform distribution, 0.5 for a perfect girdle distribution, and 1.0 for a perfect point distribution. D is a measure of the “distance“ from R, as opposed to the “squared distance“, giving a linear gradient from R to P, and from R to G. It is related to the uniformity statistic

$$D = \left[ \frac{U}{5n} \right]^{1/2} \quad (6.11)$$

giving, for example, a critical value for rejecting the null hypothesis of a uniform distribution at 99% confidence for a sample of 300 points of  $D = 0.10$ . Figure ?? shows 1000 samples of 300 random points plotted with contours of D. These indexes are further discussed with examples in Section 7.1.

## 6.6 Uniformity Tests

The Rayleigh uniformity test for directed data, a generalization of the Rayleigh uniformity test on the circle (Section 3.6), is perhaps the simplest test of uniformity. The test allows the rejection of the null hypothesis of uniformity if  $\bar{R}$  is sufficiently large (Mardia and Jupp, 2000). Reported critical values are taken, or interpolated, from tabulated values (Davis, 1986, 2002, Table 5.7).



The Rayleigh test may perform poorly for data that is symmetric, with low  $\bar{R}$  values. Additional non-eigenvector uniformity tests include the Giné and Beran tests. These test statistics are implemented following Fisher et al. (1987, Sections 5.6 and 6.7), and Mardia and Jupp (2000, Section 10.8).

Given a sample of  $n$  data points with direction cosines  $x_i$  where  $i = 1 \dots n$ , and  $j = 1 \dots n$ , then the angle between the  $i^{\text{th}}$  and  $j^{\text{th}}$  points in radians is

$$\psi_{ij} = \arccos(x_i \cdot x_j) \quad (6.12)$$

Beran's statistic for testing uniformity against alternative models that are not symmetric about the center of the sphere, is

$$A_n = n - \frac{4}{n\pi} \sum_{i=1}^{n-1} \sum_{j=i+1}^n \psi_{ij} \quad (6.13)$$

Giné's statistic for testing uniformity against alternative models that are symmetric about the center of the sphere, is

$$G_n = \frac{n}{2} - \frac{4}{n\pi} \sum_{i=1}^{n-1} \sum_{j=i+1}^n \sin \psi_{ij} \quad (6.14)$$

and a test statistic for testing uniformity against all alternative models is

$$F_n = A_n + G_n \quad (6.15)$$

The critical sample size is  $n \geq 10$ . The null hypothesis of uniformity is rejected in favor of the alternative model if the test statistic is too large. Selected percentiles for each are given by Fisher et al. (1987, Table A15). An interpolated p-value is reported based on these percentiles.

Figure 6.7 shows measurements of paleomagnetic remanence from samples of red beds from the Bowen Basin, Queensland after thermal demagnetization to  $670^\circ\text{C}$ . Data from P.W. Schmidt, in Fisher et al. (1987, Table B5). The data is in the file Example Data/Paleomagnetism/Schmidt FLE 1987 B5. This data can be used to test whether all components of magnetization have been purged. Using the *Data - Statistics* command with the *Uniformity* option selected, the following test statistics are generated

#### Tests of Uniformity (vectors)

```
-----
Rayleigh uniformity test
R bar                : 0.1474
Critical R bar (95%) : 0.2272
An (Beran, asymmetric) : 1.098, p > 0.200
Gn (Giné, symmetric)   : 0.417, p > 0.200
Fn (An + Gn)          : 1.516, p > 0.200
```

In this case, the Rayleigh uniformity test requires  $\bar{R} \geq 0.2272$  to reject uniformity. Since  $\bar{R} = 0.1474$ , it is not possible to reject the null hypothesis of uniformity at the 95% level using this test. Test statistics and the interpolated p-values are also given for the Beran and Giné tests. For  $\alpha = 0.05$  ( $1 - \alpha = 95\%$ ), for example, a value of  $p \leq 0.05$  allows rejection of the null hypothesis, indicating a significant departure from uniformity. A value of  $p > 0.05$  fails to reject the null hypothesis, indicating that there is no significant evidence to reject uniformity.

The test statistic  $F_n$  is 1.516, which is lower than point required for the 20% p-level, so  $p > 0.200$ , indicating that there is effectively no evidence that the underlying distribution is not uniform. Note that  $p > 0.200$  is reported if the statistic is smaller than the tabulated 20% point, and  $p < 0.001$  is reported if it is larger than the tabulated 0.1% point, otherwise the interpolated value is reported. The uniformity tests can be weighted.

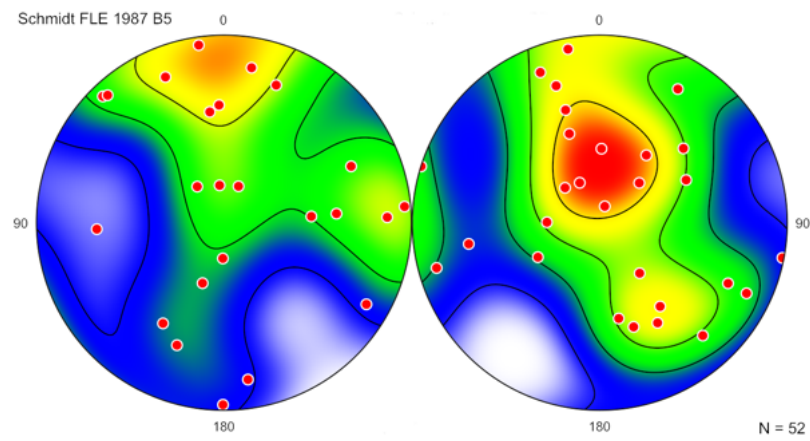


Figure 6.7: Schmidt plots of measurements of paleomagnetic remanence vectors from samples of red beds from the Bowen Basin, Queensland, after thermal demagnetization to  $670^{\circ}\text{C}$  with 5 equally spaced modified Kamb contours. Plot at left is inverted by a  $180^{\circ}$  rotation about Y to show upward directed data. Data from P.W. Schmidt, in Fisher et al. (1987, Table B5).

## 7 Eigenvalue Fabric Plots

Fabric from individual samples is typically presented on contoured Schmidt plots (Schmidt, 1925; Kamb, 1959; Turner and Weiss, 1963; Vollmer, 1995; Mardia and Jupp, 2000; Vollmer, 2015) to identify modes and types of distributions, such as a girdles or clusters. It is useful, however, to have a single plot that allows comparison of multiple samples. An eigenvector-based Cartesian plot was proposed by Woodcock (1977), and a triangular plot by Vollmer (1989, 1990).

Triangular fabric plots have been used to analyze rock foliation data (Vollmer, 1990; Darlington et al., 2016; Racek et al., 2017; Peřestý et al., 2019), magnetic fabrics (Cowan, 1999; Kratinová et al., 2010; Issachar et al., 2019), lithospheric plate Euler poles (Vérard et al., 2012), CPO data for olivine (Vauchez et al., 2005; Tommasi et al., 2008; Falus et al., 2011; Boneh et al., 2015; Chatzaras et al., 2016), pyroxene (Mauler et al., 2001; Ulrich and Mainprice, 2005; Hidas et al., 2013; Daly et al., 2019; Griffin et al., 2022), quartz (Barth et al., 2010; Singleton and Mosher, 2012; McPherren and Kuiper, 2013; Gébelin et al., 2015; Hunter et al., 2018; Larson, 2018; Long et al., 2019; Graziani et al., 2020), plagioclase (Pearce et al., 2011; Satsukawa et al., 2013; Zuza et al., 2022), and ice (Llorens et al., 2016; Wilson et al., 2019; Llorens et al., 2022).

Normally a data set generates a single point on the triangular plot, however it is possible to plot multiple points using several techniques. The first is to use the *Global* option, this will plot data from any open file on a single plot. Second, if domains are defined for the data, each domain can be plotted separately. Finally, eigenvalue data for multiple samples can be entered into a file using E1, E2, E3 data headers, and selecting the *Eigenvalue data* option. This section covers these options, including two examples using quartz CPO data from Hunter et al. (2018, 2019) and olivine data from Hansen et al. (2014).

### 7.1 Triangular Fabric Plot

The triangular fabric plot, PGR, or Vollmer plot (Howarth, 2017, p. 651), provides a summary diagram for multiple data sets, as a single point characterizes the fabric among end member point, girdle, and uniform distributions. It is a closed plot, in that all possible distributions lie within a triangle. For a set of  $n$  axis directions defined by their direction cosines,  $x_i$ , the normalized orientation tensor (Scheidegger, 1965; Watson, 1966) is, from Eq 4.6

$$\Omega = \frac{1}{n} \sum_{i=1}^n x_i x_i^T \quad (7.1)$$

with eigenvectors  $\varepsilon_1$ ,  $\varepsilon_2$ , and  $\varepsilon_3$ , where the magnitudes are  $\varepsilon_1 \geq \varepsilon_2 \geq \varepsilon_3$ . Using these the following indexes are defined (Vollmer, 1989, 1990)

$$\begin{aligned} P &= \varepsilon_1 - \varepsilon_2 \\ G &= 2(\varepsilon_2 - \varepsilon_3) \\ R &= 3\varepsilon_3 \end{aligned} \quad (7.2)$$

which have the property that

$$P + G + R = 1 \quad (7.3)$$

The indexes form the basis of the triangular fabric plot. An additional index, the cylindricity index is defined as

$$\begin{aligned} B &= P + G \\ &= 1 - R \end{aligned} \quad (7.4)$$

B is a measure of the fabric strength that weights clusters and girdles equally. Cylindrical data sets, with B near 1, plot closer to the P-G join, point distributions plot near P, girdle distributions plot near G, and randomly distributed data will plot near R.

An additional index, the fabric density,  $D$  (Eq 6.9), represents the “distance” of a data set from a uniform distribution at  $R$ . It is 0.0 for a uniform distribution, 0.5 for a perfect girdle distribution, and 1.0 for a perfect point distribution. It has a linear gradient from  $R$  to  $P$ , and from  $R$  to  $G$  (Vollmer, 2020, Section 6.5).

Figure 7.1a is a Schmidt plot of bedding plane poles from a cylindrical fold in Ordovician graywackes Vollmer (1981), and Figure 7.1b is a plot of minor fold hinges associated with the fold. The bedding plane poles define a strong girdle with a moderate maximum, and the fold hinges display a strong cluster. Figure 7.2a is a plot of ice crystallographic data from Kamb (1959), which shows a more dispersed distribution. Figure 7.2b is a triangular fabric plot summarizing these three data sets, created using the *Global* option. The plot has contours of  $D$ , with a contour interval of 0.1.

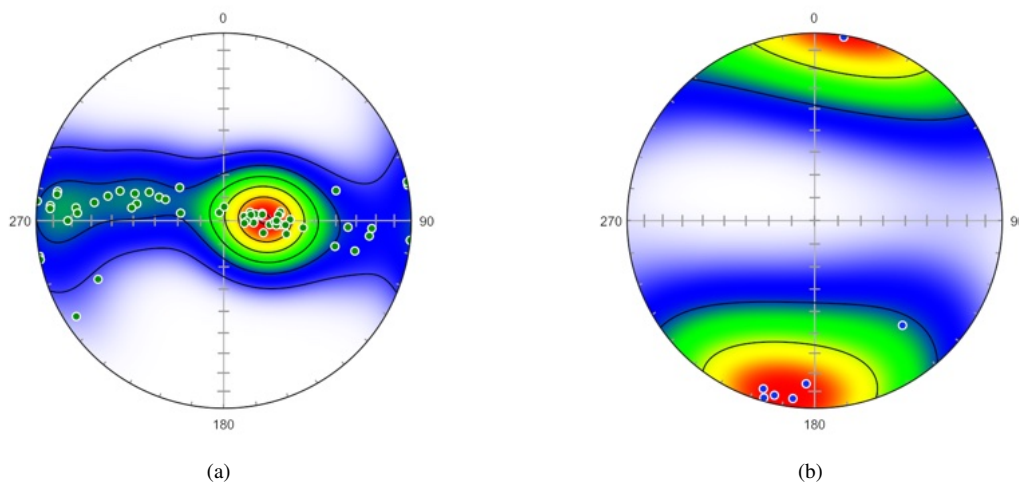


Figure 7.1: Schmidt plots of data from a fold in graywackes. Modified Kamb contours at multiples of uniform density. Data from Vollmer (1981). (a) Plot of poles to bedding, which define a strong girdle with a moderate maximum. (b) Plot of associated minor fold hinges which define a strong cluster.

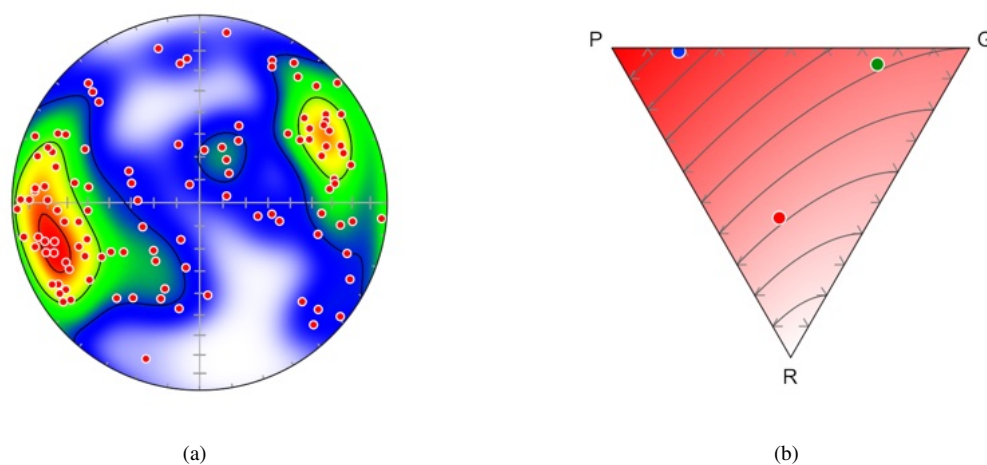


Figure 7.2: Schmidt plot of ice  $c$ -axes with modified Kamb contours at multiples of uniform density. Data from Kamb (1959). (b) Triangular fabric plot of data shown in Figures 7.1a, 7.1b, and 7.2a, created using the *Global* option. Green - bedding poles, blue - fold hinges, red - ice  $c$ -axes. Fabric density contours,  $D$ , with linear color gradient.  $D$  ranges from 0 to 1, with a contour interval of 0.1. The contours show the “distance” from  $R$ .

## 7.2 Fabric Domain Plot

The triangular fabric diagram can be used for locating structural, or fabric, domains, and to look for trends associated with refolding or deformation intensity (Vollmer, 1985, 1990, Section 16.2). An example is given here using samples of monomineralic mylonitic quartz CPO fabrics collected along a 9.5 km transect across the Main Central Thrust (MCT), NW Himalaya (Hunter et al., 2018, 2019, Table 3). The sample sizes range from 303 to 416. The data is in the file Hunter et al, 2019 Quartz.ods in the Example Data/Crystal Fabrics folder.

Figure 7.3a shows 11 samples plotted on a triangular fabric plot with contours of the fabric density index,  $D$  (Vollmer, 2020, Eq 6.9). The contour interval is 0.1, and the color gradient is linear in RGB color space from opaque white to red. The samples show a counterclockwise loop going upward through the section (white to blue, green, yellow, and red).

The samples are grouped into 5 domains by their relative distance in the tectonostratigraphic sequence (Hunter et al., 2019, Figure 1), the base is assumed to represent an undeformed protolith (white circle). The contours of  $D$  are linear from R to P (0.0 to 1.0), and from R to G (0.0 to 0.5). The contour interval is 0.1, and the  $D = 0.1$  contour provides a useful reference, as it represents the 99% confidence level for sample of 300 to reject the null hypothesis of a uniform distribution.

In Figure 7.3b, the quartz CPO fabrics are plotted using an expected density,  $D_E$  (Eq 6.10), value of  $\varepsilon_E = [0.45, 0.28, 0.27]$  from an assumed protolith (white circle). Contours of the expected density index  $D_E$  have a contour interval of 0.1.

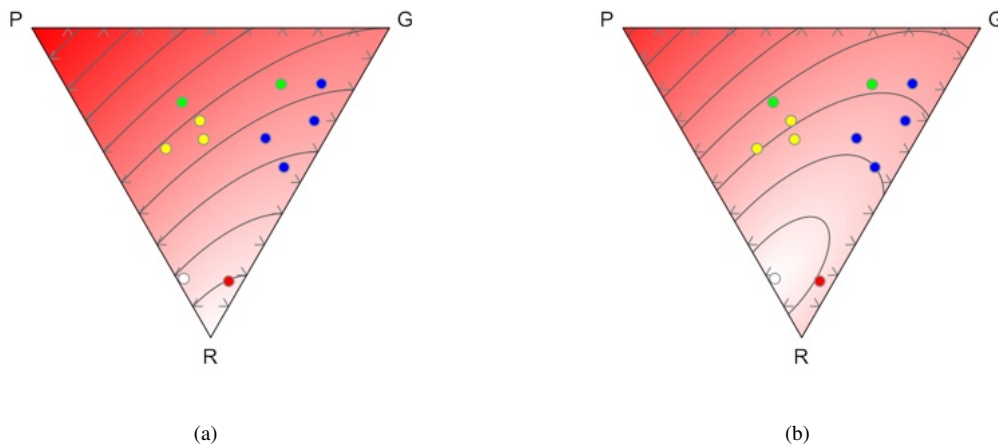


Figure 7.3: Quartz CPO fabrics collected along a 9.5 km transect across the Main Central Thrust (MCT), NW Himalaya (Hunter et al., 2019, Table 3). The samples are grouped into 5 domains based on relative distance in the sequence above the base, which is assumed to represent an undeformed protolith. The sequence is color coded using the *Interpolate* and *Domain* options, from white (protolith), to blue, green, yellow, and red (above the shear zone). The samples show a counterclockwise loop going upward. (a) Samples plotted with contours of the density index,  $D$  (Eq 6.9), with a contour interval of 0.1. (b) The same data plotted with contours of the expected density index  $D_E$  (Eq 6.10). The contour interval is 0.1.

## 7.3 Fabric Barycenter Plot

The full specification of the orientation of a rigid object may require the specification of multiple spatial directions (Downs, 1972; Mardia and Jupp, 2000). In the case of three orthogonal axes the orientation is commonly expressed as Euler angles, giving successive intrinsic (where the internal axes rotate) or extrinsic (rotations about fixed external axes) rotations about three axes. A common convention in crystallography is the Bunge intrinsic convention, which is an initial rotation about  $Z$ , followed by a rotation about  $X'$ , and then a rotation about  $Z''$ . Other equivalent conventions include Miller indexes, Rodrigues vectors, angle-axis, and quaternions (Quey, 2014).

For crystallographic data it is common to plot each of the axes, for example [100], [010], and [001], as separate *pole figures* (e.g., Schmidt or Wulff plots). In some studies, as noted above, the eigenvalues of the orientation tensors are calculated for each axis, and plotted separately on triangular (Vollmer, 1989, 1990) or Cartesian (Woodcock, 1977) fabric plots to distinguish among random, point, and girdle type fabrics. An example is given here using olivine data from Hansen et al. (2014), the four example data files are in the folder Example Data/Crystal Fabrics. In this experimental study of olivine deformation, a series of samples were deformed by increasing amounts. The shear strain, shear stress, shear strain rate, and grain size were measured, and the fabric analyzed using EBSD.

Figures 7.4 and 7.5 show triangular fabric plots of the olivine crystallographic axes. The symbol colors are plotted using a linear BCYR gradient interpolated using shear strain as the weight. Recognizing that the three axes are not independent, it is possible to plot each fabric as a single point using the eigenvalue barycenter,  $\epsilon_B$  (Vollmer, 2020)

$$\epsilon_B = \frac{1}{3}(\epsilon_{[100]} + \epsilon_{[010]} + \epsilon_{[001]}) \quad (7.5)$$

Using the barycenter of the three eigenvalues gives  $[P_B, G_B, R_B] = [0, 0, 1]$  if the axes are all uniformly distributed, and  $[1, 0, 0]$ , if all the axes are all perfectly aligned. However, due to the interdependence of the axes, it is *not* possible to get  $[0, 1, 0]$ . If two axes show a perfect girdle distribution, then the third will be a point distribution, giving  $[P_B, G_B, R_B] = [1/3, 2/3, 0]$ . Olivine fabrics are categorized into several types based on crystallographic orientation and seismic anisotropy (Hansen et al., 2014; Michibayashi et al., 2016). A perfect *A-type* fabric plots at  $[1, 0, 0]$  on the barycenter plot, while a perfect *D-type* fabric (double girdle) plots at  $[1/3, 2/3, 0]$  (Figures 7.5 and 7.6).

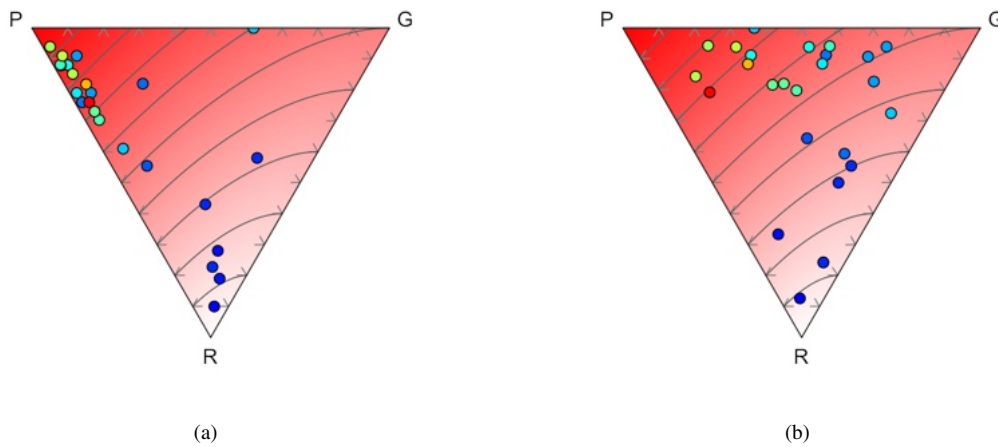


Figure 7.4: Triangular fabric plots of olivine crystallographic axes. The symbol colors are plotted using a linear BCYR gradient interpolated using shear strain as the weight. Contours are 0.1 density index. Data from Hansen et al. (2014). (a) [100] axes. (b) [010] axes.

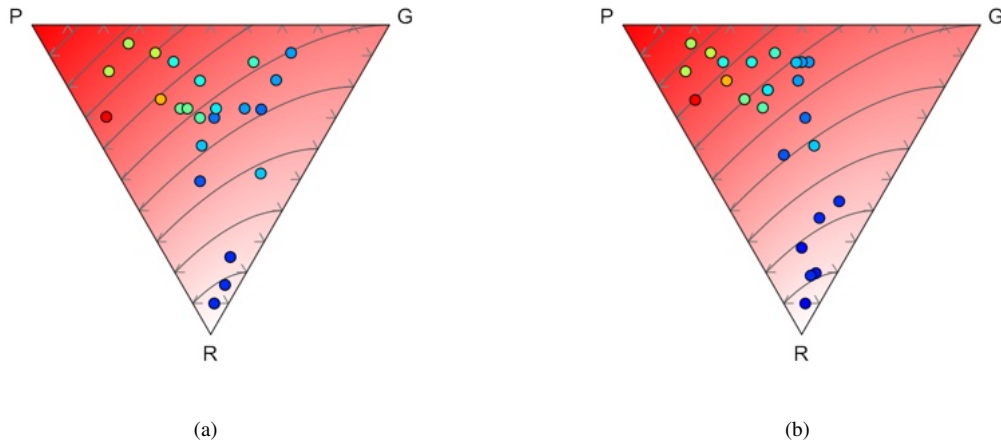


Figure 7.5: Triangular fabric plots of olivine crystallographic axes. The symbol colors are plotted using a linear BCYR gradient interpolated using shear strain as the weight. Contours are 0.1 density index. Data from Hansen et al. (2014). (a) [001] axes. (b) Fabric barycenter plot. Each point represents the eigenvalue barycenter,  $\epsilon_B$  (Eq 7.5), of the [100], [010], and [001] axes. On a fabric barycenter plot a perfect A-type fabric plots at  $[P_B, G_B, R_B] = [1, 0, 0]$ , and a perfect D-type (double girdle) at  $[1/3, 2/3, 0]$ .

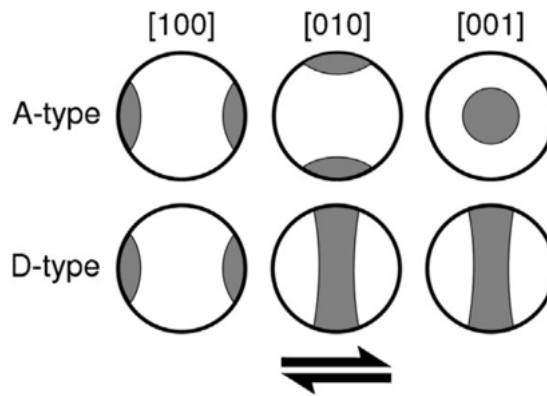


Figure 7.6: Schematic depiction of A-type (top) and D-type (bottom) crystallographic fabrics in olivine. Pole figures are shown for each of the three principal crystallographic axes. Gray regions denote the dominant orientations of grains for each fabric type. The shear sense is top to the right. From Hansen et al. (2014). A perfect A-type fabric plots at  $[P_B, G_B, R_B] = [1, 0, 0]$ , while a perfect D-type (double girdle) fabric plots at  $[1/3, 2/3, 0]$ .

## 8 Conical Data, Small Circles, and Ellipses

This chapter concerns conical data that is entered as a direction and an angle, as well as data that can be fitted to a cone. An example of the first are drill core data from cores that penetrate layers at a measured angle. Each data point is characterized by three angles  $[\theta, \phi, \alpha_c]$ , where  $[\theta, \phi]$  give the direction (e.g., trend and plunge) of the core, and  $\alpha_c$  is the semi-apical angle defining the circular cone.

Some directional data sets may define a small circle, forming a circular cone. A small circle pattern is expected, for example, if lines are rotated about an oblique axis. The intersection of an elliptic cone with the sphere gives a spherical ellipse instead of a small circle. Such cones are generated by the rotation of a line in an elliptical, rather than circular, path.

Folds, or portions of them, are commonly approximated using a cylindrical model, although it is recognized that they may deviate significantly from this geometry (Badgley, 1959; Turner and Weiss, 1963; Whitten, 1966; Wilson, 1967; Ramsay, 1967; Hobbs et al., 1976; Mynatt et al., 2007; Welker et al., 2019). Alternative simple geometric models are circular and elliptic conical, which may be applicable to some folds, or portions of folds (Wilson, 1967; Kelker and Langenberg, 1982; Stesky, 1985; Kelker and Langenberg, 1987, 1988; Mulchrone et al., 2013). Welker et al. (2019), however, caution that, while a conical model may be mathematically permissible, it may not be representative of natural fold shapes.

### 8.1 Conical Data

Data that are characterized by both a direction and an angle define a cone, which projects as a small circle on a spherical projection. In exploration geology it is common to drill a core to determine rock composition and structure. If the core intersects a plane of interest, such as a bedding plane, the angle between the core with orientation  $[\theta, \phi]$ , and the plane gives a core-plane angle,  $\alpha_c$ , defining the cone  $[\theta, \phi, \alpha_c]$ . When the core is extracted the orientation of the plane is lost, however it must lie tangent to the cone  $[\theta, \phi, \alpha_c]$ .

This is one of a class of geometric problems that are commonly solved using a stereographic net (stereonet) (Bucher, 1944; Phillips, 1954; Donn and Shimer, 1958; Badgley, 1959; Lisle and Leyshorn, 2004; Ragan, 2009). An advantage of the stereographic projection is that, because of its equal-angle property, small circles project as circular arcs (Section 4.3), and can be constructed using a compass. Unless this equal-angle property is required, however, such problems can also be solved using a Schmidt net (Section 4.4).

Conical data can be entered to plot small circles, avoiding manual construction, and aiding in the visualization and solution of drill hole problems. The direction of the drill core  $[\theta, \phi]$  is typically given by its trend and plunge, enter these, and then the semi-apical angle  $\alpha_c$  in the spreadsheet column AlphaC. Use the *View - Data Columns* command to display the column if not visible.

As an example, Table 8.1 gives the orientations of three drill cores with core-plane angles of bedding planes, from Ragan (2009), the problem is to determine the bedding plane orientation. To solve the problem, open a new data sheet, and display a projection using the *Graph - Spherical Projection* command. In the *Symbols* pane of the *Preferences* dialog, check *Small Circle*.

ID	Trend	Plunge	AlphaC
1	0.00	60.00	51.00
2	270.00	50.00	67.00
3	45.00	55.00	38.00

Table 8.1: Example drill core data, from Ragan (2009). Given the trend and plunge of three drill cores, and the core-plane angle,  $\alpha_c$  (AlphaC) of bedding planes, determine the orientation (strike and dip) of the bedding.

Use the *View - Data Columns* command to display the AlphaC column if not visible, and enter the data from Table 8.1. The resulting Schmidt plot is shown in Figure 8.1a, and lower-hemisphere stereographic projection (stereogram) in Figure 8.1b. The three cones intersect at a single point,



which represents the bedding plane orientation. Use the mouse to determine the solution on either projection. The bedding normal trend, plunge is  $T, P = 120^\circ, 60^\circ$ , and the plane strike dip is  $S, D = 210^\circ, 30^\circ$ . While an analytical solution can be calculated (Ragan, 2009), a visualization of the solution is desirable, and precision to less than a degree unlikely to be required.

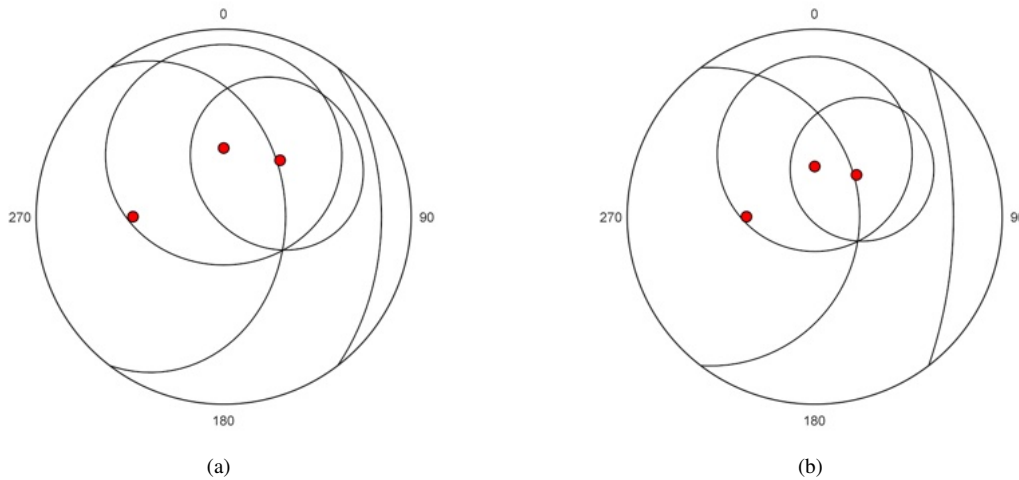


Figure 8.1: Spherical projections showing the solution finding the orientation of the plane defined by the drill core data in Table 8.1, showing the cones defined by the core-plane angles. The solution is the intersection of the three cones. (a) Solution displayed on a Schmidt plot. (b) Solution displayed on a lower hemisphere stereographic projection (stereogram).

## 8.2 Small Circles

In some cases it may be required to fit directional data to a small circle, or circular cone. Such data may be generated by the rotation of a line about an oblique axis. In geology, a common example is to determine the best fit axis,  $\lambda$  (a vector, specified, for example, by trend and plunge), and semi-apical angle,  $\psi$ , of conical folds. The most common model for folds is cylindrical, however the alternate model of conical folds may be useful in some cases (Wilson, 1967; Gray et al., 1980; Kelker and Langenberg, 1982; Stesky, 1985; Kelker and Langenberg, 1987, 1988; Mulchrone et al., 2013), although see Welker et al. (2019) for a discussion of periclinal fold geometry.

This may also be viewed as a general model for fitting vector data to great or small circles, since great circles are given by  $\psi = 90^\circ$ . Note that the data  $[\theta_i, \phi_i]$  are treated as directed (vector) data, if these are bedding measurements, any overturned beds should be entered using negative dips  $[\theta_i + 180^\circ, -\phi_i]$ .

The problem, given a data sample  $[\theta_i, \phi_i]$ , find the circular cone  $[\lambda, \psi]$ , can be formulated by minimizing the sum of the squared angular residuals (Gray et al., 1980), or the negative sum of the cosines of the angular residuals (Mardia and Gadsden, 1977). It does not have a direct solution, and requires an iterative approach (Mardia and Gadsden, 1977; Gray et al., 1980; Mancktelow, 1981; Fisher et al., 1987). The fitting method used here follows Fisher et al. (1987, p. 140-143) after Mardia and Gadsden (1977) with modifications from Gray et al. (1980) to improve the convergence rate. For a sample of  $n$  directions  $x_i$ , the procedure minimizes the sum

$$q = \frac{1}{n} \sum_{i=1}^n (1 - \cos \alpha_{c_i}) \quad (8.1)$$

where  $\alpha_{c_i}$  is the angle between  $x_i$  and the circular cone axis.

Figure 8.2a is a Schmidt plot of folded bedding planes, Australia, from Cohen 1983 (Fisher et al., 1987, Table B4), given in the file Example Datra/Folds/Cohen 1983. The fitted cone is  $[\lambda, \psi] = [3.23^\circ, 18.38^\circ, 76.19^\circ]$  given as azimuth, declination, semi-apical angle. Figure 8.2a shows the folded graywacke bedding data with the best fit small circle  $[183.63^\circ, 8.09^\circ, 85.57^\circ]$ , very close to the great circle axis  $[182.76^\circ, 2.69^\circ, 90^\circ]$  shown in Figure 4.11b.

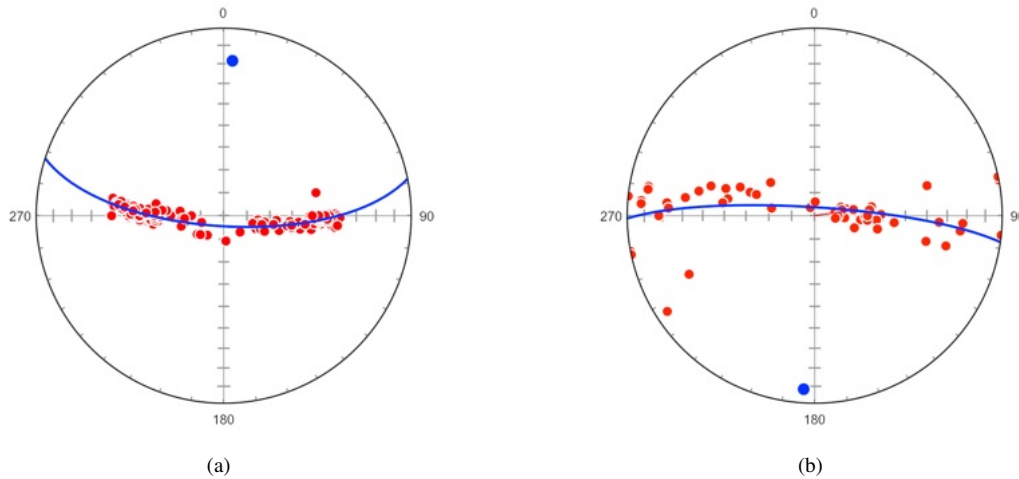


Figure 8.2: Schmidt plots of folded bedding planes fitted to cones. (a) 155 facing directions of conically folded planes. to a small circle. Data from Cohen 1983 (Fisher et al., 1987, Table B4). (b) Folded graywacke bedding data from Vollmer (1981) with best fit small circle. Compare with Figure 4.11b, which shows the best fit great circle.

### 8.3 Small Circle Confidence

The method for fitting a small circle can be extended to estimate confidence regions using bootstrap methods similar to that discussed in Section 6.3 (Fisher et al., 1987, p. 140-143). A large number of estimates of the mean are calculated from resampled replicates, and used to estimate confidence regions. Figure 8.3a shows the 95% confidence for the cone axis of the fold data calculated using 1000 replicates, and Figure 8.3b shows the data rotated to the cone axis.

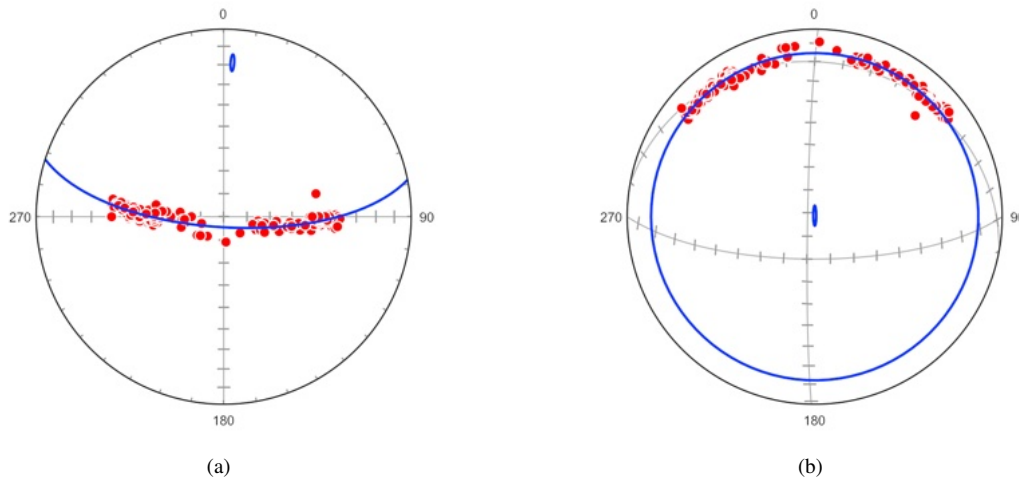


Figure 8.3: Schmidt plots of folded bedding planes fitted to cones with 95% confidence cones based on the means of 1000 bootstrap replicates. Data from Cohen 1983 (Fisher et al., 1987, Table B4). (a) Plot in local coordinates. (b) Plot rotated to the small circle pole.

### 8.4 Spherical Ellipses

A spherical ellipse is the intersection of an elliptic cone with a sphere, and is an alternative to the small circle, or circular cone, model. The method here follows Kelker and Langenberg (1987), by implementing a translation of Fortran code by Kelker, Langenberg and Charlesworth (1988), which is based on code by Stesky (1985). The code has been modified to fix an error in the spherical polygon

output displayed on the projection. For a sample of  $n$  directions  $x_i$ , the procedure minimizes the sum

$$q = \sum_{i=1}^n (\alpha_{c_i} - \hat{\alpha}_{c_i})^2 \quad (8.2)$$

where  $\alpha_{c_i}$  is the angle between  $x_i$  and the elliptic cone axis, and  $\hat{\alpha}_{c_i}$  is the angle between the cone axis and  $\hat{x}_i$ , where  $\hat{x}_i$  is the intersection of the cone with a plane defined by the cone axis and  $x_i$ .

The method is iterative and uses the minimum eigenvector as an estimate for the cylindrical fold axis (Section 4.8). This estimate is used as a starting value for fitting a circular cone, which is then used as a starting value for fitting an elliptic cone. Statistical tests are given in the *Data - Statistics* window, with estimated errors. Figure 8.4 is a Schmidt plot of 78 foliation measurements from the Wynd syncline, Rocky Mountains west of Jasper, Alberta (Kelker and Langenberg, 1987, Appendix A, example data file Kelker & Langenberg 1987.csv), with the best fit great circle in green (Section 4.8), the best fit small circle in blue (Section 8.2), and best fit spherical ellipse in red. The log output from the *Data - Statistics* command is

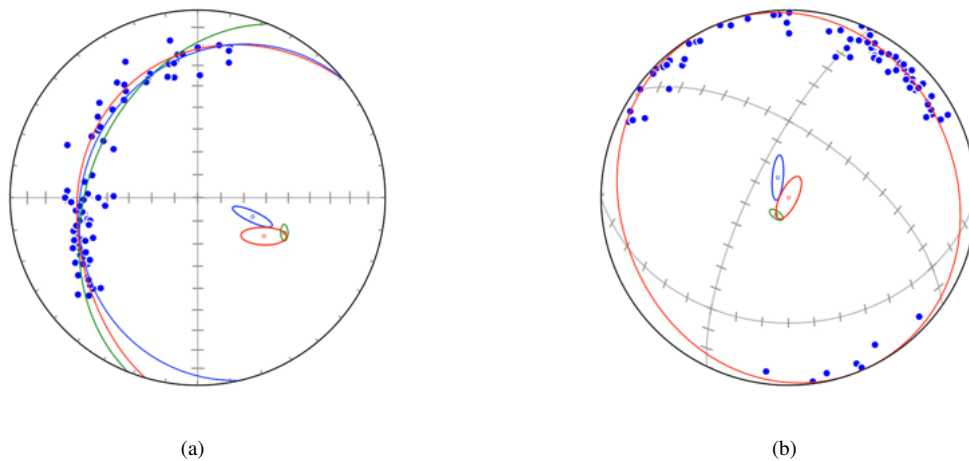


Figure 8.4: (a) Schmidt plot of the poles to 78 foliation measurements from the Wynd syncline, Rocky Mountains west of Jasper, Alberta (Kelker and Langenberg, 1987, Appendix A), with the best fit great circle in green (Section 4.8), the best fit small circle in blue (Section 8.2), and the best fit spherical ellipse in red. The 95% confidence cones are calculated from 1000 bootstrap resample means covariance matrices of the great circle, small circle, and spherical ellipse axes (Section 6.3) (b) Plot as in (a) rotated to the best-fit elliptic cone axis. The best-fit great circle and small circle traces are not shown.

2020-10-04 16:00:18

Data File : Kelker & Langenberg 1987

Data Type : Default.S

Data Domain : All

N : 78

N 2D : 78

N weighted : 78.000

Weighted : False

Kinematic : True

=====

Spherical Ellipse (Elliptic Cone)

Cylindrical Axis

Trend, Plunge : 112.010 48.724

## Circular Cone

Trend, Plunge : 109.072 64.699  
 Semi-apical angle : 76.948  
 SS residuals : 0.5981  
 95% major radius : 4.010  
 95% minor radius : 2.848  
 95% major horizontal trend : 298.295  
 F test (cylindrical vs circular) : 17.5930  
 Degrees of freedom F(1, df) : 75

## Elliptic Cone

Trend, Plunge : 120.185 56.414  
 Major semi-apical angle : 90.000  
 Minor semi-apical angle : 78.523  
 Ratio of apical angles : 1.1462  
 Major generatrix : 326.626 30.735  
 SS residuals : 0.5340  
 95% major angle : 3.134  
 95% minor angle : 3.021  
 95% major horizontal trend : 246.848  
 F test (circular vs elliptical) : 4.3822  
 Degrees of freedom F(2, df) : 73  
 Bootstrap confidence  
 Resamples : 1000  
 95% major semi-apical angle : 10.608  
 95% minor semi-apical angle : 3.854

In addition to the elliptic cone statistics, the log contains values for cylindrical and circular cone fits, as these are used as initial estimates for the iterative solution. The fitted circular cone is  $[\lambda, \psi] = [109.072^\circ, 64.699^\circ, 76.948^\circ]$  given as azimuth, declination, semi-apical angle, while the cone calculation used in Section 8.2 gives  $[109.076^\circ, 64.707^\circ, 76.943^\circ]$ . For small angular residuals, the minimization of Eq 8.1 and Eq 8.2 should give identical results, which is the case for this data sample.

Kelker and Langenberg (1987) conclude that the cylindrical and the circular conical models can be rejected based on the F statistics, and classify the fold as elliptical conical. The plotted confidence ellipse (Figure 8.4) is calculated using bootstrapping and fitting an ellipse to the covariance matrix of the bootstrapped means on a tangent plane (Section 6.3). The log output additionally gives a confidence cone based on the method of Kelker and Langenberg (1987).

## 9 Kinematic and Dynamic Analysis

Data associated with movement along faults or shear zones are comprised of planes that contain lines, such as striae on slickenside surfaces. Numerous methods exist for the determination of stress, strain, or strain-rate axes from populations of faults. Three methods are implemented here, a kinematic analysis based on M plane, or movement plane, geometry (Angelier and Mechler, 1977; Angelier, 1979; Marshak and Mitra, 1988; Marrett and Allmendinger, 1990; Twiss and Unruh, 1998; Twiss and Moores, 2007; Fossen, 2016), a dynamic Coulomb stress method based on Compton's method (Compton, 1966; Erslev et al., 2004; Erslev and Larson, 2006; C  l  rier et al., 2012), and a dynamic stress tensor analysis based on locating the most compatible reduced stress tensor (Angelier, 1984; Yamaji, 2000; C  l  rier et al., 2012; Fossen, 2016).

Numerous techniques have been developed to infer principal stress orientations from fault data (C  l  rier et al., 2012). The Mohr-Coulomb failure and frictional sliding criteria predict that faulting occurs on planes that form an acute angle with the maximum principal stress orientation,  $\sigma_1$ , allowing its orientation to be inferred (Compton, 1966; Erslev et al., 2004; Erslev and Larson, 2006; C  l  rier et al., 2012), an implementation is covered in Section 9.5. Another common method, with many variations, is to assume that slip direction on a fault depends on the orientation of the principal stresses and their aspect ratio (Wallace, 1951; Bott, 1959; Angelier, 1979; Yamaji, 2000; C  l  rier et al., 2012). These methods attempt to minimize the misfit of the angle between the measured fault slip and the resolved shear stress on the fault plane applied by the solution stress tensor  $\sigma^*$  (C  l  rier et al., 2012), as discussed in Section 9.6.

Before attempting to use kinematic or stress inversion techniques one must consider the inherent difficulties and assumptions. The Wallace-Bott assumption that slip on a fault occurs parallel to the resolved shear traction of a regional homogeneous stress tensor has been questioned, and there is debate as to whether a kinematic or dynamic solution should be sought (Marrett and Allmendinger, 1990; Pollard et al., 1993; Twiss and Unruh, 1998; Tikoff and Wojtal, 1999; Lejri et al., 2015). Field observations are related to kinematics, and there are convincing arguments that a kinematic solution should be sought, although dynamic solutions are widely used. Polyphase slip data presents an additional challenge (Yamaji, 2000; Sperner and Zweigel, 2010; C  l  rier et al., 2012). However, given carefully collected field data, and a clear statement of assumptions, these techniques can provide useful information on past displacement, strain, or stress directions, including plate convergence directions (Blenkinsop, 2006; Sperner and Zweigel, 2010).

### 9.1 Entering Line-Plane Pairs

Kinematic analysis requires entering plane-line pairs, as each data point includes both a plane, such as a fault plane, and a directed line contained in that plane, such as a fault striation. Data is commonly entered as strike (or dip direction), dip, trend, plunge, however it is also possible to enter strike and dip, and just one of the values trend or rake, and calculate the trend and plunge using the *Data - Calculate Lines* command.

Several conventions for entering kinematic data are available. A common field geology convention is to measure the strike (or dip direction) and dip of the fault plane, the trend and plunge of the slip lineation, and a designation to indicate whether the fault is normal, reverse (thrust), sinistral (left lateral), or dextral (right lateral). The *Sense* column is used to enter one of *Nor*, *Rev*, *Sin*, or *Dex* respectively. See Table 2.15 for shortcuts and file import options.

*Trend*, *Plunge* data is normally entered with positive plunges, and *Sense* used to indicate whether they are directed upward or downward. If the sense is omitted, it is possible to enter lines with negative (upward directed) plunges, however it is advisable to use the *Declination*, *Inclination* format instead. These are equivalent, but negative inclinations are kept as displayed, and it is not necessary to use the *Sense* column. Table 9.1 gives an example of data with a negative plunge.

Alternatively, the *Rake* column can be used to indicate the slip sense. The default convention is that the rake indicates the motion of the hanging wall (Pollard and Fletcher, 2005; Ragan, 2009). In this

ID	Strike	Dip	Trend	Plunge	Sense	Rake
1	0.00	30.00	90.00	30.00	Rev	-90.00
2	0.00	30.00	270.00	-30.00		-90.00

Table 9.1: The same kinematic data entered using two different conventions. Data point 1 uses the sense notation. Data point 2 uses an upward directed trend and plunge. These represent identical values. One or the other convention should be chosen, as mixing them can give confusing results. It is recommended that *Declination, Inclination* lineation format be used if the latter convention is required.

case a positive rake (clockwise from the strike) indicates a normal fault, and a negative rake indicates a reverse fault, so  $-90^\circ$  indicates a reverse fault. An alternative convention is the Aki-Richards (AR) convention, which is commonly used for seismic data. In this convention the sign is reversed, so  $-90^\circ$  indicates a normal fault. This can be selected using the *Data - Orientation Formats* command, or, when reading data from a file, using the column header Rake AR instead of Rake. When entering data using either rake convention, the *Sense* is not required, however it is necessary to use the *Data - Calculate Lines - Rake* to calculate the line trends and plunges.

Since the hanging wall is undefined for faults with a dip of  $90^\circ$ , it is recommended that a dip of  $89.9^\circ$  be entered to avoid ambiguity. Similarly, faults with a dip of  $0^\circ$  can be problematic, since the strike is undefined, and it is therefore recommended to enter a dip of  $0.1^\circ$  for these.

The Error column is read only, and contains the calculated angular error between the plane and its contained line. A common problem with field data is that it is over constrained, only three angles are required for plane-line pairs, while four are often measured. The *Data - Calculate Line* command is used to calculate, or recalculate, line-plane pairs. Given the orientation of a plane and one of the angles trend or rake, the trend and plunge can be calculated using the *Calculate Line* command. The resulting line-plane pair will have a  $0^\circ$  angular mismatch error.

## 9.2 Orthonormalization and Line Calculation

If both the plane and contained line have been measured directly using *four* angles, such as strike, dip, trend, and plunge, then the line-plane pair is over-constrained with a mismatch error. In this case the Error column will contain a non-zero angular value, the angle between the line and plane. The *Data - Calculate Line* command has two options to recalculate the line-plane pair and remove the angular error. The *Projection* option recalculates a line by projecting it onto the plane by a rotation of  $-Error$  about an axis perpendicular to both the line and the plane normal, so only the orientations of the lines are modified. The *Orthonormalize* option recalculates *both* the line and the plane to create a orthonormal frame closest to the non-orthogonal data frame.

Given over-constrained data, the selection of the option requires judgement of the source of measurement error. The angular errors should be checked first, any data point with a large error should be discarded or corrected. It is common that the plane is easier to measure accurately than the contained line, if so, the *Projection* option is the best. The *Orthonormalize* option will modify both, and is better if no assumption is made about the source of error. In both cases the rake and slip sense can also be calculated. Note that potential measurement errors depend on the orientation of the line or plane, for example, the likely error in the strike of a plane increases with decreasing dip (Ragan, 2009, p. 5-9).

If only *three* angles are measured, the strike (or dip direction), dip, and either the line rake or the line trend, the included line can be calculated using the *Rake* or *Trend* options. This will give an exact value since only three angles are specified. The rake, if not given, and the slip sense can also be calculated. The linked plane options are described in Section 2.4.

Optional calculation of line rakes requires the lines and plane normals to be orthonormal, which they will be after any of the above calculations. Potential errors may occur if the plane dips are exactly  $0^\circ$ , when the strike is undefined, or  $90^\circ$ , when the hanging wall is undefined. It is therefore prudent to enter  $89.9^\circ$  or  $0.1^\circ$  respectively.

Optional calculation of slip senses identifies the kinematic axis, *P*, *T*, or *M* (Section 9.3), with the steepest plunge using Eq 9.12. If that axis indicates a dominant strike-slip sense, the obtuse angle

between the shortening rate axis ( $P$ ) and the lineation ( $L$ ) is used to identify dextral (clockwise) versus sinistral (counterclockwise) senses.

### 9.3 *M* Planes and Tangent Lines

Each data point for kinematic analysis must include the orientation of a kinematic plane, such as the strike and dip of a fault plane, and the orientation of a movement direction in that plane, such as the trend and plunge of a fault striation, signifying the motion of the hanging wall (upper) block. Upward directed vectors, with a reverse component, can be entered using negative plunges, or by entering *Rev* (*r*) in the Sense column. This is equivalent to adding  $180^\circ$  to the trend, and negating the plunge. Fault motion can also be specified using one of two rake conventions, which may be preferable (Section 9.1).

Although the term fault is used here, the kinematic analysis can be applied to shear zones if the displacement directions can be determined. As the slip lineation lies within the fault plane, the displacement direction must lie in the plane containing the lineation and the pole to the fault, this plane is the *M* plane. Figure 9.1 shows the geometric relationships with the *M* plane shown in light gray. Two kinematic axes are defined within the *M* plane, at  $\pm 45^\circ$  from the lineation. These are commonly referred to as the  $P$  ("pressure") and  $T$  ("tension") axes, terms derived from first motion studies in seismology. However, they should not be interpreted as stress axes, as  $P$  is an incremental shortening axis, and  $T$  is an extension axis. The term *M* axis is used here as the pole to the *M* plane, in seismology, the equivalent axis is referred to as the  $B$  or  $N$ , null, axis.

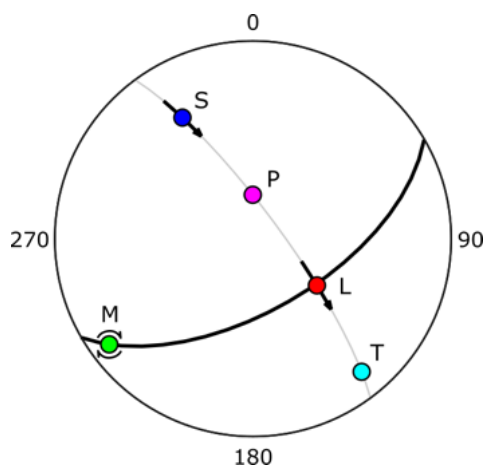


Figure 9.1: Schmidt plot of a normal fault (black great circle), with a slip lineation,  $L$ , pole to the fault,  $S$ , and the  $M$  axis. The  $M$  plane is shown in light gray. The  $P$  axis is found by a  $-45^\circ$  rotation of  $L$  about  $M$ , and the  $T$  axis is found by a  $+45^\circ$  rotation. Arrows are tangent lines that show the displacement sense of the hanging wall with respect to the footwall, an instantaneous motion as a rotation, or vorticity vector, about the  $M$  axis.

The arrows drawn through the lineation and the fault normal are *tangent lines*, directed lines tangent to a projected point on the unit sphere. In Figure 9.1 tangent lines are drawn through the lineation and the fault pole projections to show the displacement sense of the hanging wall with respect to the footwall. They can be viewed as instantaneous rotation, or vorticity vectors about the  $M$  axis. A number of conventions and names have been used for tangent lines (Marshak and Mitra, 1988; Twiss and Unruh, 1998; Twiss and Moores, 2007), for clarity here the tangent line drawn through the pole to a fault is referred to as a *pole tangent line*, and tangent line drawn through a slip lineation is referred to as a *slip tangent line*. They can be constructed using either a hanging wall or footwall reference frame.

Figure 9.2 shows tangent line diagrams of a sample of 38 Neogene normal faults from central Crete, Greece, using data from Angelier (1979), in hanging wall reference frames. Figure 9.2a is a pole tangent line plot, and Figure 9.2b is a slip tangent plot.

A final option is to draw *slip trend lines*. This option draws ticks or arrows parallel to the trend of

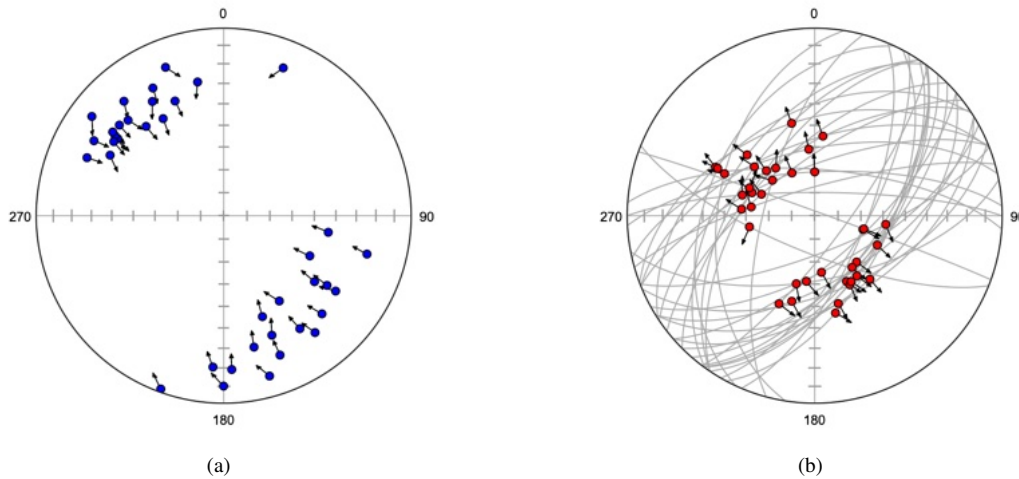


Figure 9.2: Lower hemisphere tangent line plots of a sample of 38 Neogene normal faults from central Crete, Greece. Both plots use a footwall reference frame. Data from Angelier (1979). (a) The data displayed on a *pole tangent line* plot. The arrows through the fault pole projections show the displacement sense of the hanging wall with respect to the footwall. (b) The data displayed as a *slip tangent line* plot, with fault planes shown in gray. The arrows through the slip lineations show the displacement sense of the hanging wall with respect to the footwall.

the slip lineation, in either footwall or hanging wall reference frames. While technically conveying less information, they may be easier to interpret visually than slip tangent lines.

The visibility of pole tangent, slip tangent, and slip trend lines is determined by three settings. First, they must be selected in the *Kinematics* pane. To draw a full, rather than half, arrow through the data point, set the length of one arrowhead to zero. By default the footwall (FW) arrowhead length is set to zero, to indicate the relative motion of the hanging wall (HW). Second, the *Domain* can be selected to only draw a single domain. This can be used to partition the data into two or more sets. Set the domain to 0 to display all the data. Third, pole tangent lines will only be drawn if the *type.S* symbols (Table 9.2) are checked *Visible* in the *Symbols* pane. Slip tangent and slip trend lines will only be drawn if the *type.L* symbols are checked *Visible* in the *Symbols* pane.

## 9.4 Moment Tensors

The *P* and *T* axes associated with the *M* plane (Figure 9.1) indicate shortening and extension axes respectively for individual faults. The best-fit kinematic axes for a sample can be approximated by calculating the *moment tensors* of the sample *P* and *T* axes independently, or linking them by considering one positive and one negative (Marrett and Allmendinger, 1990). The moment tensor for an axis is identical to the orientation tensor,  $\Omega$  (Eq 4.6), discussed in Section 4.8. When fault data is entered, normally a strike and dip for a fault plane, and a trend and plunge for a slip lineation, the *M*, *P*, and *T* axes are automatically calculated, giving five elements for each line-plane pair. An extension is added to the data type using dot namespace notation to indicate each of the five data elements (Table 9.2).

Type Extension	Element
.S	Plane, fault, slickenside, or shear plane
.L	Line, slip direction, slickenline, or shear direction
.M	M movement axis or plane (B or null axis in seismology)
.P	P shortening axis
.T	T extension axis

Table 9.2: Data type extensions for elements automatically generated for kinematic data.

Figure 9.3 shows the *M*, *P* and *T* kinematic axes for the sample of 38 normal faults from Angelier (1979). Each of these extended data types can be plotted and analyzed independently. For kine-



matic analysis the  $P$  and  $T$  axes are contoured (Figure 9.3b), and their maximum values and scatter determined by eigenvector analysis (Figure 9.3b, Sections 4.8 and 6.1), and for the construction of *beachball* plots (Figure 9.4). If measurements have been made of fault trace length, gouge thickness, or other proxies for displacement, the faults can be individually weighted (Section 2.12). If the data is weighted, confidence cones should be determined using a Watson or Bingham model (Section 6.1) rather than by bootstrapping (Section 6.3), since bootstrapping requires random sampling of equally weighted data points.

Using a moment tensor,  $\Omega$  (Eq 4.6), to determine kinematic axes treats the  $P$  and  $T$  axes as independent data samples. In cases where the best-fit  $P$  and  $T$  axes are not close to orthogonal, there may be discrepancies apparent in maxima plots and beachball diagrams. Discrepancies from orthogonality can be detected by plotting the great circles to the  $P$ ,  $M$ , and  $T$  axes, if the axes are orthogonal the great circles will intersect at the axes.

If the axes are not orthogonal, it is possible to force orthogonality by linking the  $P$  and  $T$  axes using a modified orientation matrix

$$\Omega_L = \frac{1}{n} \sum_{i=1}^n (P_i P_i^T - T_i T_i^T) \quad (9.1)$$

where  $P_i$  are the direction cosines of the individual  $P$  axes, and  $T_i$  are the direction cosines of the  $T$  axes. The eigenvectors of this matrix give orthogonal best-fit  $P$ ,  $M$ , and  $T$  axes. The matrix does not contain information about the minimum and intermediate axes, and, unlike  $\Omega$ , can not be weighted. Confidence cones can only be drawn about the maximum eigenvectors by using the *Bootstrap* option. This option can be selected in the *Spherical Projection - Maxima* pane *Linked* checkbox, and also effects the *Kinematics - Beachball* display.

Minimum and intermediate eigenvectors are calculated using  $\Omega$  (Eq 4.6), and the data axes are treated independently for contouring. Linked orientation matrices are also supported for  $L$  and  $S$  best-fit maxima, which can be applied to LS tectonites. This forces the best-fit  $L$  and  $S$  axes to be perpendicular, however the best-fit  $M$  axes are calculated using Eq 9.1 and may not be exactly perpendicular to  $L$  and  $S$ . While using a linked orientation matrix may be satisfactory, a more rigorous approach is to treat the *line in plane* pairs, as single data points, *orthonormal frames*, treated in Section 10.

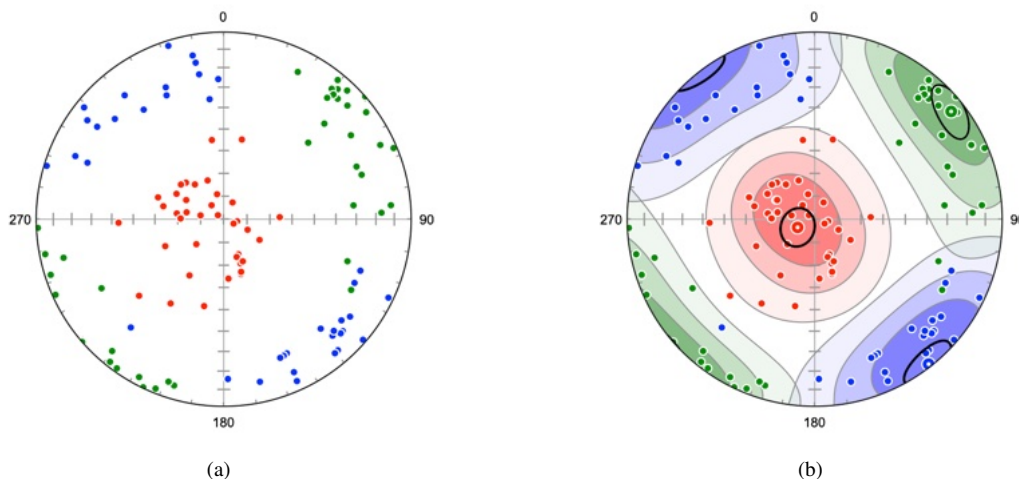


Figure 9.3: (a) Schmidt scatter plot of poles to  $M$  planes (green),  $P$  shortening axes (red), and  $T$  extension axes (blue) for sample of 38 Neogene normal faults from central Crete, Greece (Angelier, 1979). (b) The same plot with modified Kamb contours at 25% estimated density, and 95% bootstrap confidence cones (Section 6.3) about the eigenvectors of the linked orientation tensor,  $\Omega_L$  (9.1).

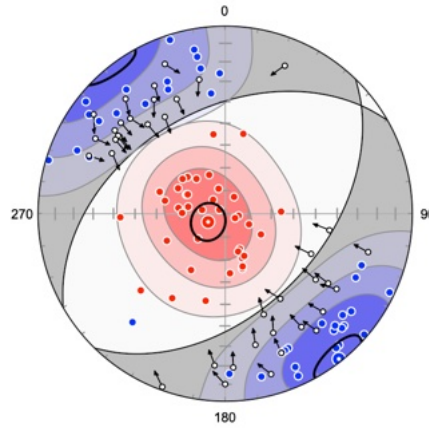


Figure 9.4: Schmidt plot summarizing the analysis of the  $P$  and  $T$  kinematic axes of the fault data from Angelier (1979) as a beachball plot showing the  $P$  shortening and  $T$  extension quadrants, bootstrap confidence ellipses, and pole tangent vectors showing hanging wall movement sense (Section 9.3).

## 9.5 Coulomb Stress Inversion

The empirical Mohr-Coulomb failure criterion is commonly used to predict brittle failure

$$\tau_S = C_0 + \mu_0 \tau_N \quad (9.2)$$

where the critical shear traction at failure  $\tau_S$  is a function of the cohesion  $C_0$ , the coefficient of internal friction  $\mu_0$ , and the normal traction  $\tau_N$ . Expressing this in terms of the angle of internal friction,  $\phi_0$

$$\tau_S = C_0 + \tan(\phi_0) \tau_N \quad (9.3)$$

For frictional sliding on preexisting surfaces, the equation becomes

$$\tau_S = \tan(\phi_F) \tau_N \quad (9.4)$$

where  $\phi_F$  is the angle of friction. Common approximations are  $\mu_0 = 0.6$  and  $\mu_F = 0.85$  (Byerlee, 1978). The Mohr-Coulomb criterion predicts that the angle between a shear fracture and  $\sigma_1$ , the orientation of the maximum principal stress, is equal to  $\phi_0$ , or  $\phi_F$  for frictional sliding (Figure 9.5).

Compton (Compton, 1966; Erslev et al., 2004; Erslev and Larson, 2006; C  lerier et al., 2012) used these relationships to develop a graphical method to determine principal paleostress orientations on shear fractures. For the case where  $\sigma_2 = \sigma_3$ , fault slip directions should plot on a small circle about  $\sigma_1$ , forming a cone with an apical angle  $\phi_F$ . For intermediate cases, fault slip directions should be more clustered. Figure 9.5 shows the relationship among the  $P$  kinematic axes of two conjugate fault surfaces,  $S_1$  and  $S_2$ , with slip directions,  $L_1$  and  $L_2$ , the angle of friction,  $\phi_F$ , and the maximum principal stress,  $\sigma_1$ .

The method used here is similar to that of Erslev et al. (2004) who used Orient 1.6 to search  $\phi_F$  space to find the orientation tensor  $\Omega^*$  for  $\sigma_1$  that maximizes the magnitude of  $\varepsilon_1$ . However, as the optimal solution is not necessarily a point maximum, the default search method here is to find  $\Omega^*$  for  $\sigma_1$  that maximizes the B index, equivalent to *minimizing* the magnitude of  $\varepsilon_3$ . If the *Maximize point* option is selected, the search will maximize the P index instead, equivalent to maximizing the magnitude of  $\varepsilon_1$  (Section 7.1) (Vollmer, 1990).

Use the *Coulomb Stress* command to search for the optimal solution of  $\phi_F$  for a given set of faults. By default it searches  $\phi_F$  in  $0.01^\circ$  increments to locate the best orientation tensor  $\Omega^*$  for  $\sigma_1$ . Press the *Calculate* button to perform the search, and then press *OK* to copy the  $\phi_F$  values to the spreadsheet (*PhiF* column).

The *Use friction* option toggles on and off the use of the friction angle (*PhiF*) when calculating *PT* axes. When *OFF* kinematic axes are calculated as normal (Section 9.4). When *ON* the *PT* axes are calculated as dynamic stress axes using the angle of friction, in this case, the calculated P, M, and

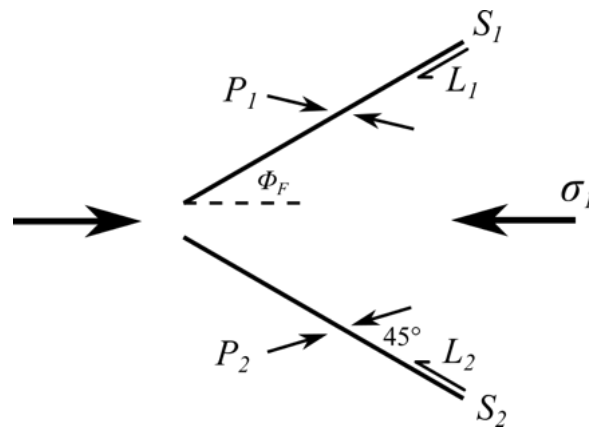


Figure 9.5: Schematic two-dimensional diagram showing the relationship among the  $P$  kinematic axes of two conjugate fault surfaces,  $S_1$  and  $S_2$ , with slip directions,  $L_1$  and  $L_2$ , the angle of friction,  $\phi_F$ , and the maximum principal stress,  $\sigma_1$ .

T axes can be interpreted as stress axes,  $\sigma_1$ ,  $\sigma_2$ , and  $\sigma_3$  respectively. This setting effects all plots and statistics.

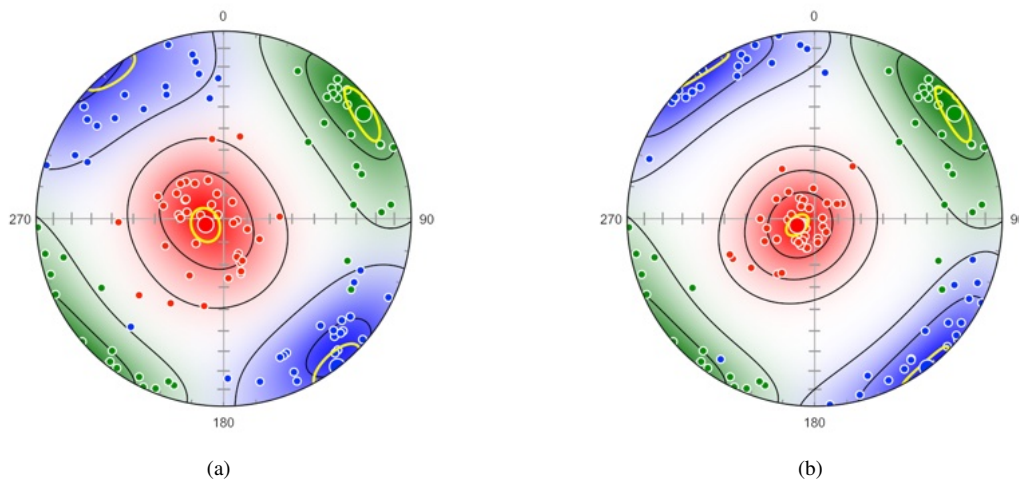


Figure 9.6: Inverse solutions for the fault data from Angelier (1979). Contours are 2 multiples of uniform density, confidence cones are bootstrap 95%. Data were orthonormalized prior to analysis. (a) Kinematic solution. Red =  $P$ , green =  $M$ , blue =  $T$  axes. (b) Dynamic Coulomb stress solution.  $\phi_F^* = 29.34^\circ$ . Red =  $\sigma_1$ , green =  $\sigma_2$ , blue =  $\sigma_3$  axes.

The solution maximizing the B index gives  $\phi_F = 29.34^\circ$ , and the solution maximizing the P index is  $27.6^\circ$  (Table 9.3). Note that the dynamic solution for  $\sigma_2$  will always be identical to the kinematic solution for  $M$ , as these axes are perpendicular to the fault normal and slip line in both cases. The solution for  $\phi_F = 45^\circ$  will give  $\sigma_1$  and  $\sigma_3$  identical to the  $P$  and  $T$  axes of the kinematic solution.

Method	$\phi_F$	P or $\sigma_1$ Trend, Plunge	T or $\sigma_3$ Trend, Plunge
Kinematic	$45.0^\circ$	$252.0^\circ, 81.8^\circ$	$142.4^\circ, 0.5^\circ$
Coulomb B	$29.3^\circ$	$249.0^\circ, 81.9^\circ$	$142.9^\circ, 0.4^\circ$
Coulomb P	$27.6^\circ$	$248.8^\circ, 81.9^\circ$	$143.0^\circ, 0.3^\circ$
Stress Tensor		$278.8^\circ, 80.5^\circ$	$128.3^\circ, 8.3^\circ$

Table 9.3: Comparison of results from kinematic and dynamic Coulomb stress inversion. B = maximizing the B eigenvalue index. P = maximizing the P eigenvalue index. Tensor = stress tensor inversion (Section 9.6).

## 9.6 Stress Tensor Inversion

The stress tensor inversion technique is based on locating the most compatible reduced stress tensor for a sample of faults (Angelier, 1984; C  lerier et al., 2012). The assumption is made that the slip

direction depends on the orientation of a homogeneous stress tensor and its aspect ratio (Wallace, 1951; Bott, 1959; Angelier, 1979; Yamaji, 2000; Célérier et al., 2012). This method has been referred to as the *classic inverse method* (Yamaji, 2000). See Célérier et al. (2012) for a review of related methods.

This inverse method is implemented as follows. Given a set of fault slip data comprised of  $p_i$  fault normals, where  $i = 1 \dots n$ , and the corresponding slip directions,  $s_i$ , the goal is to locate the best reduced stress tensor by minimizing the misfits between  $s_i$  and the resolved shear traction  $\tau_{S_i}$  on the fault  $p_i$ , or, equivalently, to maximize the fit. The reduced stress tensor is

$$\sigma = \begin{bmatrix} 1 & 0 & 0 \\ 0 & \phi_B & 0 \\ 0 & 0 & 0 \end{bmatrix} \quad (9.5)$$

where  $\phi_B$ , Bishop's ratio, is

$$\phi_B = \frac{\sigma_2 - \sigma_3}{\sigma_1 - \sigma_3} \quad (9.6)$$

Compression is positive, with  $\sigma_1 \geq \sigma_2 \geq \sigma_3$ .  $\phi_B$  varies from 0 to 1, for  $\phi_B = 0$ ,  $\sigma_2 = \sigma_3$ , and for  $\phi_B = 1$ ,  $\sigma_1 = \sigma_2$ . Note that the absolute magnitudes of the principal stresses are not determined, and the resolved shear traction orientation is constrained by four parameters, the orientations of the principal stress axes, and  $\phi_B$ . The value of  $\phi_B$  has as much influence on the resolved shear traction as do the orientations of the principal axes. A four dimensional search through the parameters that define  $\sigma_j$ , where the subscript  $j$  indicates an iteration within the four parameters, is done to locate the best solution  $\sigma^*$ .

Taking  $\tau_i$  as the traction acting on fault plane  $p_i$ , and  $\tau_{S_i}$  and  $\tau_{N_i}$  as the shear and normal components of  $\tau_i$

$$\tau_i = \sigma p_i \quad (9.7)$$

$$\tau_{N_i} = p_i^T \tau_i p_i \quad (9.8)$$

$$\tau_{S_i} = \tau_i - \tau_{N_i} \quad (9.9)$$

If the fault slip  $s_i$  is parallel to the resolved shear traction  $\tau_{S_i}$ , then current stress tensor iteration  $\sigma_j$  is compatible with the fault. After normalizing  $\tau_{S_i}$ , a measure of the goodness of fit is the dot product

$$d_i = \tau_{S_i} \cdot s_i \quad (9.10)$$

which varies from 1 if they are parallel to -1 if they are antiparallel. For  $n$ , optionally weighted faults, where  $w_i$  is a weight, such as displacement, gouge thickness, or trace length, and  $n_w$  is the sum of the  $n$  weights a mean goodness of fit,  $\bar{D}$  can be defined as

$$\bar{D} = \frac{1}{n_w} \sum_{i=1}^n d_i w_i \quad (9.11)$$

The value of  $\bar{D}$  ranges from -1 to 1, with  $\bar{D} = 1$  indicting a perfect fit for all faults. A search proceeds by a methodical search varying the four parameters, giving  $\sigma_j$  for each iteration, to find the maximum value  $\bar{D}^*$ , and the best-fit solution  $\sigma^*$ .

Due to the nonlinear nature of the problem, and the large number of possible solutions, the search procedure must be optimized to avoid returning a local maximum, and examining as many solutions as possible. The search parameters to be set by the user are: the number of nodes on a regular grid, the increment in degrees of rotation about a node, and the increment to vary  $\phi_B$ .

Data from the surface rupture of the 1999 Chi-Chi earthquake, Taiwan (Blenkinsop, 2006) is used as an example. Blenkinsop (2006) used several methods of kinematic and dynamic inversion, and compared results from field data to seismic solutions. The data is provided in the example files folder as *Blenkinsop 2006.ods*. Table 9.4 is a comparison of the field data stress inversion results of Blenkinsop (2006) to those calculated here. Prior to calculating the best reduced stress tensor the data were orthonormalized (Section 9.2).

$\sigma^*$	$\bar{D}$	$\sigma_1$	$\sigma_2$	$\sigma_3$	$\phi_B$
$B$		291, 5	21, 0	111, 85	0.2
$O_U$	0.90	293.8, 6.6	203.0, 6.7	67.8, 80.6	0.26
$B - O_U$		2.2	7.0	6.7	0.06
$O_W$	0.89	293.8, 6.6	203.0, 6.7	67.8, 80.6	0.29
$B - O_W$		2.2	7.0	6.7	0.09

Table 9.4: Stress inversion results from the 1999 Chi-Chi earthquake, Taiwan.  $B$  - Stress inversion results computed by Blenkinsop (2006).  $O_U$  - Unweighted results.  $O_W$  - Weighted results.  $B - O_U$  is the angular difference in degrees between  $B$  and  $O_U$ ,  $B - O_W$  is the angular difference between  $B$  and  $O_W$ . The best-fit principle stress,  $\sigma^*$ , axes are given as trend, plunge. The search settings were 1024 grid nodes,  $2^\circ$  increment,  $0.01 \phi_B$  increment. Each Orient result was obtained by examining approximately 28 million solutions.

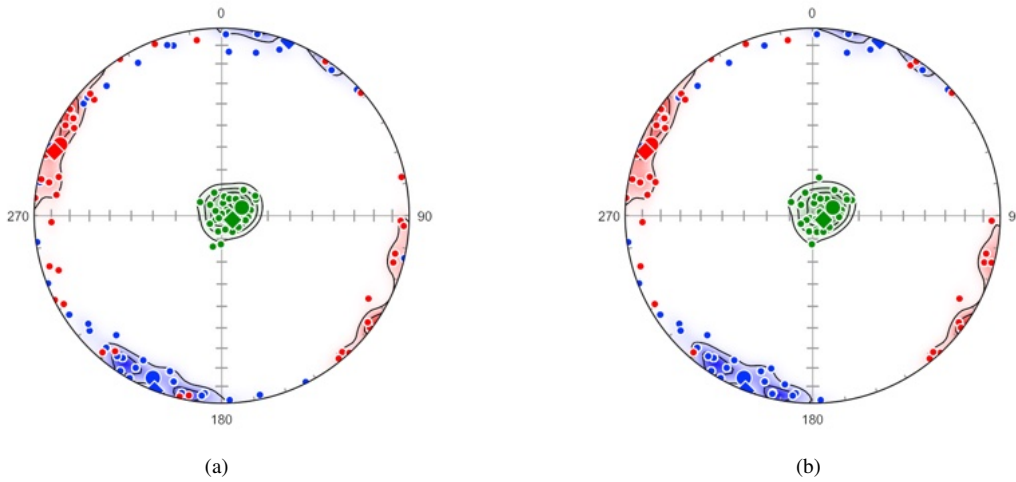


Figure 9.7: Schmidt plots of the best-fit solutions for stress inversion results from the 1999 Chi-Chi earthquake, Taiwan. Large circles are the calculated stress inversion maxima, diamonds are the solutions from Blenkinsop (2006). Red =  $\sigma_1$ , green =  $\sigma_2$ , blue =  $\sigma_3$ . Color gradients are linear from transparent white (A) to opaque color. Contours are 10 multiples of uniform density on the best 1000 solutions out of approximately 28 million. The data were orthonormalized prior to analysis. (a) Unweighted stress inversion results. (b) Weighted stress inversion results.

## 9.7 Moment Triangle Plot

Beachball and other moment tensor based plots are useful for the display of slickenside or kinematic data and earthquake focal plane solutions, but it may be desirable to display the data on a plot that summarizes each moment tensor sense (reverse, normal, or strike-slip) as a single point. One such plot, used to display focal mechanism solutions, is a triangle diagram (Apperson and Frohlich, 1988; Frohlich, 1992). To distinguish it from other triangular diagrams, it is referred to here as a *moment tensor triangle plot*, or *moment triangle plot*.

The three orthogonal moment tensor axes are referred to here as  $M$ ,  $P$ , and  $T$  axes (in seismology, the  $M$  axis is referred to as  $B$  or  $N$ , null, axis). The plunges,  $\phi$ , of these axes, satisfy the identity

$$\sin^2 \phi_M + \sin^2 \phi_P + \sin^2 \phi_T = 1 \quad (9.12)$$

As the plunges vary only from  $0^\circ$  to  $90^\circ$ , this equation defines a quarter-hemisphere. It can be projected onto a triangle using the azimuthal gnomonic projection, which forms the basis of a triangular diagram plotted using barycenter coordinates. The triangular diagram's upper vertex, labeled  $S$  for strike-slip, is where  $\phi_M = 90^\circ$ . The bottom left vertex, labeled  $N$  for normal, is where  $\phi_P = 90^\circ$ , and the bottom right vertex, labeled  $R$  for reverse (or thrust), is where  $\phi_T = 90^\circ$ . The plot center is where each plunge is  $35.26^\circ$ .

Focal mechanism categories can be drawn on the plot as follows: strike-slip for  $\phi_M > 60^\circ$ , thrust for  $\phi_P > 60^\circ$ , normal for  $\phi_T > 60^\circ$ , and hybrid for all other cases. This convention follows Okal (2011), a slightly different convention is given by Frohlich (1992).

Figure 9.8a is a moment triangle plot of a sample of 38 normal faults, from Angelier (1979). In this data set, seven faults are classified as hybrid, the rest are classified as normal. Figure 9.8b is a similar plot of 1465 *Centroid Moment Tensor* (CMT, Section 2.7.2) mechanisms for earthquakes along the southern Mid-Atlantic Ridge between  $55^{\circ}S$  and  $16^{\circ}N$ , and  $55^{\circ}W$  and  $0^{\circ}E$ . In this case, two main clusters are apparent, representing normal faults associated with ridge segments and strike-slip faults associated with transform segments. See Figure 1 in Frohlich (1992) for comparison, and Figure 2.9 for spherical projections of the data. The data is in the example file `Seismology / CMT jan76_dec17 SMAR.tsv`, and is a subset of data selected from `jan76_dec17.ndk` (Section 2.7.2), from the Global Centroid Moment Tensor Project (Dziewonski et al., 1981; Ekström et al., 2012, [www.globalcmt.org](http://www.globalcmt.org)). The CMT data is given as the strikes, dips, and rakes of the two focal mechanism nodal planes, so the focal mechanism slip lines must be calculated using the *Data - Calculate Lines* from *Rake* command.

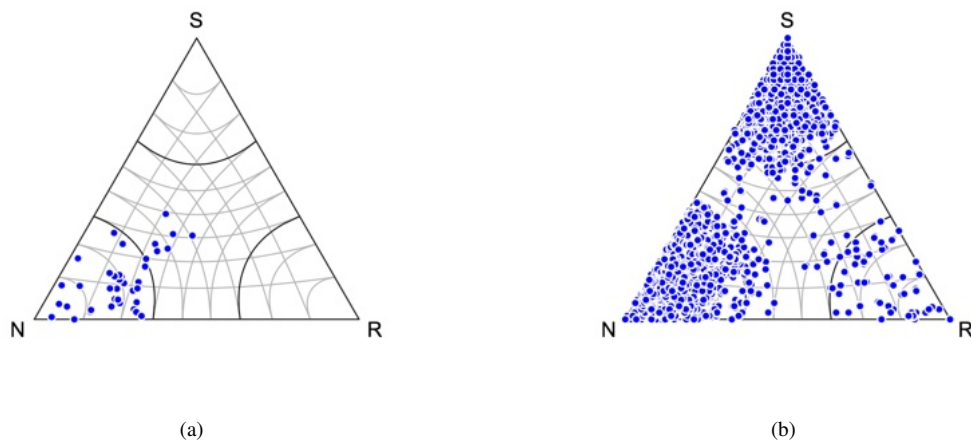


Figure 9.8: Examples of moment triangle plots. Four focal mechanism categories are drawn as described in the text. (a) 38 Neogene normal faults from central Crete, Greece. Seven of the faults are categorized as hybrid, the remainder are categorized as normal. Data from Angelier (1979). (b) 1465 CMT mechanisms for earthquakes along the southern Mid-Atlantic Ridge between  $55^{\circ}S$  and  $16^{\circ}N$ , and  $55^{\circ}W$  and  $0^{\circ}E$ . The plot shows the dominance of focal mechanisms associated with ridges (normal) and transform faults (strike-slip). See Figure 1 in Frohlich (1992) for comparison, and Figure 2.9 for spherical projections of the data. Data from CMT Project.

Figure 9.9a is a moment triangle plot of 1010 CMT nodal planes for intermediate depth earthquakes (100 to 300 km) from the Tonga-Kermadec subduction zone, with epicenters between  $16^{\circ}S$  and  $28^{\circ}S$ , and  $175^{\circ}E$  and  $170^{\circ}W$ . The subducted slab here has an approximate strike of  $200^{\circ}$  and dip of  $55^{\circ}$ , and can therefore be rotated to a vertical reference frame by a rotation of  $20^{\circ}$  about the vertical ( $Z$ ) axis, followed by a  $-35^{\circ}$  rotation about the north ( $Y$ ) axis (Section 5.5). Figure 9.9b shows the data after these two rotations, which allows faults associated with slab extension to be better identified. See Figure 5 in Frohlich (1992) for comparison, and Figure 2.10 for spherical projections of the data.

Note that after the two rotations, the *Rake* and *Sense* values are invalid, because the plane strikes, used as a reference line, have changed. Use the *Data - Calculate Lines* command with the *Orthonormalize* option to recalculate the rakes and slip senses if desired.

The Tonga-Kermadec data is in the example data file `CMT jan76_dec17 TK.tsv`. Both this file and file `CMT jan76_dec17 SMAR.tsv`, were created by opening `jan76_dec17.ndk` from the CMT Project (Section 2.7.2), and deleting focal mechanisms outside the desired range.

Note that when selecting a symbol for a moment triangle plot, any element ( $S$ ,  $L$ ,  $M$ ,  $P$ , or  $T$ ; Section 9.4) can be used to plot a symbol, as all are summarized by a single point on the plot. Therefore only one of the elements, such as  $L$ , should be set visible. Additionally, if the data are nodal planes, each of the two nodal planes plots at the same point, because their  $M$ ,  $P$ , and  $T$  axes are identical. If the data has been imported from a CMT file, the first nodal plane is identified as *Domain* = 1, and the second as *Domain* = 2, it is sufficient to plot only one of the two, such as  $L.D1$ .

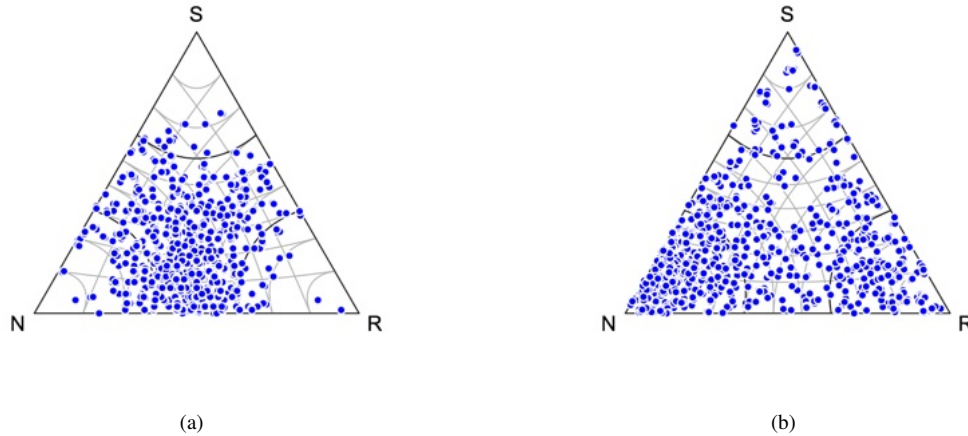


Figure 9.9: Moment triangle plots for 1010 CMT solutions for intermediate depth earthquakes (100 to 300 km) from the Tonga-Kermadec subduction zone, epicenters between  $16^{\circ}S$  and  $28^{\circ}S$ , and  $175^{\circ}E$  and  $170^{\circ}W$ . See Figure 5 in Frohlich (1992) for comparison, and Figure 2.10 for spherical projections of the data. (a) Plot of nodal plane data in unrotated local coordinates. (b) Plot of the data rotated  $20^{\circ}$  about the vertical ( $Z$ ) axis, followed by a rotation of  $-35^{\circ}$  about the north ( $Y$ ) axis (Section 5.5). This places the slab in an approximately vertical reference frame, in which faults associated with slab extension can be better identified.

Contouring the moment triangle plot is done by kernel density estimation (KDE). This topic is discussed more fully in Section 14.3. The contouring is done using multivariate kernel density estimation, a technique related to determining the optimal bin width of a histogram (Silverman, 1986). An estimate at each location, or node, is the sum of the kernel estimates about each data point using the standard normal function.

Several parameters are available to modify the contours, the *Smoothing* option is an additional smoothing factor, the default is 1.0. The *Levels* option sets the number of contour levels of the probability estimate, 10 gives contour levels at 10%, 5 gives levels at 20%. The *Nodes* option sets the number of horizontal and vertical nodes at which the density estimate is calculated. If the *Weighting* option is selected, the value in the *Weight* column is used to weight each data tensor.

Figure 9.10a is a moment tensor triangle plot of the Angelier (1979) data with 5 contour levels, or 20%, of the density range, and a linear RGB color gradient from opaque white to red. The kernel density estimate uses Silverman's rule of thumb to estimate the bandwidth (Section 14.3, Eq 14.4).

The contour lines on the plot created using the default settings (Figure 9.10a) are closely constrained by individual data points, suggesting the default estimated bandwidth using Silverman's rule of thumb under-smooths the density estimate. A subjective increase in smoothing can be applied to reduce this effect. In this case a value of the *Smoothing* parameter equal to 2.0 reduces the tendency for individual data points to effect the density estimate. This value was selected as the smallest that effectively eliminates curvature of the contours around individual data points. Figure 9.10b uses a smoothing value of 2.0, and 5 contour lines equally spaced over the density estimate.

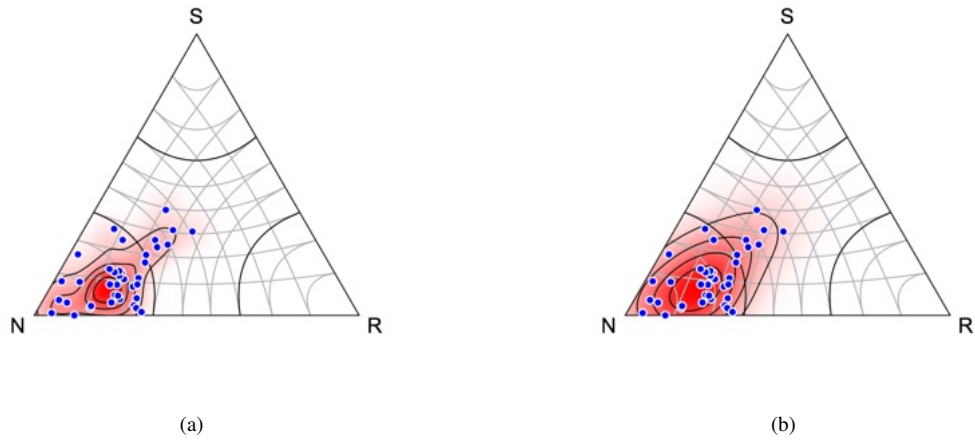


Figure 9.10: Contoured moment tensor triangle plots of the Angelier (1979) fault data, with a linear RGB color gradient from opaque white to red. (a) Plot with 5 contour levels (20%) and no additional smoothing. (b) Plot an additional smoothing of 2.0. The smoothing value was selected as the smallest that effectively eliminates curvature of the contours around individual data points.



## 10 Frames

The statistical analysis of directional data, that is, the orientations of unit axes, vectors, and poles to planes, is of fundamental interest in many disciplines in the sciences (Fisher et al., 1987; Mardia and Jupp, 2000). It is, however, a subset of the more general topic of orientation analysis where orientations specify the complete orientation of objects in three or higher dimensional coordinate systems (Downs, 1972; Mardia and Jupp, 2000; Davis and Titus, 2017).

A type of data of particular importance in geology, are *line in plane* data. These include deformed metamorphic rocks with both lineations and foliations (LS tectonites), fold axial planes with their included axes, and slickenside (fault) surfaces that contain lineations parallel to displacement directions. While the latter are *ray in plane* data, they are commonly converted into kinematic axes (Section 9.3), which are line in plane data. Line and plane data are commonly treated as two independent samples (Section 9.4), however this ignores the fact that the lines and planes are linked, and form orthonormal frames, rather than independent axes. One option is to force orthogonality using a linked orientation matrix (Eq 9.1), however a more rigorous solution is to use undirected orthonormal frames.

This section covers basic orientation statistics of undirected orthonormal frames, and gives specific examples of their practical use in the analysis of LS tectonites and kinematic indicators. The term *orthonormal frame* (Mardia and Jupp, 2000, p. 285), or simply *frame*, refers to three orthogonal unit vectors associated with an object, whose orientation can be defined as a rotation with respect to external Cartesian reference axes. In the present context of line in plane data, the term *frame* is used for undirected orthonormal frames.

The statistical analysis of more general orientations, for example crystallographic orientations, is treated by software such as the orilib C function library (Quey, 2014), the MTEX MATLAB toolbox (Mainprice et al., 2015), and the geologyGeometry library of R scripts (Davis, 2019). The latter includes a series of tutorials with geologic applications.

Weighting of data points is not supported for frame calculations as they require the use of minimization procedures that randomly select data frames. For similar reasons, bootstrap confidence calculations can be time consuming for larger sample sizes or large numbers of resamples. The default 1000 resamples is reasonable, but may be increased to 10,000 for final plots, as was done for the examples in this section. With more than 1000 resamples the plot will not update the bootstrap symbols while the plot is being dragged by the mouse.

### 10.1 Rotation Matrices

There are multiple conventions for expressing the orientations of orthonormal frames, including Euler angles, rotation matrices, angle-axis, and quaternions (Quey, 2014). However, a common convention is to use rotation matrices that can be applied to a frame to align it with external reference axes.

Consider a plane described by the unit pole  $s$  with the contained line  $l$ . If the data point has been carefully measured, these axes will be perpendicular, however the data can be orthonormalized to fix small errors if required (Section 9.2). The third axis,  $m$ , is then the vector cross product

$$m = s \times l \tag{10.1}$$

which will be a unit axis perpendicular to  $s$  and  $l$ . If  $s$  and  $l$  are unit vectors instead of axes,  $m$  will be directed to form a directed right handed frame. The rotation matrix that will rotate the data frame to the coordinate axes  $[XYZ] = [123]$  is

$$R_f = \begin{bmatrix} s_1 & s_2 & s_3 \\ l_1 & l_2 & l_3 \\ m_1 & m_2 & m_3 \end{bmatrix} \tag{10.2}$$

This rotation matrix is a *special orthogonal matrix*, and is also known as an *orientation matrix*. The term *orientation matrix*, however, is also used for the matrix used to quantify the scatter in a sample

of axes (Eq 4.6) (Fisher et al., 1987, p. 33). To differentiate these two, the term *rotation matrix* is used here.

Rotation matrices can be constructed for all  $n$  line in plane data points, to form the matrices  $R_{f_i} = [R_{f_1} \dots R_{f_n}]$ . In order to quantify this set of matrices, it is necessary to find a measure of their mean and variance. Unfortunately, the mean rotation matrix can not be found using a simple arithmetic average, instead the mean can be defined as the rotation matrix that minimizes the variance. The *Fréchet variance* (Davis and Titus, 2017, Appendix C.2) for a sample of rotation matrices,  $R_{f_i}$ , about a rotation  $R_f$  is

$$\psi(R_f) = \frac{1}{2n} \sum_{i=1}^n d(R_f, R_{f_i})^2 \quad (10.3)$$

where the function  $d$  is the angular distance between two rotations  $Q_f$  and  $R_f$

$$d(Q_f, R_f) = \arccos \frac{1}{2} (\text{tr} R_f Q_f^T - 1) \quad (10.4)$$

The mean,  $\bar{R}_f$ , is then the frame  $R_f$  which has the minimum variance (Eq 10.3) for the sample  $R_{f_i}$ , found by systematically varying  $R_f$  using a minimization procedure.

To complicate the mean calculation, the symmetry of the frame must also be considered. For example, the angle between two vectors (rays) can be determined from their scalar dot product. The angle between two undirected axes (lines), however, requires choosing the smaller of two possible angles. Extending this to a frame of three orthogonal undirected axes, symmetry results in four separate rotation matrices that all rotate the data frame to the coordinate frame, so the minimum distance,  $d$  (Eq 10.4), must be selected from four rotation matrices.

Bootstrapping can be done to calculate confidence regions about the mean, similar to the technique used in Section 6.3. In this case, however, the sample of rotation matrices,  $R_{f_i}$ , is randomly resampled with replacement  $m$  times. The resample means,  $\bar{S}_{f_j}$ , where  $j = [1 \dots m]$ , are calculated for each resample.

If  $\bar{S}_{f_j}$  are tightly clustered, *principal geodesic analysis* can be done about  $\bar{R}_f$  to obtain a covariance matrix on a three-dimensional tangent space (Davis and Titus, 2017, Appendix C.2). The eigenvectors of the covariance matrix give three axes of an ellipsoidal confidence region, and their lengths, the square roots of the eigenvalues, which are analogous to standard deviations. This analysis is only valid for tightly clustered data, so  $\bar{S}_{f_j}$  should be examined on a rotation plot to verify this.

The resample means,  $\bar{S}_{f_j}$ , are best visualized in three-dimensional rotation plots (Section 10.2). While these plots should be utilized as part of standard data analysis, it is also desirable to have a representation on a spherical projection. Such confidence regions can be calculated from  $\bar{S}_{f_j}$  by calculating the covariance about each axis (row) of the sample mean,  $\bar{R}_f$ , on a spherical tangent plane. The eigenvectors of the covariance matrix are scaled for the confidence level to give an elliptical confidence region (Figure 10.3).

## 10.2 Rotation Plots

Visualization of data samples characterized by rotations is not readily done on two-dimensional plots, such as spherical projections. Three-dimensional plots have been developed to display rotation data, but require an additional projection into two-dimensions for printed images. This section covers three plots that can be used to interactively view rotation data distributions and bootstrap confidence clouds.

Rotations can be expressed in angle-axis form, a rotation angle,  $\alpha$ , about a directed axis,  $u = [u_1, u_2, u_3]^T$ . This form can be converted into an equivalent rotation matrix,  $R_f$ . Given the matrix  $U_f$

$$U_f = \begin{bmatrix} 0 & -u_3 & u_2 \\ u_3 & 0 & -u_1 \\ -u_2 & u_1 & 0 \end{bmatrix} \quad (10.5)$$

Then

$$R_f = I + (\sin \alpha)U_f + (1 - \cos \alpha)U_f^2 \quad (10.6)$$

The inverse conversion, from a rotation matrix to an angle-axis form, is

$$\begin{aligned} \alpha &= \arccos((\text{tr}R_f - 1)/2) \\ U_f &= (2 \sin \alpha)^{-1}(R_f - R_f^T) \end{aligned} \quad (10.7)$$

with  $u$  then extracted from  $U_f$  (Davis and Titus, 2017, Appendix A.2).

The angle-axis form readily allows the construction of a three-dimensional *angle-axis* plot. The axis,  $u$ , defines a direction in Cartesian  $X, Y, Z$  space, and the angle,  $\alpha$ , varies from 0 to  $180^\circ$  (0 to  $\pi$  radians). Therefore a rotation can be represented as a ray emanating from the origin, and all possible rotations form a spherical volume with a radius of  $180^\circ$ .

Analogous to spherical azimuthal projections, it is possible to modify the properties of the rotation plot by selecting a different function specify the radial distance,  $\rho$ , from the center of the plot. For the *angle-axis* plot  $\rho = \alpha$ . This is analogous to the *equidistant* spherical projection (Section 4.5). Selecting

$$\rho = \tan(\alpha/4) \quad (10.8)$$

produces the *equal-angle* rotation plot, which is analogous to the *stereographic* or *equal-angle* spherical plot (Section 4.3). This plot should be used when it is important to preserve the angular relationships among data frames. Finally, selecting

$$\rho = \left( \frac{3}{4\pi^2}(\alpha - \sin \alpha) \right)^{1/3} \quad (10.9)$$

produces the *equal-volume* or *homochoric* rotation plot. It is analogous to the *equal-area* spherical plot (Section 4.4) and should be used when it is desirable to preserve the density distribution of the data.

Rotation plots are displayed as a spherical volumes, or *balls*, that can be interactively rotated, with data points in the volume decreasing in opacity with distance from the viewer. On each of these plots, points in clusters near the spherical surface at  $\pi$  radians may include diametrically opposed points because  $(\pi, u) = (\pi, -u)$ . The default view is an isometric projection of the sphere, with the  $X, Y, Z$  axes equally foreshortened, and positive axes towards the viewer.

### 10.3 LS Tectonites

The fabrics of rocks within ductile shear zones and their relationship to deformation have been the subject of intensive study for decades (Turner and Weiss, 1963; Ramsay, 1967, 1980; Fossen and Cavalcante, 2017). The deformed rocks within these zones are commonly characterized by a fabric that has a foliation with an included lineation, and are referred to as *LS tectonites*. Such fabrics are often related to finite strain, with the lineation parallel to the maximum finite strain axis (a *stretching lineation*), and the foliation perpendicular to the minimum finite strain axis, however the relationship between fabric and deformation is complex, especially when considering vorticity, non-plane deformation, and rigid clasts (Giorgis et al., 2016; Fossen and Cavalcante, 2017). If sense of shear indicators are present, it may be possible to use the kinematic methods discussed in Section 10.4. In all cases, it is important to clearly state the assumptions made for any interpretation of field data, and to consider alternative models.

The example here uses lineation and foliation data from the Western Idaho Shear Zone (WISZ), from Giorgis and Tikoff (2004). These fabrics were corrected for Miocene to recent extension, giving nearly vertical foliations, parallel to the shear zone boundaries, and steep lineations. Figure 10.1a is a Schmidt plot of the WISZ data in their corrected orientations, after being orthonormalized, with the

calculated mean frame orientations,  $\bar{R}_f$ . Figure 10.1b is the plot rotated to better display the calculated mean frame axes, with rays extending from the mean axes to the center.

Figure 10.2a shows the means of 10,000 resampled data frames superimposed on the data and  $\bar{R}_f$ . Large data samples or large numbers of resamples may require lengthy calculations, although only a few seconds were required in this example. It is recommended that the default value of 1000 be used except for final plots. Figure 10.2a shows the 95% confidence ellipses calculated from the covariance of the projected mean frame axes.

Figure 10.3a superimposes the mean maximum eigenvectors and 95% confidence ellipses for the data treated as independent axes instead of frames (black), illustrating the difference between the two solutions. Figure 10.3b is a rotated view that better illustrates the frame axes compared to the maximum eigenvectors axes. For this data set the difference is relatively small.

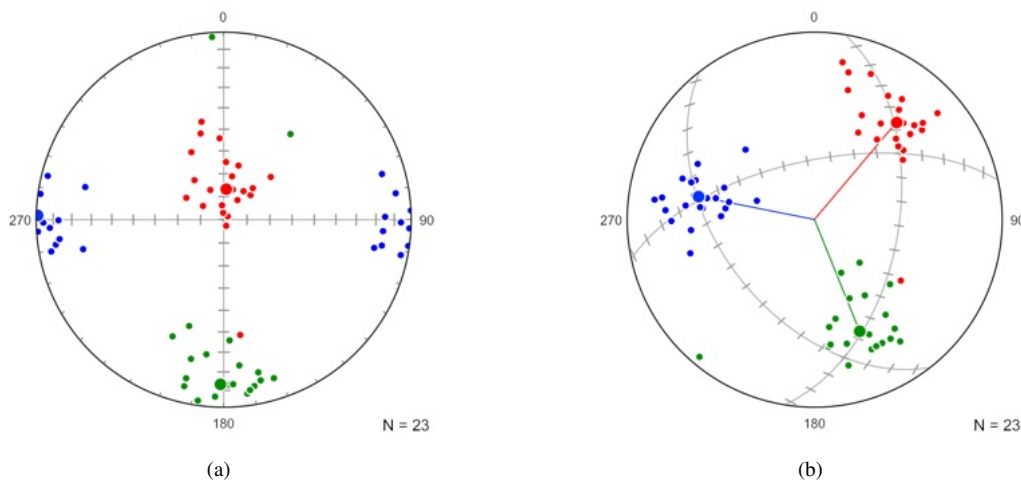


Figure 10.1: Schmidt plots of 23 foliation-lineation pairs from the Western Idaho Shear Zone (WISZ) corrected for Miocene to recent extension (Giorgis and Tikoff, 2004) with the mean orientation frame,  $\bar{R}_f$  (large symbols). Blue = foliation poles ( $s_i$ ), red = lineations ( $l_i$ ), green =  $m_i$  ( $s_i \times l_i$ ). Data were orthonormalized prior to analysis. (a) Plot of data in their corrected orientations with mean frame,  $\bar{R}_f$ . (b) Plot rotated to better display the calculated mean frame axes.

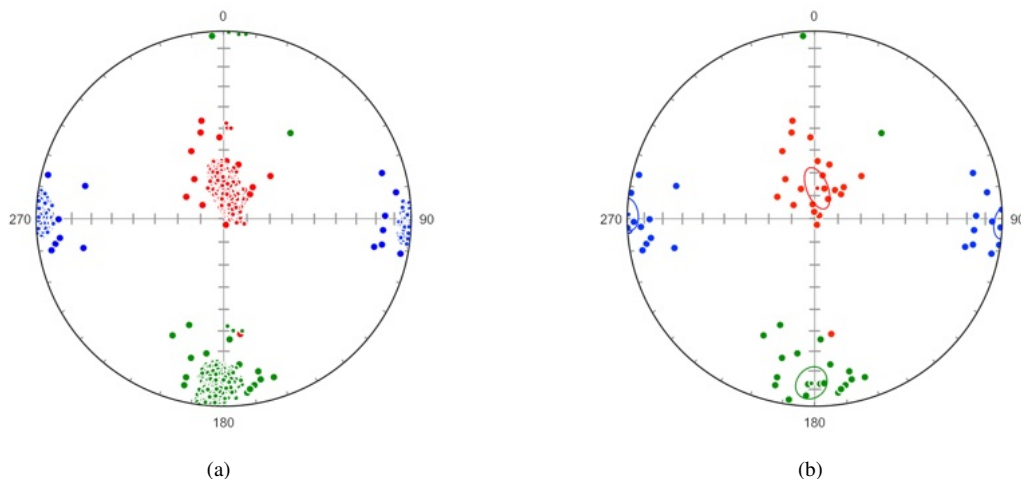


Figure 10.2: Schmidt plots of the WISZ data as in Figure 10.1a, with bootstrap analysis using 10,000 bootstrap resample means of the orientation frames. (a) Plot showing the resample means (small black circles). (b) Plot of 95% confidence ellipses calculated from the resample means.

The following is the log output for the WISZ data

2021-01-24 13:37:51

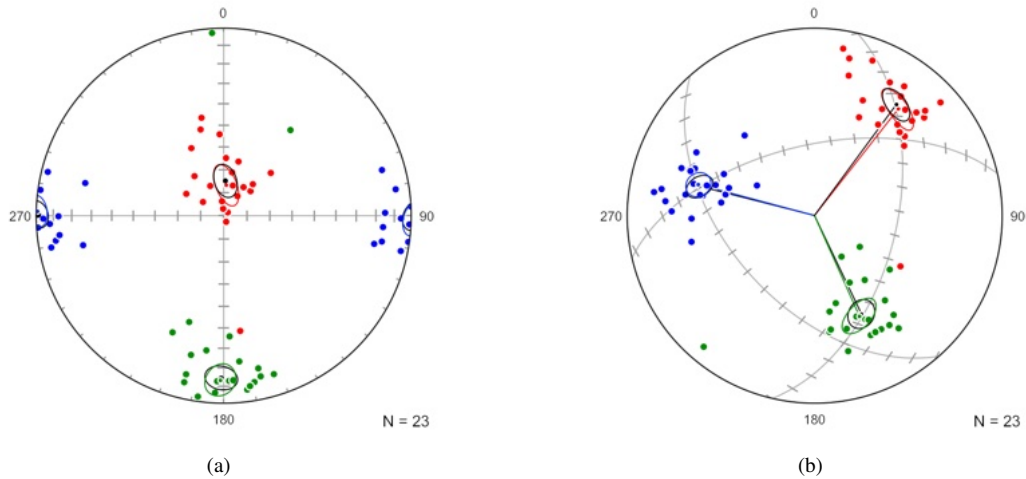


Figure 10.3: Schmidt plots of the WISZ data as in Figure 10.2b, with means and confidence cones (black) about the maximum eigenvectors of the data treated as independent axes instead of frames, illustrating the difference between the two solutions. (a) Plot of the data in their corrected orientations. (b) Plot rotated to better display the calculated mean frame axes, and the maximum eigenvector axes (black), with rays drawn to the center.

Data File : Giorgis & Tikoff 2004

Data Type : Default

Data Domain : All

N : 23

Weighted : False

=====

SL Frame Statistics

Mean rotation matrix:

0.99963589 -0.02294526 0.01419881  
 0.01907264 0.22861172 -0.97333083  
 0.01908731 0.97324724 0.22896611

Mean axes (trend, plunge)

S : 271.315 0.814  
 L : 4.769 76.738  
 M : 181.124 13.236

Bootstrap confidence:

Resamples : 10000  
 Axes (trend, plunge)  
 S : 271.308 0.832  
 L : 4.840 76.731  
 M : 181.112 13.242

95% max (angle, direction)

S : 5.965 268.908 6.295  
 L : 9.441 353.963 67.850  
 M : 8.924 179.749 22.071

95% min (angle, direction)

S : 4.655 275.577 2.693  
 L : 4.504 19.955 74.256  
 M : 5.143 186.357 13.918

Geodesic covariance:

0.00291269 0.00032776 -0.00123536

```

0.00032776 0.00556381 -0.00033869
-0.00123536 -0.00033869 0.00539459
Geodesic principal axes (sd):
4.51398476 4.15986882 2.80277269
Geodesic principal axes (95%):
12.61898952 11.62904701 7.83524116
Geodesic principal directions (dir cos)
0.33799824 0.17086925 0.92550575
0.56763159 -0.82139954 -0.05565233
-0.75070072 -0.54415669 0.37462238

```

The log output first gives the mean rotation matrix,  $\bar{R}_f$ , whose rows are the direction cosines of the mean axes for  $S, L, M$ , these are also given as the trends and plunges of the axes. These will vary a small amount from run to run, do to the minimization procedure. The bootstrap confidence section first gives the mean of the bootstrap resample means,  $\bar{S}_{f_j}$ , which should be very close to  $\bar{R}_f$ . This is followed by the confidence ellipses computed about  $\bar{R}_f$  by projecting  $\bar{S}_{f_j}$  onto a spherical tangent plane.

The last section is a principal geodesic analysis that characterizes the spread of the bootstrap means in a three-dimensional tangent space as visualized in a rotation plot. The geodesic principal axes are the lengths of the confidence ellipsoid axes in degrees, and are analogous to standard deviations. A principal geodesic analysis is only valid for tightly clustered data, so this should be confirmed on a rotation plot.

Although it may not be immediately obvious how rotation plots relate to the orientations of data frames measured in the field, they provide a better visualization of the data distributions than spherical projections. Ideally, the distributions are viewed in interactive three-dimensional plots, which are difficult to show in printed figures. Figure 10.4a is an *axis-angle* (equidistant) rotation plot of the WISZ data, where the rotations angles plot as the radial distance from the center of the sphere.

Figure 10.4b is an *equal-angle* rotation plot of the same data, where the angular relationships among data are preserved. Figure 10.5a in *equal-volume* rotation plot, which preserves the density distribution of the data, shown in Figure 10.5b with an outlier selected, illustrating that, due to frame symmetry, each data frame plots as four equivalent positions within the sphere. Each of these plots show four clusters, two of which include diametrically opposed points because  $\alpha_i$  in the cluster are close to  $180^\circ$  ( $\pi$  radians).

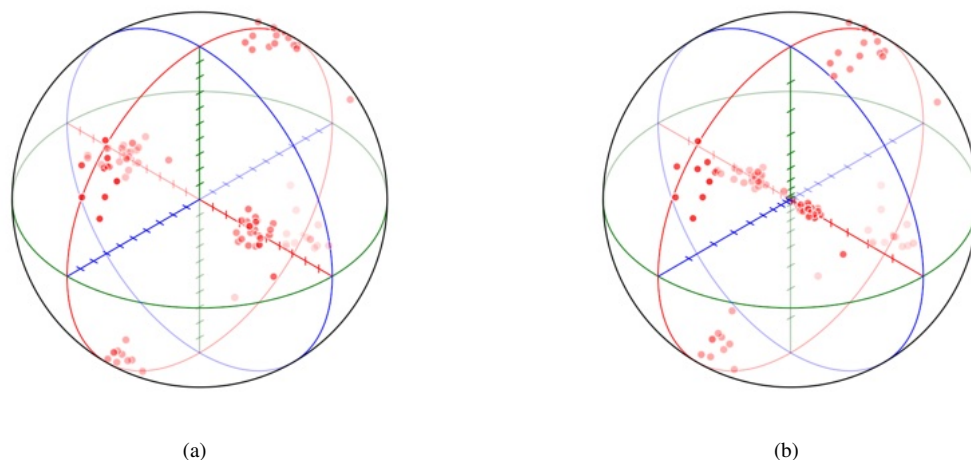


Figure 10.4: Rotation plots of 23 foliation-lineation pairs from the orthonormalized WISZ data. The plots show four clusters, two of which include diametrically opposed points because  $\alpha_i$  in the cluster are close to  $180^\circ$  ( $\pi$  radians). (a) *Axis-angle* (equidistant) rotation plot, where the rotations angles plot as the radial distance from the center of the sphere. (b) *Equal-angle* rotation plot, which preserves angular relationships among the data.

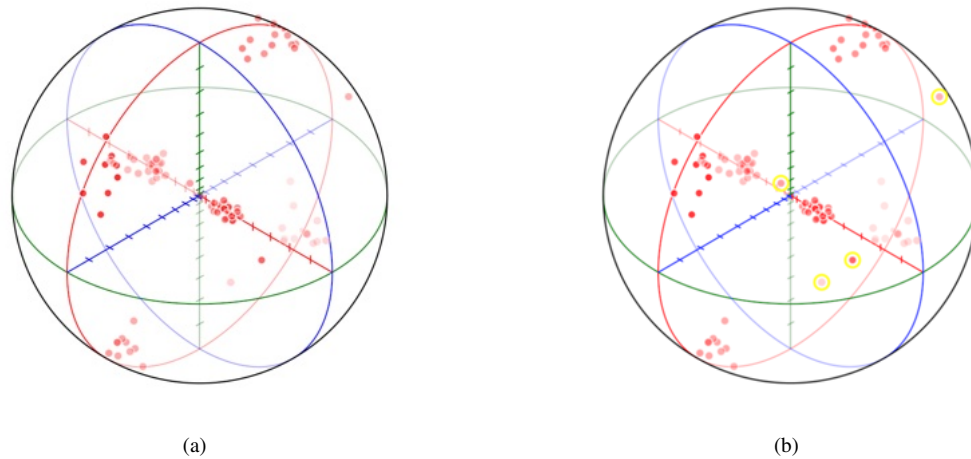


Figure 10.5: *Equal-volume* rotation plots of 23 foliation-lineation pairs from the orthonormalized WISZ data, which preserve the density distribution of the data. The plots show four clusters, two of which include diametrically opposed points because  $\alpha_i$  in the cluster are close to  $\pi$  radians. (a) Plot of the data frames. (b) Plot with an outlier selected.

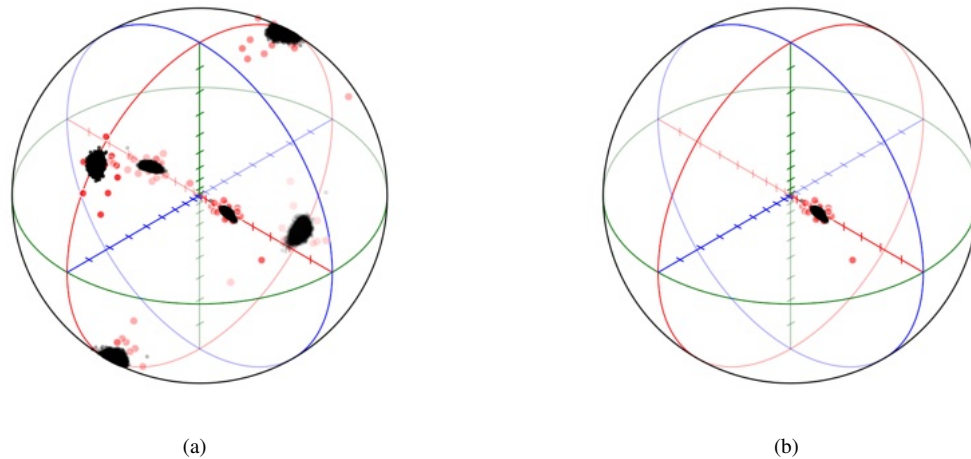


Figure 10.6: Equal-volume rotation plot of the WISZ data showing the data frames (red) and the means of 10,000 bootstrap resamples (black). (a) Plot of all four symmetry groups. There are four equivalent points within the sphere due to the frame symmetry. The two clouds near the surface of the sphere, at  $\pi$  radians, include points near the negative mean axis because  $(\pi, u) = (\pi, -u)$  (b) Plot of the symmetry group closest to the plot origin, which has the minimum rotation angle. The bootstrap resample means form a compact cloud, suggesting that principal geodesic analysis is valid.

## 10.4 Kinematics

Fault data are ray in plane data, however they are commonly transformed into line in plane data by determining  $P$  and  $T$  axes (Section 9.3). Commonly these  $P$  and  $T$  axes are treated as independent data samples, for example by calculating their moment tensors (Section 9.4, Eq 4.6). However this ignores the fact that they are linked to form an orthonormal frame, and are not independent axes.

Consider a fault plane described by the directed unit pole  $s$  with the contained directed lineation, or ray,  $l$ . Care must be taken to use a consistent convention for the fault plane pole, especially for vertical faults (Section 9.1). If the data has been carefully measured, these axes will be perpendicular, however the data can be orthonormalized to fix small errors if required (Section 9.2).

The third axis,  $m$ , is then the vector cross product

$$m = s \times l \quad (10.10)$$

which will be directed to form a directed right handed frame. A rotation matrix for a  $-45^\circ$  rotation of  $l$  about  $m$  then gives  $p$ , and a  $+45^\circ$  rotation gives  $t$  (Figure 9.1. The rotation matrix that will rotate the data frame to the coordinate axes  $(1, 2, 3) = (X, Y, Z)$  is

$$R = \begin{bmatrix} p_1 & p_2 & p_3 \\ t_1 & t_2 & t_3 \\ m_1 & m_2 & m_3 \end{bmatrix} \quad (10.11)$$

The analysis can then proceed in a similar fashion to that used for LS tectonites (Section 10.3). The mean frame axes are calculated, and confidence ellipses found by bootstrapping the sample.

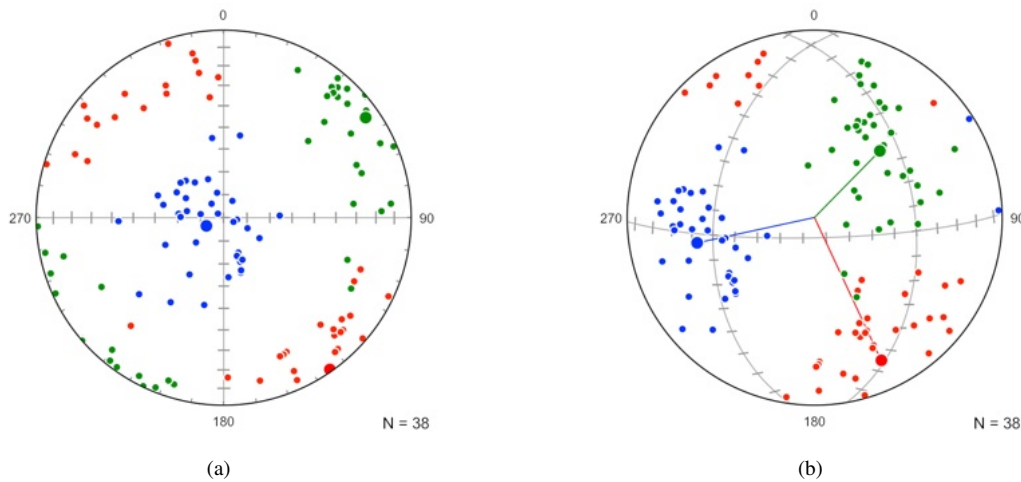


Figure 10.7: Schmidt plots of 38 P-T axis pairs of normal faults from Crete, Greece (Angelier, 1979) with the mean orientation frame,  $\bar{R}$  (large circles). Blue = P axes ( $p_i$ ), red = T axes ( $t_i$ ), green =  $m_i$  ( $p_i \times t_i$ ). Data were orthonormalized prior to analysis. (a) Plot of data with mean frame  $\bar{R}$ . (b) Plot rotated to better display the calculated mean frame axes.

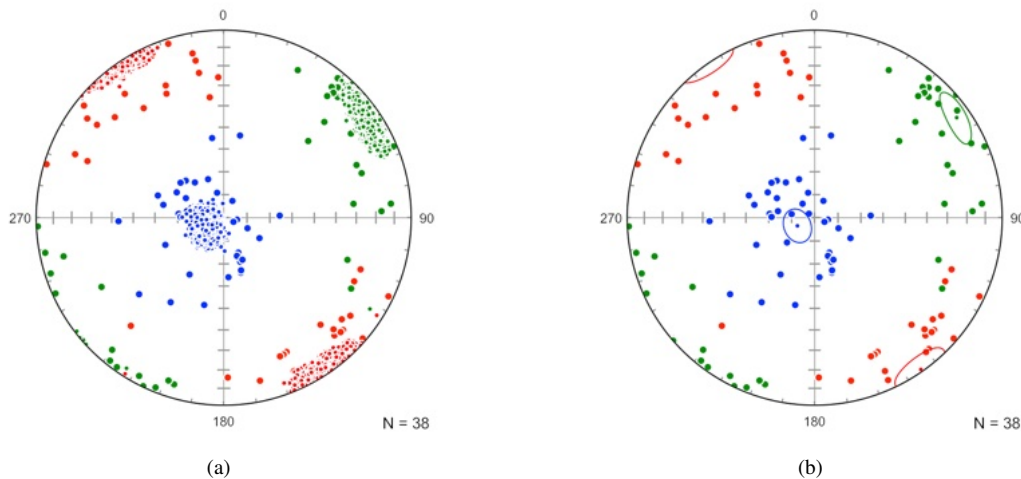


Figure 10.8: Schmidt plots of the normal fault data as in Figure 10.7a, with 10,000 bootstrap resample means of the data sample frames. Each resample mean gives three axes, which are used to calculate confidence regions about the axes. (a) Plot showing resample means (small filled circles). (b) Plot of 95% confidence ellipses calculated from the sample means.

The following is the log output for the normal fault data

```
2021-01-24 13:56:16
Data File : Angelier 1979
Data Type : SL
Data Domain : All
```



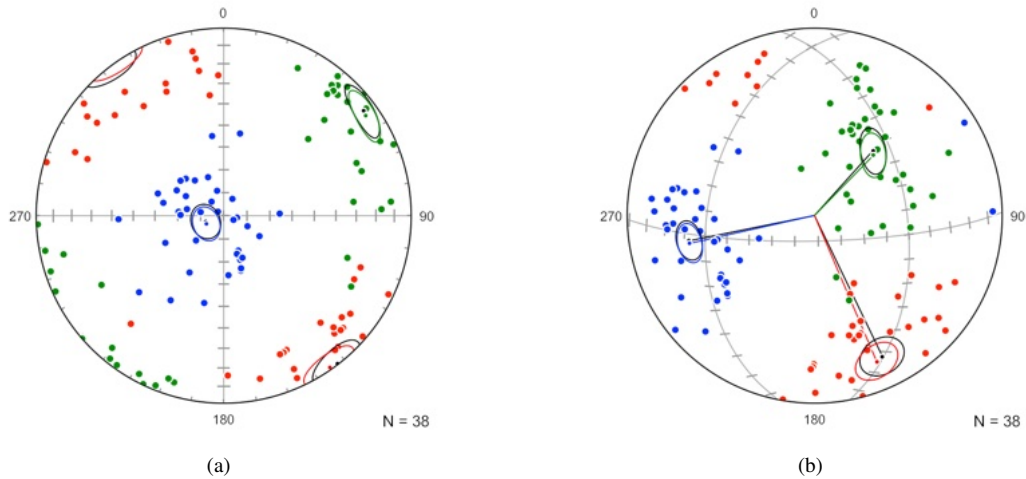


Figure 10.9: Schmidt plots of the normal fault data as in Figure 10.8b, with means and confidence cones (black) about the maximum eigenvectors of the data treated as independent axes instead of frames, illustrating the difference between the two solutions. (a) Plot of the data in their corrected orientations. (b) Plot rotated to better display the calculated mean frame axes, and the maximum eigenvector axes (black).

N : 38

Weighted : False

=====

PT Frame Statistics

Mean rotation matrix:

0.13012508 0.06169274 0.98957641  
 -0.57305276 0.81915856 0.02428555  
 -0.80912175 -0.57023965 0.14194627

Mean axes (trend, plunge)

P : 244.634 81.720  
 T : 145.025 1.392  
 M : 54.825 8.160

Bootstrap confidence:

Resamples : 10000

Axes (trend, plunge)

P : 244.715 81.737  
 T : 144.987 1.406  
 M : 54.786 8.141

95% max (angle, direction)

P : 7.488 288.875 79.243  
 T : 9.302 135.801 2.915  
 M : 9.578 64.059 10.995

95% min (angle, direction)

P : 5.874 246.316 75.871  
 T : 7.424 146.222 8.727  
 M : 5.522 56.498 2.888

Geodesic covariance:

0.00460701 0.00085555 0.00004267  
 0.00085555 0.00720295 -0.00024443  
 0.00004267 -0.00024443 0.00621614

Geodesic principal axes (sd):

```

4.96132270 4.50574567 3.77620666
Geodesic principal axes (95%):
13.86953712 12.59595688 10.55650713
Geodesic principal directions (dir cos)
0.27726065 0.10622109 0.95490503
0.94544686 0.14677128 -0.29084088
-0.17104607 0.98345070 -0.05973249

```

The log output first gives the mean rotation matrix,  $\bar{R}_f$ , whose rows are the direction cosines of the mean axes for  $P$ ,  $T$ ,  $M$ , these are also given as the trends and plunges of the axes. These will vary a small amount from run to run, due to the minimization procedure. The bootstrap confidence section first gives the mean of the bootstrap resample means,  $\bar{S}_{f_j}$ , which should be very close to  $\bar{R}_f$ . This is followed by the confidence ellipses computed about  $\bar{R}_f$  by projecting  $\bar{S}_{f_j}$  onto a spherical tangent plane.

The last section is a principal geodesic analysis that characterizes the spread of the bootstrap means in a three-dimensional tangent space as visualized in a rotation plot. The geodesic principal axes are the lengths of the confidence ellipsoid axes in degrees, and are analogous to standard deviations. A principal geodesic analysis is only valid for tightly clustered data, so this should be confirmed on a rotation plot.

As with the LS tectonite data (Section 10.3, the kinematic data frames can be plotted on rotation plots to provide a better visualization of the data distributions than is possible on spherical projections. Ideally the distributions are viewed on interactive three-dimensional plots, which are difficult to show in printed figures. Figure 10.10a is an *equal-volume* rotation plot of the normal fault data in the default isometric view. Figure 10.10b is the same plot rotated to better visualize the four data clusters, with large red circles at the sample mean. Figure 10.11a is an equal-volume rotation plot of 10,000 bootstrap resample means, with a small red circle at the sample mean. Figure 10.11b is the same plot rotated to better visualize the four clouds.

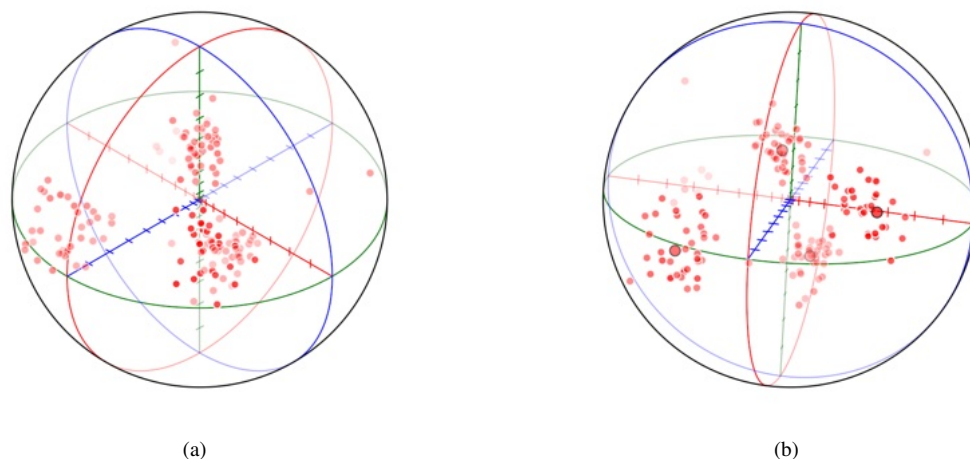


Figure 10.10: Equal-volume rotation plots of the normal fault data. (a) Plot of data in the default isometric view. The data forms four clusters on the plot, two appear to overlap but can be distinguished by the opacity of the points, which decreases with distance from the viewer. (b) Plot rotated to better display the four data clusters, with large red symbols at the sample mean.

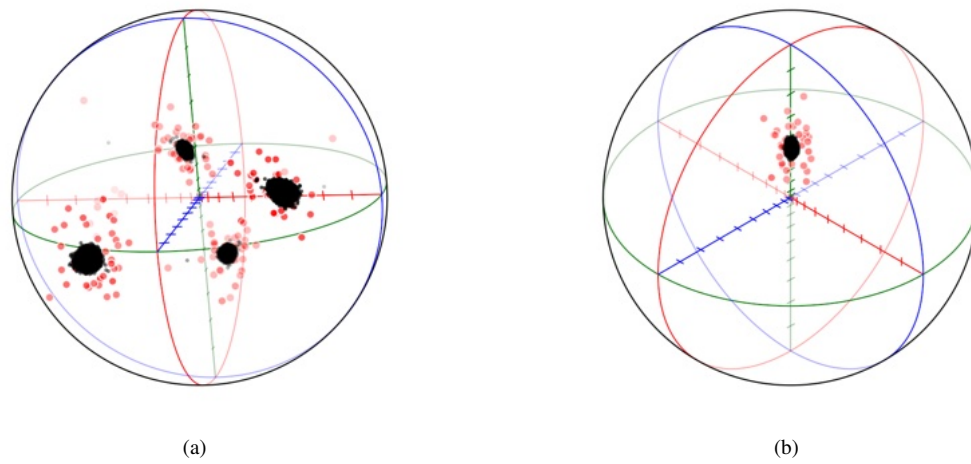


Figure 10.11: Equal-volume rotation plots of the normal fault data (red) with 10,000 bootstrap resample means (black). (a) The data and bootstrap resample means form four clouds on the plot, here rotated to display the four symmetry groups. (b) Plot of the rotation group closest to the plot center, which has the minimum rotation angle. The bootstrap resample means form a compact cloud, suggesting that principal geodesic analysis is valid.

## 11 Cluster Analysis

Many samples of directional data are multimodal, and, while contouring (Section 4.10) may be sufficient to identify modes, or “clusters“, it is desirable to use numerical techniques to objectively partition the sample into discrete clusters. A common application is geologic fracture analysis, in which the orientations of fracture or joint planes are measured, and subdivided on the basis of their orientations. This chapter discusses methods to partition such multimodal samples into clusters. The process is a form of *unsupervised learning*, in which algorithms discover hidden data groupings without human intervention.

Cluster analysis methods include *Gaussian mixture* and *k-means* models (Press et al., 2007). Gaussian mixture models assume the data are a mixture of  $k$  distributions, and the goal of the analysis is to determine their means and covariances. The k-means model was developed separately, but may be considered a simpler limiting case of the Gaussian mixture model. In this model each data point is assigned to one of the  $k$  distributions based only on the Euclidean, or other, distance from the cluster mean.

Cluster analysis of directional data may be considered to have begun with Schmidt (1925), who contoured equal-area spherical projections to visually identify modes that represent deviations from uniformity. However, numerous computational methods have been developed to objectively identify such clusters (Shanley and Mahtab, 1975, 1976; Schaeben, 1984; Klose et al., 2005; Jimenez-Rodrigueza and Sitara, 2006; Yamaji and Sato, 2011; Esmaeilzadeh and Shahriar, 2019).

Eigenvalue index maximization (Vollmer, 1990, 2022) locates a solution that maximizes the sum of eigenvalue, or vector mean, indexes for multiple clusters. This allows weighting of data points, and is implemented for axis, vector, and girdle distributions (*Axis*, *Vector*, and *Girdle* options). This is extended to line in plane data, such as kinematic data (Section 11.4), using the *Axis* or *Linked* clustering options.

Distance-based k-means analysis (Hammah and Curran, 1999; Klose et al., 2005; Jimenez-Rodrigueza and Sitara, 2006) locates cluster centers by minimizing the sum of the mean distances from the center to the nearest data points. In hard clustering (*Distance* option) the points are assigned to a cluster (0 or 1) by selecting the closest cluster center. Soft, or fuzzy, clustering (*Fuzzy* option) uses the concept of membership (0 to 1) in a cluster, so a point can belong to more than one cluster, but it is assigned to the cluster with highest membership.

A density-based approach (Ester et al., 1996; Schubert et al., 2017) applied to directional data (*Density* option) maximizes the densities of the clusters, generally giving much different results than k-means methods. Approaches not implemented here include spectral clustering (Jimenez-Rodrigueza and Sitara, 2006), and mixed Bingham (Yamaji and Sato, 2011). An example data set is used to compare the results for these different methods (Section 11.6).

Partitioning requires selecting the number of clusters, from  $k = 2 \dots 9$ . The selection of  $k$  may be based on examination of a contoured Schmidt plot, or by theoretical expectation. Methods for the evaluation of the choice of  $k$  are given in Section 11.6. Clusters are found by iterative procedures starting with random seeds, which may not converge to unique solutions for distributions that do not have distinct modes. Each cluster is identified by a *Domain* number, where 0 denotes the complete data set. The *Domain* number is also used in structural domain analysis for spatially partitioning orientation data (Section 16).

k-means clustering is a simple model that is readily applied to geologic data, which is often noisy, and does not require an assumption of the probability distribution. The assumption is that a cluster can be defined by the nearest data points, or by their membership. In contrast, Gaussian mixture models require the estimation of not only the means, but also the covariances, which means that clusters can overlap. For directional data, a Gaussian model may be extended to a Bingham distribution (Yamaji and Sato, 2011). While such distribution based models are powerful, the simpler non-parametric k-means method is suitable for most geologic data sets.

## 11.1 Axis Partitioning

Axis cluster partitioning is a common type of cluster analysis in geology, due to its practical application to fracture analysis in mining and geotechnical projects, and numerous methods have been proposed for such partitioning (Shanley and Mahtab, 1975, 1976; Schaeben, 1984; Hammah and Curran, 1999; Klose et al., 2005; Jimenez-Rodrigueza and Sitara, 2006; Yamaji and Sato, 2011; Esmaeilzadeh and Shahriar, 2019). A benchmark data set is a sample of 286 fracture surfaces measured in San Manuel copper mine, Arizona (Shanley and Mahtab, 1975, 1976), which is used here as an example.

For k-means clustering it is necessary to define what is meant by the "distance" from a data point on the sphere to a cluster center, so the point can be assigned to the nearest cluster. There are a number of possible measures of distance, including Euclidean, arc angle, and sine-based (Hammah and Curran, 1999; Jimenez-Rodrigueza and Sitara, 2006). As the orientation tensor,  $\Omega$  (Eq 4.6), is a measure of moments about three perpendicular axes, a perpendicular distance from the axis, a sine-based similarity measure seems appropriate and is used here

$$d_A(x,y) = 1 - (x \cdot y)^2 \quad (11.1)$$

where  $x \cdot y$  is the scalar, or dot, product of the two direction cosines.  $d_A$  varies from 0, when the axes are parallel, to 1, when the axis are perpendicular.

The fabric for a single cluster,  $j$ , can be quantified by its orientation tensor,  $\Omega_j$  (Eq 4.6), and the strength of its clustering by its  $P_j$  eigenvalue index (Eq 7.1). To identify multiple clusters *P-maximization* is done, where the following quantity is maximized for  $k$  clusters

$$P^* = \frac{1}{n} \sum_{j=1}^k P_j n_j \quad (11.2)$$

where  $n$  is the total number of data points, and  $n_j$  is the number of points in cluster  $j$ . This follows Vollmer (1990), maximizing the  $P$  rather than  $B$  eigenvalue index (Eq 16.2). If the values are weighted,  $n$  and  $n_j$  are replaced by the sum of the weights,  $n_w$  and  $n_{wj}$ .

P-maximization is done by initializing  $k$  random cluster axes, and assigning the data points to the nearest cluster axis. The process iteratively calculates new cluster axes, determines a  $P^*$  test value from  $\Omega_j$ , and reassigns the data to clusters. This is repeated until  $P^*$  converges to a maximum. Convergence may fail for low sample sizes, high  $k$ , or poorly defined clusters.

Figure 11.1a is a Schmidt plot of the San Manuel mine fracture data prior to cluster partitioning, Figure 11.1b is the same data after partitioning into three clusters. The selection of  $k = 3$  was made by inspection of the full contoured data set.

Figure 11.2a is a triangular fabric plot (Section 7.1) summarizing the change in fabric type following partitioning, with the three clusters plotting closer to the  $P$ , point or cluster, vertex than the total data set, shown as a white circle. Contours are 10% fabric density (Section 6.5).

Figure 11.2b compares the solutions of six clustering methods applied to the San Manuel mine data. Details of the solutions are listed in Table 11.1, which show that deviations among the six methods are relatively small. As there is no one "correct" solution among these, one must also use geologic principles to assist in selecting a reasonable solution.

Cluster	Counting (S)	Fuzzy (H)	Vector (K)	Spectral (J)	Bingham (Y)	P-max (V)
1	072/14	070/10	068/15	073/12	071/15	073/11
2	163/14	166/09	171/10	167/08	166/09	167/08
3	303/81	308/73	310/73	314/76	300/72	327/77

Table 11.1: Comparison of six axis clustering methods on the San Manuel mine fracture data given as the trend and plunge of the mean fracture normal. References: S - Shanley and Mahtab (1976), K - Klose et al. (2005), H - Hammah and Curran (1999), J - Jimenez-Rodrigueza and Sitara (2006), Y - Yamaji and Sato (2011), V - after Vollmer (1990). Compiled values from Jimenez-Rodrigueza and Sitara (2006) with the addition of mixed Bingham and P-maximization.

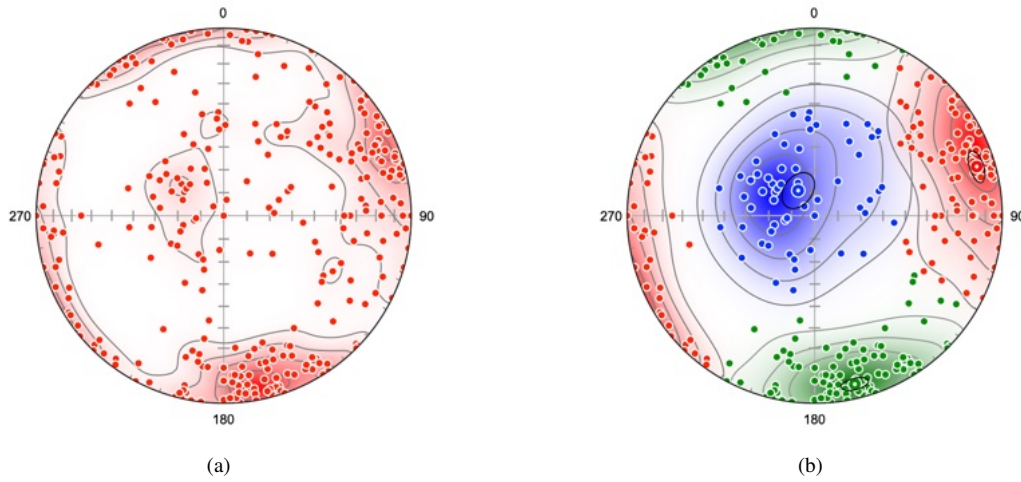


Figure 11.1: Schmidt plots of the San Manuel copper mine fracture data (Shanley and Mahtab, 1975). Contours are modified Kamb equally spaced at 20% over the density estimates. (a) Contoured plot of the data prior to partitioning. Note the presence of three modes, which were used to select three clusters,  $k = 3$ , for the analysis. (b) Plot after partitioning with  $k = 3$ . The large circles with central dots indicate the best-fit cluster axes, confidence ellipses are 95% bootstrap.

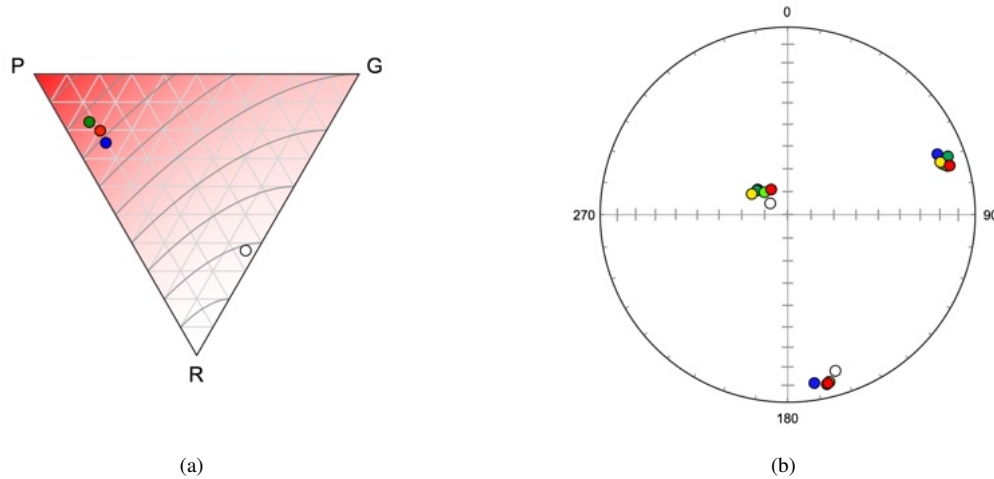


Figure 11.2: (a) A triangular fabric plot (Section 7.1) summarizing the change in fabric type following partitioning of the San Manuel mine fracture data, with the three domains plotting closer to the  $P$ , point or cluster, vertex than the total data set, shown as a white circle. Contours are fabric density (Section 6.5). Symbol colors are the same as the cluster colors in Figure 11.1b. (b) Comparison of the solutions of six clustering methods applied to the San Manuel mine data. White - counting method (Shanley and Mahtab, 1976). Blue - vector quantization (Klose et al., 2005). Green - fuzzy k-means (Hammah and Curran, 1999). Lime - spectral clustering (Jimenez-Rodriguez and Sitara, 2006). Yellow - mixed Bingham (Yamaji and Sato, 2011). Red - P-maximization. See Table 11.1 for values.

### 11.2 Vector Partitioning

Vector cluster partitioning is similar to axis cluster partitioning (Section 11.1), except the maximization procedure is done using the vector mean and  $\bar{R}$  (Section 4.8), rather than the  $P$  eigenvector index, so the following quantity is maximized

$$R^* = \frac{1}{n} \sum_{j=1}^k \bar{R}_j n_j \tag{11.3}$$

The similarity measure used is

$$d_V(x,y) = (1.0 - x \cdot y)/2 \tag{11.4}$$

where  $x \cdot y$  is the scalar, or dot, product of the two direction cosines.  $d_V$  varies from 0, when the axes are parallel, to 1, when the axes are antiparallel.

Figure 11.3a is a Schmidt plot of magnetic remanence data from Schmidt and Embleton (1985) (Fisher et al., 1987, Table B6), Figure 11.3b is the same data after vector cluster partitioning with  $k = 2$ . Figure 11.4a shows the data rotated to the vector mean of cluster 1, and Figure 11.4b shows the data rotated to the vector mean of cluster 2.

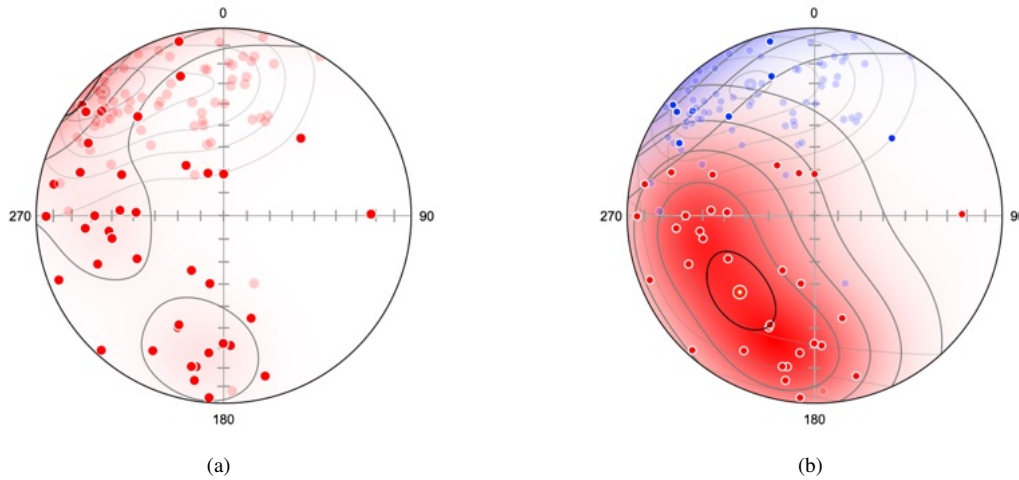


Figure 11.3: Schmidt plots of magnetic remanence vectors, data from Schmidt and Embleton (1985) (Fisher et al., 1987, Table B6). Modified Kamb contour interval is 20% density, the bootstrap 95% confidence cones are centered on the cluster vector means. Symbols on the upper hemisphere are 30% opaque. (a) Plot of full data set. (b) Plot after vector cluster partitioning with  $k = 2$ .

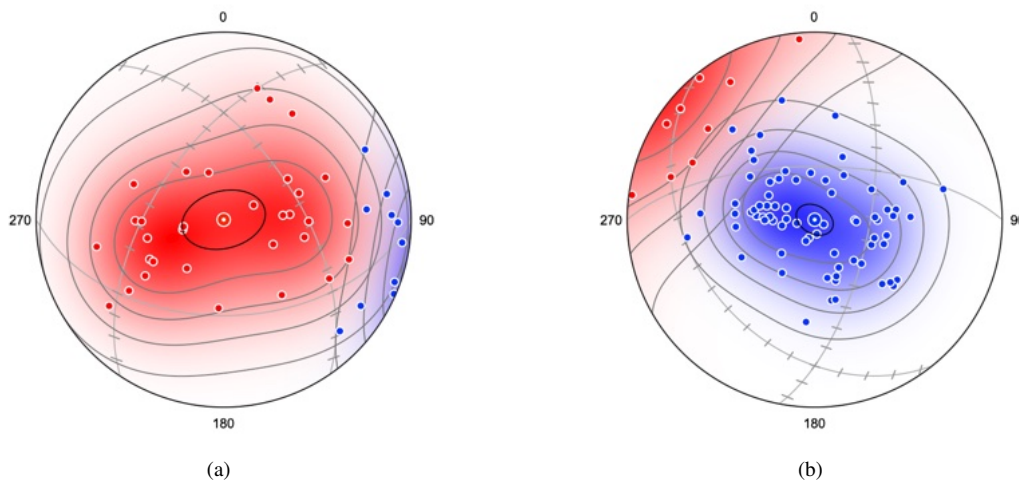


Figure 11.4: Schmidt plots as in Figure 11.3. (a) Plot rotated to the cluster vector mean of cluster 1. (b) Plot rotated to the cluster vector mean of cluster 2. Both clusters have oblong contours, suggesting the possibility of four modes.

Both clusters have oblong shapes (Figure 11.4), suggesting the possibility that they could be partitioned to form four modes, assuming circular modes. Fisher et al. (1987, p. 144-145) note that, on theoretical grounds, this data may contain four modes, although they do not perform a cluster analysis. Figure 11.5 shows the data after partitioning into four modes. The evaluation of  $k$  for this data is discussed in Section 11.6.

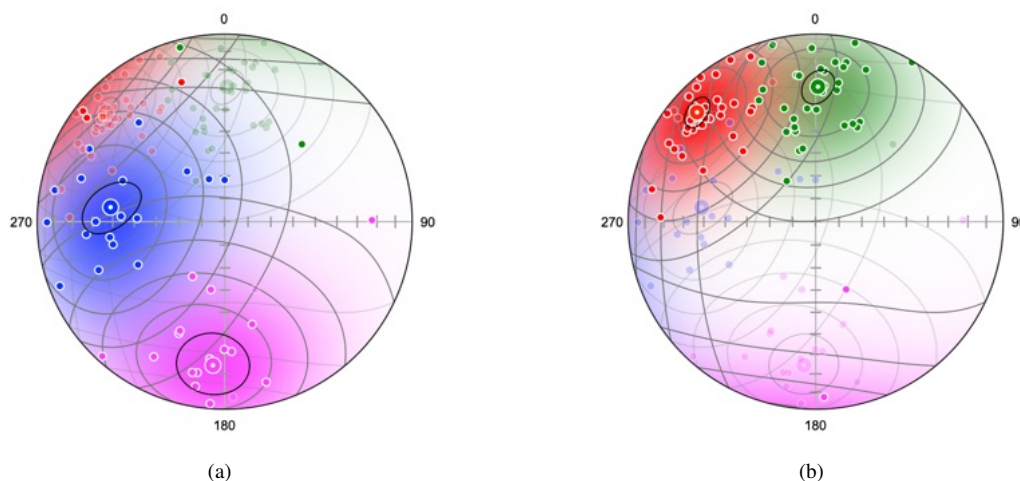


Figure 11.5: Equal-area spherical projections of the paleomagnetic data partitioned into four vector clusters, as suggested on a theoretical basis. (a) Lower hemisphere plot, with upper hemisphere symbols drawn at 30% opacity. (b) Upper hemisphere plot with lower hemisphere symbols drawn at 30% opacity.

### 11.3 Girdle Partitioning

Girdle cluster partitioning, where an attempt is made to partition more than one girdle distribution from a sample, is similar to axis cluster partitioning (Section 11.1), except the maximization procedure is done using the G eigenvector index instead of the P eigenvector index (Section 7.1).

$$G^* = \frac{1}{n} \sum_{j=1}^k G_j n_j \quad (11.5)$$

A test example is shown in Figure 11.6, which is a subsample of foliation data from Grøvdalen, Møre og Romsdal, Norway (Vollmer, 1985), Figures 15.2 and 15.3, which suggests refolding into tens of kilometer scale sheath folds. Figure 11.6 shows the data before and after girdle partitioning. Girdle clustering on the data may identify multiple girdles, however spacial cluster analysis, or domain analysis, Sections 16, includes location as well as orientation, and may be more effective.

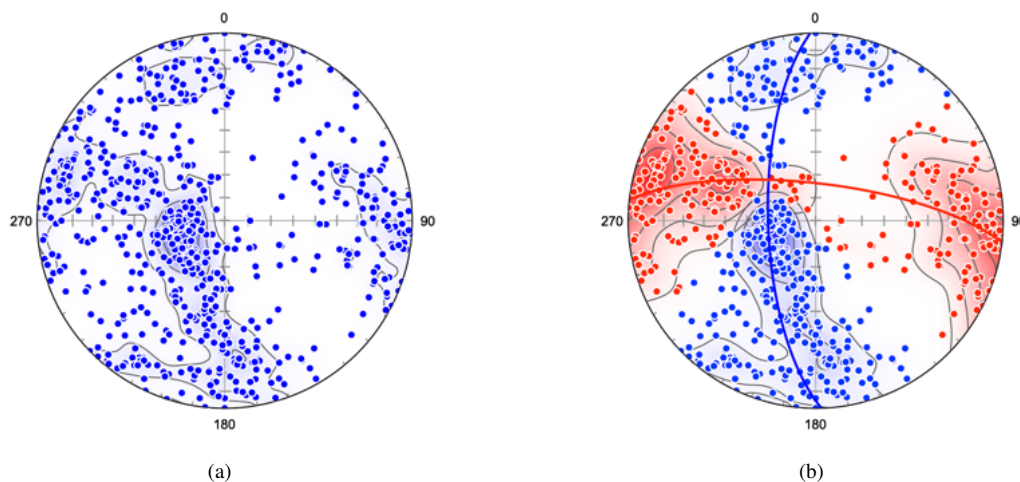


Figure 11.6: Schmidt plots of 625 poles to foliations from a subsample of foliation data from Grøvdalen, Møre og Romsdal, Norway (Vollmer, 1985). Modified Kamb contours are 20% (a) Plot of the data prior to partitioning. (b) Plot after partitioning the data into two girdle clusters.



## 11.4 Slip Partitioning

Partitioning of slip into strike-slip and reverse components has been documented along some major transpressional fault systems, such as the Denali Fault in northwestern North America (Bemis et al., 2015). The partitioning of slip along oceanic ridges into normal and strike-slip transform segments is a fundamental tenet of plate tectonic theory (Sykes, 1967). Other fault populations may contain polyphase data from more than one event (C  lerier et al., 2012). Such multimodal data sets are challenging to evaluate, however cluster analysis may assist in objectively identifying multiple slip modes. This section discusses the analysis of such data sets by partitioning kinematic axes (Section 9.3).

An example data set is from the southern Mid-Atlantic Ridge, between  $55^\circ$  S and  $16^\circ$  N, and  $55^\circ$  W and  $0^\circ$  E, imported from the CMT Project (Section 2.7.2). This data is in the file `Example Data/Seismology/CMT_jan76_dec17 SMAR Cluster.tsv`. It contains 1465 moment tensor solutions, the same as in file `CMT_jan76_dec17 SMAR.tsv`, except only one nodal plane is included, since the kinematic axes are the same for each of the two nodal planes. The `Calculate_lines` command is first used to determine the slip lines from rakes, after which the  $P$ ,  $M$ , and  $T$  kinematic axes are automatically defined.

Figure 11.7a is a Schmidt plot of the full data set.  $P$  axes are shown in red, and  $T$  axes in blue. Figure 11.7b is a moment triangle plot (Section 9.7) of the full data set. The moment triangle plot shows a clear bimodal distribution of normal and strike-slip faults, although sinistral and dextral faults can not be differentiated on this plot. The Schmidt plot suggests that three modes are present. While there are a number of ways to subdivide the data into modes, the goal here is to use an objective unsupervised learning method that might be useful for data sets that have less clearly defined modes.

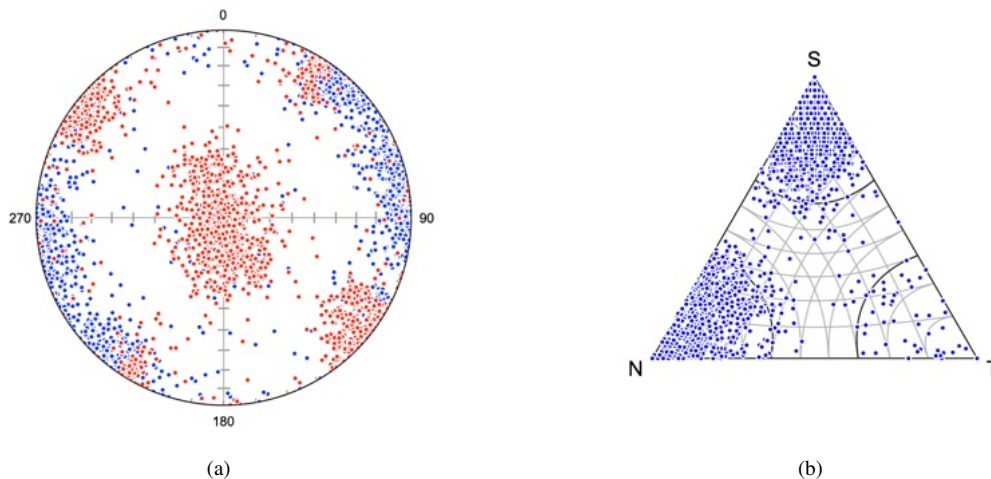


Figure 11.7: Plots of 1465 moment tensor solutions from the southern Mid-Atlantic Ridge data set `Seismology/CMT_jan76_dec17 SMAR Cluster.tsv`. (a) Schmidt plot of the full data set, the distribution of  $P$  axes suggests three slip modes.  $P$  axes are shown in red, and  $T$  axes in blue. (b) Moment triangle plot (Section 9.7) of the full data set, suggesting two or three slip modes, as sinistral and dextral slip modes are not distinguished on this plot.

Since the Schmidt plot (Figure 11.7a) shows three modes for  $P$  axes, clustering is done on  $P$  axes using  $k = 3$ . Figure 11.8a is a beachball plot of cluster 1 after unweighted cluster analysis with  $k = 3$  Axis clustering on  $P$ , showing a normal slip mode. Figure 11.8b is a beachball plot of cluster 2 indicating a strike-slip mode, and Figure 11.9a is a beachball plot of cluster 3, indicating an opposing strike-slip mode. Figure 11.9b is a moment triangle plot with the three modes color coded.

The `Linked` clustering option has been found to be useful for some data sets. This links each of the  $P$ - $T$  data pairs using Eq 9.1. For this data set, however, it gives the same solution as the unlinked  $P$  axes.

Unsupervised slip partitioning on  $P$  with  $k = 3$  has clearly differentiated three slip modes, one normal, and two opposing strike-slip modes for this data, consistent with plate tectonic models. The same technique may be useful for other data sets where more than one slip mode is expected, or is

suggested by Schmidt plots of the data.

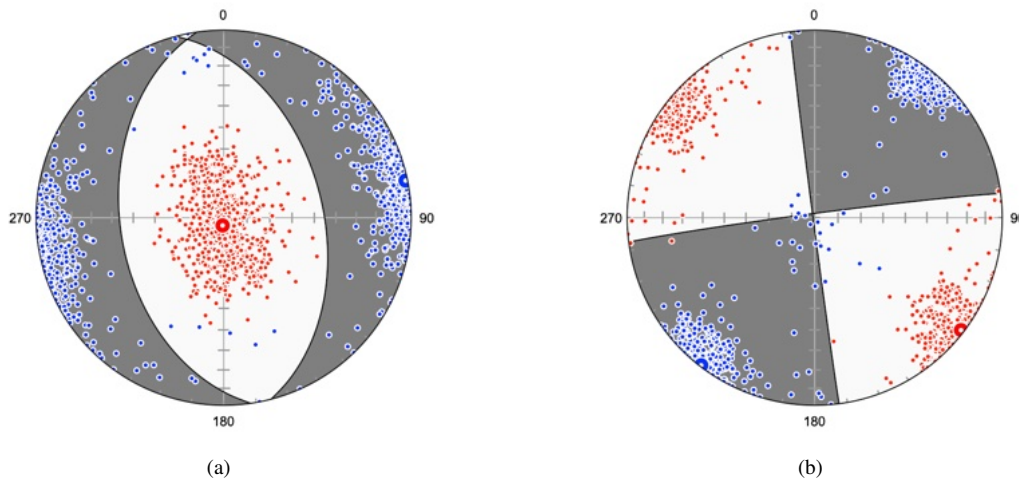


Figure 11.8: Schmidt beachball plots of fault slip data set after unweighted axis cluster analysis with  $k = 3$  Axis clustering on  $P$ .  $P$  axes are shown in red, and  $T$  axes in blue. (a) Cluster 1 showing a normal slip mode. (b) Cluster 2 showing a strike-slip mode, consistent with a dextral sense on east-west striking faults.

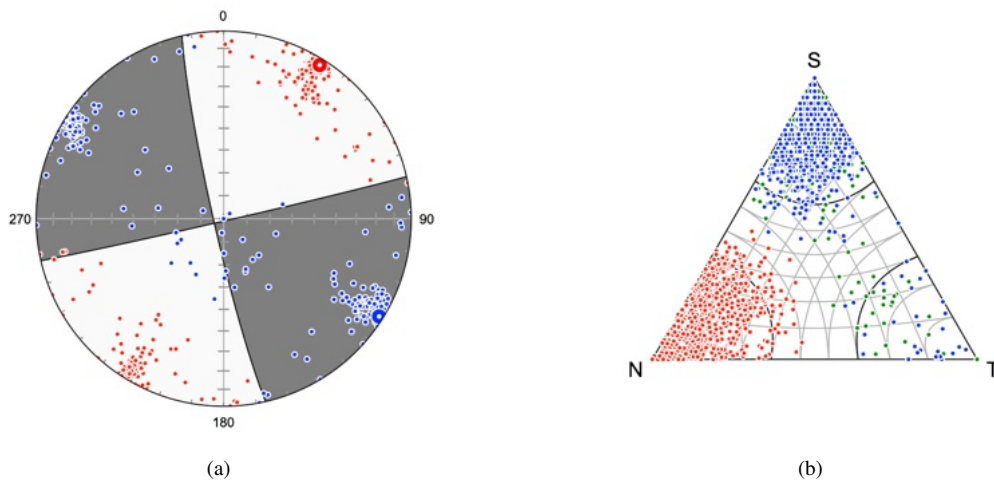


Figure 11.9: (a) Schmidt beachball plot of fault as in Figure 11.8, showing the opposing sense of slip as in Figure 11.8b, consistent with a sinistral sense on east-west striking faults. (b) Moment triangle plot with the three identified slip modes, cluster 1 (red), cluster 2 (blue), and cluster 3 (green).

## 11.5 Distance Minimization

The previous cluster methods attempt to maximize an eigenvector, or resultant vector, index summed over  $k$  clusters using an approach suggested by Vollmer (1990). An alternative is to minimize the scalar objective function (Hammah and Curran, 1999; Klose et al., 2005; Jimenez-Rodrigueza and Sitara, 2006)

$$d^* = \frac{1}{n} \sum_{i=1}^n \sum_{j=1}^k \mu_{ij} d(x_i, c_j) \quad (11.6)$$

where  $n$  is the number of data points, and  $k$  is the number of clusters.  $\mu_{ij}$  is 1 if data point  $i$  is in cluster  $j$ , and 0 if it is not.  $c_j$  is the unit axis, or vector, of cluster center  $j$ . The function  $d$  used here is  $d_A$  (Eq 11.1) for axes or  $d_V$  (Eq 11.4) for vectors. Select the *Distance* clustering option, and uncheck or

check *Directed* for axes or vectors. In the log output, the result of the minimization is reported under Clustering as  $D_{\max}(1 - d^*)$ , which varies from 0 to 1, with a value of 1 indicating perfect clustering. This method does not support weighting, girdle distributions, or axis linking.

Tests suggest the results for distance minimization are similar or identical to eigenvalue axis and vector results for many data sets. The results for the San Manuel copper mine fracture data (Shanley and Mahtab, 1975, 1976), magnetic remanence data from Schmidt and Embleton (1985) (Fisher et al., 1987, Table B6), and the southern Mid-Atlantic Ridge data are identical. However, both methods require minimization techniques that utilize random number generation, and small or poorly clustered data sets at high values of  $k$ , show more variations in the solutions. This should be considered when using methods to evaluate the selection of  $k$ , as discussed in Section 11.6.

## 11.6 Evaluation of Partitioning

The selection of the number of clusters,  $k$ , in k-means partitioning may be done by inspection of a contoured Schmidt plot, or by theoretical expectation, however it is desirable to have an objective methodology. Cluster analysis plays an important role in a wide variety of fields, and there is a significant literature on methods for the determination of the optimal choice of  $k$  (Rousseeuw, 1987; Yamaji and Sato, 2011; Fujita et al., 2014; Zhao and Fränti, 2014; Mur et al., 2016). While there is no definitive method for optimizing  $k$ , this section presents some simple and complementary nonparametric methods which can be helpful guides in evaluating the selection of  $k$ .

These evaluation methods are based on mean distance minimization (Section 11.5), which reliably converges for small poorly clustered data sets, and is the basis for the distance and silhouette tests described here. Additional metrics that can be used for evaluation include  $P^*$  (Eq 11.2), for axes, and  $R^*$  (Eq 11.3), for vectors.

A common metric for the evaluation of  $k$  is a mean silhouette score (Rousseeuw, 1987). First a *mean intra-cluster distance*,  $a(i)$ , is calculated for each data point,  $i$ . This is the mean distance between the point and all other data points in the *same* cluster. Second, a *mean nearest-cluster distance*,  $b(i)$ , is calculated. For each data point the mean distance is calculated to each data point in a *different* cluster.  $b(i)$  is the minimum of these, giving the next best cluster for that data point.

The silhouette for each point is then

$$s(i) = \frac{b(i) - a(i)}{\max[a(i), b(i)]} \quad (11.7)$$

$s(i)$  varies between  $-1$  and  $+1$ , for higher values the data is well clustered, for  $s(i) = 0$  the cluster assignment is indeterminate, and for negative values the assignment is incorrect. The mean of  $s(i)$  gives a mean silhouette score.

Figure 11.10 shows plots used to evaluate the selection of  $k$ . Plots are of  $k$  versus  $D_{\max}(1 - d^*)$ , Eq 11.6), mean silhouette (Eq 11.7),  $P_{\max}$  (for axis data,  $P^*$ , Eq 11.2), and  $R_{\max}$  (for vector data,  $R^*$ , Eq 11.3). Figure 11.10a is a plot of the San Manuel mine fracture axis data showing knees in  $D_{\max}$  and  $P_{\max}$  at  $k = 3$ , and a maximum mean silhouette at  $k = 3$ , suggesting that  $k = 3$  is an optimal value. Figure 11.10b is a plot of the magnetic remanence vector data showing a knee at  $k = 2$ , and a maximum mean silhouette at  $k = 2$ , suggesting that  $k = 2$  is an optimal value. Fisher et al. (1987, p. 144-145) suggest, on theoretical grounds, that this data may contain four modes, however only two are identified using these tests.

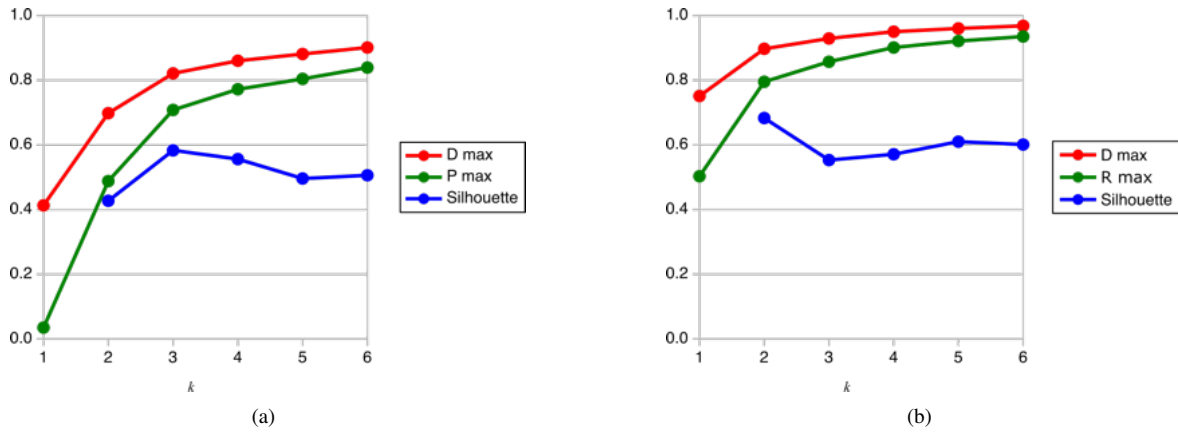


Figure 11.10: Plots used to evaluate the selection of  $k$ . Plots are  $k$  versus D max ( $1 - d^*$ , Eq 11.6), mean silhouette (Eq 11.7), P max (for axis data,  $P^*$ , Eq 11.2), and R max ( $R^*$ , for vector data, Eq 11.3). (a) Plot of the San Manuel mine fracture axis data showing knees in D max and P max at  $k = 3$ , and a maximum mean silhouette at  $k = 3$ , suggesting that  $k = 3$  is an optimal value. (b) Plot of the magnetic remanence vector data showing a knee in D max and R max at  $k = 2$ , and a maximum mean silhouette at  $k = 2$ , suggesting that  $k = 2$  is an optimal value.

## 11.7 Fuzzy Partitioning

The  $k$ -means clustering methods presented in Sections 11.1, 11.2, 11.3, and 11.5 are *hard* partitioning methods, in that a data point is considered to be in one, and only one, cluster. This is reflected by the term  $\mu_{ij}$  in Eq 11.6 which equals 0 or 1. An alternative is *soft* partitioning, where a data point has a degree of membership in all clusters with values that range from 0 to 1. *Fuzzy  $k$ -means* clustering (Zadeh, 1965; Hammah and Curran, 1999) is an example of soft partitioning. To determine cluster membership for soft partitioning, the term  $\mu_{ij}$  is redefined as (Hammah and Curran, 1999)

$$\mu_{ij} = \frac{\left[ \frac{1}{d(x_i, c_j)} \right]^{1/(f-1)}}{\sum_{l=1}^k \left[ \frac{1}{d(x_i, c_l)} \right]^{1/(f-1)}} \quad (11.8)$$

where  $f$  is a weighting exponent greater than one. Lower values of  $f$  give harder partitioning, closer to the distance based  $k$ -means model (Section 11.5). The value of  $\mu_{ij}$  ranges from 0 to 1, giving a membership value of the data point for each cluster. The data point is assigned to the cluster with the largest  $\mu_{ij}$ .

A modified orientation matrix for a cluster  $j$  is now

$$\Omega_{Fj} = \frac{1}{\sum_{i=1}^n \mu_{ij}^f} \sum_{i=1}^n \mu_{ij}^f x_i x_i^T \quad (11.9)$$

with the cluster axis given by the maximum eigenvector. Extension to directed data gives a modified mean vector for cluster  $j$

$$\bar{x}_{Fj} = \frac{1}{\sum_{i=1}^n \mu_{ij}^f} \sum_{i=1}^n \mu_{ij}^f x_i \quad (11.10)$$

which is normalized to give the cluster axis. Note that the calculation of  $\mu_{ij}$  requires iterating through all of the data points for each cluster, so the calculation can take some time.

Figure 11.11a is a Schmidt plot of fracture surfaces measured in the San Manuel copper mine, Arizona (Shanley and Mahtab, 1975, 1976), after fuzzy partitioning using  $k = 3$  and  $f = 2$ . Compare this to Figure 11.1b, which shows the results after axis partitioning, and assigns 3 points to different

clusters. Figure 11.11b is a lower hemisphere equal-area plot of magnetic remanence vector data from Schmidt and Embleton (1985) in Fisher et al. (1987, Table B6) after fuzzy partitioning using  $k = 4$  and  $f = 2$ . Compare this with Figure 11.5b, which shows the results after vector partitioning, assigning 1 point to a different cluster.

In these examples, there is little difference in the results from eigenvector index or distance-based methods. While fuzzy k-means has the advantage of allowing points to have membership in all clusters, it has the disadvantage of requiring an additional input parameter,  $f$ , the exponential term.

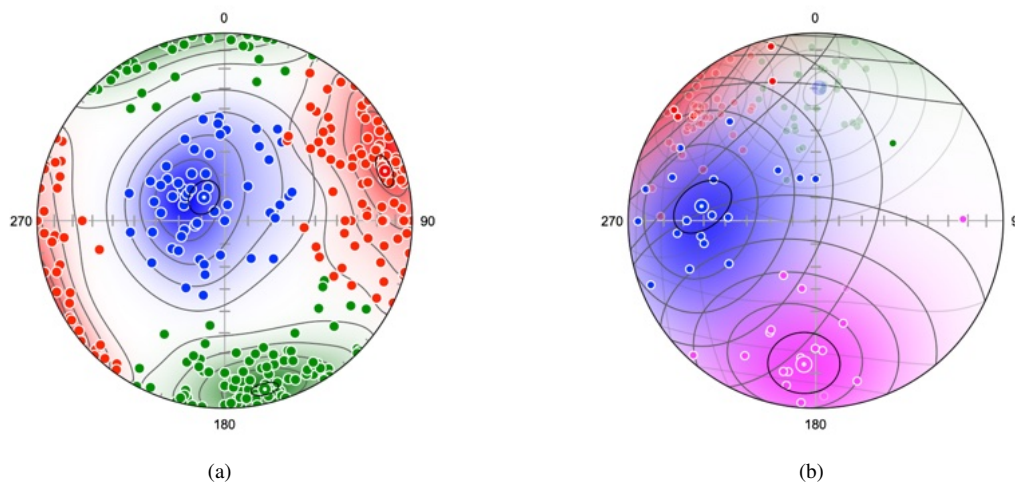


Figure 11.11: (a) Schmidt plot of fracture surfaces measured in the San Manuel copper mine, Arizona (Shanley and Mahtab, 1975, 1976), after fuzzy partitioning using  $k = 3$  and  $f = 2$ . Compare this to Figure 11.1b, which shows the results after axis partitioning, assigning 3 points to different clusters. (b) Lower hemisphere equal-area plot of magnetic remanence vector data from Schmidt and Embleton (1985) in Fisher et al. (1987, Table B6) after fuzzy partitioning using  $k = 4$  and  $f = 2$ . Compare with Figure 11.5b, which shows the results after vector partitioning, assigning 1 point to a different cluster. Upper hemisphere data is 30% opaque.

## 11.8 Density Partitioning

The previously discussed clustering methods are based on subdividing a data sample into  $k$  clusters. An alternative is to attempt to subdivide the sample into clusters by examining a neighborhood around each data point to locate regions where the data are tightly clustered. A widely used algorithm for this is DBSCAN (Ester et al., 1996; Schubert et al., 2017). The method requires specifying the *radius of the neighborhood* around each point, and the *minimum number of points* required to define a *core point*. Core points are points that have at least the minimum number of points in their neighborhood. A cluster is then expanded from the core points to include points that are *reachable* from the core points, that is, they lie within the neighborhood of one of the core points. Points that are not reachable from a cluster are defined as *noise*, these are designated by a cluster domain of  $-1$ .

DBSCAN requires the definition of a function that returns the distance between two points. It is adapted here to directional data by defining a similarity, or distance, measure for vectors

$$d_V(x, y) = \arccos(x \cdot y) \quad (11.11)$$

using the scalar vector product. The similarity measure for axes,  $d_A$ , is the smaller supplementary angle of  $d_V$ .

This algorithm does not require specification of the number of clusters, works with arbitrary cluster shapes, and can detect outliers (noise). However, selecting the appropriate neighborhood radius and minimum points is not straightforward, and it does not work well with clusters of different densities.

Figures 13.1a and 13.1b show examples of directional data density clustering. Figure 13.1a is an artificial data sample which can be partitioned into two clusters, with noise, after adjusting the neighborhood parameters. Figure 13.1b shows partitioning of the San Manuel mine fracture data

(Shanley and Mahtab, 1976), after selecting the neighborhood parameters. This plot identifies a cluster of steeply dipping fractures (blue), and a set of shallowly dipping fractures (red), along with two smaller clusters, and noise.

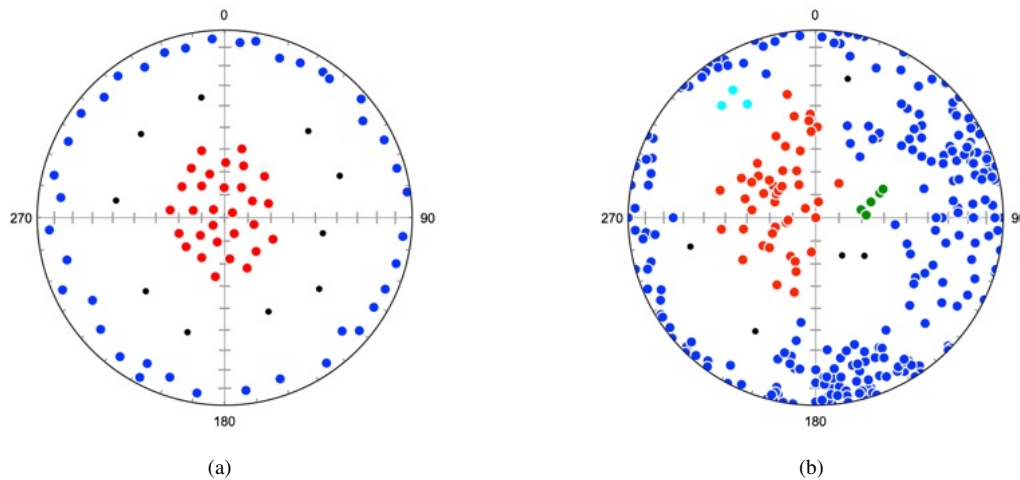


Figure 11.12: Examples of density partitioning. Noise points, unassigned to clusters, are black. (a) Partitioning of artificial data sample (cluster density test.tsv) into two clusters. Neighborhood radius =  $14^\circ$ , points = 3. (b) Partitioning of the San Manuel mine fracture data (Shanley and Mahtab, 1976). Neighborhood radius =  $12^\circ$ , points = 3.

## 12 Slope Stability

The evaluation of the stability of rock slopes, including road cuts and open pit mine faces, is an essential part of rock mechanics and geotechnical engineering. Rock bodies normally contain numerous bedding planes, fractures, and joints, which may be prone to failure, and factors such as earthquakes, porewater pressure, and complex geometries require the application of numerous techniques (Goodman, 1989; Hudson and Harrison, 1997; Wyllie and Mah, 2005; Meier et al., 2009; Wyllie, 2017; Jaiswal et al., 2023).

A common initial approach to establishing slope stability is to use *kinematic analysis* (Hudson and Harrison, 1997; Wyllie and Mah, 2005). This refers to the study of possible movements, without the consideration of forces. Some geometries of slope and discontinuities, allow movement, while others do not. This chapter focuses on the kinematic analysis of slope failure using spherical projections, estimation of safety factors is not treated.

### 12.1 Plane Failure

In order for a plane slide to occur, the material above the plane must be able to move out into open space, or *daylight* (Wyllie, 2017, p. 6-7). Daylighting is possible when the dip direction of a discontinuity is in the direction of the rock face. To quantify this, a *daylight envelope* is calculated. The envelope includes all planes whose down-dip lines lie within the plane of the rock face. Each point on the envelope is defined by a line on the rock face rotated  $90^\circ$  in a vertical plane.

As an example, consider the initial evaluation of San Manuel mine fracture data (Shanley and Mahtab, 1976), and a hypothetical mine face oriented with a dip of  $70^\circ$  and a dip direction of  $220^\circ$ . Figure 12.1a shows the poles to the fracture data contoured using modified Kamb contours at 20% density, and the daylight envelope, in red. A large number of poles to fracture planes fall within the daylight envelope, suggesting the possibility of failure on those planes.

An additional constraint is the *cone of friction*. Given a frictional sliding angle, a vertical cone is constructed with that semi-apical angle. Planes whose poles lie within the cone are unlikely to fail by sliding. For this example,  $30^\circ$  is used, a common angle for frictional sliding without pore fluid

pressure. Figure 12.1b shows the rock slope and bedding planes with the cone of friction. Planes with poles *inside* the daylight envelope and *outside* the friction cone are most prone to sliding.

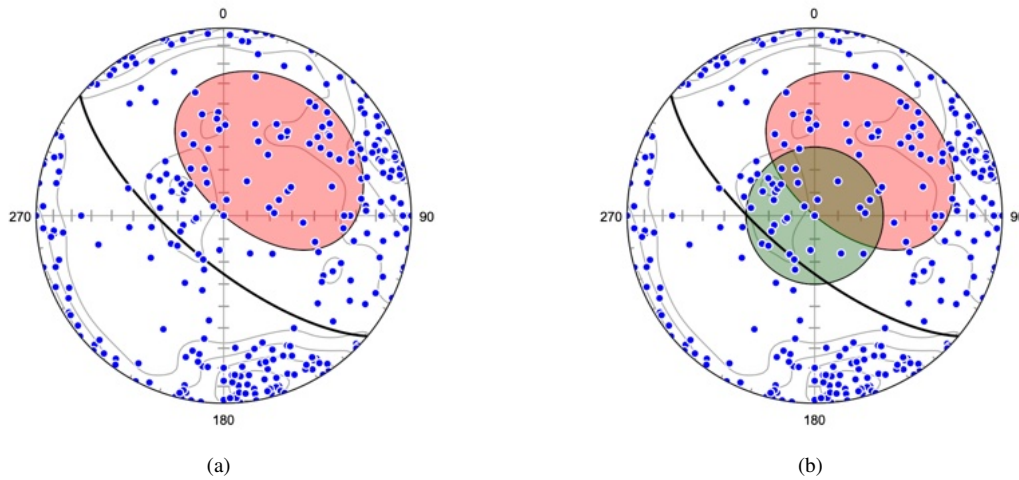


Figure 12.1: Contoured Schmidt plots showing kinematic analysis for planar sliding using the San Manuel mine fracture data (Shanley and Mahtab, 1976), and a hypothetical mine face oriented with a dip of  $70^\circ$  and a dip direction of  $220^\circ$  (black). (a) The daylight envelope (red) shows planes with dip directions that could potentially fail by sliding out of the slope, poles to potential failure planes lie within the envelope. (b) Plot with the addition of a  $30^\circ$  pole cone of friction (green). Planes with poles *inside* the daylight envelope and *outside* the friction cone are most prone to sliding.

Empirical observations suggest that that failure tends to occur mainly within a certain angular range of the slope face dip direction, typically a value of  $\pm 20^\circ$  to  $\pm 30^\circ$  (Hudson and Harrison, 1997, Chapter 18). Figure 12.2a shows the plot with the addition of lateral limits of  $\pm 20^\circ$  (yellow). Planes whose poles lie *within* the lateral limits are more prone to failure. To summarize, planes whose poles lie inside the daylight envelope, inside the lateral limits, and outside the friction cone are most likely to be problematic. For comparison, Figure 12.2b shows the same analysis for a  $70^\circ$  slope with a dip direction of  $040^\circ$ , where fewer planes are potentially unstable.

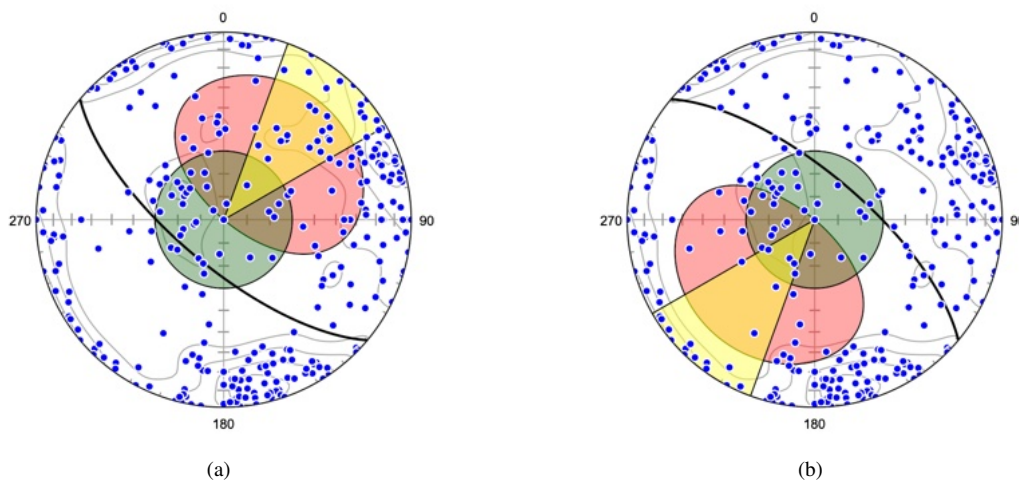


Figure 12.2: Schmidt plot showing kinematic analysis for planar sliding as in Figure 12.1, with the addition of lateral limits of  $\pm 20^\circ$  (yellow). (a) Planes whose poles lie *inside* the daylight envelope, *inside* the lateral limits, and *outside* the friction cone are most likely to be problematic. (b) The same analysis for a  $70^\circ$  slope with a dip direction of  $040^\circ$ , where fewer planes are potentially unstable.

## 12.2 Wedge Failure

In rock exposures with multiple planes of weakness, failure may occur as wedges following the line of intersection between two planes. To illustrate this, Figure 12.3a shows two planes with strikes and dips of  $310^\circ, 60^\circ$  and  $085^\circ, 70^\circ$  (red) intersecting a rock slope oriented  $045^\circ, 70^\circ$  (black, dip direction of  $135^\circ$ ). The line of intersection between the two planes has a trend and plunge of  $102^\circ, 39^\circ$  (blue). This line has a plunge *less than* its projection on the slope, and therefore *daylights* allowing the kinematic possibility of failure.

Figure 12.3b is the same plot with the addition of the slope's plane pole daylight envelope (yellow), and a line friction cone of  $30^\circ$  (red). Neither of the two planes has a pole within the daylight envelope, suggesting that they are kinematically unable to fail independently. However, the intersection line *does* daylight, and lies *inside* the line friction cone, suggesting wedge failure is likely.

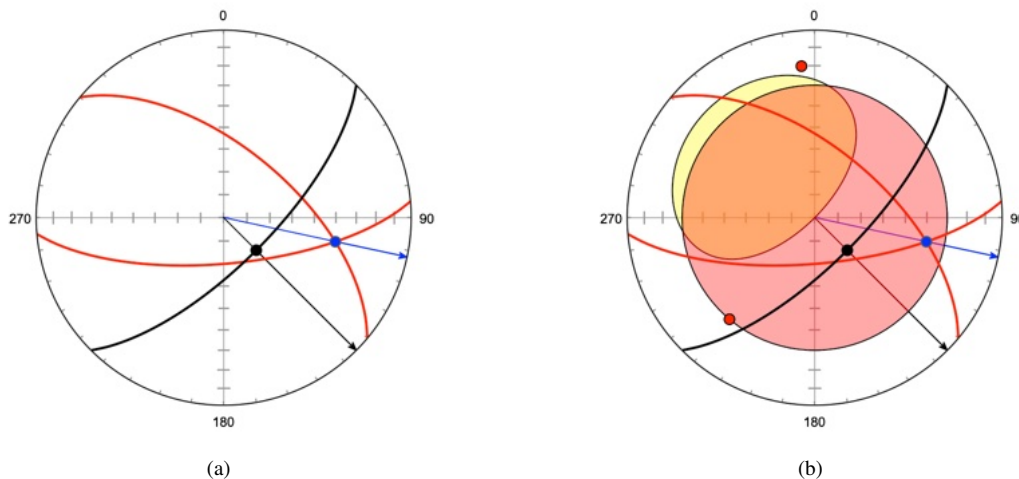


Figure 12.3: Schmidt plots showing kinematic analysis for wedge failure along two planes (red) exposed in an outcrop face (black). (a) The intersection of the two planes daylight on the slope, because the plunge of the intersection (blue) is less than the apparent dip of the slope. This geometry allows the possibility of wedge failure. Redrawn from Figure 2.17a of Wyllie and Mah (2005). (b) Plot with slope pole daylight envelope (yellow), and line friction cone of  $30^\circ$  (red). Neither of the two plane poles lie within the daylight envelope, suggesting they are unlikely to fail independently, however the line of intersection lies *inside* the cone, suggesting wedge failure is likely.

Given multiple planes it is possible for failure to occur on a single plane, or as a wedge, sliding on both planes simultaneously. Figure 12.4a is a Schmidt plot for two planes (strike, dip of  $315^\circ, 60^\circ$  and  $070^\circ, 70^\circ$ ) exposed in a slope (strike, dip of  $020^\circ, 70^\circ$ ). The planes intersect in a line with a trend, plunge of  $094^\circ, 48^\circ$ . Both dip directions (red arrows) lie *outside* the included angle between the intersection line (blue arrow at  $094^\circ$ ) and the slope dip line (black arrow at  $110^\circ$ ), kinematically favoring wedge failure.

Figure 12.4b is a Schmidt plot for two planes (strike, dip of  $020^\circ, 50^\circ$  and  $075^\circ, 70^\circ$ ) exposed in a slope (strike, dip of  $030^\circ, 70^\circ$ ). The planes intersect in a line with a trend, plunge of  $100^\circ, 50^\circ$ . One plane's dip direction (red arrow at  $110^\circ$ ) lies *inside* the included angle between the intersection line (blue arrow at  $100^\circ$ ) and the slope dip line (black arrow at  $120^\circ$ ), kinematically favoring plane failure on  $020^\circ, 50^\circ$  instead of wedge failure.

For a data set with numerous potential failure planes, such as the San Manuel mine fracture data (Shanley and Mahtab, 1976) (Figure 12.1a), it is possible to calculate all possible wedge intersection lines using the *Data - Calculate Intersections* command, however this can result in a very large number of intersections, for  $n$  planes the number of intersections is

$$C_2^n = \frac{n!}{2(n-2)!} \quad (12.1)$$

The 286 fractures of the San Manuel mine data can potentially generate 40755 intersections, and,



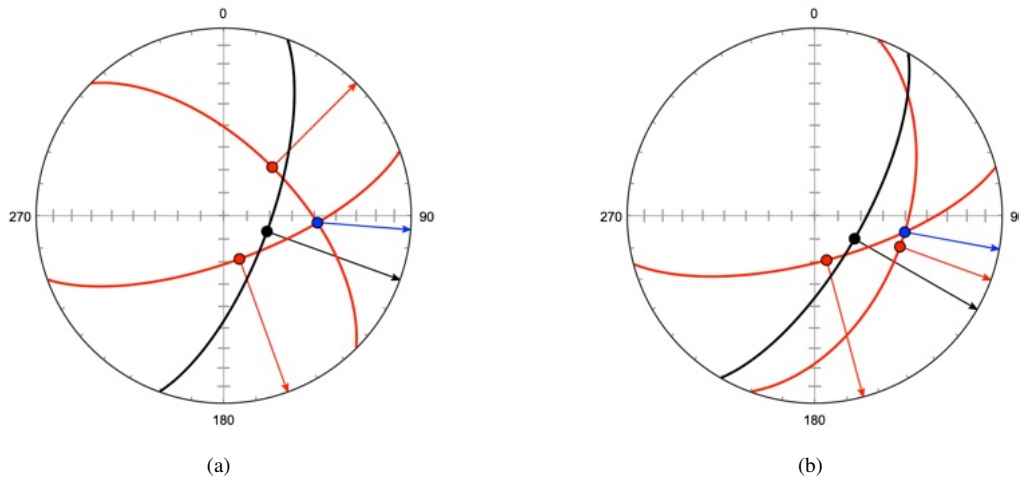


Figure 12.4: Schmidt plots showing kinematic analysis for wedge failure along two planes (red) exposed in an outcrop face (black). The planes intersect in a line (blue). Redrawn from Figure 2.17 of Wyllie and Mah (2005). (a) Plot of two planes with dip lines and directions (rays). Both dip directions lie *outside* the included angle between the intersection line and the slope dip line, favoring wedge failure. (b) Two intersecting planes where one plane's dip direction lies *inside* the included angle between the intersection line and the slope dip line. Failure is kinematically favored on this plane, instead of wedge failure.

even if excluding near parallel planes, these may not all be statistically meaningful, as each plane generates  $n - 1$  intersections (Figure 12.5a). In this case it may be preferable to use the mean of data clusters rather than all individual fracture planes (Figure 12.5b, Chapter 11).

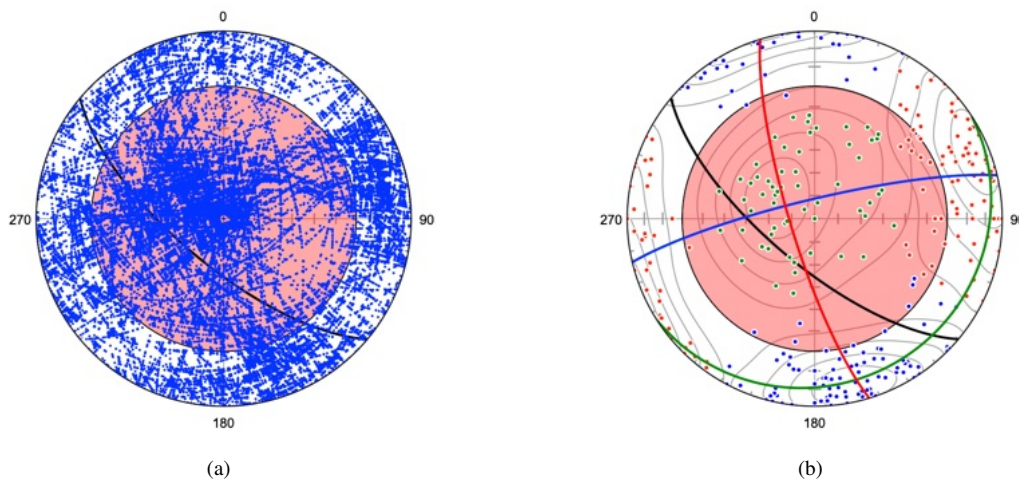


Figure 12.5: Schmidt plots showing kinematic analysis for wedge failure of the San Manuel mine fracture data (Shanley and Mahtab, 1976). A line friction cone of  $30^\circ$  is shown in red, and a hypothetical slope face is shown with a dip direction, dip of  $220^\circ$ ,  $70^\circ$  (black). (a) Plot of 39738 fracture intersections determined using the *Data - Calculate Intersections* command. The intersections of planes making an angle of less than  $10^\circ$  are excluded. Note the large number of intersections that fall along great circles, these are not likely to be statistically significant. (b) Fracture data after cluster analysis into three plane axis clusters (Chapter 11). The best fit planes are shown in red, green, and blue. Two of the best fit plane intersections (blue/green and green/red) are well outside the friction cone, so are unlikely to fail. The red/blue intersection lies within the friction cone, but does not daylight out of the slope.

### 12.3 Toppling Failure

A toppling failure occurs when steeply dipping planar slabs fall or rotate outward from a slope face. The planes' dip directions must be close to the dip direction of the rock slope, so toppling lateral

limits are defined at about  $\pm 10^\circ$  from the dip direction of the slope, as shown in Figure 12.6a.

Also, for toppling to occur, interlayer slip must occur along the faces of the slabs. For a slope dip of  $\delta_S$  with planes having an interlayer friction angle of  $\phi_P$ , a plane must have a dip  $\delta_P$

$$\delta_P > (90^\circ - \delta_S) + \phi_P \quad (12.2)$$

for toppling to occur (Wyllie and Mah, 2005, Eq 2.3). Figure 12.6a illustrates an example kinematic analysis for topple failure of the San Manual mine fracture data (Shanley and Mahtab, 1976). Lateral limits are defined at  $\pm 10^\circ$  from the dip direction of the slope, which restrict likely failure to planes with poles within this range. Figure 12.6b additionally shows a  $50^\circ$  plane pole cone defined by Eq 12.2, using  $\phi_P = 30^\circ$ . Planes with poles *outside* the cone and *inside* the toppling limits wedge are most prone to toppling.

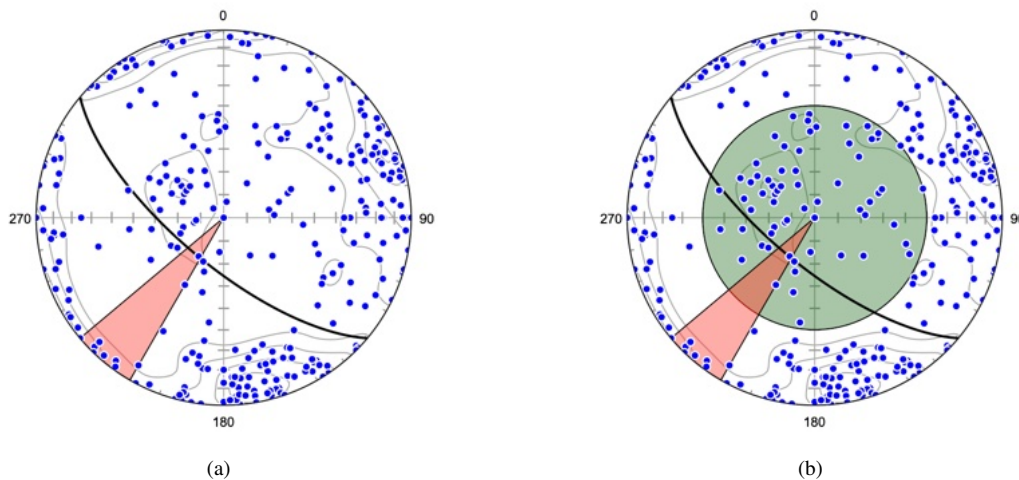


Figure 12.6: Schmidt plots showing kinematic analysis for topple failure of the San Manual mine fracture data (Shanley and Mahtab, 1976) on a hypothetical slope face with a dip direction, dip of  $220^\circ, 70^\circ$  (black). (a) Lateral limits are defined at  $\pm 10^\circ$  from the dip direction of the slope (red), only planes with poles in these limits are likely to fail by toppling. (b) Plot with the addition of a pole cone of  $50^\circ$  (green), using Eq 12.2. Planes with poles inside this cone are not likely to topple. Planes with poles *outside* the cone and *inside* the toppling limits wedge are most prone to toppling.

## 13 Multiple Point Calculations

Selecting two or more points in the spreadsheet displays information in the status bar on their mean value, and the intersection of two or more planes, or the normal to two or more planes. Click on the status bar to alternate between line and plane orientation formats. This can be useful for example, for determining the intersection of two planes such as bedding (S0) and cleavage (S1) measured at the same location. This chapter discusses several additional calculations that can be made on selected rows.

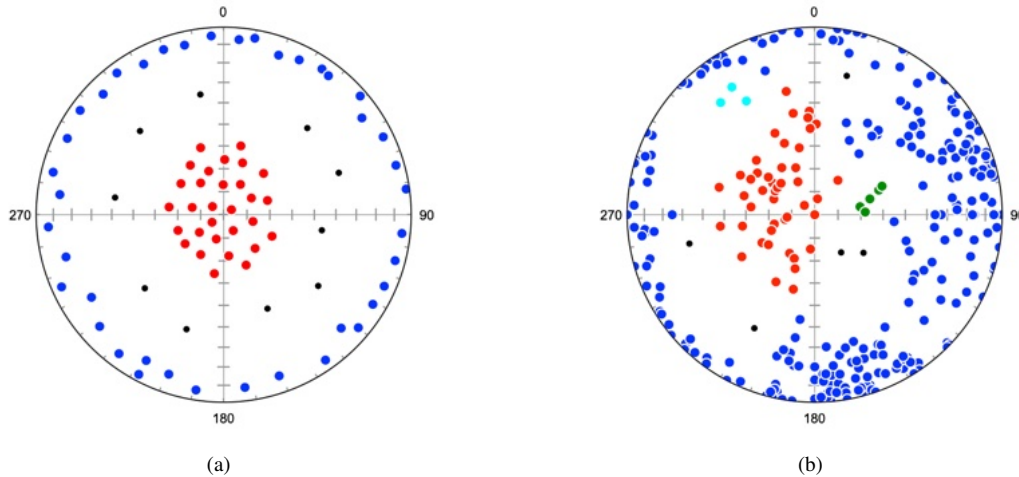


Figure 13.1: Examples of density partitioning. Noise points, unassigned to clusters, are black. (a) Partitioning of artificial data sample (cluster density test.tsv) into two clusters. Neighborhood radius =  $14^\circ$ , points = 3. (b) Partitioning of the San Manuel mine fracture data (Shanley and Mahtab, 1976). Neighborhood radius =  $12^\circ$ , points = 3.

### 13.1 Maxima Calculations

The *Data - Calculate Maxima* command gives similar results to the status bar display when two or more rows in the spreadsheet are selected, but gives more complete results in the log that can be cut and pasted into other documents. A common application is for the determination of bedding (S0) and cleavage (S1) intersections that serve as useful proxies for fold hinge line measurements. The command displays a dialog box in which either the *Lines* or *Planes* radio button may be selected. Select the desired spreadsheet rows, and press the *Calculate* button. If desired, and weights are available, check the *Weighted* checkbox to apply weighting to the calculations. The following are example log outputs

2018-01-11 15:20:30

Data File : Vollmer 1981b

=====

Number of planes : 11

Strike, Dip:

Maximum eigenvector (undirected mean) : 23.928, 18.897

Vector mean (directed mean) : 298.804, 76.233

Trend, Plunge:

Minimum eigenvector (undirected axis) : 190.740, 4.466

2018-01-11 15:21:13

Data File : Vollmer 1981b

=====

Number of lines : 4

Trend, Plunge:

Maximum eigenvector (undirected mean) : 190.568, 6.254

Minimum eigenvector (undirected axis) : 285.969, 40.654

Vector mean (directed mean) : 192.131, 13.542

Much more extensive results with statistics are obtained for each data type using the *Data - Statistics* command. The *Calculate Maxima* command is intended for rapid calculation of subsets of one data type, or for selections across more than one data type.

### 13.2 Trend Surface Analysis

Trend surface analysis can be regarded as an extension of the familiar linear least-squares fitting of  $[x,y]$  data points to a line, to the fitting of a surface to a set of  $[x,y,z]$  points in three-dimensions. It is commonly applied in geology to determine the regional trends of a surface, such as a subsurface economic horizon. It may be desired to determine the orientation of the surface, or to examine the residuals from that surface, the differences between the measured elevation values at locations,  $z_i$  and the estimated values,  $\hat{z}_i$  (Davis, 1986, 2002).

The trend surface command allows the rapid determination of the best-fit plane, a first order trend surface, through a set of data points containing  $[x,y,z]$  (easting, northing, elevation) values, including solving simple *three point problems*, a common calculation in structural geology and hydrogeology. The  $z$  coordinate is taken as the dependent variable, and the solution minimizes the sum of the squares of the vertical distances of  $z_i$  from the plane. Note that the solution to a three point problem will give zero for each of the three residuals.

To illustrate the command, open the file Trend Surface/Davis 1966 5-16. Select all 10 data rows, run the command *Data - Trend Surface*, and press *Calculate*. The following will be appended to the log

2020-05-25 13:53:56

Data File : Davis 1966 5-16

=====  
Elevation points : 10

Best-Fit Plane

Strike, Dip : 202.356, 0.297

$z' = -621.0417 + (0.0048)x + (-0.0020)y$

R = 0.9489

Convex Hull

Centroid (x, y) : 53245.9585, 51346.7802

Centroid  $z'$  : -467.2273

Area : 5577500000.0000

Minimum radius : 36786.2705

Maximum radius : 56881.4960

Residuals

-58.3605

82.7457

-48.1245

52.8582

-33.7697

26.2318

0.5589

-25.4179

-40.9081

44.1860

The best-fit plane passing through the  $[x, y, z]$  coordinates is calculated using linear least squares fitting with  $z$  as the dependent variable. The strike and dip (or dip direction and dip, depending on the preference settings) of the plane, are displayed along with the equation of the plane, and the coefficient of multiple correlation,  $R$ . The latter gives a measure of the goodness of fit, for a perfect fit,  $R = 1$ . Finally the residuals,  $z_i - \hat{z}_i$ , are listed if desired, these can be useful for identifying and discarding outliers..

In order to assign a location to the plane, the *convex hull* of the  $[x, y]$  coordinates is calculated, giving a convex polygon enclosing the  $[x, y]$  coordinates. The centroid, or center of mass, of that polygon may be used as the coordinates of the location of the estimated plane, and the estimated elevation,  $\hat{z}$  ( $z'$  in the log) is given for that location. An estimate of the size and extent of the polygon is given as the area of the hull, and the minimum and maximum hull radii, distances from the centroid to the points defining the hull. Ideally the radii should not be widely different for a stable estimate.

## 14 Ternary Plots

Ternary plots are triangular plots used to display the relative proportions of three components, and are commonly used in petrology, mineralogy, physical chemistry, metallurgy, and other fields. Geologic examples include the sedimentary rock QFL (Quartz-Feldspar-Lithic) plot, the igneous rock QAP (Quartz-Alkali feldspar-Plagioclase) plots, and petrologic ternary phase diagrams.

### 14.1 Geometry of Ternary Plots

A ternary plot can be understood geometrically as the projection of three-dimensional Cartesian vectors onto the octahedral plane that passes through the points  $x = [1, 0, 0]$ ,  $[0, 1, 0]$ ,  $[0, 0, 1]$  (Figure 14.1a). The coordinates on this plane are positive and sum to 1. Figure 14.1b illustrates the basic method for plotting points as percentages on a ternary plot.

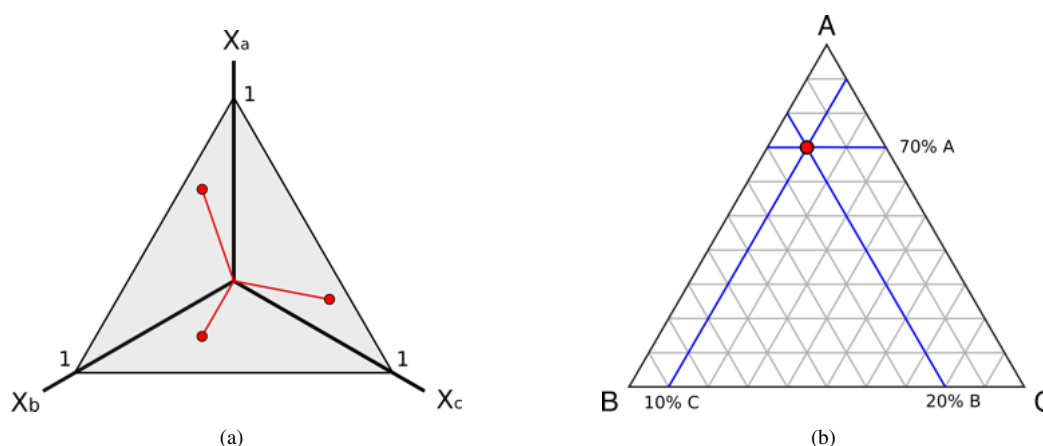


Figure 14.1: (a) Geometric interpretation of the ternary plot as the projection of three-dimensional Cartesian vectors onto the octahedral plane through  $[1, 0, 0]$ ,  $[0, 1, 0]$ ,  $[0, 0, 1]$ . Coordinates in that plane are positive and sum to 1. (b) Location of a point as percentages on the ternary plot with coordinates  $x = [0.7, 0.1, 0.2]$ .

Creating a ternary plot requires the opening of a data file with headers  $X_a$ ,  $X_b$ ,  $X_c$  for columns containing the relative proportions of three components. The components will be normalized to  $X_a + X_b + X_c = 1$  when plotted using the *Ternary Plot* command. The data may be optionally weighted if data weights are included using a *Weight* file header and the *Weighted* option is selected.

### 14.2 Tutorial: QFL Plot

The file *Provenance.ods*, in the *Example Data/Ternary* folder, contains percentages of sedimentary clasts in a sedimentary rock analysis. For this example, three sums were created in the spreadsheet,  $Q$  = quartz + chert,  $F$  = plagioclase + kfeldspar, and  $L$  = shale + volcanic. These three components are summed in the column *Total*, and then each divided by *Total* (normalized) to give columns  $X_a$ ,  $X_b$ , and  $X_c$ . Note that the three components will be normalized if they do not sum to one, for example if they are listed as percentages.

Open the file *Provenance.ods* and select *Plot - Ternary Plot*. The default ternary plot appears as shown in Figure 14.2a. In the *Preferences* dialog box *Ternary Plot* pane, set the symbol stroke color to white. In the *Grid* pane, uncheck *Minor Grid* lines and *Major Tick* marks. In the *Labels* pane enter  $Q$ ,  $F$ , and  $L$  in place of  $A$ ,  $B$ ,  $C$ . The plot should now look as shown in Figure 14.2b.

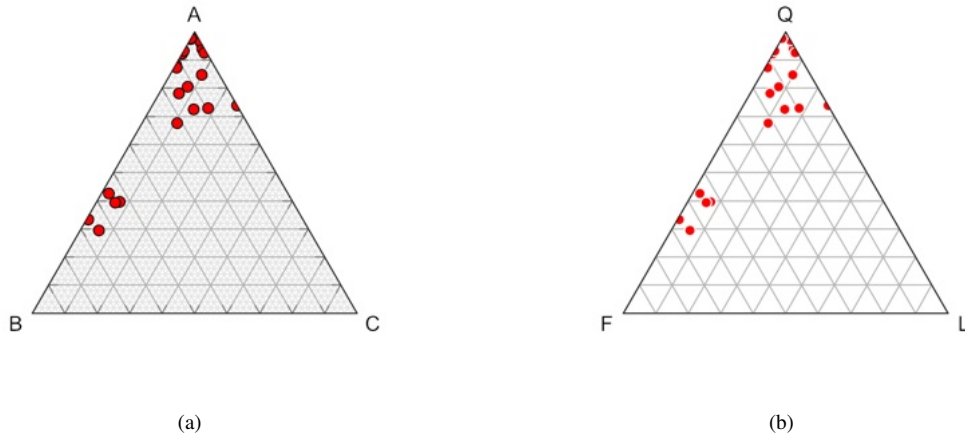


Figure 14.2: Ternary plots of the Provenance.ods QFL data. (a) Plot with default settings. (b) Plot after removing the minor grid, changing symbol strokes to white, and changing the apex labels to Q, F, and L.

### 14.3 Contouring Ternary Plots

Contouring the ternary plot is done using multivariate kernel density estimation (KDE), a technique related to determining the optimal bin width of a histogram (Silverman, 1986). Each location (node) density estimate is the sum of the kernel estimates about each data point. An estimate of the density function,  $f$ , is given by

$$\hat{f}_H(x) = \frac{1}{n} \sum_{i=1}^n K_H(x - x_i) \quad (14.1)$$

where  $x$  is the location vector of the estimate (node),  $x_i$  are the  $n$  data vectors, and  $K_H$  is

$$K_H(x) = |H|^{-1/2} K(H^{-1/2}x) \quad (14.2)$$

where  $H$  is the bandwidth matrix, and  $K$  is the kernel function, taken here as the standard normal function

$$K(x) = \frac{1}{\sqrt{2\pi}} e^{-\frac{1}{2}x^2} \quad (14.3)$$

This function is symmetrical, centered on 0, and has a total area under the curve of 1. Estimation of the bandwidth determines the level of smoothing, Silverman's rule of thumb is used here

$$\sqrt{H_{ij}} = \left( \frac{4}{d_K + 2} \right)^{\frac{1}{d_K + 4}} n^{\frac{-1}{d_K + 4}} \sigma_i \quad (14.4)$$

where  $H_{ij} = 0$  for  $i \neq j$ ,  $\sigma_i$  is the standard deviation of the  $i^{\text{th}}$  variable, and  $d_K$  is the number of dimensions, here 3. Note that  $H$  determines both the amount and the orientation of smoothing.

There are several parameters that can be changed to modify contouring. The *Smoothing* option multiplies  $H$  by an additional smoothing factor, the default is 1. The *Levels* option sets the number of contour levels of the probability estimate, 10 gives contour levels at 10%, 5 gives levels at 20%. The *Nodes* options sets the number of horizontal and vertical nodes at which the density estimate is calculated. The *Weighting* option uses the value in the *Weight* column to weight each data vector,  $x$  ( $X_a, X_b, X_c$ ).

Figure 14.3a is a ternary plot of the Provenance.ods QFL data with 10 contour levels, or 10%, of the density range. The kernel density estimate uses Silverman's rule of thumb (Eq 14.4) to estimate the bandwidth. Figure 14.3b is the same plot with a color gradient applied.

The contour lines on these plots are overly constrained by individual data points, suggesting the default estimated bandwidth using Silverman's rule of thumb under-smooths the density estimate. A subjective increase in smoothing can be applied to reduce this effect. In this case a value of the *Smoothing* parameter equal to 1.5 reduces the tendency for individual data points to effect the density estimate. This subjective value was selected as the smallest that effectively eliminates curvature of the contours around individual data points. Figure 14.3c shows the resulting plot with a smoothing value of 1.5, and 5 contour lines equally spaced over the density estimate.

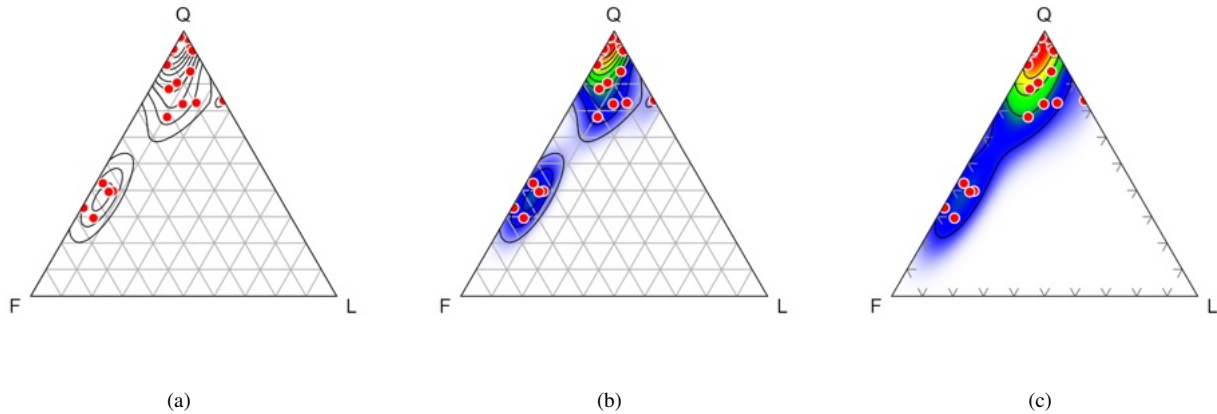


Figure 14.3: Contoured ternary plots of the Provenance.ods QFL data with default smoothing. The 10 contour levels, each represent 10%, of the density estimate. (a) Plot with contours only. (b) Plot with contours and color gradient. (c) Plot with a *Smoothing* value of 1.5 to minimize the effect of individual data points on the density estimate. This value was selected as the smallest that effectively eliminates curvature of the contours around individual data points. The plot has 5 contour levels, or 20%, of the density range.



## 15 UTM, Web Maps, and Google Earth

Spherical projections aid in the analysis of the directional data, such as rock foliations, but they do not display their spacial distribution. Understanding the spacial relationships of directional data is often one of the primary goals of geologists, particularly structural geologists. A number of tools are provided to assist with spacial analysis. These include coordinate conversions, integration with mapping websites, and integration with Google Earth.

### 15.1 UTM, Latitude, Longitude, Conversion

Coordinate conversion routines includes UTM to latitude, longitude and latitude, longitude to UTM conversions (Snyder, 1987; Dutch, 2015). Conversions among 14 datums, including WGS 1984 and NAD 1983, are available. The *Data - UTM Conversion* dialog (Figure 15.1) can be accessed when there are either easting, northing coordinates, or latitude, longitude coordinates. Select the conversion, and the desired datum. The hemisphere can be specified using the UTM grid zone, or by hemisphere.

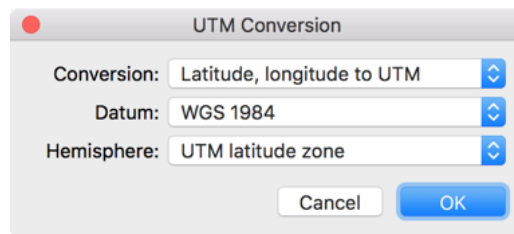


Figure 15.1: UTM, latitude, longitude conversion dialog.

### 15.2 Google and Web Maps

Numerous internet web sites offer access to maps, including street maps, topographic maps, and terrain maps, by entering search terms or geographic coordinates, Google Maps is probably the best known of these. The *Data - Show Location* commands can open many of these sites, including Google Maps, ACME Mapper (which has many topographic maps), Bing Maps, Coperix, HERE Maps, OpenStreetMaps, and others in your default browser. If a data set contains latitude and longitude coordinates, these can be opened directly by selecting a data row and entering the command. If the data contains UTM coordinates, they must first be converted to latitude, longitude as covered in Section 15.1.

To see the location displayed in your default browser, select a data row containing latitude, longitude coordinates, and choose a website from the *Data - Show Location* menu. Note that the web maps options all currently work in the United States, but their availability may depend on your location and region localization settings.

### 15.3 Google Earth

The program Google Earth is an invaluable tool in numerous areas, and has become widely used in geologic mapping. Google provides an interface using klm (keyhole markup language) files that can contain geographic coordinates, viewing instructions, and many other details. This interface can be used to display outcrop locations, and symbols for directional data measurements. Symbols are selected from the *Preference dialog Orientation Map Settings Symbols* pane where various symbols can be selected, as well as color, size, and line width. The symbol size is set in meters in the *KML Length* edit box, and the width in the *KML Width* edit box. To save the file, use the *File Export to Google Earth KML* command. Double click the resulting file to open in Google Earth.

An example KLM file, Diligencia Basin, Blair Schoene.kml, is given in the Example Data/Google Earth folder (Figure 2.8). This was created using the data file Diligencia Basin, Blair Schoene.xlsx

in the Example Data/StraboSpot folder, which was imported from the StraboSpot website (Section 2.7.1). The symbol for *bedding.S* was set to a red strike and dip symbol, with the *KML length* set to 5 meters, and *KML width* to 4.

A second example is shown in Figure 15.2, which is a Google Earth view of Grøvdalen, Møre og Romsdal, Norway (Western Gneiss District), showing 957 foliation strikes and 439 lineations color coded into five structural domains. The *KML length* here is set to 40 meters, and the *KML width* to 4. The example file Vollmer 1985 Grovudal.kml can be opened in Google Earth. A portion of this data set is used in Section 16.3. Data from Vollmer (1985).

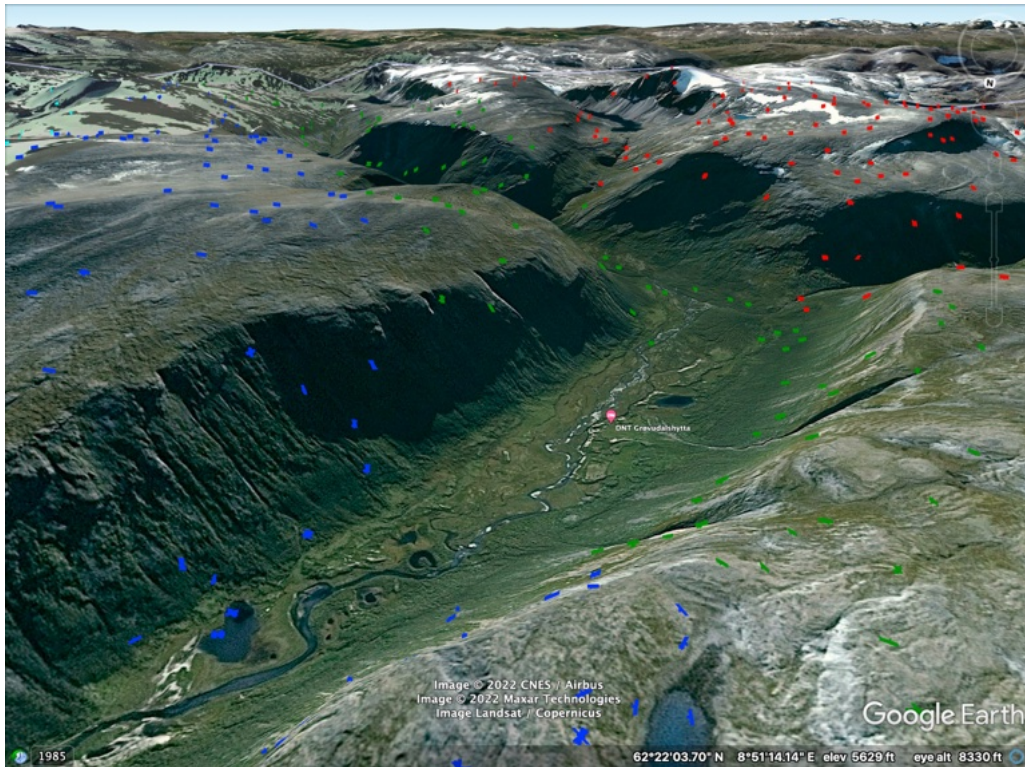


Figure 15.2: Google Earth image of Grøvdalen, Møre og Romsdal, Norway (Western Gneiss District), showing 957 foliation strikes and 439 lineations color coded into five structural domains displayed using a kml file created in Orient. The *KML length* here is set to 40 meters, and the *KML width* to 4. The example file Vollmer 1985 Grovudal.kml can be opened in Google Earth. A portion of this data set is used in Section 16.3. Grøvdalshytta, a mountain lodge, is indicated by the red icon at center. Local relief in the image is about 1086 m (3563 ft). Data from Vollmer (1985).

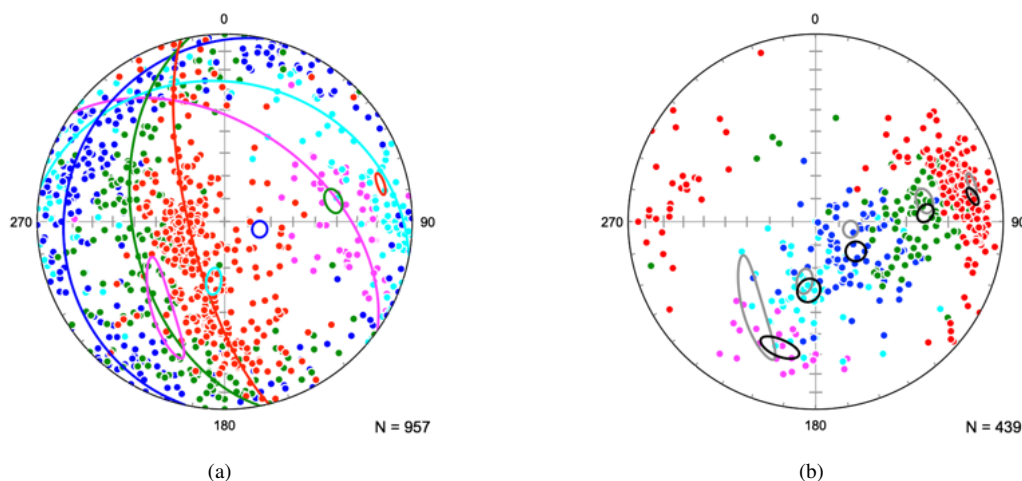


Figure 15.3: Schmidt plots of data from Grøvdalen, Møre og Romsdal, Norway (Western Gneiss District), Figure 15.2 color coded into five structural domains. Data from Vollmer (1985). (a) Poles to 957 foliation strikes with bootstrap 95% confidence cones on the minimum eigenvectors. (b). 439 lineations with bootstrap 95% confidence cones on the maximum eigenvectors. Light gray confidence cones are the foliation minima from b.

## 15.4 Tutorial: UTM Conversion and Web Maps

Open the file *World Earthquakes 1980-1990 Map* from the *Example Data/Seismology* folder, in any of the provided file formats. Note that the file *World Earthquakes 1980-1990 Sphere* is formatted to plot the data on a spherical projection, and is not the one for this tutorial. This data is a set of 14,229 earthquake epicenters between 1980 and 1990 with magnitudes greater than 4.5, data from NOAA. Select all the data rows using the *Select All* command.

Next, open the *UTM Conversion* dialog (Figure 15.1), select *Latitude, Longitude to UTM, WGS 1984*, and *UTM latitude zone*. Press *OK*, and the conversion is done. UTM grid zones and coordinates should now all be displayed, if not, select *View - Data Columns* and check *Zone, Easting*, and *Northing*.

Select one of the earthquake data rows, and select *Data - Show Location Google Maps Satellite*. As this is a global data set, you may need to zoom out before determining where you are. Data point ID 49 is an interesting example of a non-plate boundary seismic event. Zoom out from there to see Sedan Crater, about 5 km to the north, created in 1962 as part of the short lived Operation Plowshare, a program to investigate the feasibility of using nuclear explosions for large civilian excavation projects, such as harbors and canals.

## 15.5 Tutorial: Web Maps and Google Earth

Open the file *Sky Top* from the included *Example Data/Google Earth* folder, in any of the provided file formats. This is a demonstration file with simulated geologic data for use in this tutorial. You may wish to use the *View - Data Columns* command to close some of the unused columns.

The file contains the latitude, longitude coordinates of one marker location, and eight simulated data points of four different types of geologic data, bedding, cleavage, joints, and slickenside lineations. For web map access, select one of the locations and choose a websites from the *Data Show Location* menu. The selected web map will display the location of the data point, you can then zoom in, or change display options as needed.

In order to display directional data symbols, as well as location, KML files are written for Google Earth, so directional symbols and complete data sets can be viewed. Open the *Preferences* dialog by clicking on its icon, select the *Orientation Map Settings* option, and the *Symbols* pane. Select the data types from the pulldown menu, and check just one symbol for each data type. For J, check *Strike*, select a strike line with two ticks, and set *Stroke Color* to light green. For L, check *Line*, select an

arrow symbol, and set *Stroke Color* to magenta. For S0 check *Strike*, select a strike line symbol, and set *Stroke Color* to red. For S1, check *Strike*, select a strike line with a tooth, and set *Stroke Color* to red. Press *OK* when done.

Save the file as *Sky Top.kml* using the *File Export to Google Earth KML* command. Double click on it to open in Google Earth. The location should come into view with the data symbols (Figure 15.4). For a quicker demonstration, there is a copy of the resulting *Sky Top.kml* file in the *Example Data/Google Earth* folder.



Figure 15.4: Example data (simulated) from the file *Sky Top* viewed in Google Earth. Example data types are S0 (bedding, red), S1 (cleavage, blue), J (joints, green), and a lineation (L, magenta).

## 16 Orientation Fields and Domains

Spherical projections aid in the analysis of directional data, but they do not show their spacial distribution. This chapter describes tools for analyzing the spacial variation of directional data, including orientation fields and structural domain analysis. Orientation fields are a way to look for regional patterns in data by defining subdomain *eigenfoliations* and *eigenlineations* on a grid over the area (Vollmer, 1985, 1990). One method is to define discrete subdomains that include all data within them, for example a one kilometer square area. A second method is to apply a weighting function to produce area-smoothed orientation values. The fields are defined by calculating an orientation tensor at grid locations, and using its eigenvectors and eigenvalues to characterize the fabric.

### 16.1 Orientation Fields

There are many geologic problems related to the change in the orientations of structural features across a map area. For example, a common problem in mapping areas of complex geologic structure is to identify cylindrical fold domains within a map area (Ramsay, 1967; Marshak and Mitra, 1988; Fossen, 2016). Figure 16.1a is a Schmidt scatter plot of poles to foliations from an area in the Doverfjell mountains, Norway (Vollmer, 1985), and Figure 16.1b is a contour plot of the data. Their spacial distribution is shown in Figure 16.2a, plotted using the *Orientation Map* command. The strike tick marks are the horizontal projections of the dip lines using the  $\perp$  symbol, so planes with steeper dips have shorter tick marks.

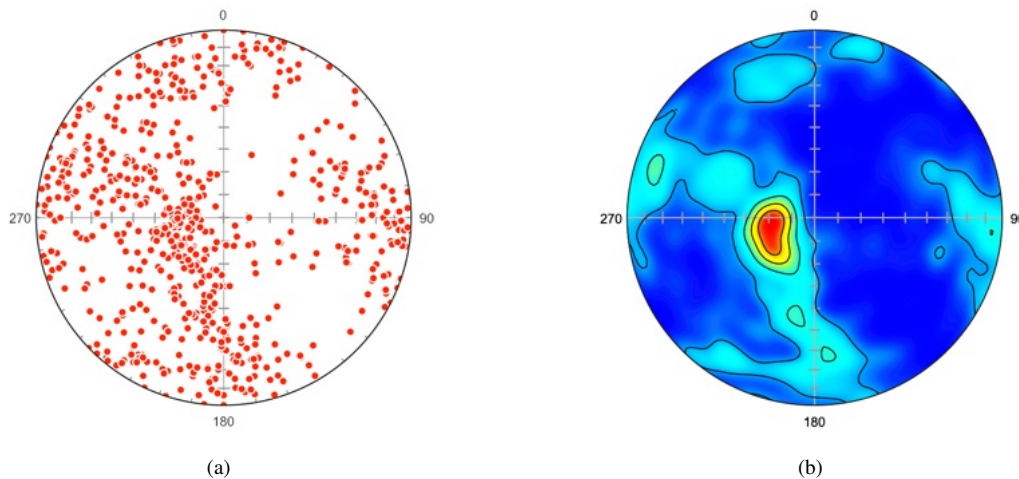


Figure 16.1: Schmidt plot of poles to 625 foliation planes from the Doverfjell Mountains, Norway, a subset of data from Vollmer (1985). (a) Scatter plot. (b) Contour plot with contour levels at 20% density.

The geometry of the structure defined by the foliations in Figure 16.2a is not obvious. Figure 16.2b is a subdomain orientation field defined on a one kilometer grid. Note that the number of data points within each subdomain varies, and that each has a discrete boundary. As in Figure 16.2a, the strike tick marks represent the horizontal projections of the dip lines using the  $\perp$  symbol.

Figures 16.3a and 16.3b are *weighted orientation fields* where each grid node is generated as a weighted sum of all other data points. In Figure 16.3a the strike tick marks represent the horizontal projections of the dip lines, while in Figure 16.3 the same eigenfoliations are shown as projected dip lines, so steeper dips are displayed with shorter lines. The grid has 13 by 16 nodes spaced at a one kilometer interval.

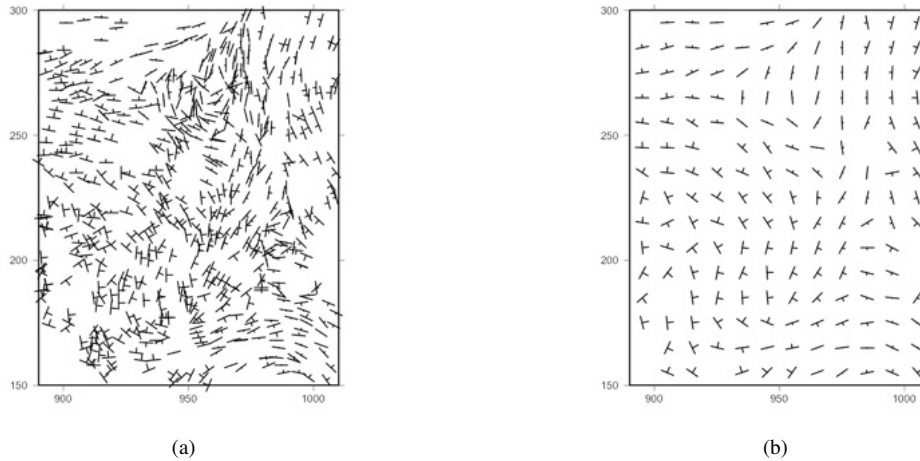


Figure 16.2: Orientation maps of foliation strikes of the data shown in Figure 16.1. The strike tick marks represent the horizontal projection of the dip line using the  $\vdash$  symbol, so shorter tick marks indicate steeper dips. Grid units are decameters. (a) Map of all the foliation data, see Figure ?? for a Google Earth image of the full data set. (b) Subdomain field of eigenfoliation strikes generated from the data using 12 by 15 subdomains, each one square kilometer.

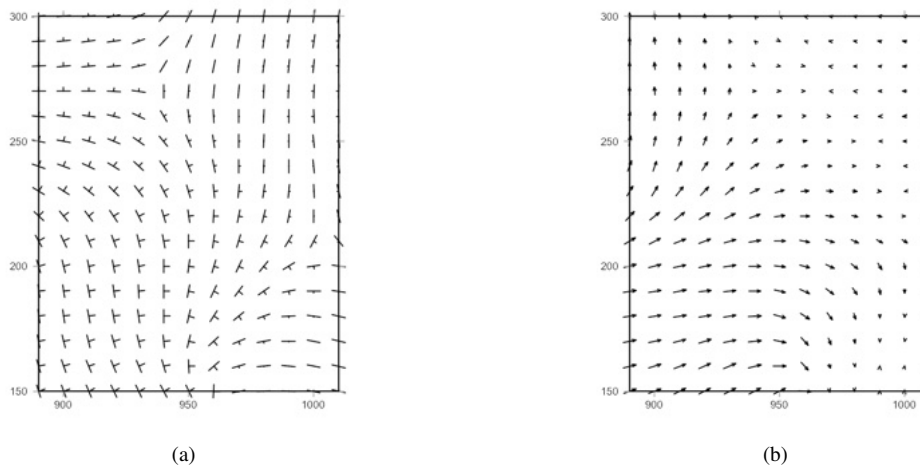


Figure 16.3: *Weighted orientation field* of eigenfoliations generated from the data shown in Figure 16.2a. The grid has 13 by 16 nodes spaced at a one kilometer interval. Each node is calculated as a distance weighted sum of the entire data set. Grid units are decameters. (a) Field shown using strike symbols,  $\vdash$ . The tick marks are the horizontal projection of the dip line, so shorter ticks represent steeper dips. Each (b) Field represented as dip lines. The arrows are the horizontal projections of the dip line, so shorter arrows have greater plunges.

## 16.2 Structural Domain Analysis

*Structural domain analysis* is done by attempting to maximize a quantity, or index, related to a given problem (Vollmer, 1985, 1990). Several indexes can be maximized, including point, girdle, and cylindricity indexes (Section 7.1). To locate areas of cylindrical folding the cylindricity index,  $B$  (Eq 7.4), is maximized

$$\begin{aligned}
 B &= P + G \\
 &= 1 - R \\
 &= 1 - 3\varepsilon_3
 \end{aligned}
 \tag{16.1}$$

where  $\varepsilon$  are the normalized eigenvalues of the orientation tensor,  $\Omega$  (Eq 4.6). For a set of  $k$  domains the normalized sum of the products of the domain indexes  $[B_1, B_2, B_3, \dots, B_k]$  and the number of data

points within each domain  $[n_1, n_2, n_3, \dots, n_k]$

$$B^* = \frac{1}{n} \sum_{i=1}^k B_i n_i \quad (16.2)$$

is maximized. The value of  $B^*$  varies from 0 to 1, with 1 indicating that all domains are perfectly cylindrical, or non-uniform. Maximizing this value is identical to minimizing uniformity.

The settings for the *Orientation Map* command are in the *Preferences* dialog *Orientation Map* panels. For each data point, or field value, it is possible to plot a symbol in four directions, *Line*, *Dip Line*, *Strike*, and *Strike 180* (Figure 16.4a).

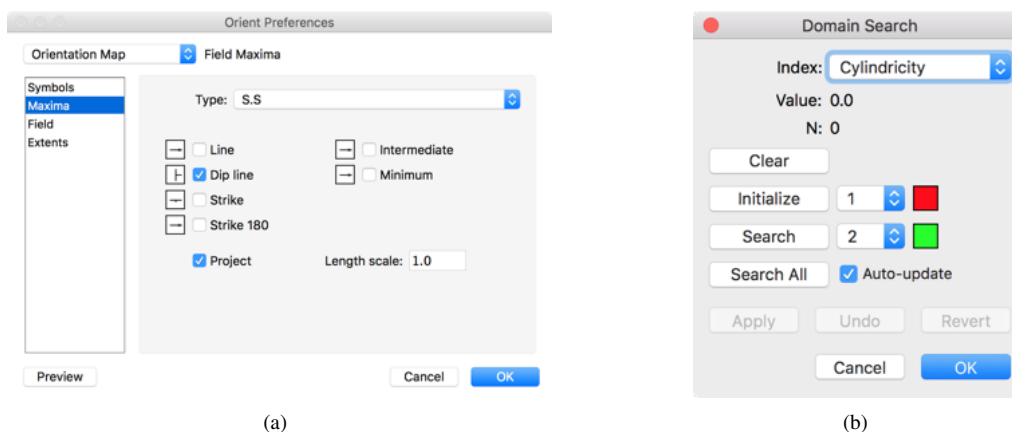


Figure 16.4: (a) Preference dialog showing the *Orientation Map Symbols* pane. The options shown are to project dip lines using the  $\perp$  symbol as in Figure 16.2. (b) The *Domain Search* dialog box. The *Auto-update* option automatically updates the data domains and data plots.

*Line* is the direction of a line, or plane normal ( $\theta$ ). *Dip line* is the opposing direction ( $\theta + 180^\circ$ ), and used to display a plane's dip direction. *Strike* is the plane strike ( $\theta + 90^\circ$ ), and *Strike 180* is the opposing direction ( $\theta - 90^\circ$ ). Only *Line* and *Dip line* can be projected. To display a projected strike symbol, select *Dip line* and the symbol  $\perp$ . The *Length scale* scales the length of the symbol. The KLM settings are for the display of data in Google Earth (Section 15.3).

If you wish to use latitude and longitude as the map coordinates, instead of UTM, enter them as signed decimal degrees in the spreadsheet columns for Northing and Easting. Then, in the *Preferences* dialog *Orientation Map - Extents* pane, enter the *Scale* factor for the latitude of the center of the map. The scale factor is the secant (cosine - 1) of the latitude, or can be measured off the map by dividing the distance between two lines of latitude by the distance between two lines of longitude that have an equal angular distance, such as 1 minute of arc. For example, the scale factor at  $0^\circ$  latitude is 1.000, at  $45^\circ$  it is 1.414, and at  $80^\circ$  it is 5.759.

To conduct a domain search, define the extents of the map area in the *Extents* panel, select *Subdomain Method* in the *Field* panel, along with the number of subdomains. Then use the *Domain Search* command, which displays the dialog shown in Figure 16.4b. This is used to maximize the fabric index using an automated search process. The *Value* is the current value of the index, and *N* is the number of points used to calculate it. Domains are numbered from 1 to 9, zero represents an unassigned domain. *Clear* resets all subdomains to zero. *Initialize* sets all domains to the active search domain. *Search* will attempt to grow the search domain. The search iteratively checks to see if subtracting a subdomain from one domain and adding it to the search domain will increase the index. It can only do so if both domains remain connected. *Search All* cycles through all active domains and searches each.

If the *Auto-update* option is on, the data domains and all open plots will automatically be updated each time the domain configuration changes. This is useful to display Schmidt plots and a PGR plot during a search, but it takes longer to calculate. Use the *New Plot View* command to display additional Schmidt plots to view each domain's data separately. If *Auto-update* is not selected, the *Apply* button

is used to update the data Domain field in the spreadsheet to the current domain configuration, and update all open data plots.

The *Undo* button steps the domain configuration back to the previous state, if *Auto-update* is selected the data domains will be changed and any open data plots will be updated. *Revert* sets the domain configuration back to the state when the *Domain Search* dialog was opened. *Cancel* additionally resets the data Domain field to its state before the search started, and ends the search. *OK* accepts the domain configuration and data domains, and ends the search.

The domains can also be edited manually, moving the mouse over the map will display subdomain information in the status bar, and clicking on a subdomain will add it to the search domain if possible. Dragging the mouse will select a rectangular block of subdomains. Note that only subdomains in the block that can be added while maintaining connectivity, will be added. The constraint that the domains remain connected can cause edge effects, and vacant subdomains may also effect connectivity. The general procedure is to do a search on a desired number of domains, then manually edit them, and search again to see if a better solution is found. The *Auto-update* option may be used to automatically updates all data plots, normally one or more Schmidt plots and a PGR diagram.

Subdomains with Domain = 0 are not required to be contiguous, and it is not possible to do an automatic search on them. They will not be added or removed from a domain during an automatic search for other domains. If Domain 0 is selected in the *Search* drop down list, the *Search* button will be disabled, but it is then possible to use the mouse to set subdomains to Domain = 0. This allows areas of the map to be excluded from the search, and is useful if the map area is not rectangular.

Once the search is completed, if *Auto-update* is off, press *Assign* to assign domains to each of the data points, then press *OK* to end the search. The domains are added as attributes of the data, use the *View - Data Columns* to view the Domain column. Extended data types are named using a dot namespace notation, appending domain extensions, D1 to D9, to the data type so each domain can be treated as a separate data set. To update the results during a search, set *Auto-update* on or click on the *Apply* button. This will apply the domains to the data and will update other graphs that are open. If a spherical projection of the data is open it is possible to color code the data by domain to get a visualization of the distribution.

### 16.3 Tutorial: Domain Analysis

Open the file Vollmer 1985 included in the Example Data/Folds folder, in any of the provided file formats. This is the data displayed in Figures 16.1, 16.2, and 16.3, 625 foliation planes from the Doverfjell mountains, Norway, a subset of the data from Vollmer (1985). See Figure ?? for a Google Earth image of the full data set. While folds are clearly present, the spherical projections (Figure 16.1) do not display a girdle pattern that would indicate cylindrical folding. Complex fold patterns are also suggested by outcrops in this area, and the adjacent Trollheimen range, that contain spectacular sheath folds. The map of foliations (Figure 16.2) shows some areas of consistent orientation, but the location of cylindrical domains is not obvious.

Click on the *Orientation Map* icon to display a map of the foliation data, then in the *Orientation Map* window, click on the *Preferences* icon. In the *Orientation Map - Extents* pane

- Uncheck *Auto scale*.
- Enter 890 for the minimum X (Easting) Map coordinate.
- Enter 150 for the minimum Y (Northing) Map coordinate.
- Enter 1010 for the maximum X Map coordinate.
- Enter 300 for the maximum Y Map coordinate.
- Leave the X and Y scale factors at 1.
- Set *Ticks* on with an increment of 50 (the units are decimeters), a length of 4 points, *Outside*.

To view the data, uncheck all symbols in the *Maxima* pane, check only *Dip line* and *Project* in the *Symbols* pane, and select the ⊢ symbol. The result should appear as in Figure 16.2a.

To set up the domain search, uncheck *Dip line* in the *Symbols* pane, check only *Dip line* and *Project* in the *Maxima* pane, and again select the ⊢ symbol. In the *Field* pane



- Set the *Method* to *Subdomain*.
- Uncheck *Directed*.
- Enter 12 for the number of X subdomains.
- Enter 15 for the number of Y subdomains, giving 1 kilometer square subdomains.
- Check *Visible*.

To begin the domain search, select the *Plot - Domain Search* command from the menu (Figure 16.4b)

- Press *Initialize* to set all subdomains to 1.
- Press *Search* to grow domain 2.
- Change the search domain to 3, and press *Search* again.

The result is shown in Figure 16.5a, which has a cylindricity index,  $B^* = 0.738$ . There are some edge effects, particularly where domain 1 (red) wraps around the other two. Move the mouse over the map to see information about each subdomain. Clicking on one will change it to the current search domain, if all domains remain connected. If you have the *Auto-update* option on, the domains will be automatically updated in the spreadsheet and on any open data or PGR plots. Use the *New Plot View* command if you wish to open one spherical projection for each domain.

Edit the domains by selecting a search domain and clicking on the map. In particular, clean up the areas where edge effects are obvious. In this case, domain 1 (red) wraps around the other two, this is more likely an edge artifact rather than a geologically viable solution. When done, go back to the dialog and search on each domain again. If the domains are stable, they will not change. Repeat this iterative process until the index no longer increases. Figure 16.5b shows a stable solution with  $B^* = 0.851$ , an improvement over the previous value. Press *OK* when done.

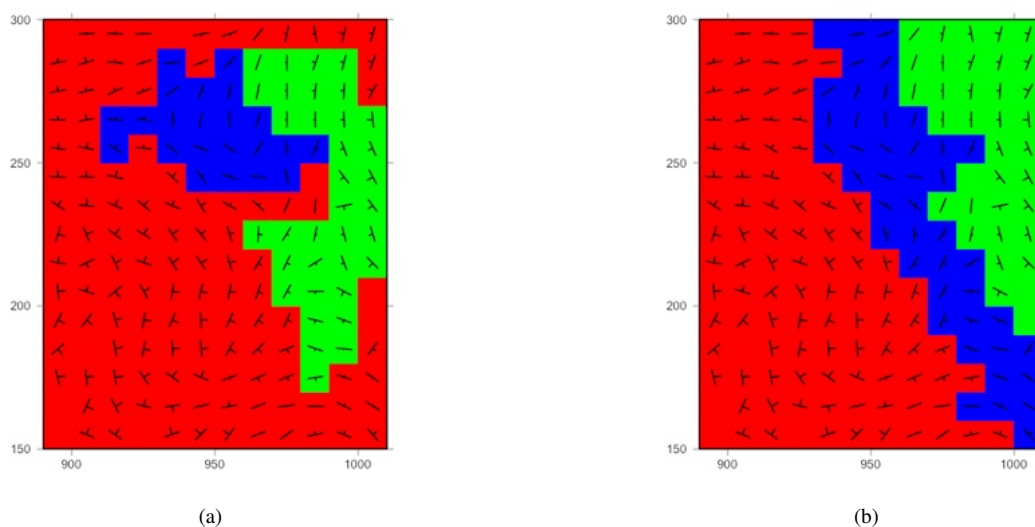


Figure 16.5: Results of domain searches to maximize cylindricity,  $B^*$ . (a) Configuration after an initial automatic domain search for three domains maximizing cylindricity. This configuration has a mean cylindricity index,  $B^* = 0.738$ . (b) Configuration after iterative domain editing followed by automatic searches. This configuration has a mean cylindricity index,  $B^* = 0.851$ .

Now open a spherical projection by clicking on the *Spherical Projection* icon in the data spreadsheet window, and then the *Preferences* dialog. In the *Spherical Projection - Net* pane, uncheck *Great circles* and *Small circles* for the Y axis, check *Major tick marks* for the X, Y, and Z axes, and *Axes*.

In the *Symbols* pane, uncheck *Symbol* for data type S.S. Then for data types S.S.D1, S.S.D2, and S.S.D3, the new data types, set the symbol *Fill* colors to red, green, and blue respectively. Set the symbol sizes to 6, and the symbol *Stroke color* to white. In the *Maxima* pane, select only the *Minimum eigenvector* for S.S.D1, S.S.D2, and S.S.D3, and set *Minimum eigenvector Great circle* on

with a *Stroke width* of 2. The result should be as in Figure 16.6a. Note that the three domains show well defined girdles. Turning off the data symbols, and turning on 95% bootstrap confidence cones gives a synoptic diagram, Figure 16.6b, which suggests refolding of earlier folds about a northwest plunging axis.

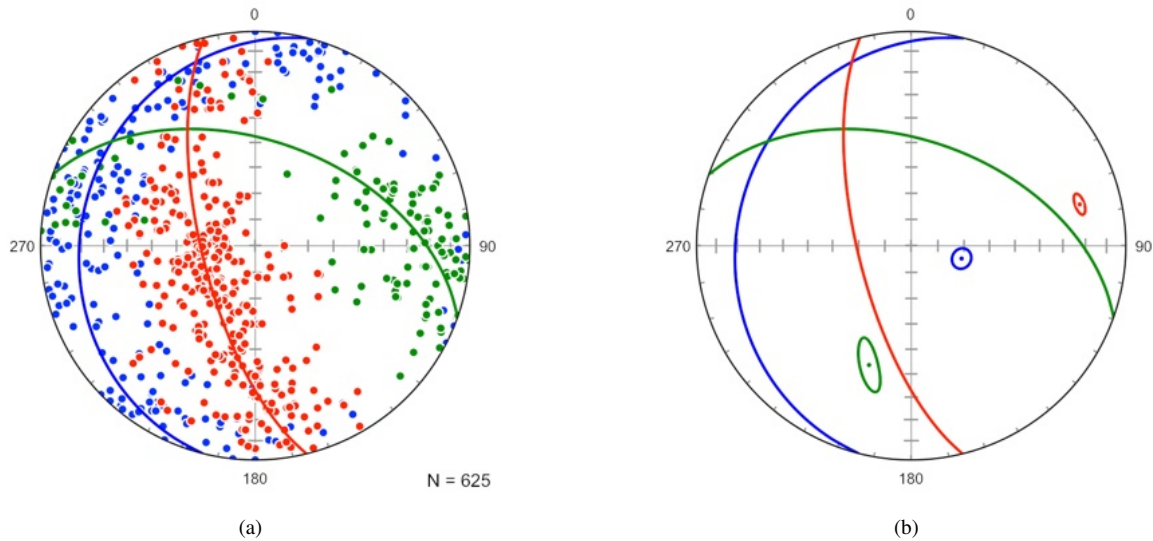


Figure 16.6: Synoptic Schmidt plots of data from Figure 16.2a after domain analysis. The plot is color-coded red, blue, and green by domain, and the great circle normal to the minimum eigenvector drawn for each domain. (a) Poles to foliations. (b) Plot with 95% confidence cones about each domain's minimum eigenvector.

Next, open a triangular fabric plot (Point Girdle Random) using the *PGR Plot* icon in the data spreadsheet window. In the *Preferences* dialog *PGR Plot* pane set the *Symbol Fill Color* for S.S to white, and then for S.S.D1, S.S.D2, and S.S.D3, to red, green, and blue respectively, and set the symbol sizes to 10. In the *Grid* pane uncheck *Minor Grid lines* and *Tick marks*. The resulting triangular fabric plot (Figure 16.7a) shows the relative changes in cylindricity from the whole area to the three domains. Note that domain 2 (green) has the strongest point distribution, and domain 3 (blue) has the strongest girdle distribution.

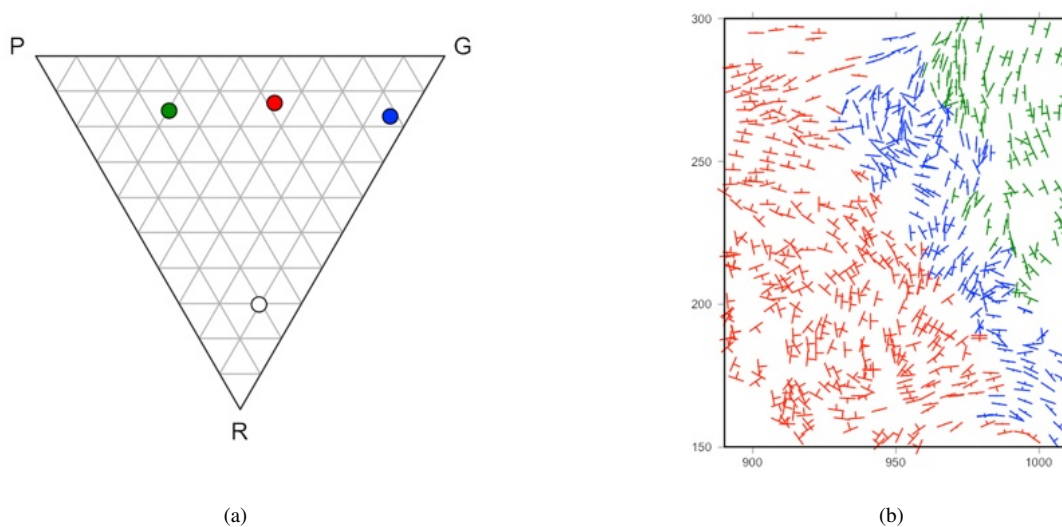


Figure 16.7: (a) Triangular fabric plot of the domains compared to the total data set (white). The search process has resulted in three domains with a significant increase in cylindricity, which increases upward on the plot. (b) Data as in Figure 16.2a color coded by domain.

To display the data color coded by domain, turn off the display of the maxima in the *Orientation*

Map - Maxima pane, turn off display of data type S.S symbols, and set *Dip direction* on using the  $\perp$ , and set the *Stroke Color* for S.S.D1, S.S.D2, and S.S.D3, to red, green, and blue respectively, and set *Project* on, giving the map in Figure 16.7b.

As a final step, prepare contoured Schmidt plots (Section 4.10) of the foliation poles of the three domains (Figure 16.8). See Vollmer (1985, 1990) for additional details on the domain search process.

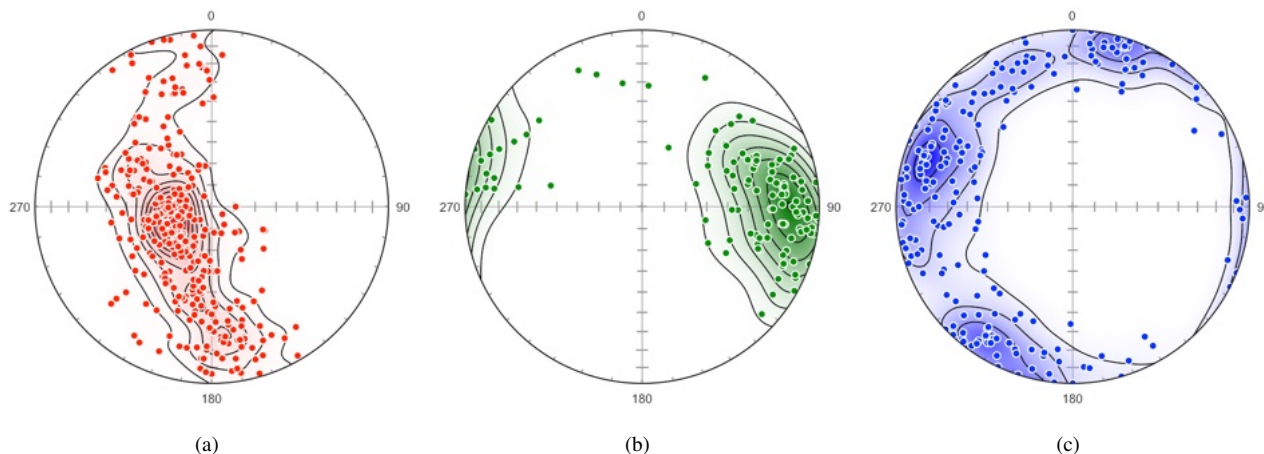


Figure 16.8: Schmidt plots of poles to foliations for the final domains shown in Figure 16.5. Contours are multiples of uniform density. The color gradient is linear RGB from transparent white (A) to opaque color. (a) Domain 1 (red). (b) Domain 2 (green). (c) Domain 3 (blue).

The search process produces well-defined domains with this data set, however domains in other areas may not always be easily identified. A few suggestions are

- It is suggested that, as was done in this area, lineations and minor fold axes be used to independently verify the domains by maximizing their P index (Vollmer, 1985, 1990).
- A systematic progression across the domains, as here, suggests a plausible solution has been found. Fault-bounded blocks might not be systematic, but should be discrete if rotation has occurred.
- Open a Schmidt plot for each domain and a PGR plot (Figure 16.7a). The domain symbols on the PGR plot should move upward, and in general should all be higher than the symbol for all the data.
- Create a synoptic plot such as Figure 16.6a, with eigenvector maximum, minimum, great circle about the minimum, and 95% bootstrap confidence cones to show how distinct and robust the domains are.
- Avoid gerrymandering, if domains wiggle around it may be possible to get higher numbers even though it does not make geological sense.
- Holes, subdomains without data, can be a problem, try interpolating through them using geologic judgment.
- Once a plausible solution has been found on a coarse grid, try a finer grid to refine the domains.
- A domain search is a tool, use geologic sense and knowledge of the area to assist in defining reasonable structural domains.

## Acknowledgements

Orient was initially released in 1986, based on algorithms developed at the University of Minnesota, where Peter J. Hudleston provided support and mentoring. The Computer Oriented Geological Society (COGS) provided distribution channels via modem prior to the World Wide Web. Eric Erslev, Colorado State University, was a supportive early, pre-Web, user. The program's name is derived from the orientation tensor (Scheidegger, 1965; Watson, 1966). Orient has undergone decades of development, and translations into multiple computer languages and operating systems. I have tried to reference the authors of critical algorithms, however it is not possible to cite the thousands of programmers who developed mathematical routines, algorithms, compilers, and development environments over many decades. I can only say thanks, and offer a tip of my cap.

A major revision of the user manual was prepared for *Teaching Structural Geology, Geophysics, and Tectonics in the 21st Century, On the Cutting Edge*, held in 2012 at the University of Tennessee, Knoxville, and that conference spurred renewed development. I thank the conveners Barbara Tewksbury, Gregory Baker, William Dunne, Kip Hodges, Paul Karabinos, and Michael Wyession. Eric Erslev, Steven Wojtal, Haakon Fossen, Christian D. Klose, Josh Davis, Sarah Titus, Yvette Kueiper, Peter Hudleston, Robert Bauer, Mark Brandon, Dazhi Jiang, Jonathan Saul Caine, Willem Langenberg, and William S.F. Kidd provided helpful suggestions or discussions leading to improvements. Haakon Fossen kindly hosted me at the University of Bergen for a sabbatical leave in 2015, where many of his suggestions were implemented.

In 2016 a short on the analysis of geologic directional data using Orient was given at the *Structural Geology and Tectonics Forum*, at Sonoma State University, California. Thanks to Matty Mookerjee and the organizers, as well as the short course participants, who provided helpful feedback.

Thanks to Emily Lubich (City College of New York), Chistopher Gahn (Vassar College), Ben Michael Frieman (Colorado School of Mines), Tammy Xinran He (Colorado School of Mines), Steven Coombes (Rio Tinto Exploration, Canada), Andrea Bistacchi (University of Milano-Bicocca, Italy), John Waldron (University of Alberta), Raphaël Gottardi (University of Louisiana at Lafayette), William Howard (Precious Metals Exploration), Kristopher Aadahl (SUNY New Paltz), Andrew C. Duncan (ADAW Pty Ltd, Australia), Filip Tomek (Czech Academy of Sciences), Cleber Peralta Gomes Júnior (University of São Paulo), Dinarte Lucas (Brazil), Hailey Springston (SUNY New Paltz), Scott M. Larson (HighPoint Resources, Colorado), Allan López (University of Costa Rica), Michael Frothingham (United States Geological Survey & University of Colorado Boulder), Matthew Ruggiero (SUNY New Paltz), Anastasia Kushnareva (Saint Petersburg University), Theron Finley (University of Victoria), Cris Carman (CEC Geology, Rhode Island), Steven Scott (Consultant), Brandon Lutz (Rangefront Mining Services, Oregon), Shahla Feizi (University of Oklahoma), Tobias Eberlei (University of Vienna), Jeffrey Webber (Stockton University), Bobak Karimi (Wilkes University) for suggestions and bug reports.

The colormaps coolwarm (smooth cool warm) by Kenneth Moreland (ParaView), viridis, plasma, inferno, and magma by Nathaniel J. Smith, Stefan van der Walt, and Eric Firing (Matplotlib) are licensed under BSD-compatible licenses (Moreland, 2015). Anton Mikhailov released the turbo colormap (Mikhailov, 2019). Bessel functions are from Jean-Pierre Moreau based on code from Donald E. Amos, and Tuan Dang Trong. Some random number functions are from Alan Miller and ESB Consultancy. Some mathematical functions, including fast Fourier transforms, curve fitting, eigenvalues, matrix inversion, and function minimization, are from Jean Debord and Viatcheslav V. Neseterov (LPGL). An extensive team of developers and contributors maintain the Free Pascal compiler (GPL/LPGL) and Lazarus IDE (GPL/LGPL).

## Disclaimer

Mention of the use of research techniques by Federal employees does not imply endorsement by the U.S. Government.

## References

- Aguilón F d (1613) *Opticorum libri sex philosophis juxta ac mathematicis utiles* (Six books of optics, useful for philosophers and mathematicians alike). Anvers
- Allmendinger R W (2019) Faultkin. <https://www.rickallmendinger.net/faultkin>
- Andrews R J (2022) Florence nightingale's data revolution. *Scientific American* 327(2):78–85
- Angelier J (1979) Determination of the mean principal directions of stresses for a given fault population. *Tectonophysics* 56:T17–T26
- Angelier J (1984) Tectonic analysis of fault slip data. *Journal of Geophysical Research* 89(B7):5835–5848
- Angelier J, Mechler P (1977) Sur une méthode graphique de recherche des contraintes principales également utilisable en tectonique et en sismologie: la méthode des dièdres droits. *Bulletin de la Société géologique de France* 19(6):1309–1318
- Apperson K D, Frohlich C (1988) Sums of moment tensors for earthquakes near subduction zones. *EOS, Transactions of the American Geophysical Union* 69:1438
- Arvo J (1992) Fast random rotation matrices. *Graphics Gems III* :117–120
- Badgley P C (1959) *Structural methods for the exploration geologist*. New York: Harper and Brothers
- Barnes J W (1995) *Basic Geologic Mapping*. Milton Keynes, UK: Open University Press, 3 edition
- Barth N C, Hacker B R, Seward G G, Walsh E O, Young D, Johnston S (2010) Strain within the ultrahigh-pressure Western Gneiss region of Norway recorded by quartz CPOs. *Geological Society Special Publication* 335:663–685, ISSN 03058719
- Bemis S P, Weldon R J, Carver G A (2015) Slip partitioning along a continuously curved fault: Quaternary geologic controls on Denali fault system slip partitioning, growth of the Alaska Range, and the tectonics of south-central Alaska. *Lithosphere* 7(3):235–246, ISSN 1941-8264
- Berens P (2009) *CircStat: A MATLAB Toolbox for Circular Statistics*. *Journal of Statistical Software* 31(10):1–21, ISSN 00085286
- Best D J, Fisher N I (1986) Goodness-of-fit and discordancy tests for samples from the Watson distribution on the sphere. *Australian Journal of Statistics* 28(1):13–31
- Billings M P (1942) *Structural Geology*. New York: Prentice-Hall
- Billings M P (1954) *Structural Geology*. New York: Prentice-Hall, 2 edition
- Bingham C (1964) Distributions on the sphere and on the projective plane. Ph.D. thesis, Yale University, New Haven, Connecticut
- Bingham C (1974) An antipodally symmetric distribution on the sphere. *The Annals of Statistics* 2(6):1201–1225
- Blenkinsop T G (2006) Kinematic and dynamic fault slip analyses: implications from the surface rupture of the 1999 Chi-Chi, Taiwan, earthquake. *Journal of Structural Geology* 28(6):1040–1050, ISSN 01918141
- Boneh Y, Morales L F G, Kaminski E, Skemer P (2015) Modeling olivine CPO evolution with complex deformation histories: Implications for the interpretation of seismic anisotropy in the mantle. *Geochemistry Geophysics Geosystems* 16(1):267–300, ISSN 0012821X
- Bott M (1959) The mechanics of oblique slip faulting. *Geological Magazine* 96(2):109–117
- Bucher W H (1944) The stereographic projection, a handy tool for the practical geologist. *Journal of Geology* 52(3):191–212
- Byerlee J (1978) Friction of Rocks. *Pageoph* 116:615–626
- Caine J C (2001) Fracture network, fault zone, and geologic data collected from the Turkey Creek watershed, Colorado Rocky Mountain Front Range. Open File Report 01-416, United States Geological Survey, Denver, CO
- Célérier B, Etchecopar A, Bergerat F, Vergely P, Arthaud F, Laurent P (2012) Inferring stress from faulting: From early concepts to inverse methods. *Tectonophysics* 581:206–219, ISSN 00401951
- Chatzaras V, Kruckenberg S C, Cohen S M, Medaris Jr L G, Withers A C, Bagley B (2016) Axial-type olivine crystallographic preferred orientations: The effect of strain geometry on mantle texture. *Journal of Geophysical Research: Solid Earth* 121(7):4895–4922
- Cheaney R F (1983) *Statistical Methods in Geology*. London: George Allen & Unwin
- Compton R R (1966) Analyses of Pliocene-Pleistocene Deformation and Stresses in Northern Santa Lucia Range, California. *Geological Society of America Bulletin* 77(September):1361–1380
- Cowan E J (1999) Magnetic fabric constraints on the initial geometry of the Sudbury Igneous Complex: A folded sheet or a basin-shaped igneous body? *Tectonophysics* 307(1-2):135–162, ISSN 00401951
- Daly L, Piazzolo S, Lee M R, Griffin S, Chung P, Campanale F, Cohen B E, Hallis L J, Trimby P W, Baumgartner R, Forman L V, Benedix G K (2019) Understanding the emplacement of Martian volcanic rocks using petrofabrics of the nakhlite meteorites. *Earth and Planetary Science Letters* 520:220–230, ISSN 0012821X
- Darlington V, Blenkinsop T, Dirks P, Salisbury J, Tomkins A (2016) The Lawn Hill annulus: An Ordovician meteorite impact into water-saturated dolomite. *Meteoritics and Planetary Science* 51(12):2416–2440, ISSN 10869379
- Davis J C (1986) *Statistics and Data Analysis in Geology*. New York: Wiley, 2 edition
- Davis J C (2002) *Statistics and Data Analysis in Geology*. New York: Wiley, 3 edition
- Davis J R (2019) The geologygeometry library for R. <http://www.joshuadavis.us/software/index.html>
- Davis J R, Titus S J (2017) Modern methods of analysis for three-dimensional orientational data. *Journal of Structural Geology* 96:65–89, ISSN 01918141
- De Sitter L U (1956) *Structural Geology*. London: McGraw-Hill Book Company, Inc
- Diggle P J, Fisher N I (1985) Sphere: a contouring program for spherical data. *Computers & Geoscience* 11:725–766
- Donn W L, Shimer J A (1958) *Graphic Methods in Structural Geology*. New York: Appleton-Century-Crofts, Inc.
- Downs T D (1972) Orientation statistics. *Biometrika* 59(3):665–676
- Dutch S (2015) Converting utm to latitude and longitude (or vice versa)
- Dziewonski A M, Chou T A, Woodhouse J H (1981) Determination of earthquake source parameters from waveform data for studies of global and regional seismicity. *Journal of Geophysical Research* 86:2825–2852
- Ekström G, Nettles M, Dziewonski A M (2012) The global CMT project 2004–2010: Centroid-moment tensors for 13,017 earthquakes. *Physics of Earth and Planetary Interiors* 200–201:1–9
- Erslev E A, Holdaway S M, Mearns S A O, Jurista B, Selvig B (2004) Laramide minor faulting in the Colorado Front Range. *New Mexico Bureau of Geology & Mineral Resources Bulletin* 160(Gries 1983):181–203
- Erslev E A, Larson S (2006) Testing Laramide hypotheses for the Colorado Front Range arch using minor faults. *Mountain Geologist* 43(1):45–64, ISSN 0027254X (ISSN)
- Esmailzadeh A, Shahriar K (2019) Optimized Fuzzy Cmeans – Fuzzy Covariance – Fuzzy Maximum Likelihood Estimation Clustering Method Based on Differential Evolutionary Optimization Algorithm for Identification of Rock Mass Discontinuities Sets. *Periodica Polytechnica Civil Engineering* ISSN 1587-3773, 0553-6626
- Ester M, Kriegel H P, Sander J, Xu X (1996) A density-based algorithm for discovering clusters in large spatial databases with noise. In *Proceedings of the Second International Conference on Knowledge Discovery and Data Mining, KDD'96*, AAAI Press, 226–231
- Falus G, Tommasi A, Soustelle V (2011) The effect of dynamic recrystallization on olivine crystal preferred orientations in mantle xenoliths deformed under varied stress conditions. *Journal of Structural Geology* 33(11):1528–1540, ISSN 01918141
- Fisher N I (1989) Smoothing a sample of circular data. *Journal of Structural Geology* 11(6):775–778, ISSN 01918141
- Fisher N I, Lewis T, Embleton B J J (1987) *Statistical Analysis of Spherical Data*. Cambridge University Press
- Fossen H (2016) *Structural Geology*. Cambridge: Cambridge University Press, 2 edition

- Fossen H, Cavalcante G C G (2017) Shear zones – A review. *Earth-Science Reviews* 171(January):434–455, ISSN 00128252
- Frohlich C (1992) Triangle diagrams: ternary graphs to display similarity and diversity of earthquake focal mechanisms. *Physics of the Earth and Planetary Interiors* 75(1-3):193–198, ISSN 00319201
- Fujita A, Takahashi D Y, Patriota A G (2014) A non-parametric method to estimate the number of clusters. *Computational Statistics and Data Analysis* 73:27–39, ISSN 0167-9473
- García-Portugués E (2013) Exact risk improvement of bandwidth selectors for kernel density estimation with directional data. *Electronic Journal of Statistics* 7:1655 – 1685
- Gébelin A, Teyssier C, Heizler M T, Mulch A (2015) Meteoric water circulation in a rolling-hinge detachment system (northern snake range core complex, Nevada). *Bulletin of the Geological Society of America* 127(1-2):149–161, ISSN 19432674
- Giorgis S, Michels Z, Dair L, Braudy N, Tikoff B (2016) Kinematic and vorticity analyses of the western Idaho shear zone, USA. *Lithosphere* 9(2):223–234, ISSN 19474253
- Giorgis S, Tikoff B (2004) Constraints on kinematics and strain from feldspar porphyroclast populations. *Geological Society of London Special Publication* 224:265–285
- Goodman R E (1989) *Introduction to Rock Mechanics*. New York: John Wiley & Sons, Ltd., 2 edition
- Gray N H, Geiser P A, Geiser J R (1980) On the least-squares fit of small and great circles to spherically projected orientation data. *Mathematical Geology* 12(3):173–184
- Graziani R, Larson K P, Soret M (2020) The effect of hydrous mineral content on competitive strain localization mechanisms in felsic granulites. *Journal of Structural Geology* 134:104015, ISSN 0191-8141
- Griffin S, Daly L, Keller T, Piazzolo S, Forman L V, Lee M R, Baumgartner R J, Trimby P W, Benedix G K, Irving A J, Hoefnagels B (2022) Constraints on the emplacement of martian nakhlite igneous rocks and their source volcano from advanced micro-petrofabric analysis. *Journal of Geophysical Research: Planets* 127(6):e2021JE007080, e2021JE007080 2021JE007080
- Hammah R E, Curran J H (1999) On distance measures for the fuzzy k-means algorithm for joint data. *Rock Mechanics and Rock Engineering* 32(1):1–27
- Hansen L N, Zhao Y H, Zimmerman M E, Kohlstedt D L (2014) Protracted fabric evolution in olivine: Implications for the relationship among strain, crystallographic fabric, and seismic anisotropy. *Earth and Planetary Science Letters* 387:157–168, ISSN 0012821X
- Hidas K, Garrido C J, Tommasi A, Padrón-Navarta J A, Thielmann M, Konc Z, Frets E, Marchesi C (2013) Strain localization in pyroxenite by reaction-enhanced softening in the shallow subcontinental lithospheric mantle. *Journal of Petrology* 54(10):1997–2031, ISSN 00223530
- Hill G W (1981) Statistics for von Mises' and Fisher's Distributions of Directions:  $11(x)/I0(x)$ ,  $11.5(x)/I0.5(x)$  and Their Inverses. *ACM Transactions on Mathematical Software* 7(2):233–238
- Hills E S (1963) *Elements of Structural Geology*. London: Chapman & Hall
- Hobbs B, Means W D, Williams P F (1976) *An Outline of Structural Geology*. New York: Wiley
- Howarth R J (1999) Measurement, portrayal and analysis of orientation data and the origins of early modern structural geology (1670-1967). *Proceedings of the Geologists' Association* 110:273–309
- Howarth R J (2017) *Dictionary of Mathematical Geosciences*. Springer
- Hudson J A, Harrison J P (1997) *Engineering Rock Mechanics: An Introduction to the Principles*. Pergamon Press
- Hunter N J, Weinberg R, Wilson C, Luzin V, Misra S (2019) Quartz deformation across interlayered monomineralic and polymineralic rocks: A comparative analysis. *Journal of Structural Geology* 119(December 2018):118–134, ISSN 01918141
- Hunter N J, Weinberg R F, Wilson C J, Luzin V, Misra S (2018) Microscopic anatomy of a "hot-on-cold" shear zone: Insights from quartzites of the Main Central Thrust in the Alaknanda region (Garhwal Himalaya). *Bulletin of the Geological Society of America* 130(9-10):1519–1539, ISSN 19432674
- Issachar R, Levi T, Marco S, Weinberger R (2019) Strain Field Associated With a Component of Divergent Motion Along the Southern Dead Sea Fault: Insights From Magnetic Fabrics. *Tectonics* 38(1):335–353, ISSN 19449194
- Jaiswal A, Verma A, Singh T (2023) Evaluation of slope stability through rock mass classification and kinematic analysis of some major slopes along nh-1a from ramban to banihal, north western himalayas. *Journal of Rock Mechanics and Geotechnical Engineering* ISSN 1674-7755
- Jammalamadaka S R, Sengupta A (2001) *Topics in Circular Statistics*, volume 5 of Series on Multivariate Analysis. World Scientific
- Jammalamadaka S R, Terdik G (2022) Simulation and visualization of 3d-spherical distributions. In *Directional Statistics for Innovative Applications: A Bicentennial Tribute to Florence Nightingale*, Singapore: Springer Nature Singapore, ISBN 978-981-19-1044-9, 119–145
- Jimenez-Rodriguez R, Sitara N M S (2006) A spectral method for clustering of rock discontinuity sets. *International Journal of Rock Mechanics and Mining Sciences* 43:1052–1061
- Kamb W B (1959) Ice petrofabric observations from Blue Glacier, Washington, in relation to theory and experiment. *Journal of Geophysical Research* 64(11):1891–1909, ISSN 0148-0227
- Kanamori H (1978) The quantification of earthquakes. *Nature* 271:411–414
- Kelker D, Langenberg C W (1982) A mathematical model for orientation data from macroscopic conical folds. *Mathematical Geology* 12(4):289–307
- Kelker D, Langenberg C W (1987) A mathematical model for orientation data from macroscopic elliptical conical folds. *Mathematical Geology* 19(8):729–743
- Kelker D, Langenberg C W (1988) Statistical classification of macroscopic folds as cylindrical, circular conical, or elliptical conical. *Mathematical Geology* 20(6):717–730
- Kent J T (1982) The fisher-bingham distribution on the sphere. *Journal of the Royal Statistical Society B* 44(1):71–80
- Klose C D, Seo S, Obermayer K (2005) A new clustering approach for partitioning directional data. *International Journal of Rock Mechanics and Mining Sciences* 42(2):315–321, ISSN 13651609
- Knopf E B, Ingerson E (1938) *Structural petrology*. Memoir 6, Geological Society of America
- Kratinová Z, Ježek J, Schulmann K, Hrouda F, Shail R K, Lexa O (2010) Noncoaxial K-feldspar and AMS subfabrics in the Land's End granite, Cornwall: Evidence of magmatic fabric decoupling during late deformation and matrix crystallization. *Journal of Geophysical Research: Solid Earth* 115(9):1–21, ISSN 21699356
- Lambert F H (1772) *Anmerkungen und zusätze zur entwerfung der land und himmelscharten*. Leipzig: Verlag von Wilhelm Engelmann, 1894
- Larson K P (2018) Refining the structural framework of the Khimti Khola region, east-central Nepal Himalaya, using quartz textures and c-axis fabrics. *Journal of Structural Geology* 107(November 2017):142–152, ISSN 01918141
- Lejri M, Maerten F, Maerten L, Soliva R (2015) Paleostress inversion: A multi-parametric geomechanical evaluation of the Wallace-Bott assumptions. *Tectonophysics* 657:129–143, ISSN 00401951
- Li K, Wong C (1993) Random sampling from the watson distribution. *Communications in Statistics - Simulation and Computation* :997–1009
- Lisle R (1985) The use of the orientation tensor for the description and statistical testing of fabrics. *Journal of Structural Geology* 7:115–117
- Lisle R J, Leyshorn P R (2004) *Stereographic Projection Techniques for Geologists and Civil Engineers*. Cambridge: Cambridge University Press, 2 edition
- Llorens M G, Griera A, Bons P D, Roessiger J, Lebensohn R, Evans L, Weikusat I (2016) Dynamic recrystallisation of ice aggregates during co-axial viscoplastic deformation: A numerical approach. *Journal of Glaciology* 62(232):359–377, ISSN 00221430
- Llorens M G, Griera A, Bons P D, Weikusat I, Prior D J, Gomez-Rivas E, de Riese T, Jimenez-Munt I, García-Castellanos D, Lebensohn R A (2022) Can changes in deformation regimes be inferred from crystallographic preferred orientations in polar ice? *The Cryosphere* 16(5):2009–2024

- Long S P, Mullady C L, Starnes J K, Gordon S M, Larson K P, Pianowski L S, Miller R B, Soignard E (2019) A structural model for the South Tibetan detachment system in northwestern Bhutan from integration of temperature, fabric, strain, and kinematic data. *Lithosphere* 11(4):465–487, ISSN 19474253
- Mainprice D, Bachmann F, Hielscher R, Schaeben H (2015) Descriptive tools for the analysis of texture projects with large datasets using <math>\langle \text{MTEX} \rangle</math>: strength, symmetry and components. Geological Society, London, Special Publications 409(1):251–271, ISSN 0305-8719
- Mancktelow N S (1981) A least-squares method for determining the best-fit point maximum, great circle, and small circle to nondirectional orientation data. *Mathematical Geology* 13(6):507–521
- Mardia K, Gadsden R (1977) A small circle of best fit for spherical data and areas of vulcanism. *Applied Statistics* 26(3):238–245
- Mardia K, Jupp P (2000) *Directional Statistics*. Chichester, United Kingdom: John Wiley & Sons, Ltd.
- Mardia K V (1972) *Statistics of Directional Data*. London, New York: Academic Press
- Mardia K V, Zemroch P J (1977) Table of maximum likelihood estimates for the bingham distribution. *Journal of Statistical Computation and Simulation* 6(1):29–34
- Marrett R A, Allmendinger R W (1990) Kinematic analysis of fault-slip data. *Journal of Structural Geology* 12(8):973–986, ISSN 01918141
- Marshak S, Mitra G (1988) *Basic Methods of Structural Geology*. Prentice Hall
- Mauler A, Godard G, Kunze K (2001) Crystallographic fabrics of omphacite, rutile and quartz in vendee eclogites (armorican massif, france). consequences for deformation mechanisms and regimes. *Tectonophysics* 342:81–112
- McPherrren E D, Kuiper Y D (2013) The effects of Dissolution-Precipitation Creep on quartz fabrics within the Purgatory Conglomerate, Rhode Island. *Journal of Structural Geology* 51:105–117, ISSN 01918141
- Meier J, Datcheva M, Moser M, Schanz T (2009) Identification of constitutive and geometrical parameters for slope instability modelling - application to mountain-splitting area reutte/tyrol (austria). *Austrian Journal of Earth Sciences* 102:81–89
- Michibayashi K, Mainprice D, Fujii A, Uehara S, Shinkai Y, Kondo Y, Ohara Y, Ishii T, Fryer P, Bloomer S H, Ishiwatari A, Hawkins J W, Ji S (2016) Natural olivine crystal-fabrics in the western Pacific convergence region: A new method to identify fabric type. *Earth and Planetary Science Letters* 443(June):70–80, ISSN 0012821X
- Mikhailov A (2019) Turbo, an improved rainbow colormap for visualization. Google Research
- Moreland K (2015) Why we use bad color maps and what you can do about it. Sandia National Lab
- Mulchrone K F, Pastor-Galán D, Gutiérrez-Alonso G (2013) Mathematica code for least-squares cone fitting and equal-area stereonet representation. *Computers and Geosciences* 54:203–210, ISSN 00983004
- Mur A, Dormido R, Duro N, Dormido-Canto S, Vega J (2016) Determination of the optimal number of clusters using a spectral clustering optimization. *Expert Systems with Applications* 65:304–314, ISSN 0957-4174
- Mynatt I, Bergbauer S, Pollard D D (2007) Using differential geometry to describe 3-D folds. *Journal of Structural Geology* 29(7):1256–1266, ISSN 01918141
- Nemec W (1988) The shape of the rose. *Sedimentary Geology* 59(1):149–152, ISSN 0037-0738
- Nightingale F (1858) Mortality of the British army : at home and abroad, and during the Russian war, as compared with the mortality of the civil population in England. Harrison and Sons, Martin's Lane
- Núñez J R, Anderton C R, Renslow R S (2018) Optimizing colormaps with consideration for color vision deficiency to enable accurate interpretation of scientific data. *PLOS ONE* 13(7):1–14
- Okal E A (2011) Earthquake, focal mechanism. In Gupta H K, editor, *Encyclopedia of Solid Earth Geophysics*, Dordrecht: Springer Netherlands, ISBN 978-90-481-8702-7, 194–199
- Parker J (1942) Regional systematic jointing in slightly deformed sedimentary rocks. *Geological Society of America Bulletin* 53:381–408
- Pearce M A, Wheeler J, Prior D J (2011) Relative strength of mafic and felsic rocks during amphibolite facies metamorphism and deformation. *Journal of Structural Geology* 33(4):662 – 675, ISSN 0191-8141
- Peřestý V, Lexa O, Jeřábek P (2019) Restoration of early-variscan structures exposed along the tepláshear zone in the bohemian massif: constraints from kinematic modelling. *International Journal of Earth Sciences*
- Phillips F C (1954) *The use of stereographic projection in structural geology*. London: Edward Arnold
- Pollard D D, Fletcher R C (2005) *Fundamentals of Structural Geology*. Cambridge: Cambridge University Press
- Pollard D D, Saltzer S D, Rubin A M (1993) Stress inversion methods: are they based on faulty assumptions? *Journal of Structural Geology* 15(8):1045–1054, ISSN 01918141
- Press W H, Teukolsky S A, Vetterling W T, Flannery B P (2007) *Numerical Recipes: The Art of Scientific Computing*, 3rd edition. Cambridge University Press, Cambridge, 1235 p. Press, W.H, Teukolsky, S.A., Vetterling, W.T., and Flannery, B.P., 2007. *Numerical Recipes: The Art of Scientific Computing*. Cambridge: Cambridge University Press, 3 edition
- Quey R (2014) *Orientation Library: Documentation for 2.0.3, a collection of routines for orientation manipulation*. École Nationale Sup é rieur des Mines de Saint-Étienne, France.
- Ráček M, Lexa O, Schulmann K, Corsini M, Štípská P, Maierová P (2017) Re-evaluation of polyphase kinematic and  $^{40}\text{Ar}/^{39}\text{Ar}$  cooling history of Moldanubian hot nappe at the eastern margin of the Bohemian Massif. *International Journal of Earth Sciences* 106(2):397–420, ISSN 14373262
- Ragan D (2009) *Structural Geology: An Introduction to Geometrical Techniques*. Cambridge: Cambridge University Press, 4 edition
- Ramsay J (1980) Shear zone geometry: A review. *Journal of Structural Geology* 2(1):83 – 99, ISSN 0191-8141, shear zones in rocks
- Ramsay J G (1967) *Folding and Fracturing of Rocks*. New York: McGraw-Hill Book Company
- Rousseeuw P J (1987) Silhouettes: A graphical aid to the interpretation and validation of cluster analysis. *Journal of Computational and Applied Mathematics* 20:53–65, ISSN 0377-0427
- Sander B (1970) *An Introduction to the Study of Fabrics of Geological Bodies*, 1st English edition (Translated from Sander, 1948, 1950, German edition). Oxford: Pergamon Press
- Sango Otieno B, Anderson-Cook C M (2003) A more efficient way of obtaining a unique median estimate for circular data. *Journal of Modern Applied Statistical Methods* 2(1):168–176, ISSN 15389472
- Satsukawa T, Ildefonse B, Mainprice D, Morales L F, Michibayashi K, Barou F (2013) A database of plagioclase crystal preferred orientations (CPO) and microstructures-implications for CPO origin, strength, symmetry and seismic anisotropy in gabbroic rocks. *Solid Earth* 4(2):511–542, ISSN 18699510
- Schaeben H (1984) A new cluster algorithm for orientation data. *Journal of the International Association for Mathematical Geology* 16(2):139–153
- Scheidegger A (1965) On the statistics of the orientation of bedding planes, grain axes, and similar sedimentological data. *Geological Survey Professional Paper* 525:164–167
- Schmidt W (1925) Gefügestatistik. *Tschermaks Mineralogische und Petrographische Mitteilungen* 38:392–423
- Schubert E, Sander J, Ester M, Kriegel H P, Xu X (2017) Dbscan revisited, revisited: Why and how you should (still) use dbscan. *ACM Trans Database Syst* 42(3), ISSN 0362-5915
- Shanley R J, Mahtab M A (1975) Fractan: a computer code for analysis of clusters defined on the unit hemisphere. United States Bureau of Mines Circular 8671
- Shanley R J, Mahtab M A (1976) Delineation and analysis of clusters in orientation data. *Mathematical Geology* 8(1):9–23
- Silverman B W (1986) *Density estimation for statistics and data analysis*. Chapman & Hall

- Singleton J S, Mosher S (2012) Mylonitization in the lower plate of the Buckskin-Rawhide detachment fault, west-central Arizona: Implications for the geometric evolution of metamorphic core complexes. *Journal of Structural Geology* 39:180–198, ISSN 01918141
- Smith N J, van der Walt S, Firing E (2015) *New matplotlib colormaps*. GitHub
- Snyder J P (1987) *Map projections: A working manual*. Professional Paper 1395, United States Geological Survey
- Sperner B, Zweigel P (2010) A plea for more caution in fault-slip analysis. *Tectonophysics* 482(1-4):29–41, ISSN 00401951
- Sra S (2012) A short note on parameter approximation for von mises-fisher distributions: and a fast implementation of  $i s(x)$ . *Computational Statistics* 27(1):177–190
- Stesky R M (1985) Least-squares fitting of a noncircular cone. *Computers and Geosciences* 11(4):357–368, ISSN 00983004
- Streckeisen A (1976) To each plutonic rock its proper name. *Earth-Science Reviews* 12(1):1–33
- Swan A R N, Sandilands M (1995) *Introduction to Geological Data Analysis*. Oxford: Blackwell Science
- Swinbank R, Purser R J (2006) Fibonacci grids: a novel approach to global modeling. *Quarterly Journal of the Royal Meteorological Society* 132(619):1769–1793
- Sykes L R (1967) Mechanism of earthquakes and nature of faulting on the mid-oceanic ridges. *Journal of Geophysical Research* (1896-1977) 72(8):2131–2153
- Tauxe L (2003) *Paleomagnetic Principles and Practice*. Springer
- Taylor C C (2008) Automatic bandwidth selection for circular density estimation. *Computational Statistics and Data Analysis* 52(7):3493–3500
- Terzaghi R D (1965) Sources of errors in joint surveys. *Geotechnique* 15:287–304
- Tikoff B, Wojtal S F (1999) Displacement control of geologic structures. *Journal of Structural Geology* 21(8-9):959–967, ISSN 01918141
- Tommasi A, Vauchez A, Ionov D A (2008) Deformation, static recrystallization, and reactive melt transport in shallow subcontinental mantle xenoliths (tok cenozoic volcanic field, SE siberia). *Earth and Planetary Science Letters* 272(1-2):65–77
- Turner F, Weiss L (1963) *Structural Analysis of Metamorphic Tectonites*. New York: McGraw-Hill Book Company
- Twiss R J, Moores E M (2007) *Structural Geology*. New York: W.H. Freeman, 2 edition
- Twiss R J, Unruh J R (1998) Analysis of fault slip inversions: do they constrain stress or strain rate? *Journal of Geophysical Research* 103(B6):12205–12222, ISSN 0148-0227
- Ulrich S, Mainprice D (2005) Does cation ordering in omphacite influence development of lattice-preferred orientation? *Journal of Structural Geology* 27(3):419–431, ISSN 01918141
- Van der Pluijm B, Marshak S (2004) *Earth Structure*. New York: W. W. Norton, 2 edition
- Vauchez A, Dineur F, Rudnick R (2005) Microstructure, texture and seismic anisotropy of the lithospheric mantle above a mantle plume: Insights from the Labait volcano xenoliths (Tanzania). *Earth and Planetary Science Letters* 232(3-4):295–314, ISSN 0012821X
- Vérard C, Hochard C, Stampfli G (2012) Non-random distribution of euler poles: Is plate tectonics subject to rotational effects? *Terra Nova* 24(6):467–476, ISSN 09544879
- Vollmer F W (1981) *Structural studies of the Ordovician flysch and melange in Albany County, New York*. Master's thesis, State University of New York at Albany
- Vollmer F W (1985) *A structural study of the Grovudal fold-nappe, western Norway*. Ph.D. thesis, University of Minnesota, Minneapolis
- Vollmer F W (1988) A computer model of sheath-nappes formed during crustal shear in the western gneiss region, central norwegian caledonides. *Journal of structural geology*, v. 10, p. 735-743. vollmer, f.w., 1988. a computer model of sheath-nappes formed during crustal shear in the western gneiss region, central norwegian caledonides. *Journal of Structural Geology* 10:735–743
- Vollmer F W (1989) A triangular fabric plot with applications for structural analysis. *Eos Transactions American Geophysical Union* 70:463
- Vollmer F W (1990) An application of eigenvalue methods to structural domain analysis. *Geological Society of America Bulletin* 102(6):786–791, ISSN 00167606
- Vollmer F W (1993) A modified kamb method for contouring spherical orientation data. *Geological Society of America Abstracts with Programs* 25:170
- Vollmer F W (1995) C program for automatic contouring of spherical orientation data using a modified Kamb method. *Computers & Geosciences* 21(1):31–49, ISSN 00983004
- Vollmer F W (2011) Automatic contouring of two-dimensional finite strain data on the unit hyperboloid and the use of hyperboloidal stereographic, equal-area and other projections for strain analysis. *Geological Society of America Abstracts with Programs* 43(5):605
- Vollmer F W (2015) Orient 3: A new integrated software program for orientation data analysis, kinematic analysis, spherical projections, and schmidt plots. *Geological Society of America Abstracts with Programs* 47(7):49
- Vollmer F W (2018) Automatic contouring of geologic fabric and finite strain data on the unit hyperboloid. *Computers & Geosciences* 115:134–142
- Vollmer F W (2020) Representing progressive fabric paths on a triangular plot using a fabric density index and crystal axes eigenvector barycenters. *Geological Society of America Abstracts with Programs* 52(6)
- Vollmer F W (2022) An eigenvalue based k-means approach to geologic cluster analysis. *Geological Society of America Abstracts with Programs* 54(5)
- Vollmer F W, Walker J (2009) The classic Barrovian metamorphic sequence of Dutchess County and its structural and stratigraphic context in the Taconic Orogeny, volume 81, chapter 11. *New York State Geological Association*, 11.1–11.20
- Wallace R E (1951) Geometry of shearing stress and relation to faulting. *The Journal of Geology* 59(2):118–130
- Warren L M, Hughes A, Silver P G (2007) Earthquake mechanics and deformation in the tonga-kermaDEC subduction zone from fault plane orientations of intermediate- and deep-focus earthquakes. *Journal of Geophysical Research Atmospheres* 112
- Watson G (1966) The statistics of orientation data. *The Journal of Geology* 74(5):786–797
- Welker A J, Hogan J P, Eckert A, Tindall S, Liu C (2019) Conical folds – An artefact of using simple geometric shapes to describe a complex geologic structure. *Journal of Structural Geology* 123(January):96–104, ISSN 01918141
- Whitten E H T (1966) *Structural Geology of Folded Rocks*. Chicago: Rand McNally
- Wilson C J, Hunter N J, Luzin V, Peternell M, Piazzolo S (2019) The influence of strain rate and presence of dispersed second phases on the deformation behaviour of polycrystalline D2O ice. *Journal of Glaciology* 65(249):101–122, ISSN 00221430
- Wilson G (1967) The geometry of cylindrical and conical folds. *Proceedings of the Geologists' Association* 78(1):179–209
- Woodcock N (1977) Specification of fabric shapes using an eigenvalue method. *Geological Society of America Bulletin* 88:1231–1236
- Wyllie D C (2017) *Rock Slope Engineering: Civil Applications*. CRC Press, 5 edition
- Wyllie D C, Mah C W (2005) *Rock Slope Engineering: Civil and Mining*. Spon Press, 4 edition
- Yamaji A (2000) The multiple inverse method applied to meso-scale faults in mid-Quaternary fore-arc sediments near the triple trench junction off central Japan. *Journal of Structural Geology* 22(4):429–440, ISSN 01918141
- Yamaji A (2008) Theories of strain analysis from shape fabrics: A perspective using hyperbolic geometry. *Journal of Structural Geology* 30:1451–1465
- Yamaji A, Sato K (2011) Clustering of fracture orientations using a mixed Bingham distribution and its application to paleostress analysis from dike or vein orientations. *Journal of Structural Geology* 33(7):1148–1157, ISSN 01918141
- Zadeh L A (1965) Fuzzy sets. *Information and Control* 8(3):338–353
- Zhao Q, Fränti P (2014) Wb-index: A sum-of-squares based index for cluster validity. *Data & Knowledge Engineering* 92:77–89, ISSN 0169-023X
- Zuza A V, Cao W, Rodriguez-Arriaga A, DesOrmeau J W, Odlum M L (2022) Strain localization at brittle-ductile transition depths during miocene magmatism and exhumation in the southern basin and range. *Journal of Structural Geology* 163:104709, ISSN 0191-8141



## FAQ

- *How do I cite Orient?*  
See section *Preface Citation*.
- *Does Orient support dip direction?*  
Yes, Orient has always supported dip direction, although strike is the default. Use the *Data - Orientation Formats* command to set the default to *Dip Direction*. When reading data from a spreadsheet use the header *Dip Direction* instead of *Strike*. The British version of the right hand rule, *StrikeB* is also supported.
- *Why aren't my kinematic maxima (LS and PMT axes) orthogonal?*  
For *unlinked* data, LS and PMT maxima are not guaranteed to be orthogonal because they are calculated using five orientation matrices,  $\Omega$  (Eq 4.6). For *linked* data, LS and PMT are calculated using two matrices  $\Omega_L$  (Eq 9.1). PMT are orthogonal, and LS are orthogonal, but LS are not guaranteed to be orthogonal to M. For *frames* (Section 10), LMS and PMT are guaranteed to be orthogonal. This approach, however, does not work well for poorly clustered data.

## Appendix I

Orient's default *sinusoid* colormap is formed by the sinusoidal interpolation of the colors blue, cyan, yellow and red (BCYR). It is similar to the *jet* colormap, but is lighter at the extrema and has wider color bands in the cyan and yellow hues. See Figure 1.11 for an example data plot. Figure 16.9a compares sinusoid and jet, and Figure 16.9b is a plot of the relative values of the RGB components.

MATLAB/Octave code to generate it is given below. Acknowledgment is appreciated, but no copyright or other claim of ownership is made on the generated colormap. The code is released under the MIT license.

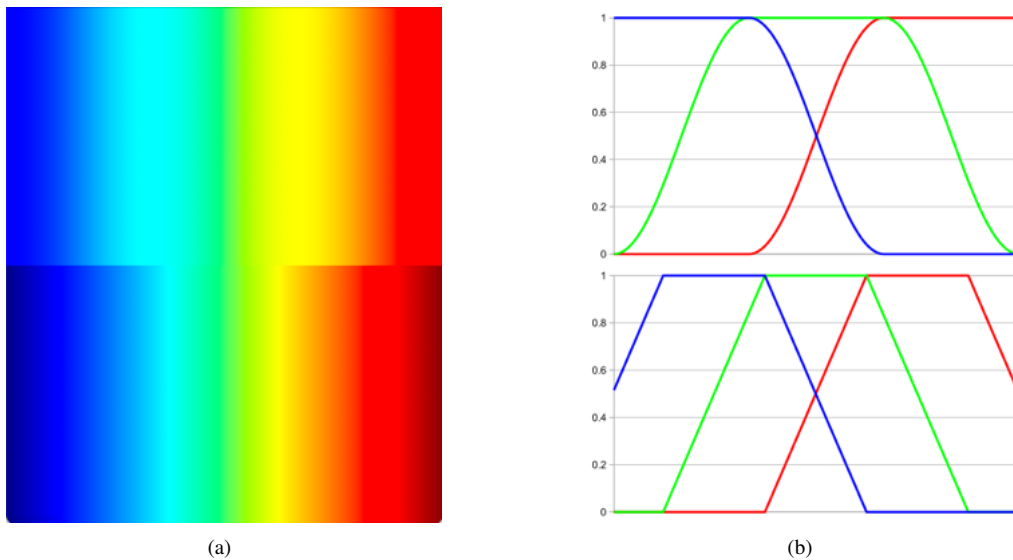


Figure 16.9: (a) Comparison of the sinusoid (top) and the jet (bottom) colormaps. (b) Plot of the relative values of the RGB components in the sinusoid (top) and jet (bottom) colormaps.

```
% MATLAB/Octave sinusoid colormap
% Notice: Copyright 2023-2024 Frederick W. Vollmer
% License: MIT license
% Usage: colormap sinusoid(256)

function c = sinusoid(n)
    % Colormap by sinusoidal interpolation among blue, cyan, yellow, and red.
    c = zeros(n,3);
    for i = 1:n
        c(i,1:3) = sinterp4([0 0 1], [0 1 1], [1 1 0], [1 0 0], (i-1)/(n-1));
    end

function c = sinterp2(c0, c1, t)
    % Sinusoidal interpolation between two colors, t = [0..1].
    f = 0.5 * (sin(t*pi - 0.5*pi) + 1.0);
    c = (1-f) * c0 + f * c1;

function c = sinterp4(c0, c1, c2, c3, t)
    % Sinusoidal interpolation among four colors, t = [0..1].
    if t < 1/3
        c = sinterp2(c0, c1, t*3);
    elseif t < 2/3
        c = sinterp2(c1, c2, t*3-1);
    else
        c = sinterp2(c2, c3, t*3-2);
    end
```

This page intentionally left blank

